UNIVERSIDAD COMPLUTENSE DE MADRID
FACULTAD DE CIENCIAS QUÍMICAS
Departamento de Química Orgánica

TESIS DOCTORAL

Design and synthesis of small molecules for photo voltaics

Diseño y síntesis de moléculas pequeñas para fotovoltaica

MEMORIA PARA OPTAR AL GRADO DE DOCTOR

PRESENTADA POR

Rafael Sandoval Torrientes

Directores

Nazario Martín León
José Manuel Santos Barahona

Madrid, 2018

UNIVERSIDAD COMPLUTENSE DE MADRID
FACULTAD DE CIENCIAS QUÍMICAS
Departamento de Química Orgánica I

UNIVERSIDAD
COMPLUTENSE
MADRID

TESIS DOCTORAL

Design and synthesis of small molecules for photovoltaics

Diseño y síntesis de moléculas pequeñas para fotovoltaica

MEMORIA PARA OPTAR AL GRADO DE DOCTOR

PRESENTADA POR

Rafael Sandoval Torrientes

Directores
Nazario Martín León
José Manuel Santos Barahona

Madrid, 2017

UNIVERSIDAD COMPLUTENSE DE MADRID
FACULTAD DE CIENCIAS QUÍMICAS
Departamento de Química Orgánica I

UNIVERSIDAD
COMPLUTENSE
MADRID

DESIGN AND SYNTHESIS OF SMALL MOLECULES FOR PHOTOVOLTAICS

DISEÑO Y SÍNTESIS DE MOLÉCULAS PEQUEÑAS PARA FOTOVOLTAICA

TESIS DOCTORAL

Rafael Sandoval Torrientes

Madrid, 2017

UNIVERSIDAD
COMPLUTENSE
MADRID

DESIGN AND SYNTHESIS OF SMALL MOLECULES FOR PHOTOVOLTAICS

DISEÑO Y SÍNTESIS DE MOLÉCULAS PEQUEÑAS PARA FOTOVOLTAICA

Directores:

Nazario Martín León
José Manuel Santos Barahona

Memoria que para optar al grado de
DOCTOR EN CIENCIAS QUÍMICAS
presenta

Rafael Sandoval Torrientes

Madrid, 2017

D. Nazario Martín León, Catedrático de Universidad del Departamento de Química Orgánica I de la Universidad Complutense de Madrid y **D. José Manuel Santos Barahon**a, Investigador del Departamento de Química Orgánica I de la Universidad Complutense de Madrid,

CERTIFICAN

Que la presente Memoria titulada "Design and synthesis of small molecules for photovoltaics" se ha realizado bajo su dirección en el Departamento de Química Orgánica I de la Universidad Complutense de Madrid, por el licenciado en Química D. Rafael Sandoval Torrientes y autorizan su presentación para ser calificada como tesis doctoral.

Y para que conste, firmo el presente certificado en Madrid a 28 de Marzo de 2017.

Fdo. Dr. Nazario Martín León Fdo. Dr. José Manuel Santos Barahona

The results presented in this thesis have been partially published in the listed below:

1) R. Sandoval-Torrientes, J. Calbo, D. García-Fresnadillo, J. Santos, E. Ortí, N. Martín, *Org. Chem. Front*., **2017**, DOI: 10.1039/C6QO00760K.

2) R. Sandoval-Torrientes, J. Calbo, W. Matsuda, W. Choi, J. Santos, S. Seki, E. Ortí, N. Martín, *ChemPlusChem* **2017**, DOI: 10.1002/cplu.201700047.

Para empezar un proyecto hace falta valentía,

pero para acabarlo hace falta perseverancia.

"Anónimo"

Acknowledgments

El presente trabajo ha sido realizado en el Departamento de Química Orgánica de la Universidad Complutense de Madrid bajo la dirección del Prof. Nazario Martín y del Dr. José Santos.

Querría comenzar dando las gracias a mis dos directores:

Nazario, gracias por brindarme tu confianza desde el primer día que toqué la puerta de tu despacho para poder pertenecer todos estos años a tu grupo de investigación. Gracias por transmitirme tus conocimientos e inquietudes y más sobre todo por dedicar mucho de tu tiempo para sacar este trabajo adelante. Ha sido un placer y un honor el pertenecer a este grupo de investigación y estaré eternamente agradecido contigo, ya que hiciste que mi sueño se hiciera realidad.

Jose, gracias por guiarme y enseñarme tanta química durante el día a día. Echaré de menos todas nuestras discusiones de química y no química, que tantos buenos momentos nos han dado. Creo que no solo has sido mi director, también te has convertido en un amigo. De verdad, gracias.

También me gustaría nombrar a otra persona que en su pasado perteneció al grupo: Gracias Juan Luis. Nuestro breve encuentro a principio de todo esto me hizo aprender la dinámica de este grupo de una manera eficaz y rápida. Un placer haber trabajado y aprendido contigo.

En la realización de este trabajo han participado otros grupos de investigación a los que agradezco enormemente su colaboración y contribución:

Al grupo de investigación del Prof. Vladimir Dyakonov de la Universidad de Würzburg (Alemania) por las medidas fotovoltaicas de las células solares orgánicas, al grupo de investigación Prof. Shu Seki de la Universidad de Kyoto (Japón) por los estudios de conductividad que se recogen en este trabajo, al grupo de investigación del Prof. Enrique Ortí del Instituto de Ciencia Molecular, Universidad de Valencia (Paterna) por los cálculos teóricos también recogidos en esta memoria, al grupo del Prof. Nazeeruddin de la Escuela Politécnica Federal de Lausane (Suiza) por las medidas fotovoltaicas de las células solares de tipo perovskita.

Al grupo del Dr. Larry Lüer de IMDEA Nanociencia (Madrid), que me ayudaron a comprender los procesos físicos de las células solares orgánicas.

A continuación, me gustaría agradecer a todos los compañeros, excompañeros y amigos del laboratorio, por todo lo que ha significado tenerlos tan cerca:

Los químicos no pertenecientes al grupo que me acogieron en mi llegada a Madrid: Florencio, Esther, Josué, Mercedes y Luis, nuestros comienzos fueron duros pero teneros cerca hizo que todo fuera mucho más fácil. Gracias.

Agradecer a los químicos más mayores del grupo: Mª Ángeles, Salvo, Beti, Carmen, David, Ángel, Andreas, y por supuesto a las secretarias Virginia, Helena y Ana por estar siempre disponible para cualquier consulta y hacer que todo fluya y funcione.

Toda la gente del laboratorio de la Complutense, Los que están en mi misma situación: Sara, Marina y Sonia. A todos los que vienen detrás pisando fuerte: Mikiko, Rosa, Antonio, Alfonso, Valentina, Andrés, Alicia. A los doctores: Laura, Marta, Chus, Paul. a los que ya se fueron: Muchachito, María, Javi, Tony. Con todos y cada uno he compartido algún que otro momento, haciéndome sentir muy a gusto.

A mis compañeros y amigos IMDEANOS del laboratorio: Inés, fuiste la primera persona que me encontré nada más llegar al instituto, gracias por poner el punto sensato en el laboratorio y por compartir todos y cada uno de los momentos. Agus, gracias por compartir tus experiencias y tu conocimiento, y por todas las veces que has tenido que aguantar mis bromas. Javi, tu llegada al grupo para mi supuso un punto y aparte, compañero de vitrinas y de muchas otras cosas. Gracias por ser como eres, por ayudarme siempre que te lo he pedido y por tu paciencia con mis días no tan buenos. En general quería deciros que no creo que encuentre nunca un grupo de trabajo tan humano en el que haya tan buena energía de trabajo.

Alejandro y Alberto IMDEANOS de fuera del grupo, desearos todo lo mejor en vuestra nueva etapa y agradeceros siempre vuestra ayuda para cualquier cosa pero sobre todo para el cambio de disolventes anhidros.

Así mismo, quiero agradecer al CAI de RMN, al laboratorio de RMN de IMDEA, destacando a Javi por sus charlas sobre resonancia y fútbol y al SIDI de la Universidad Autónoma de Madrid, por su gran ayuda y dedicación en la realización de experimentos, siempre un trato excepcional.

Pasando ahora al resto de gente fuera del ámbito químico: Gracias a mis amigos de Miranda de Ebro, siempre apoyando y aguantando mis fricadas. Dani y Rober por echarme no una, sino dos manos con la portada.

A mis excompañeros de piso el italiano Antonio y el griego Christos, hicisteis que mi estancia en Madrid durante esos años fuera muy amena y cómoda .

Y para terminar, las personas más importantes de mi vida:

A mis abuelos, gracias por quererme tantísimo y confiar siempre en mí, dándome vuestro apoyo en la lejanía, oír vuestra voz por el teléfono me ha llenado de energía para poder seguir hacia mi meta. De vosotros he aprendido que hay que ser valiente en esta vida y sobre todo decidido.

Elia y Chechu, ambos hacéis que cada reunión familiar sea única. Gracias por estar ahí.

A Jordan y a Julio, mi primo aunque casi mi hermano y mi tío, siempre me habéis hecho reír y habéis compartido conmigo tantos buenos momentos, que faltaba menos el no poneros en la dedicatoria. Sois todo corazón y nobleza. Gracias.

A mis padres, que han sido y serán durante tantos años mi vital punto de apoyo, me comprenden y se preocupan por todas y cada una de las cosas que hago o que decido. Sabéis que el camino hasta llegar aquí no ha sido nada fácil, y es por esto que os quiero agradecer vuestra total confianza en mí. Sois todo un ejemplo a seguir, os debo todo lo que soy y mi máxima admiración por vosotros.

A mi hermana, la persona que más echo de menos cuando estoy lejos, gracias por tu amistad y cariño y por saber que puedo contar contigo para cualquier cosa, estoy orgullosísimo de ti y sé que llegarás a ser lo que te propongas porque para mí, tú lo vales.

A Silvia, mi compañera de viaje, son muchas las cosas que podría decirte en agradecimiento de esta memoria. Has estado a mi lado durante buena parte de la tesis y decirte que sin tu apoyo diario y tu saber escuchar y aconsejar nada de esto se hubiera hecho posible. Me siento muy afortunado de haberme cruzado contigo.

Table of Contents

Index of abbreviations and acronyms **1**

Summary **5**

Resumen **15**

Introduction **25**

Chapter 1. Small molecules for organic solar cells

1.1. Background **33**

1.1.1. Architectures of OSC 33

1.1.2. OSC functioning mechanism 35

1.1.3. Loss processes: charge recombination 38

1.1.4. Photovoltaic parameters 40

1.1.5. A brief survey of OSCs 42

1.1.6. Non-fullerenic acceptors based OSCs 46

1.1.7. Small molecule donors (SMD) for OSCs 48

1.2. Objectives **57**

1.2.1. A-D-A structures 57

1.2.2. D-A-D structures 58

1.3. Results and discussion **63**

1.3.1. A-D-A Small molecules based on BDT-BTD 63

1.3.2. D-A-D Small molecules based on rhodanine acceptors 81

1.3.2.1. 1st Generation D-A-D small molecules 81

1.3.2.2. 2nd Generation D-A-D small molecules 96

1.4. Conclusions **109**

1.4.1. A-D-A Small molecules based on BDT-BTD 109

1.4.2. D-A-D Small molecules based on rhodanine acceptors 109

1.4.2.1. 1st Generation D-A-D small molecules 109

1.4.2.2. 2nd Generation D-A-D small molecules 110

1.5. Experimental section 113

1.5.1. Synthesis of A-D-A small molecules based on BDT-BTD 113

1.5.2. Synthesis of D-A-D small molecules based on rhodanine acceptors 123

1.5.2.1. 1st Generation D-A-D small molecules 123

1.5.2.2. 2nd Generation D-A-D small molecules 132

Chapter 2. Small molecules as hole transporting material for perovskite solar cells.

2.1. Background 145

2.1.1. Structure 145

2.1.2. Brief history of perovskites 146

2.1.3. Charge transporting layers 150

2.1.4. Perovskite solar cells functioning mechanism 151

2.1.5. A brief survey of HTMs 152

2.2. Objectives 163

2.2.1. Hemi-spiro HTMs 163

2.2.2. HTMs with different electron donor strength based on dibenzothiophene (DBT) 164

2.2.3. HTMs with planar central core based on anthradithiophene (ADT) 164

2.2.4. HTMs bearing four donor groups 164

2.3. Results and discussion 169

2.3.1. Hemi-spiro HTMs 169

2.3.2. HTMs based on dibenzithiophene (DBT) 179

2.3.3. HTMs based on anthradithiophene (ADT) 186

2.3.4. HTMs bearing four donor groups 194
2.4. Conclusions.....205
2.4.1. Hemi-spiro HTMs.....205
2.4.2. HTMs based on dibenzithiophene (DBT).....205
2.4.3. HTMs based on anthradithiophene (ADT) 206
2.4.4. HTMs bearing four donor groups 206
2.5. Experimental section 211
2.5.1. Synthesis of Hemi-spiro HTMs 211
2.5.2. Synthesis of HTMs based on dibenzithiophene (DBT) 214
2.5.3. Synthesis of HTMs based on anthradithiophene (ADT).....217
2.5.4. Synthesis of HTMs bearing four donor groups.....220
References 225

Index of abbreviations and acronyms

The following terms have been used in this manuscript:

A	acceptor
a.u.	arbitrary units
AFM	atomic force microscopy
BDT	benzodithiophene
BHJ	bulk heterojunction
BINAP	(±)-2,2’-Bis(diphenylphosphino)-1,1’-binaphthyl
c	speed of light
CIGS	copper indium gallium diselenide
CN-PPV	cyano-polyphenylenevinylene
CT	charge transfer
CuPc	copper phthalocyanine
CV	cyclic voltammetry
D	donor
D	diffusion coefficient
d	doublet
dd	double doublet
DFT	density functional theory
DPM-12	1,1-bis(4,4’-dodecyloxyphenyl)-(5,6) C_{61}
DSSC	dye-sensitized solar cell
DPA	diphenylamine
DSC	differential scanning calorimetry
DTP	dithienopyrrole
DTS	dithienosilole
e	electron
EQE	external quantum efficiency
FF	fill factor
h	Planck’s constant
HOMO	highest occupied molecular orbital
HTM	hole transporting material
ICT	internal charge transfer
IQE	internal quantum efficiency
ITO	indium-tin-oxide
J_0	incident light density
J_{SC}	short-circuit current density

L_D	exciton diffusion length
LUMO	lowest unoccupied molecular orbital
MDMO-PPV	poly[2-methoxy-5-(3',7'-dimethyloctyloxy)-1,4-phenylenevinylene]
MEH-PPV	poly[2-methoxy,5-(2'-ethyl-hexyloxy)-1,4-phenylenevinylene]
NDI	naphthalenediimide
N_e	number of photoinduced charges extracted out of the cell
NHE	normal hydrogen electrode
N_{photon}	number of incident photons
OFET	organic field effect transistor
OPV	organic photovoltaic
OSC	organic solar cell
P3HT	poly(3-hexylthiophene)
$PC_{61}BM$	[6,6']-Phenyl-C_{61}-butyric-acid-methyl ester
$PC_{71}BM$	[6,6']-Phenyl-C_{71}- butyric-acid-methyl ester
PCE	power conversion efficiency
PDI	perylenediimide
PTD	pyridothiadiazole
PV	photovoltaic
P_{inc}	incident power
q	charge of the electron
Rh	rhodanine
rr	regioregular
s	singlet
SC	solar cells
SMD	small molecule donor
SubPC	subphthalocyanines
t	triplet
TGA	thermogravimetric analysis
Th	thiophene
TPA	triphenylamine
TRMC	time-resolved microwave conductivity
UV-vis	ultraviolet-visible
V_{OC}	open circuit voltage
XRD	X-ray diffraction
λ	wavelength
τ_0	exciton lifetime

Summary

Design and synthesis of small molecules for photovoltaics

Introduction

The current energetic regime, which relies on non-renewable polluting energy sources, is unsustainable from societal, economical, geopolitical, and environmental points of view. The only fully renewable source able to meet world's huge and always growing energy demand is solar energy. Photovoltaic technologies, directly converting sunlight into electricity, represent one of the most promising candidates to meet this demand.

Objectives

Chapter 1: Development of new small molecules for organic solar cells (OSC).

Chapter 2: Development of new small molecules as hole transporting materials (HTM) for perovskite solar cells.

Results and Discussion

Chapter 1. *Small molecules for organic solar cells*

i) A−D−A Small molecules based on BDT-BTD

Electroactive molecules featuring A−D−A architecture that employ some of the best performing electron donor and acceptor fragments found in the literature, namely benzodithiophene (BDT, as donor) and benzothiadiazole (BTD, as acceptor) have been designed and synthesized. Thiophene bridges of increasing length have been inserted in between A and D moieties (Figure S1a) in order to improve the absorption and aggregation properties.

Optical, electrochemical and computational studies have revealed their electroactive nature and their ability to form well-ordered crystalline thin films. Photovoltaic devices employing these materials as donors in blends with fullerene derivatives showed poor performances, with best performing material (**31**) providing 0.72% PCE (Figure S1b).

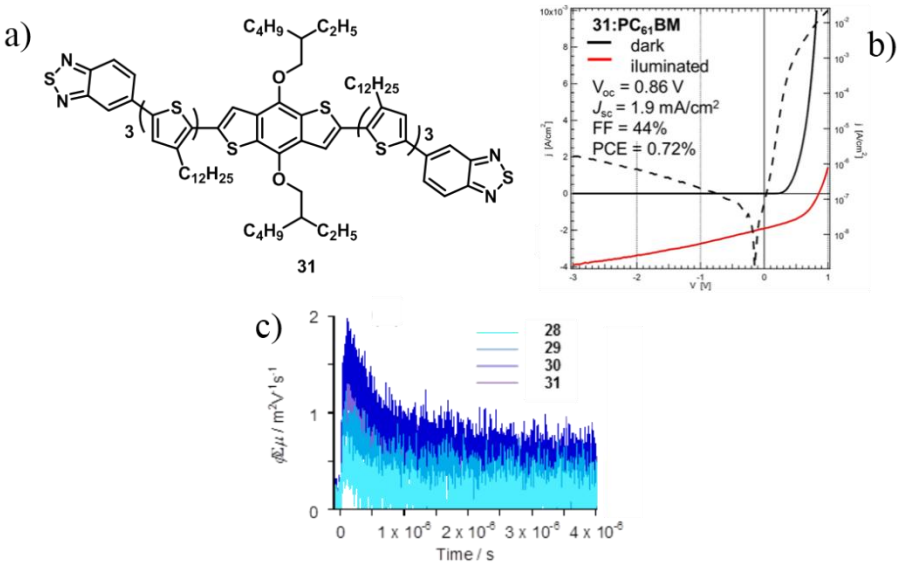

Figure S1. a) Molecular structure of compound **31**. b) Photovoltaic parameters of **31**-device. c) Kinetic traces of the transient conductivity.

Time resolved microwave conductivity (TRMC) studies unveiled that these new molecules just presented n-type charge transport. Remarkably, high electron mobilities of around 0.1 $cm^2\ V^{-1}\ s^{-1}$ were measured (Figure S1c).

ii) D−A−D Small molecules based on rhodanine acceptors

D−A−D architectures are not as common as their A−D−A counterparts. In this regard, the main challenge was finding an appropriate acceptor core. Rhodanine is a great acceptor group that provides excellent photovoltaic performances.

a) 1st Generation D-A-D small molecules

A series of D−A−D small molecules bearing different rhodanine acceptors and butyltriarylamine donors (Figure S2a) have been designed and synthesized. The use of D and A units of different strength allowed obtaining dyes with the ability to harvest light in the entire optical range of the visible spectrum (400-800 nm).

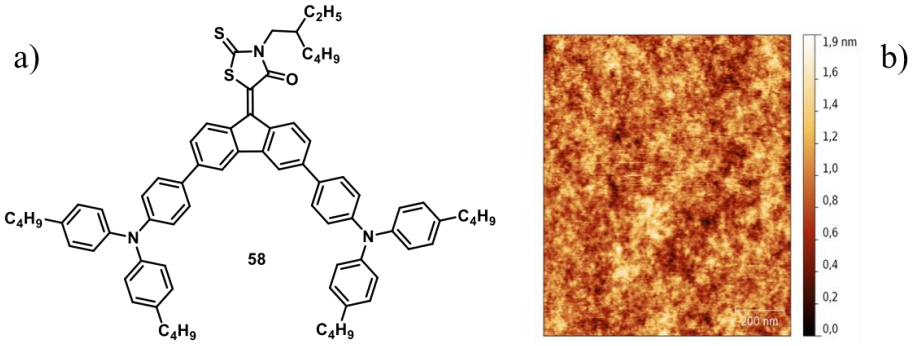

Figure S2. a) Molecular structure of compound **58**. b) AFM image of **58**/$PC_{71}BM$ blend in film.

Obtained materials blended with fullerene derivatives were employed to fabricate OSC. The low performance of the devices (PCE < 0.25%) was explained by AFM studies that revealed smooth morphologies lacking the necessary granulation to produce percolative pathways for charges to the electrodes (Figure S2b).

b) 2nd Generation D-A-D small molecules

Keeping the same D/A motifs of the 1st generation materials, new ones were designed and synthesized by removing butyl side-chains from the triarylamines. In this case, arylamines with substituents that provide varying donor strength (TPA, TPA-Me, TPA-OMe, and DPA-OMe) were introduced (Figure S3a).

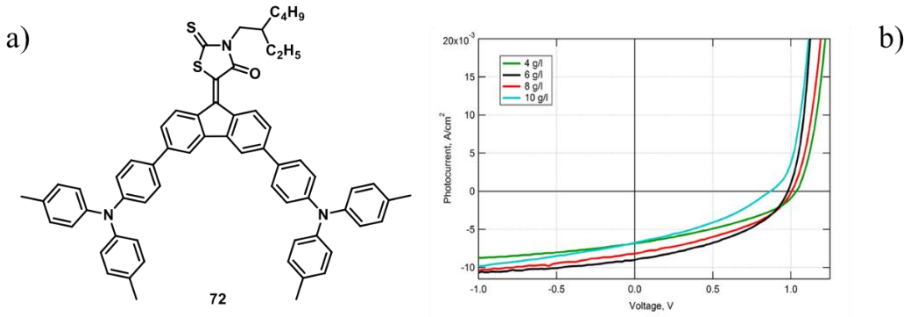

Figure S3. a) Molecular structure of compound **72**. b) *J*/*V* curves showing the effect of thickness within active layer over the photovoltaic performance of **72** based devices.

Photovoltaic studies evidenced that the effect of thickness within the active layer over photovoltaic performance is crucial and a PCE of 3.7% was reached by **72** blended with $PC_{71}BM$ in a 1:3 ratio (Figure S3b).

Chapter 2. *Small molecules for perovskite solar cells*

i) Hemi-spiro HTMs

With the aim of finding new HTMs that may outperform spiro-OMeTAD, new derivatives displaying hemi-spiro structure were synthesized (Figure S4a). The new derivatives present good thermal stability within the operating temperature range of the cells. Spectroscopic and electrochemical characterizations allowed calculating HOMO/LUMO values. Devices fabricated with **98** and **99** showed moderate efficiencies of PCE 13.5% and 14.6 %, respectively, presenting pronounced hysteresis (Figure S4b).

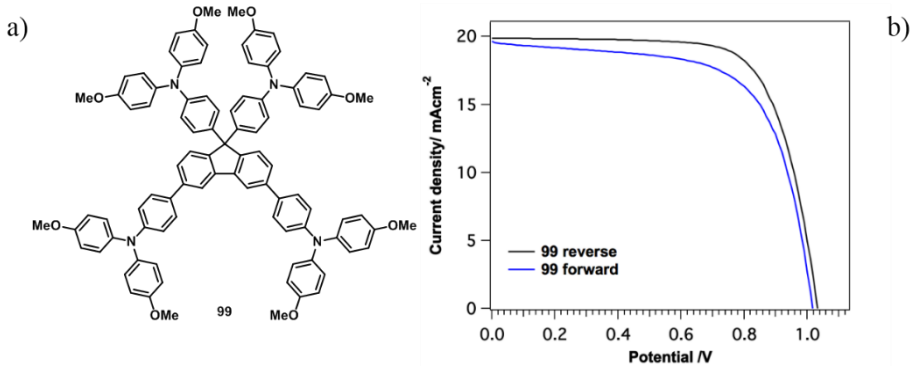

Figure S4. a) Representative example of hemi-spiro structure. b) *J*/*V* curves of **99**:$MAPbI_3$ device.

ii) HTMs based on dibenzothiophene (DBT)

With the aim of exploring different central cores for the development of new HTMs, a series of compounds using DBT as central core were synthesized (Figure S5a). Electron donors of different strength were employed as pendant groups (*i.e.* diphenylamine, triphenylamine and phenothiazine). Spectroscopic characterization of the compounds revealed HOMO energy levels of −5.23 and −5.36 eV for compounds **105** and **104**, respectively. The obtained values are lower in energy than the HOMO of spiro-OMeTAD (−5.16 eV) and close to the valence band of the perovskite. As shown in Figure S5b, the performance of the perovskite devices employing **104**−**106** as HTMs gave rise to poor to

moderate PCE values. Values ranging from 4.0% for **104** to 12.7% for **106** were obtained.

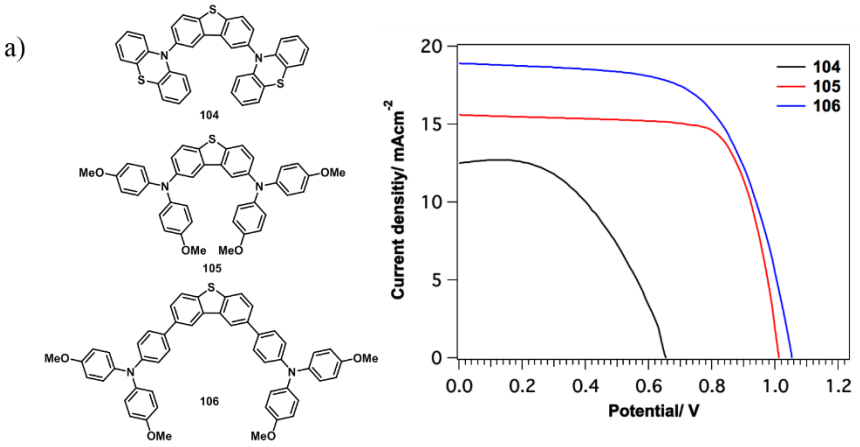

Figure S5. a) Series of HTMs based on DBT. b) *J*/*V* curves of compounds **104**-**106** (right).

iii) HTMs based on anthradithiophene (ADT)

The use of an anthracene core with two fused thiophene rings yielded the distinctive building block of ADT, to which DPA and TPA strong donors were attached (Figure S6a). The resulting materials showed excellent thermal properties. A PCE of 17.6% was reached by compound **113** featuring TPA groups, presenting low hysteresis (Figure S6b), whereas DPA bearing **112** exhibited a PCE of 12.8%. EQE measurement unveiled that the integrated density current (21.1 mA cm^{-2}) was in good agreement with the J_{sc} value obtained from the *J*/*V* curves (22.2 mA cm^{-2}) (Figure S6c).

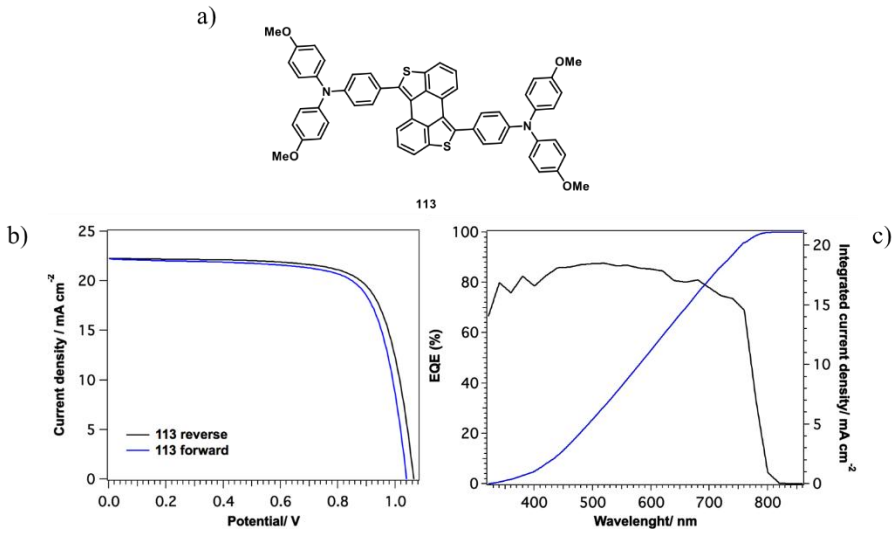

Figure S6. a) Representative example of HTM based on ADT. b) *J*/*V* curves of **113**:$MAPbI_3$ cell. c) EQE spectrum of best performing material **113**.

ii) HTMs bearing four donor groups

As the last approach taken into consideration, the study of two different scaffolds able to carry up to four TPA groups was performed. With this aim, two different central cores were used (BDT and DTP) and decorated with four TPA electron-rich moieties (Figure S7a). Thermal characterization evinced good thermal stability of the materials within the operating temperature range. Spectroscopic and electrochemical characterizations revealed that compound **116** has a good band alignment with the perovskite. Accordingly, the devices prepared from **116** produced a remarkable PCE value of 18.1% (Figure S7b), noticeably higher than that observed for spiro-OMeTAD (17.7%). On the other hand, compound **120** performed worse, presenting pronounced hysteresis, and showing a PCE value of 15.6%.

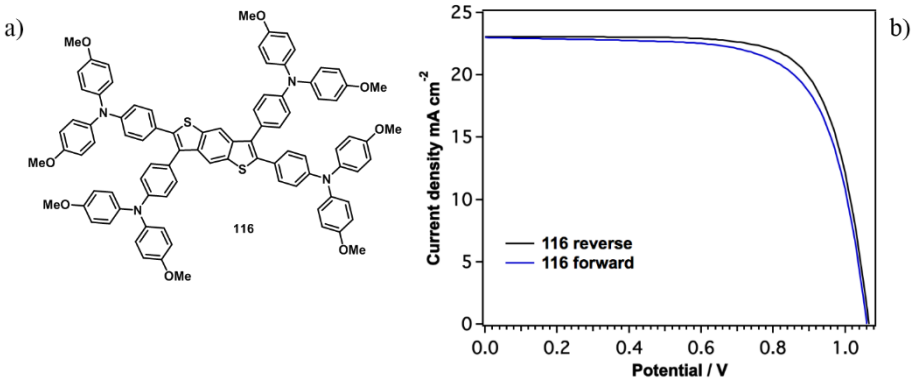

Figure S7. a) Chemical structure of compound **116**. b) *J/V* curves of **116**:$MAPbI_3$.

Conclusions

Chapter 1: A collection of new small molecules with different molecular architectures, namely A−D−A and D−A−D, have been synthesized, permitting a deep evaluation in their use as donors in BHJ SCs. A complete characterization of all systems has been carried out. Compound **72** was found to be the best performing material.

Chapter 2: New small molecules for their use as HTMs have been synthesized, combining the design of new central cores and electron donor moieties which decorate them. Derivative **116** exhibited the highest PCE value up to 18.1%, making it a strong candidate to compete with well-known spiro-OMeTAD.

Resumen

Diseño y síntesis de moléculas pequeñas para fotovoltaica

Introducción

El actual régimen energético, que se basa en fuentes de energía contaminantes no renovables, es insostenible desde los puntos de vista social, económico, geopolítico y ambiental. La única fuente totalmente renovable capaz de satisfacer la enorme y siempre creciente demanda energética del mundo es la energía solar. Las tecnologías fotovoltaicas, que convierten directamente la luz solar en electricidad, representan uno de los candidatos más prometedores para satisfacer esta demanda.

Objetivos

Capítulo 1: Desarrollo de moléculas pequeñas para células solares orgánicas.

Capítulo 2: Desarrollo de moléculas pequeñas como materiales transportadores de huecos para células solares de perovskita.

Resultados y discusión

Capítulo 1. *Moléculas pequeñas para células solares orgánicas*

i) Moléculas pequeñas A−D−A basadas en BDT-BTD

Se han diseñado y sintetizado moléculas electroactivas que presentan una arquitectura de tipo A-D-A, la cual se emplea en algunos de los mejores fragmentos electrón dadores y aceptores encontrados en la literatura, concretamente, benzoditiofeno (BDT, como dador) y benzotiadiazol (BTD, como aceptor). Puentes tiofeno de longitud creciente han sido insertados entre los grupos aceptor y dador (Figura R1a), para mejorar la absorción y las propiedades de agregación.

El estudio óptico, electroquímico y computacional ha revelado la naturaleza electroactiva de los compuestos y su habilidad para formar capas finas altamente ordenadas. Los dispositivos fotovoltaicos fabricados emplearon una mezcla de estos materiales con distintos derivados de fullereno como dador y aceptor, respectivamente, mostrando un comportamiento fotovoltaico pobre. El material con el mejor comportamiento (**31**) presentó una eficiencia de conversión energética (PCE) del 0.72% (Figura R1b).

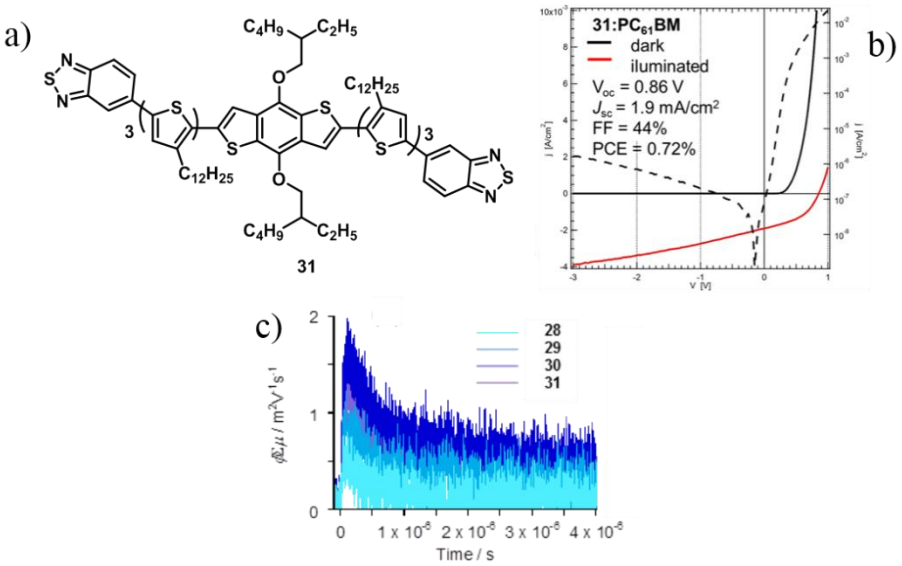

Figura R1. a) Estructura molecular del compuesto **31**. b) Parámetros fotovoltaicos del dispositivo-**31**. c) Trazas cinéticas de la conductividad con resolución temporal.

Estudios de TRMC revelaron que estas nuevas moléculas presentaban un transporte de carga de tipo-n. Es de resaltar que se obtuvieron elevadas movilidades electrónicas de hasta 0.1 $cm^2\ V^{-1}\ s^{-1}$ (Figura R1c).

ii) Moléculas pequeñas D−A−D basadas en aceptores de rodanina

Las arquitecturas de tipo D−A−D no son tan comunes como las de tipo A-D-A. En este aspecto, el principal reto fue encontrar un aceptor apropiado. La rodanina es un gran grupo aceptor que tiene un excelente comportamiento fotovoltaico.

a) 1ª Generación de moléculas pequeñas D-A-D

Han sido diseñadas y sintetizadas una serie de moléculas pequeñas D-A-D portando diferentes aceptores de rodanina, y butiltriarilamina como dadores (Figura R2a). El uso de distintas unidades D o A con diferente fuerza relativa, permitió obtener colorantes con la habilidad de captar luz en todo el rango del espectro visible (400-800nm).

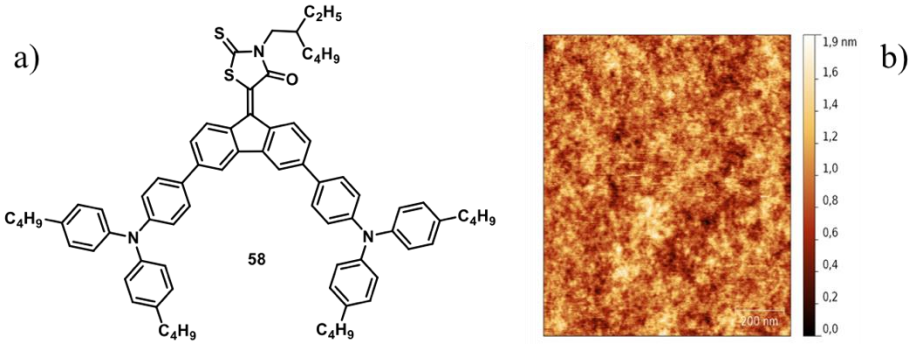

Figura R2. a) Estructura molecular del compuesto **58**. b) Imagen de AFM de un film de **58**/$PC_{71}BM$.

Se fabricaron células solares orgánicas empleando estos materiales mezclados con fullereno como capa activa. La baja eficiencia mostrada por los dispositivos fabricados (PCE< 0.25%) se debe a la mezcla eficiente de D y A, que impide la formación de caminos percolativos para el transporte de cargas hacia los electrodos. Esto se evidencia por AFM mostrando una morfología altamente uniforme (Figura R2b).

b) 2ª Generación de moléculas pequeñas D-A-D

Manteniendo la estructura general D/A de la 1ª generación de materiales, la nueva generación fue diseñada eliminando las cadenas de butilo de las trifenilaminas. En este caso, se empleó arilaminas con sustituyentes de fuerza dadora variable (TPA, TPA-Me, TPA-OMe, y DPA-OMe) (Figura R3a).

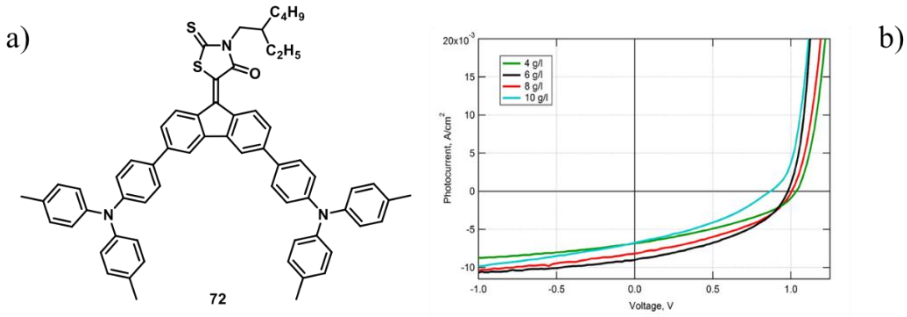

Figura R3. a) Estructura molecular del compuesto **72**. b) Curvas corriente/voltaje mostrando el efecto del espesor en la capa activa sobre el comportamiento fotovoltaico de los dispositivos basados en **72**.

El estudio fotovoltaico evidenció que el efecto del espesor de la capa activa sobre la eficiencia es crucial, alcanzando un PCE de 3.7% para las células fabricadas con **72** mezclado con $PC_{71}BM$ en una proporción 1:3 (Figura R3b).

Capítulo 2. ***Moléculas pequeñas para células solares de perovskita***

i) Hemi-spiro HTMs

Con el fin de encontrar nuevos HTMs capaces de mejorar el spiro-OMeTAD, se sintetizaron nuevos derivados de estructura semi-spiránica (Figura R4a). Los nuevos derivados presentan buena estabilidad térmica en el rango de temperaturas en el que operan las células. La caracterización espectroscópica y electroquímica permitió el cálculo de los valores de HOMO/LUMO. Los dispositivos fabricados con **98** y **99** mostraron eficiencias moderadas con PCE de 13.5 y 14.6%, respectivamente, presentando una histéresis pronunciada (Figura R4b).

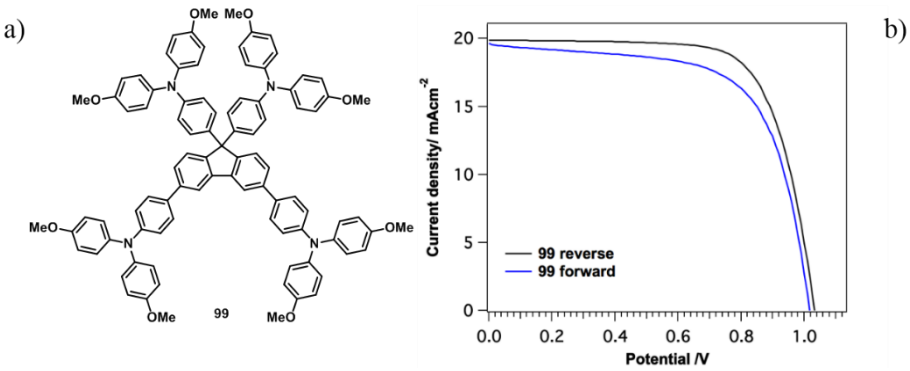

Figura R4. a) Ejemplo representativo de estructura semi-spiránica. b) Curvas *J*/*V* del dispositivo **99**:$MAPbI_3$.

ii) HTMs basadas en dibenzotiofeno (DBT)

Con el propósito de explorar diferentes núcleos centrales para el desarrollo de nuevos HTMs, una serie de compuestos usando DBT como núcleo central fueron sintetizados (Figura R5a). Como dadores electrónicos se emplearon grupos de diferente intensidad dadora (por ejemplo, difenilamina, trifenilamina y fenotiazina).

La caracterización espectroscópica de los compuestos reveló un nivel de energía HOMO de −5.23 y −5.36 eV para los compuestos **105** y **104** respectivamente. Los valores obtenidos son más bajos en energía que el

HOMO del spiro-OMeTAD (−5.16 eV) y están más cerca de la banda de valencia de la propia perovskita. Como se muestra en la Figura R5b, la actividad de los dispositivos de perovskita empleando **104**−**106** como HTMs mostró valores variables de PCE. Los valores obtenidos varían desde el 4.0% para **104** hasta 12.7% para **106**.

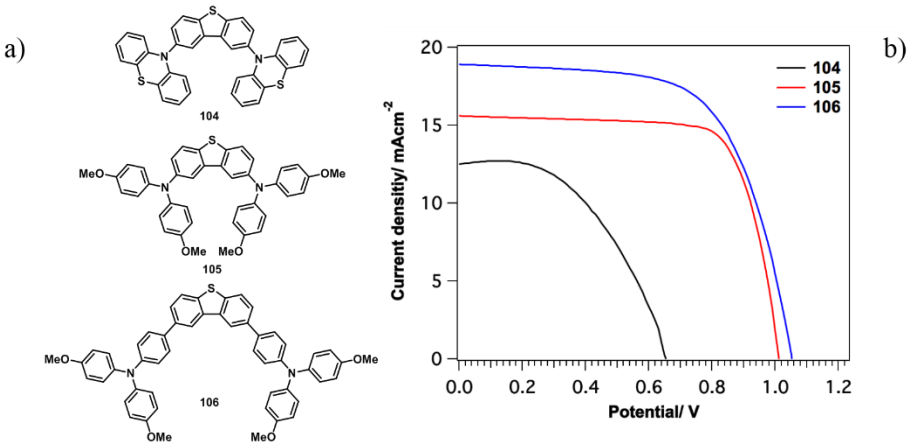

Figura R5. a) Serie de HTMs basados en DBT. b) Curvas *J*/*V* de los compuestos **104**-**106**.

iii) HTMs basadas en antraditiofeno (ADT)

El uso del núcleo de antraceno con dos tiofenos fusionados dio lugar a la poco común estructura de ADT, a la que se le introdujo dadores fuertes de DPA y TPA (Figura R6a). Los materiales resultantes mostraron excelentes propiedades térmicas. Un PCE de 17.6% fue alcanzado por el compuesto **113** que usa grupos TPA como dadores, mostrando baja histéresis (Figura R6b), mientras que portando DPA **112** exhibió un PCE de 12.8%. Las medidas de EQE revelaron que la densidad de corriente integrada (21.1 mA cm^{-2}) estaba en consonancia con el valor de J_{sc} obtenido a partir de las curvas *J*/*V* (22.2 mA cm^{-2}) (Figura R6c).

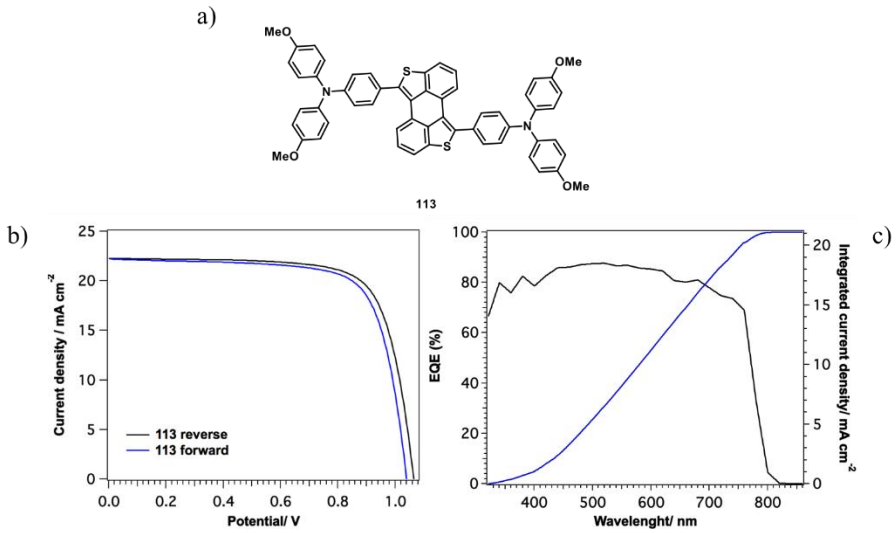

Figura R6. a) Ejemplo representativo de HTM basado en ADT. b) Curvas *J*/*V* de la célula **113**:$MAPbI_3$. c) Espectro de EQE del material con mejor comportamiento **113**.

iv) HTMs portando cuatro grupos dadores

Como última aproximación tenida en consideración, se llevó a cabo el estudio de dos *building-blocks* distintos, capaces de portar hasta cuatro grupos de TPA. Con este propósito, dos núcleos centrales fueron utilizados (BDT, DTP) y decorados con cuatro grupos ricos en electrones de TPA (Figura R7a). La caracterización térmica evidenció la buena estabilidad térmica de los materiales en el rango de temperaturas en el que operan las células. La caracterización espectroscópica y electroquímica reveló que el compuesto **116** tiene un buen alineamiento electrónico con la perovskita. Por consiguiente, los dispositivos preparados a partir de **116** produjeron el destacado valor de 18.1% de PCE (Figura R7b), sensiblemente superior que el observado para el spiro-OMeTAD (17.7%). Por otro lado, la actividad del compuesto **120** fue peor, presentando una pronunciada histéresis, mostrando un valor de PCE de 15.6%.

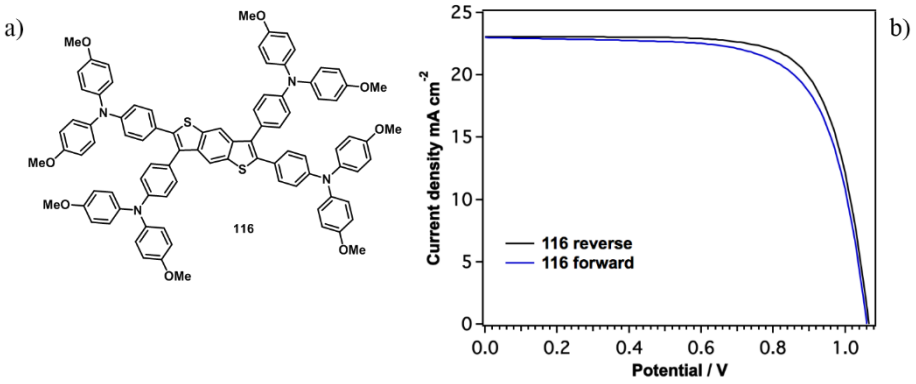

Figura R7. a) Estructura química del compuesto **116**. b) Curvas *J/V* de **116**:$MAPbI_3$.

Conclusiones

Capítulo 1: Se ha sintetizado una colección de nuevas moléculas con diferentes arquitecturas moleculares (A−D−A y D−A−D), permitiendo una profunda evaluación en su uso como dadores en células solares de heterounión masiva. El compuesto **72** resultó ser el material que mejor comportamiento fotovoltaico mostró.

Capítulo 2: Nuevas moléculas pequeñas para su uso como HTMs han sido sintetizadas, combinando el diseño de nuevos núcleos centrales con diferentes grupos dadores de electrones. El derivado **116** exhibió un PCE de 18.1%, valor que lo convierte en un sólido candidato para competir con el spiro-OMeTAD.

Introduction

INTRODUCTION

All living beings base their existence in drawing energy from different environmental sources, converting it into other forms of energy useful for life. In our case as species, we long time ago learnt to use energy not only for survival but in order to improve our living conditions. Since the Industrial Revolution to nowadays, mankind has developed and expanded its ability to use and harvest new energy sources (*e.g.* coal, oil, fissile materials...). All this progress has allowed human kind to reach life standards never seen before in our existence as species.

The toll to be paid for the welfare derived from progress is an always increasing colossal energy consumption. Historically, energy production has relied on non-renewable energy sources. However, current energy consumption rates are not only rapidly depleting these natural energy reservoirs, but they are also generating severe environmental problems (global warming, water and air pollution, nuclear waste management…). All these considered, has resulted in an almost unanimous international consensus to gradually shift to greener and renewable energy sources. In this sense, much attention has been devoted to technologies that allow harvesting the energy provided by the Sun.

Our star is the most powerful and abundant energy source available in the Solar System. Solar energy is generated by a sustained nuclear fusion reaction inside of the Sun. From its total radiated energy, our planet is continuously exposed to 340.2 W m^{-2}, nearly a third of this energy is reflected back to the space by clouds, atmosphere and the surface itself, leaving a total of 165.0 W m^{-2} readily available at the surface.[1] Efforts into harnessing this type of energy have drawn many resources due to its virtually unlimited and almost ubiquitous availability.

Among the different strategies employed to harness solar energy, photovoltaic (PV) approach is the one that directly converts light into electric energy. Total PV installed capacity was calculated to be 227.1 GW in 2015, representing a 0.6% of the global power generation.[2] Conventional and commercially

[1] G. L. Stephens, J. Li, M. Wild, C. A. Clayson, N. Loeb, S. Kato, T. L'Ecuyer, P. W. Stackhouse Jr, M. Lebsock, T. Andrews, *Nat. Geoscience* **2012**, *5*, 691−696.

[2] Source: International Energy Agency−Photovoltaic Power Systems Programme: www.iea-pvps.org.

available solar cells (SC) are usually classified into first and second generation materials.[3]

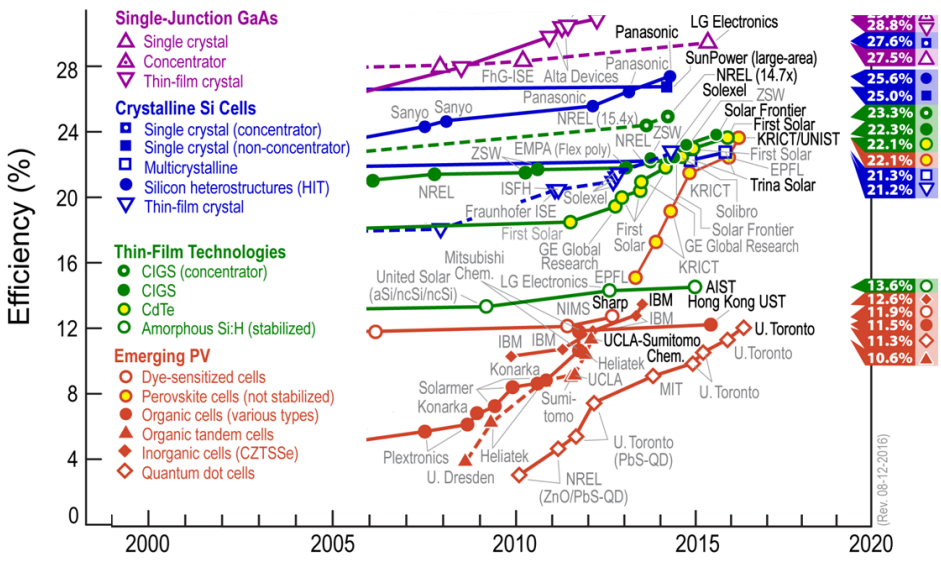

Figure 1. Efficiency-chart of best research solar cells summarized by National Renewable Energy Laboratory (NREL).

First generation cells are based in silicon semiconductors (silicon wafers); best performing ones, based on Si single crystals, achieving 27.6% power conversion efficiency (PCE). Although, because of the high costs involved in Si single crystal production, other less efficient technologies based on multicrystaline Si (*ca.* 21% PCE) are the ones usually being implemented. Second generation SC, also known as Thin-Film Technologies, take advantage of employing a fewer amount of semiconducting material, which include amorphous Si, cadmium telluride and copper indium gallium di-selenide (CIGS), with PCEs ranging from 13.6 to 23.3% (Figure 1).[4]

Alternatively, to these inorganic SC, so-called emerging PV bring the promise of a new generation of materials with improved properties, such as lightweight, flexibility, and lower fabrication costs. Emerging PV comprise several

[3] G. Conibeer, *Materials Today* **2007**, *10*, 42−50.

[4] Source: National Renewable Energy Laboratory (NREL) webpage http://www.nrel.gov.

technologies, of which, within the framework of this Thesis, we will focus on organic solar cells (OSC), dye-sensitized solar cells (DSSC), and perovskites solar cells because these are the only ones of relevance from the organic chemistry synthetic perspective.

Dye-sensitized solar cells. DSSC are photo-electrochemical systems based on metal oxide semiconductors (ZnO or TiO_2) formed between a dye-sensitized photo-anode and an electrolyte. First functional device was reported as early as 1968 by Gerischer *et al*.,[5] although it was not until 1988 when Michael Grätzel re-invented the modern version of the cell, obtaining a PCE of 7% by using a ruthenium based complex as photosensitizer. This complex was absorbed over a TiO_2 nanoporous film acting as photoanode and iodide/triiodide (I^-/I^{3-}) as a redox electrolyte.[6] DSSC rapidly reached 12% efficiency and have experienced a slow improvement up to the current record of 13%, achieved by employing a sensitizer based on zinc-porphyrin featuring the prototypical structure of a donor–π-bridge–acceptor, along with a cobalt (II/III) redox shuttle.[7]

Perovskites solar cells. Perovskites have experienced a scientific research boost in the photovoltaic field since they were firstly used as light absorbers in a DSSC by Miyasaka and collaborators.[8] The use of $CH_3NH_3PbI_3$ and $CH_3NH_3PbBr_3$ as photosensitizers in combination with iodide/triiodide (I^-/I^{3-}) liquid electrolyte showed PCEs of 3.8% and 3.1%, for triiodide and tribromide perovskites, respectively. Organometaltrihalide perovskites exhibit exceptional intrinsic properties such as wide light absorption from visible to near-infrared range, high extinction coefficient, long electron–hole diffusion lengths, a direct band gap as well as high charge carrier mobilities, among others.[9] Most of the

[5] H. Gerischer, M.E. Michel-Beyerle, F. Rebentrost, H. Tributsch, *Electrochim. Acta* **1968**, *13*, 1509−1515.

[6] B. O'Regan, M. Grätzel, *Nature* **1991**, *353*, 737−740.

[7] S. Mathew, A. Yella, P. Gao, R. Humphry-Baker, F. E. CurchodBasile, N. Ashari-Astani, I. Tavernelli, U. Rothlisberger, M. K. Nazeeruddin, M. Grätzel, *Nat. Chem.* **2014**, *6*, 242−247.

[8] A. Kojima, K. Teshima, Y. Shirai, T. Miyasaka, *J. Am. Chem. Soc*. **2009**, *131*, 6050−6051.

[9] a) Y.-C. Hsiao, T. Wu, M. Li, Q. Liu, W. Qin, B. Hu, *J. Mater. Chem. A*. **2015**, *3*, 15372−15385. b) J. M. Ball, S. D. Stranks, M. T. Hörantner, S. Hüttner, W. Zhang, E. J.W. Crossland, I. Ramirez, M. Riede, M. B. Johnston, R. H. Friend, H. J. Snaith,

research carried out in perovskite SC field consists in the development of new more efficient charge transport layers, with emphasis on hole transporting materials (HTM). So far, the best performing device shows a PCE value of 22.1%.[4]

Energy Environ. Sci. **2015**, *8*, 602−609. c) D. Shi, V. Adinolfi, R. Comin, M. Yuan, E. Alarousu, A. Buin, Y. Chen, S. Hoogland, A. Rothenberger, K. Katsiev, Y. Losovyj, X. Zhang, P. A. Dowben, O. F. Mohammed, E. H. Sargent, O. M. Bakr, *Science* **2015**, *347*, 519−522.

Chapter 1.

Small molecules for organic solar cells.

1.1. Background

1.1. BACKGROUND

1.1.1. Architectures of OSC

A swift description for an OSC might consider it as a device consisting in an organic active layer which is sandwiched in-between two electrodes that are able to extract photogenerated charges from the organic active layer upon excitation by light. First proofs of concept were demonstrated in the early 1970's showing PCEs as low as 0.01%, slowly evolving until the 2000's when their actual development is considered to start.[10] The organic active layer usually consisted in an electron donor (D) organic semi-conducting material blended with an electron acceptor (A).

From the device fabrication perspective, several architectures and configurations of the active layer have been tested in their evolution: single layer cells, bilayer cells, bulk heterojunction (BHJ) cells and tandem cells (Figure 2).

a) Single layer OSCs. The first OSCs were fabricated using a single layer of photoactive organic material, which was sandwiched between a semi-transparent electrode and non-transparent one.[11] Single layer cells are often referred to as Schottky type devices, since charge separation occurs as in the rectifying (Schottky) junction with one electrode. The reported quantum efficiencies were very low due to the poor charge mobilities that the organic semi-conducting materials usually show (below 10^{-3} cm^2/Vs) when compared with their inorganic counterparts. This fact, combined with the low interfacial area between the charge extracting electrodes and the organic layer, dragged the efficiency of single layer OSCs to very low <0.1% values.

b) Bilayer OSCs. Also known as planar heterojunctions, they consist in a bilayer of p- and n- type organic semiconductors. When compared with single

[10] a) A. K. Ghosh, D. L. Morel, T. Feng, R. F. Shaw, C. A. Rowe *J. Appl. Phys.* **1974**, *45*, 230−236. b) S. Glenis, G. Tourillon, F. Garnier, *Thin Solid Films* **1986**, *139*, 221−328. c) S. Karg, W. Riess, V. Dyakonov, M. Schwoerer, *Synth. Metals* **1993**, *54*, 427−433.

[11] a) C. W. Tang, A. C. Albrecht, *J. Chem. Phys*. **1975**, *62*, 2139−2149. b) V. Y. Merritt, H. J. Hovel, *Appl. Phys. Lett*. **1976**, *29*, 414−415. c) F. J. Kampas, M. Gouterman, *J. Phys. Chem*. **1977**, *81*, 690−695.

layer OSCs, charge carriers show a much enhanced mobility. Nevertheless, efficiency of this type of OSC is still limited by low charge generation due to: i) a low D/A heterojunction interfacial area that hinders excitons splitting into separated charges, which, in turn, causes exciton recombination, and ii) a short exciton diffusion length in the D/A phases (typically 5-20 nm).[12]

c) Bulk heterojunction (BHJ) OSCs. One logical approach to enhance the D/A binary heterojunction organic photovoltaic (OPV) devices efficiency is to maximize the D/A interfacial area, while decreasing the exciton diffusion pathways to the D/A interface. This can be achieved by forming an interpenetrating network of donor and acceptor materials that creates percolative pathways for the charge carriers to reach the electrodes. The higher efficiency of BHJ OSCs compared to bilayer OSCs is attributed to the decrease of exciton losses, due to the reduced dimensions of D and A domains in which excitons have to diffuse to reach D/A interface and a larger D/A interfacial area.[13]

d) Tandem OSCs. Most of photoactive compounds used for OSCs are not able to absorb in the whole solar spectrum and have relatively low carrier mobility, requiring thinner films for an efficient charge extraction.[14] To efficiently harvest solar radiation, a recurring strategy is to stack multiple junctions, so that top junctions not absorbed light may be absorbed by underlying ones.[15] Considering that most of D/A couples do not span the entire visible range, some authors have designed tandem cells with different D/A couples in a

[12] A. L. Ayzner, C. J. Tassone, S. H. Tolbert, B. J. Schwartz, *J. Phys. Chem. C* **2009**, *113*, 20050–20060.

[13] a) Y. Huang, E. J. Kramer, A. J. Heeger, G. C. Bazan, *Chem. Rev.* **2014**, *114*, 7006–7043. b) J. L. Delgado, P.-A. Bouit, S. Filippone, M. A. Herranz, N. Martín, *Chem. Commun.* **2010**, *46*, 4853–4865. c) A. J. Heeger, *Adv. Mater*. **2014**, *26*, 10–28.

[14] a) C. J. Brabec, C. Winder, N. S. Sariciftci, J. C. Hummelen, A. Dhanabalan, P. A. van Hal, R. A. J. Janssen, *Adv. Funct. Mater*. **2002**, *12*, 709–712. b) P. T. Boudreault, A. Najari, M. Leclerc, *Chem. Mater*. **2011**, *23*, 456–469. c) J. Hou, H.-Y. Chen, S. Zhang, G. Li, Y. Yang, *J. Am. Chem. Soc*. **2008**, *130*, 16144-16145.

[15] Y. Liu, C.-C. Chen, Z. Hong, J. Gao, Y. Michael Yang, H. Zhou, L. Dou, G. Li, Y. Yang, *Sci. Rep*. **2013**, *3*, 3356.

fashion that fully covers the visible spectrum. So far, tandem solar cells have proved to represent a successful strategy, allowing achieving PCEs over 10%.[16]

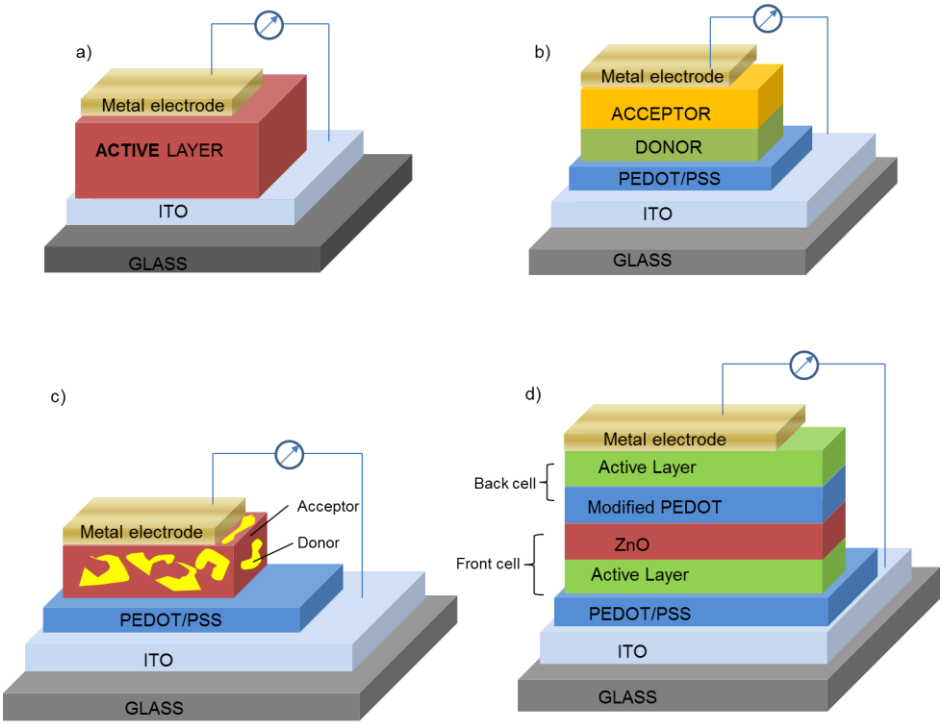

Figure 2. Different architectures for a OSC device: (a) single-layer cell, (b) bilayer cell, (c) bulk heterojunction cell, and (d) tandem cell.

1.1.2. OSC functioning mechanism

As depicted in Figure 3, functioning principles of OSCs may be described as a stepwise mechanism consisting in: 1) photon absorption inside the active layer and formation of an exciton; 2) exciton diffusion to the D/A interface (<20 nm); 3) exciton splitting into separated charges by charge transfer (CT) reaction, after overcoming the Coulombic barrier; 4) CT state is dissociated, and the charges migrate to their corresponding electrodes.

[16] J. You, L. Dou, K. Yoshimura, T. Kato, K. Ohya, T. Moriarty, K. Emery, C.-C. Chen, J. Gao, G. Li, Y. Yang, *Nat. Commun*. **2013**, *4*, 1446.

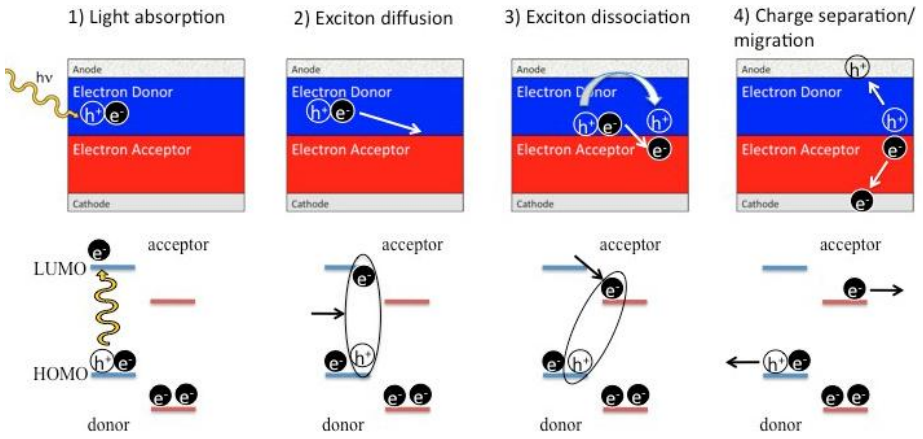

Figure 3. Photovoltaic process mechanism of an OSC, considering photoexcitation of the donor (analogous mechanism may be considered if acceptor is excited).

1) Light absorption.

The first step in the photovoltaic process consists in the absorption of light. In most OSCs just a small percentage of the incident light is absorbed by the organic dyes, the main reasons are: i) high band gaps commonly *ca.* 2 eV neglect most of the incoming light; ii) small layer thicknesses (typically between 20-100 nm). Due to the limited charge carrier mobilities exhibited by organic materials, the exciton diffusion length is limited to less than 20 nm. Thus, forcing layers to be thin enough (usually between 20 and 100 nm) to allow exciton diffusion. Fortunately, the high optical absorption coefficients showed by organic dyes allow fabricating devices of just a few tens of nanometers.

2) Exciton diffusion.

Excitons in inorganic semiconductors are usually of Wannier-Mott type. Their radius is in most cases larger than the lattice spacing, so charges may be considered as quasi-free. In contrast, the attractive force between electrons and holes in organic solids, where the exciton is initially localized in one molecule, is stronger and the binding energy is therefore higher. These strongly bound excitons are considered Frenkel type excitons.[17]

[17] J. Frenkel, *Phys. Rev*. **1931**, *38,* 309−320.

Upon exciton generation, diffusion through the donor or acceptor domains to the D/A interface takes place, followed by dissociation into free charges. Alternatively, recombination may occur if excitons fail to reach the D/A interface. Ideally, all photoexcited excitons should reach the D/A interface, but due to the small diffusion length of excitons some recombine before reaching the D/A interface. The exciton diffusion length can be estimated by Equation 1.

Equation 1. $L_D = \sqrt{D\,\tau_0}$

Where τ_0 is the lifetime of the exciton and D is the diffusion coefficient. L_D can vary from 1 nm to more than 50 nm.[18] Exciton movement is not affected by the electric field and, consequently, they diffuse through the organic semiconductor isotropically. This diffusion is usually known as Förster-type incoherent energy transfer process.[19]

Only excitons that are able to reach the D/A interface may contribute to the photocurrent. Therefore, considering the sensitive effect L_D exerts, a tradeoff between light absorption (the thicker the better) and recombination (the thinner the better) must be reached.

3) Charge transfer process.

The strongly bound excitons might dissociate once they have reached the D/A interface, thus generating charge carriers that may, in turn, diffuse to the electrodes. The dissociation of the exciton happens *via* an intermediate state, a so-called CT state. The electrons will be transferred to the electron acceptor material, provided that the exciton binding energy is overcome by this charge transfer process. This requirement is often satisfied by an energetic offset between the donor and acceptor LUMOs. If the electron is transferred from the LUMO of the excited donor to the LUMO of the neighboring acceptor, CT exciton is formed, where the resulting electron-hole pairs still experience coulombic attraction because donor and acceptor phases are physically close to each other at the interfaces. Then, in this intermediate state the two charges are

[18] a) S. Yoo, B. Domercq, B. Kippelen, *Appl. Phys. Lett*., **2004**, *85*, 5427−5429. b) Y. Terao, H. Sasabe, C. Adachi, *Appl. Phys. Lett*. **2007**, *90*, 103515.

[19] T. Förster, *Naturwissenschaften* **1946**, *33*, 66.

located on separate neighboring molecules.[20] The binding energy of the CT state is reported to be in the range of 0.1–0.5 eV, which is significantly larger than the thermal energy at room temperature (~25 meV).[21]

4) Charge transport.

Once separated, free charges must be transported from de D/A interface towards their respective electrodes, through percolative pathways formed by the D and A microdomains. The charge transport process in organic materials can be described by a "hopping" model,[22] instead of the band transport one. In the case of solar cells, the driving force is mainly generated by the gradient of the concentration of electrons and holes. Therefore, free charges (either electrons or holes) diffuse to their corresponding electrodes. The only possible loss mechanism in the charge transport process is recombination between electrons and holes during their journey to the electrodes (bimolecular recombination).

5) Charge collection.

Charge injection from the active layer into the electrodes is another critical step in the photocurrent generation process. Miss-alignment between electrodes metal work-functions and valence/conduction bands of the active layer makes necessary the insertion of interlayers between them. These interlayers help in improving the photovoltaic efficiency by: 1) minimizing the energy barrier for charge injection/collection at the metal/organic contacts; 2) working as selective charge filters; 3) determining the relative polarity of the device.[23]

1.1.3. Loss processes: charge recombination

The main factors limiting the OSC performance are the charge recombination processes. Depending on the recombination mechanism involved, these loss

[20] B. A. Gregg, J. van de Lagemaat, *Nature Photon*. **2012**, *6*, 278–280.

[21] a) X.-Y. Zhu, Q. Yang, M. Muntwiler, *Acc. Chem. Res*. **2009**, *42*, 1779−1787. b) M. Hallermann, S. Haneder, E. Da Como, *Appl. Phys. Lett*. **2008**, *93*, 053307.

[22] H. Bässler, *Phys. Stat. Sol*. (*b)* **1993**, *175*, 15−56.

[23] L.-M. Chen, Z. Xu, Z. Hong, Y. Yang, *J. Mater. Chem*. **2010**, *20*, 2575−2598.

processes fall into two categories: geminate and non-geminate recombination (Figure 4).

Geminate recombination. This process takes place when a coulombically bound electron-hole pair (exciton) recombines before being separated into free charges. [24] Despite the mechanism it is not well understood, geminate recombination seems to show a strong dependence on the internal electric field for many polymer and small molecule systems.[25] It is also known that the time scale for geminate recombination lies within the nanoseconds after the absorption.[26]

Non-geminate recombination. This process, also known as bimolecular recombination, consists in the recombination of free charge carriers and embraces both trap-assisted (Shockley-Read-Hall) and bimolecular mechanisms (Langevin). Non-geminate recombination losses are carrier density dependent and typically occur within the micro to millisecond time scale, when illumination conditions are comparable to 1.0 sun.[27] Non-geminate recombination takes place via defect states in the gap (Shockley-Read-Hall), where a free electron (or hole) is captured by a trapped hole (or electron). Commonly, it is usually referred in the literature as bimolecular recombination, in the sense that electron and hole that recombine come from different dissociated excitons.

[24] L. Onsager, *Phys. Rev*. **1938**, *54*, 554−557.

[25] a) W. Tress, A. Merten, M. Furno, M. Hein, K. Leo, M. Riede, *Adv. Energy Mater.* **2013**, *3*, 631−638. b) C. M. Proctor, S. Albrecht, M. Kuik, D. Neher, T.-Q. Nguyen, *Adv. Energy Mater.* **2014**, *4*, 1400230.

[26] D. Credgington, F. C. Jamieson, B. Walker, T. -Q. Nguyen, J. R. Durrant, *Adv. Mater.* **2012**, *24*, 2135–2141.

[27] C. G. Shuttle, B. O'Regan, A. M. Ballantyne, J. Nelson, D. D. C. Bradley, J. R. Durrant, *Phys. Rev. B* **2008**, *78*, 113201.

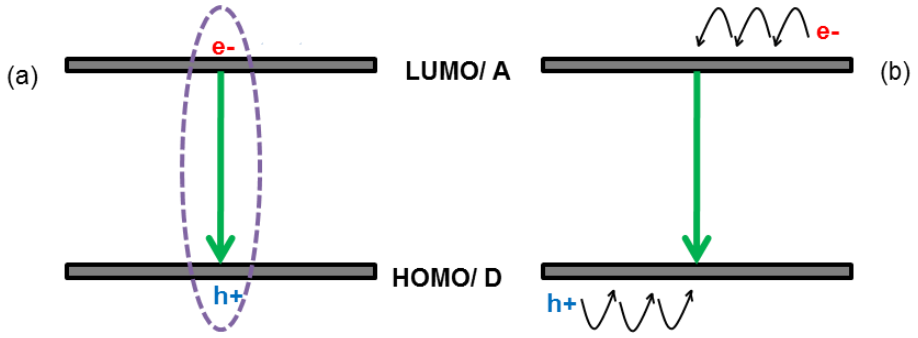

Figure 4. Loss mechanisms in BHJ devices: a) geminate recombination; b) non geminate recombination (bimolecular recombination).

1.1.4. Photovoltaic parameters

Organic solar cells performance is evaluated by measuring the generated current upon illumination against the applied bias, as depicted in Figure 5. The directly measurable parameters of an OSC are the open circuit voltage (V_{OC}), the short-circuit current (J_{SC}), the fill factor (FF), and the power conversion efficiency (PCE).

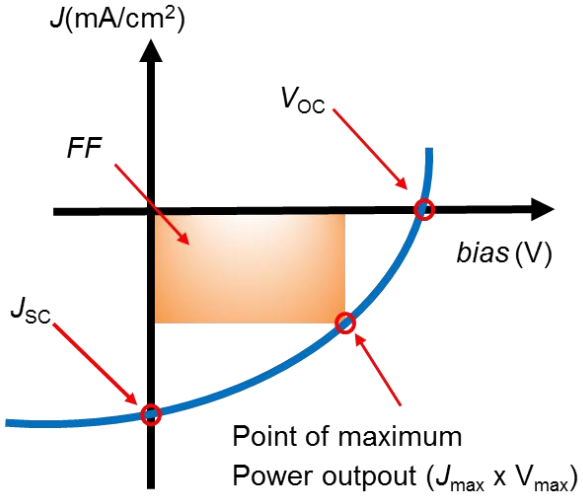

Figure 5. An example of current density-voltage (J-V) curve for a solar cell under simulated sun light.

Open circuit voltage (V_{OC}). The voltage at zero current is known as the open circuit voltage. Several studies have demonstrated the strong dependence of

V_{OC} on the energy difference (ΔE) between the HOMO-LUMO offset at the D/A interface of OSC (see Figure 6).[28] Moreover, V_{OC} is also found to depend on the work function of the electrode,[29] the D/A ratio,[30] etc.

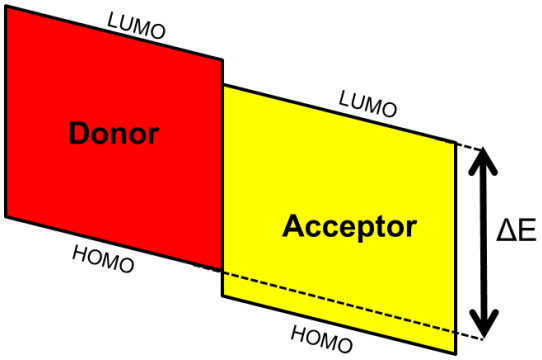

Figure 6. Energy levels alignment at the D/A interface.

Short-circuit current (J_{SC}). It may be described as the flowing current when no voltage is applied to the device, J_{sc} is entirely based on photo generated charge carriers. Thus, for monochromatic exposure the spectral dependence of the charge carrier generation can be measured. The J_{SC} is influenced by the amount of light absorbed by the cell within the active layer and the relative efficiencies of internal processes (such as charge separation and recombination).

Fill Factor (*FF*). This parameter is defined as the ratio between the maximum power output of the cell (the point on the curve where $J \times V$ maximizes) and the product $J_{SC} \times V_{OC}$. The FF is an indicator of the quality of an OSC and is determined by the mobilities of charge carriers in the active layer of the OSC.

[28] C. Brabec, A. Cravino, D. Meissner, N. Sariciftci, T. Fromherz, M.Rispens, L. Sanchez, J. C. Hummelen. *Adv. Funct. Mater*. **2001**, *11*, 374–380.

[29] V. D. Mihailetchi, P. W. M. Blom, J. C. Hummelen, M. T. Rispens, *J. Appl. Phys*. **2003**, *94*, 6849−6854.

[30] Q. Peng, K. Park, T. Lin, M. Durstock, L. M. Dai, *J. Phys. Chem. B* **2008**, *112*, 2801–2808.

Power conversion efficiency (PCE). The PCE is the ratio of the maximum power output over the power of the light incident to the device, which can be expressed according to Equation 2:

Equation 2. $$\mathrm{PCE} = \frac{J_{max} \times V_{max}}{P_{inc}} = \frac{\mathrm{Jsc} \times \mathrm{Voc} \times \mathrm{FF}}{P_{inc}}$$

Where J_{max} and V_{max} are the current density and voltage at the point of maximum power output and P_{inc} is the power incident on the cell from the simulated solar light (AM 1.5) which is used for device characterization. From this equation, it is apparent that maximizing PCE requires maximizing the J_{SC}, V_{OC}, and *FF*.

External quantum efficiency (EQE). The external quantum efficiency is termed, as the ratio of the number of incident photons N_{photon} and the number of photo induced charges extracted out of the cell N_e. It is smaller than the internal quantum efficiency (IQE), which represents the absorbed photons conversion into charge carriers within the cell. The reason is that EQE takes into account the losses formed by reflection, recombination and scattering. EQE can be measured directly from the short-circuit current J_{SC} and the incident light intensity J_0 according to Equation 3:

Equation 3. $$EQE = \frac{N_e}{N_{photon}} = \frac{J_{sc}}{J_0} \times \frac{h\,c}{\lambda\,q}$$

Where q is the single electron charge, c is the speed of light, λ is the wavelength of the incident light, and h is Planck's constant.

1.1.5. A brief survey of OSCs

The outbreak of OSCs in the 2000's was preceded by three benchmarks. The first device exceeding the meagre performance of the early prototypes fabricated on the 1970's was a bilayer-type OCS developed by Tang based on small molecules and showed 0.9% PCE. The active layer consisted in a thin layer of copper phthalocyanine (CuPc) acting as p-type material and a thin layer of a perylenediimide (PDI) derivative as n-type material (see Figure 7), all confined within ITO and silver electrodes.[31]

[31] C.W. Tang, *Appl. Phys. Lett*. **1986**, *48*, 183−185.

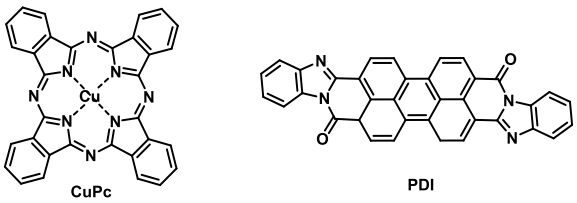

Figure 7. Structures of CuPc and PDI acting as D and A, respectively, used in Tang's cell.

A second milestone may be attributed to Sariciftci and colaborators, when they demonstrated that photo-excitation of a blend of a conjugated donating polymer of poly[2-methoxy,5-(2'-ethyl-hexyloxy)-*p*-phenylenevinylene] (MEH-PPV) and accepting fullerene (C_{60}) resulted in an ultra-fast charge transfer within picoseconds upon excitation, evidenced by the almost total quench of the donor polymer photoluminescence when blended with the fullerene (Figure 8).[32] Probably, ever since then, fullerene derivatives became almost ubiquitous as acceptors in OCS due to their excellent electronic properties, showing high electron mobility and low reorganization energy, among others.

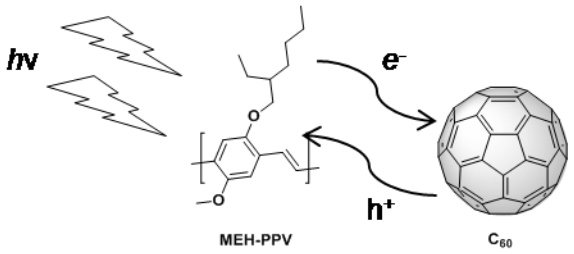

Figure 8. Photoinduced electron transfer from semiconductor polymer MEH-PV to C_{60}.

The last pioneering work is related to the fabrication of the first bulk heterojunction (BHJ) cell, made out of a mixture of donor and acceptor polymers, MEH-PPV and Cyano-Polyphenylenevinylene (CN-PPV), respectively, (Figure 9) almost simultaneously by Friend and collaborators and by Heeger's group.[33,34] The relevance of these two works lies on being the first

[32] N. S. Sariciftci, L. Smilowitz, A. J. Heeger, F. Wudl, *Science* **1992**, *258*, 1474−1476.

[33] J. J. M. Halls, C. A. Walsh, N. C. Greenham, E. A. Marseglia, R. H. Friend, S. C. Moratti, A. B. Holmes, *Nature* **1995**, *376*, 498−500.

ones measuring the mobilities of both types of charge carriers (electrons and holes) in an OSC.

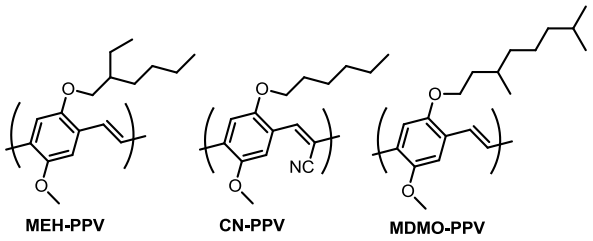

Figure 9. Polyphenyleneinylene (PPV) based polymers for OSC.

The relevance of the latter meant the outbreak of OSCs based on PPV polymers (Figure 9). These materials used as D showed efficiencies up to 3.3%, with high V_{OC} = 0.86 V, owed to their relatively high laying HOMO (5.4 eV). Although, due to their high band gaps, these materials lacked of low currents (J_{SC} = 5−6 mA cm^{-2}).[35]

Soon afterwards, and in parallel with the synthesis of numerous PPVs, a second generation of polymers based on thiophene polymers emerged. The most representative of this family of polymers was regioregular poly(3-hexylthiophene) (rr-P3HT).[36] Main improvement of P3HT-based materials was its noticeably higher J_{SC} (over 10 mA cm^{-2}), attributed to its lower band gap (1.9 eV), as well as to its enhanced π-stacking and crystallinity, which allowed higher hole mobilities. Despite the low V_{OC} of about 0.6 V (attributed to its relatively high laying HOMO of 5.1 eV) these cells showed efficiencies of *ca.* 5%.[37]

---

[34] G. Yu, A. J. Heeger, *J. Appl. Phys*. **1995**,*78*, 4510−4515.

[35] a) S. E. Shaheen, C. J. Brabec, N. S. Sariciftci, F. Padinger, T. Fromherz, J. C. Hummelen, *Appl. Phys. Lett.* **2001**, *78*, 841−843. b) C. J. Brabec, S. E. Shaheen, C. Winder, N. S. Sariciftci, *Appl. Phys. Lett.* **2002**, *80*, 1288−1290.

[36] a) Y. Kim, S. Cook, S. M. Tuladhar, S. A. Choulis, J. Nelson, J. R. Durrant, D. C. Bradley, M. Giles, I. McCulloch, C.-S. Ha, M.Ree, *Nature Mater.* **2006**, *5*, 197−203; b) G. Dennler, M. C. Scharber,C. J. Brabec, *Adv. Mater.* **2009**, *21*, 1323−1338.

[37] a) M. Reyes-Reyes, K. Kim, D. L. Carroll, *Appl. Phys. Lett.* **2005**, *87*, 083506. b) J. Y. Kim, S. H. Kim, H. H. Lee, K. Lee, W. L. Ma, X. Gong, A. J. Heeger, *Adv. Mater*. **2006**, *18*, 572–576.

The standard material used as electron acceptor has typically been [6,6]-phenyl-C_{61}-butyric acid methyl ester ($PC_{61}BM$). Although, our research group developed an easier to synthesize fullerene derivative, diphenylmethanofullerene (DPM-12) (Figure 10), that showed enhanced V_{OC} when blended with P3HT. Resulting cells exhibited an increase of 100 mV compared to analogously built $PC_{61}BM$ ones, with just slightly worse PCE (1.98% *vs.* 2.03%).[38]

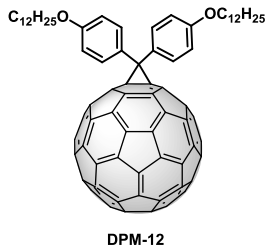

Figure 10. Chemical structure of fullerene derivative DPM-12.

Both PPV and P3HT based polymers had in common being homopolymers. This characteristic left very limited room in order to introduce chemical modifications that might allow improving their performance. After a brief impasse, some groups came with what it might be considered the third generation of OSC materials. This consisted in copolymers, rather than homopolymers, where both an A and a D moieties were merged. This strategy allowed to fine tune the band gap of the polymers, as the internal charge transfer (ICT) induced by the presence of both D and A units within the polymer led to low energy states that allowed harvesting light in almost all the optical range. One unique feature of the D−A polymers is that the HOMO and LUMO energy levels are largely localized over the donor and the acceptor moiety, respectively (though HOMO is usually more delocalized along the D−A structure).[39] Ever since, most of the conjugated polymers for OSC reported so far are based on this D−A concept. This new strategy, along with the great development of OSC fabrication and engineering (addition of

[38] A. Sánchez-Díaz, M. Izquierdo, S. Filippone, N. Martín, E. Palomares, *Adv. Funct. Mater.* **2010**, *20*, 2695–2700.

[39] a) J.-L. Brédas, J. E. Norton, J. Cornil, V. Coropceanu, *Acc. Chem. Res*. **2009**, *42*, 1691–1699. b) H. Zhou, L. Yang, S. Stoneking, W. You, *ACS Appl. Mater. Interfaces* **2010**, *2*, 1377–1383.

additives, inverted devices, annealing processes…) has allowed reaching never seen before efficiencies of up to 11% PCE. In this sense, top notch polymers are illustrated in Figure 11.[40]

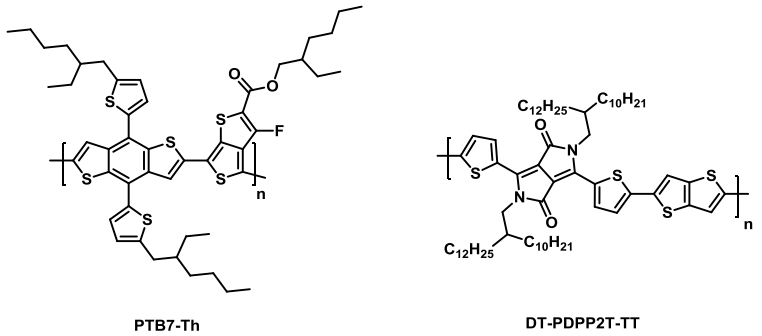

Figure 11. Best performing, when blended with fullerenes as acceptor, D-A polymer structures.

1.1.6. Non-fullerenic acceptors based OSCs

Fullerene and its derivatives, overwhelmingly represented by $PC_{61}BM$ and $PC_{71}BM$, have ever since the dawning of organic photovoltaic been the electron-acceptor material of the BHJ. Their dominance stems from their rather unique properties, including (i) the ability to accept and transport electrons in three dimensions thanks to a LUMO that is delocalized over the whole surface of the molecule, (ii) multiple reversible electrochemical reductions, (iii) high electron mobilities, (iv) low reorganization energy, and (v) the ability to aggregate in BHJ to form both pure and mixed domains of the appropriate length scale for charge separation. Fullerene derivatives have some intrinsic drawbacks including limited visible light absorption, high synthetic cost and instability of morphology in the blend film.[41] Nevertheless, their most significant disadvantage arises from the constraint represented by their hard to tune LUMO energy. Presenting the right electronic matching between D and A LUMO promotes effective exciton splitting, along with improved J_{SC}.

[40] a) H. Choi, S.-J. Ko, T. Kim, P.-O. Morin, B. Walker, B. H. Lee, M- Leclerc, J. Y. Kim, A. J. Heeger, *Adv. Mater.* **2015**, *27*, 3318−3324. b) J. Huang, J. H. Carpenter, C.-Z. Li, J.-S. Yu, H. Ade, A. K.-Y. Jen, *Adv. Mater.* **2016**, *28*, 967−974.

[41] C. B. Nielsen, S. Holliday, H.-Y. Chen, S. J. Cryer, I. McCulloch, *Acc. Chem. Res.*, **2015**, *48*, 2803−2812.

Therefore, the development of new generation non-fullerenic electron acceptor materials is of the outmost importance.

As a result, there has been a surge of n-type materials aiming to replace fullerenic ones. In this sense, long utilized n-type materials for OFET naphthalene diimide (NDI) and perylenediimide (PDI) have been revisited, and demonstrated to perform similarly to $PC_{71}BM$. The most representative example of PDI based on small molecule acceptor has recently been presented by L. Yu *et al.*, consisting in four PDIs linked to a dithieno-benzodithiophene (BDT-Th) central core (TPB, **1**) (Figure 12). When TPB is blended with PTB7-Th as donor in an inverted device configuration cells show a maximum PCE of 8.47%.[42]

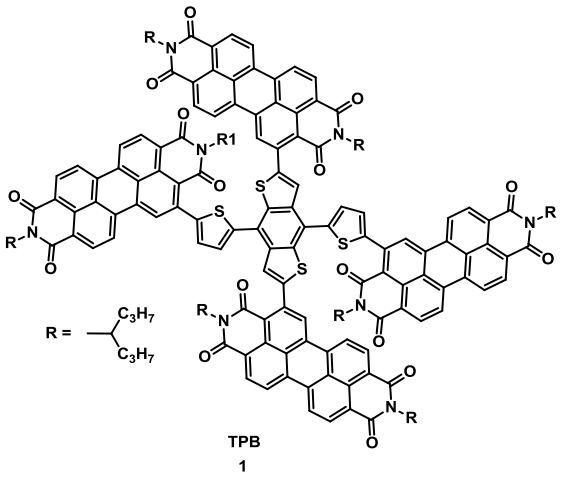

Figure 12. Chemical structure of TPB (**1**).

Some other materials have also successfully been tested as small molecule acceptors, some demonstrating to perform akin to fullerene derivatives like boron subphthalocyanines (SubPc),[43] and some showing to outperform them as for ITIC like materials (see Figure 13). This family of compounds can be

[42] Q. Wu, D. Zhao, A. M. Schneider, W. Chen, L. Yu, *J. Am. Chem. Soc.* **2016**, *138*, 7248−7251.

[43] a) B. Verreet, B. P. Rand, D. Cheyns, A. Hadipour, T. Aernouts, P. Heremans, A. Medina, C. G. Claessens, T. Torres, *Adv. Energy Mater.* **2011**, *1*, 565–568; b) K. Cnops, B. P. Rand, D. Cheyns, B. Verreet, M. A. Empl, P. Heremans, *Nature Commun.* **2014**, *5*, 3406.

reduced to an electron rich central polyheteroaromatic core end-capped by two strongly accepting 3-Oxo-$\Delta^{1,\alpha}$-indanmalonitrile moieties. Most promising structures seem to be the central core being indacenodithieno[3,2-b]thiophene systems. To the date this Thesis was written, the record performance OSC was born by a methylated ITIC derivative, so called IT-M, blended with PBDB-T (Figure 13). This system, reported by J. Hou *et al.*, showed an astonishing 12.05% maximum PCE.[44]

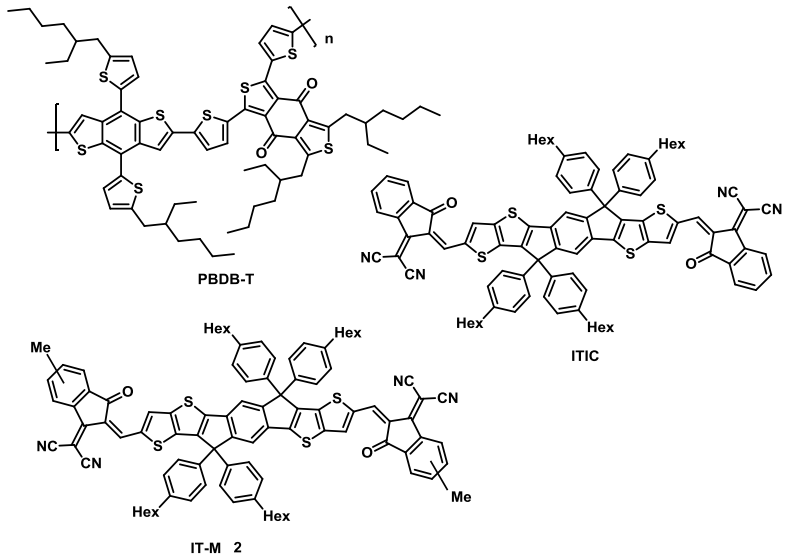

Figure 13. Chemical structures of ITIC, and OSC record bearing PBDB-T/IT-M (**2**) blend.

1.1.7. Small molecule donors (SMD) for OSCs

Despite the remarkable results achieved by conjugated polymers, this kind of materials drag a number of drawbacks related to synthetic reproducibility and purification issues. Moreover, thiophene based/bearing polymers synthesis is quite prone to create defects (insertions to wrong positions, ligand insertions…) which critically hamper J_{SC}. All considered, small molecules represent an interesting alternative: reproducible synthesis, simple purification, properties relatively easy to tune by chemical modification and, more

[44] S. Li, L. Ye, W. Zhao, S. Zhang, S. Mukherjee, H. Ade, J. Hou, *Adv. Mater*. **2016**, *28*, 9423–9429.

importantly, small molecules tend to generate well-ordered crystalline structures.

Notable advances have already been attained with small molecule donors in BHJ solar cells, with most representative examples showing PCE values up to 10%.[45] Despite the high performances already demonstrated, many efforts are being devoted in order to synthesize new better performing molecules. The ease to chemically modify small molecules is allowing seeing many publications devoted to explore the effect of inserting different side chains, substituents (-F, -CN…),[46] altering the ordering of the subunits, *etc*.[47]

Along the evolution of organic photovoltaics, some structures seem to recursively show up. In this sense, it is almost impossible to neglect the extensive presence of thiophene. This molecule is either employed as π-conjugated spacer separating alternating D and A subunits, or used itself as electron donating unit. Its use seems to induce enhanced aggregation via π-stacking and S···S interactions.

Once evidenced the beneficial effect of flat conjugated sulphur bearing π-surfaces the next obvious step was to extend these aromatic surfaces by ring-fusing its components. This wise, many polycyclic products have arisen along the years:

Dithienosilole (DTS): When bithiophene molecule is ring-closed with a Si atom within its 3,3' positions, the resulting dithieno[3,2-b:2',3-d]silole is a more conjugated, stronger electron donating molecule, and also with enhanced solubility.

A series of systems synthesized by Bazan *et al.* illustrate the importance of the relative positions of the internal constituents of a small molecule employing DTS as donor in a A−D−A configuration, where A was pyridothiadiazole

[45] B. Kan, M. Li, Q. Zhang, F. Liu, X. Wan, Y. Wang, W. Ni, G. Long, X. Yang, H. Feng, Y. Zuo, M. Zhang, F. Huang, Y. Cao, T. P. Russell, Y. Chen, *J. Am. Chem. Soc.* **2015**, *137*, 3886−3893.

[46] J.-L. Wang, Q.-R. Yin, J.-S. Miao, Z. Wu, Z.-F. Chang, Y. Cao,R.-B. Zhang, J.-Y. Wang, H.-B. Wu, Y. Cao, *Adv. Funct. Mater.* **2015**, *25*, 3514–3523.

[47] J. Du, A. Fortney, K. E. Washington, C. Bulumulla, P. Huang, D. Dissanayake, M. C. Biewer, T. Kowalewski, M. C. Stefan, *ACS Appl. Mater. Interfaces* **2016**, *8*, 33025−33033.

(PTD), gave dramatically different performances depending on whether the N of the pyridine ring faced inwards or towards the outside (Figure 14). Whereas the latter (**3**) OCS, blended with $PC_{71}BM$, showed 3.2% PCE,[48] the former (**4**) yielded 4.5% PCE, improving to 6.7% when 0.25% v/v of DIO was used as additive.[49]

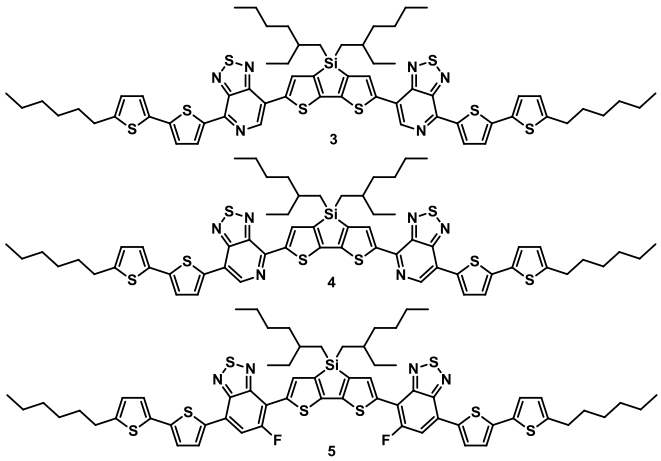

Figure 14. Chemical structures of solution processable small molecule donors bearing DTS.

A further example of the key role played by substituents is observed for the case of molecule **5**, where PTD is replaced by a benzothiadiazole (BTD) unit featuring a fluorine atom facing the DTS core. In this case, insertion of this electron withdrawing substituent enhances performance in blends with $PC_{71}BM$ to a 7.0% PCE, with high FF of 60% and V_{OC} = 0.81 V.[50]

Dithienopyrrole (DTP): An even stronger D unit is created when nitrogen is used instead of silicon, giving rise to dithieno[3,2-b:2'.3'-d]pyrrole. This molecule is one of the molecules with higher reductive power described in the

[48] a) G. C. Welch, L. A. Perez, C. V. Hoven, Y. Zhang, X.-D. Dang, A. Sharenko, M. F. Toney, E. J. Kramer, T.-Q. Nguyen, G. C. Bazan, *J. Mater. Chem.* **2011**, *21*, 12700−12709. b) Z. B. Henson, G. C. Welch, T. van der Poll, G. C. Bazan, *J. Am. Chem. Soc.* **2012**, *134*, 3766−3779.

[49] Y. Sun, G. C. Welch, W. L. Leong, C. J. Takacs, G. C. Bazan, A. J. Heeger, *Nat. Mater.* **2012**, *11*, 44−48.

[50] T. S. van der Poll, J. A. Love, T. Q. Nguyen, G. C. Bazan, *Adv. Mater.* **2012**, *24*, 3646−3649.

literature, providing also with good hole transport properties. Bäuerle and coworkers extensively explored the effect of solubilizing side-chains size and positioning over an A−D−A system (Figure 15).[51] The series consisted in a DTP core bridged to dicyanovinylene acceptor by a bithiophene linker. Along with strong CT character of the molecules, the relative positioning of the side-chains and the chain length showed to strongly affect the packing of the molecules, therefore affecting the overall performance of the devices. Molecules **6a**−**c** showed better *as cast* performances (3.8−4.8% PCE), although solvent vapor annealing induced a strongly beneficial effect over the performance of devices built with **7a**−**c** (4.4−6.1% PCE). Absorption spectroscopy, AFM and XRD experiments suggested that exposure to chloroform vapor allows for a re-organization of the blend, which increases both the absorption and crystallinity of the donor and hence leads to higher order in the BHJ.

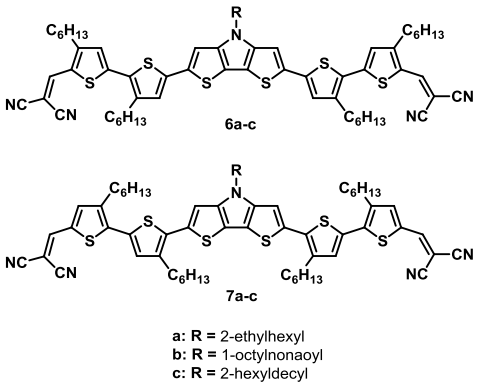

Figure 15. Chemical structures of solution processable small molecule donors bearing DTP.

Benzodithiophene (BDT): Another ubiquitous electron-donating molecule is benzo[1,2-b:4,5-b']dithiophene (BDT). This system plays a very important role in high performance small molecule OSC due to its symmetric and planar conjugated structure. This centrosymmetric planar structure induces cofacial π-π stacking in the solid state, favoring charge transport and, therefore, yielding

[51] C. D. Wessendorf, G. L. Schulz, A. Mishra, P. Kar, I. Ata, M. Weidelener, M. Urdanpilleta, J. Hanisch, E. Mena-Osteritz, M. Lindén, E. Ahlswede, P. Bäuerle, *Adv. Energy Mater.* **2014**, *4*, 1400266.

higher FF. Many examples of its use in OSC can be found in the literature due to its outstanding performance and thanks to its versatility in terms of chemical modification. Most common modifications of this widespread molecule are implemented over the central benzene ring; this is found either bare or substituted with a variety of ancillary alkyl, alkoxy, thioalkyl and aromatic (thiophene, bithiophenes, phenyl…) side-chains. These substitutions allow not only to engineer the structure of the systems, but also to enhance their optical and electronic properties.[52]

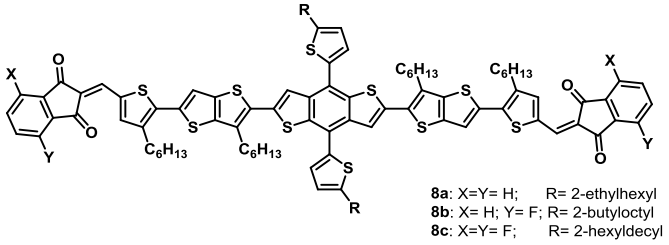

Figure 16. Systems bearing BDT donating core end capped with different 1,3-indandione derivatives as acceptor.

Quite recently, new structures bearing BDT as donor core in an archetypical A−D−A arrangement, using 1,3-indandione derivatives as acceptor, have been reported. The molecules, somehow resembling ITIC small molecule acceptors, make use of a thienothiophen-thiophene to bridged core unit to the end-capping acceptors. This study evidences once again the pivotal importance of F substituents, showing how device performance enhances from **8a** to **8c** (Figure 16), as more F substituents are incorporated to the A moiety. So far, **8c** is the record bearing material in devices blended with $PC_{71}BM$ with 11.3% PCE,

[52] a) Y. Liu, X. Wan, F. Wang, J. Zhou, G. Long, J. Tian, Y. Chen, *Adv. Mater.* **2011**, *23*, 5387–5391. b) J. Zhou, X. Wan, Y. Liu, Y. Zuo, Z. Li, G. He, G. Long, W. Ni, C. Li, X. Su, Y. Chen, *J. Am. Chem. Soc.* **2012**, *134*, 16345–16351. c) S. Shen, P. Jiang, C. He, J. Zhang, P. Shen, Y. Zhang, Y. Yi, Z. Zhang, Z. Li, Y. Li, *Chem. Mater.* **2013**, *25*, 2274−2281. d) B. Kan, Q. Zhang, M. Li, X. Wan, W. Ni, G. Long, Y. Wang, X. Yang, H. Feng, Y. Chen, *J. Am. Chem. Soc*. **2014**, *136*, 15529–15532. e) M. Li, F. Liu, X. Wan, W. Ni, B. Kan, H. Feng, Q. Zhang, X. Yang, Y. Wang, Y. Zhang, Y. Shen, T. P. Russell, Y. Chen, *Adv. Mater*. **2015**, *27*, 6296–6302.

closely followed by **8b** (10.4%) and in contrast with non-fluorine bearing **8a** (8.3%).[53]

Rhodanine (Rh): Also named 2-thioxo-4-thiazolidinone, this electron deficient molecule is widespread used in chemical synthesis for applications as far apart as drug design and organic electronics. Screening of different electron deficient moieties in A−D−A architectures[54] ended up with Rh being an excellent electron acceptor group, which provided unprecedented performances in small molecule OPV.

Best performing materials employing Rh as acceptor have always been presented as A−D−A like systems due to synthetic reasons. Most representative ones normally make use of oligothiophene or BDT as electron rich fragments, as depicted in Figure 17.

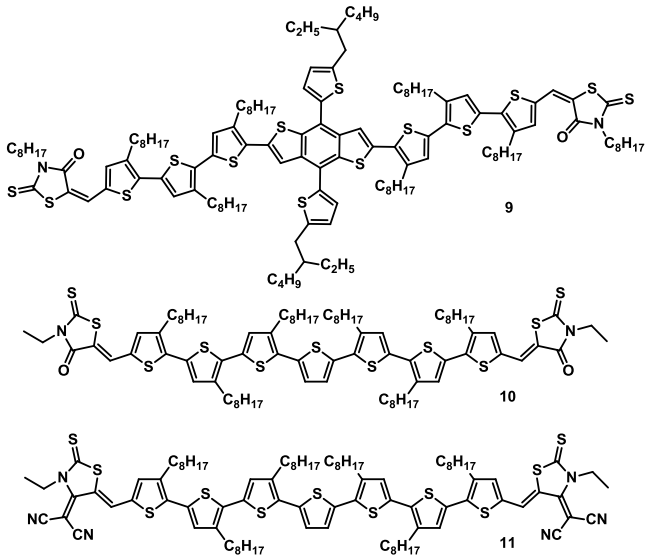

Figure 17. Representative A−D−A structures bearing Rh as acceptor.

[53] D. Deng, Y. Zhang, J. Zhang, Z. Wang, L. Zhu, J. Fang, B. Xia,Z. Wang, K. Lu, W. Ma, Z. Wei, *Nature Commun.* **2016**, *7*, 13740.

[54] a) Z. Li, G. He, X. Wan, Y. Liu, J. Zhou, G. Long, Y. Zuo, M. Zhang, Y. Chen, *Adv. Energy Mater.* **2012**, *2*, 74–77. b) R. Fitzner, E. Mena-Osteritz, A. Mishra, G. Schulz, E. Reinold, M. Weil, C. Körner, H. Ziehlke, C. Elschner, K. Leo, M. Riede, M. Pfeiffer, C. Uhrich, P. Bäuerle, *J. Am. Chem. Soc.* **2012**, *134*, 11064–11067; c) G. He, Z. Li, X. Wan, Y. Liu, J. Zhou, G. Long, M. Zhang, Y. Chen, *J. Mater. Chem.* **2012**, *22*, 9173–9180.

Resulting from the combination of a BDT-Th donor core with Rh, molecule **9** showed very interesting properties when blended with $PC_{71}BM$. Performance of films *as cast* exhibited 7.2% PCE, the good performance of the devices was attributed to the high crystallinity of the films, which in term benefits the charge transport (V_{OC} = 0.93 V; J_{SC} = 11.4 mA cm^{-2}). Addition of 0.5 mg mL^{-1} of polydimethylsiloxane (PDMS) further improved device performance by inducing nanofibril formation, allowing to obtain PCE = 8.1% thanks to the enhanced charge transport facilitated by the nanofibrilar morphology (V_{OC} = 0.94 V; J_{SC} = 12.5 mA cm^{-2}). Interestingly, authors also fabricated double junction tandem devices with 10.1 % PCE.[55]

Engineering over the Rh acceptor unit allowed to insert a dicyanovinylene fragment (molecule **11**, Figure 17); such modification resulted in broader and red-shifted absorption of this A−D−A system. Thermal annealed devices showed excellent characteristics (PCE = 9.3%; V_{OC} = 0.91 V; J_{SC} = 14.87 mA cm^{-2}; FF = 48.7%) when compared with compound **10** (PCE = 6.1%; V_{OC} = 0.92 V; J_{SC} = 13.98 mA cm^{-2}; FF = 47.4%). Deeper comprehension on how such a small structural modification yielded such a dramatic change in performance was provided when microstructure and morphology were studied. For compound **11** a morphology with an optimized interpenetrating network was found, consisting of ∼10 nm diameter highly crystalline fibrils, thus resulting in little geminate or non-geminate recombination.[56]

[55] Y. Liu, C.-C. Chen, Z. Hong, J. Gao, Y. (M.) Yang, H. Zhou, L. Dou, G. Li, Y. Yang, *Sci. Rep.* **2013**, *3*, 3356.

[56] Q. Zhang, B. Kan, F. Liu, G. Long, X. Wan, X. Chen, Y. Zuo, W. Ni, H. Zhang, M. Li, Z. Hu, F. Huang, Y. Cao, Z. Liang, M. Zhang, T. P. Russell, Y. Chen, *Nature Photonics* **2015**, *9*, 35−41.

1.2. Objectives

1.2. OBJECTIVES

As can be deduced from small molecule OSC literature, most of the reported structures present an A−D−A architecture, where A and D moieties are usually linked by π-conjugated bridges (e.g. thiophene, thienothiophene) that provide solubility (by incorporating ancillary side-chains) and enhance the intermolecular solid-state packing by means of π-π interactions. This A−D−A arrangement seems to have been the privileged design, although without any apparent reason other than synthetic ease, despite the equally feasible D−A−D display. In this sense, this Chapter is split in two parts, the first one dedicated to the more common A−D−A architectures, whereas in the second one, the less-known D−A−D structures are explored (Figure 18).

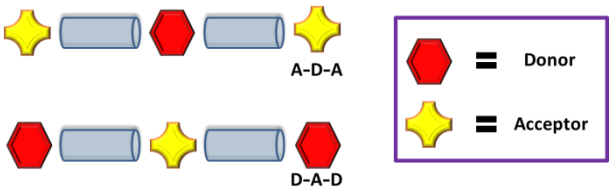

Figure 18. Schematic A−D−A and D−A−D architectures employed in BHJ OSCs.

1.2.1. A−D−A structures

Among the wide variety of readily available molecules for organic photovoltaics, BDT-based molecules (BDT: benzodithiophene) may probably be considered the best performing electron donating fragments, giving rise to the best performing polymers for OSCs.[57] Taking advantage of the benefits BDT donor provides, we designed a series of molecules employing BDT as central D moiety flanked by BTD acceptors (BTD: benzothiadiazole); in-between D and A, thiophene bridges of increasing length were inserted as depicted in Figure 19. Whereas most of the reported systems bearing BTD moieties incorporate them with a 4,7-substitution pattern, we considered of interest exploring the non-explored 5-substitution, due to the novelty it represents. Furthermore, such substitution pattern exposing the thiadiazole

[57] H. Yao, L. Ye, H. Zhang, S. Li, S. Zhang, J. Hou, *Chem. Rev.* **2016**, *116*, 7397−7457.

rings, in an almost linear geometry, may enhance the solid-state interactions, thus improving the PV performance.

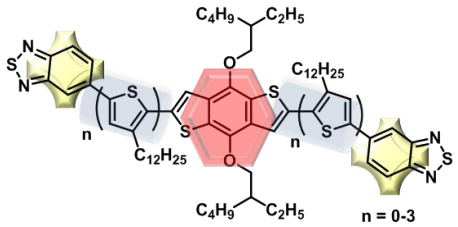

Figure 19. Series of A−D−A based on BTD−Th_n−BDT−Th_n−BTD.

1.2.2. D−A−D structures

As aforementioned, it is unclear the reason because there is a limited number of D−A−D systems when compared to A−D−A ones. Since there is no reason to consider D−A−D systems less appealing, we decided to design a novel electron accepting central core flanked by arylamine donors.

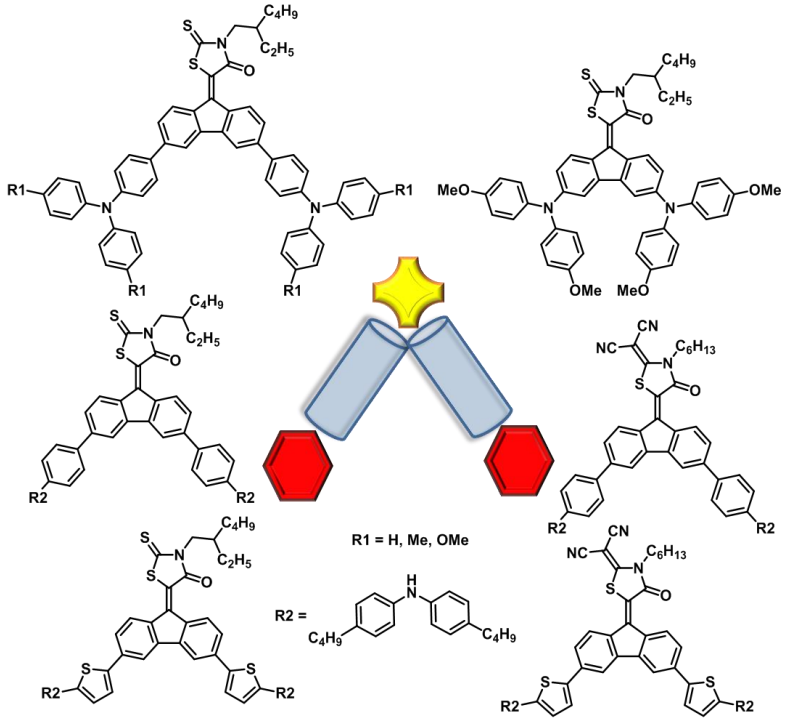

Figure 20. Series of D−A−D based on rhodanines of varying electron acceptor strength.

After a thorough literature review, we came to consider rhodanine acceptor as a most interesting candidate to incorporate to our system. So far, Rh has always been introduced into A−D−A structures by Knoevenagel reaction with the corresponding dialdehyde. Thus, utilizing Rh in a central A core, it implies condensing it with a molecule bearing a ketone functional group. The most suitable building block for this purpose was found to be fluorenone. As illustrated in Figure 20, by using electron donors and acceptors of different relative strengths, the optoelectronic properties of the molecules could be fine-tuned and explored.

1.3. Results and discussion

1.3. RESULTS AND DISCUSSION

1.3.1. A−D−A Small molecules based on BDT-BTD

As aforementioned in the introductory part of this Chapter, molecules bearing fragments of either benzodithiophene (BDT) donor or benzothiadiazole (BTD) acceptor are easily found among the best performing materials for BHJ-OSC. Thus, we have developed a series of molecules combining both molecules in an A−D−A arrangement, where π-conjugated thiophene bridges of increasing length were introduced to modulate both their optical properties and their solid-state aggregation, as well as to improve their solution processability. Additionally, conjugation of BTD to the central core through its 5-position intends to explore the resulting new geometry's ability to enhance the intermolecular interactions, by exposing the thiadiazole rings as "spearheads".

Synthesis

The synthesis of BDT central core, functionalized with 2-ethylhexyloxy solubilizing side-chains, was carried out following a procedure from the literature with some modifications (see Scheme 1).[58] Exposure of thiophene-3-carboxylic acid (**12**) to oxalyl chloride in the presence of a catalytic amount of DMF gave acid chloride **13**. Amide **14** was readily obtained by condensation of **13** with excess of diethylamine. Lithiation of **14** at 0 ºC with n-BuLi generated quinone **15** by dimerization reaction. Reductive O-alkylation of quinone **15** with Zn in basic tetrabutylammonium hydroxide solution, followed by addition of 2-ethylhexyl bromide in presence of catalytic KI, allowed obtaining BDT **16** as thick oil. Finally, organotin derivative **17** was achieved by lithiation of **16**, followed by quenching with trimethyltin chloride.[59]

[58] J. Hou, M.-H. Park, S. Zhang, Y. Yao, L.-M. Chen, J.-H. Li, Y. Yang, *Macromolecules* **2008**, *41*, 6012−6018.

[59] K. R. Graham, C. Cabanetos, J. P. Jahnke, M. N. Idso, A. El Labban, G. O. N. Ndjawa, T. Heumueller, K. Vandewal, A. Salleo, B. F. Chmelka, A. Amassian, P. M. Beaujuge, M. D. McGehee, *J. Am. Chem. Soc.* **2014**, *136*, 9608−9618.

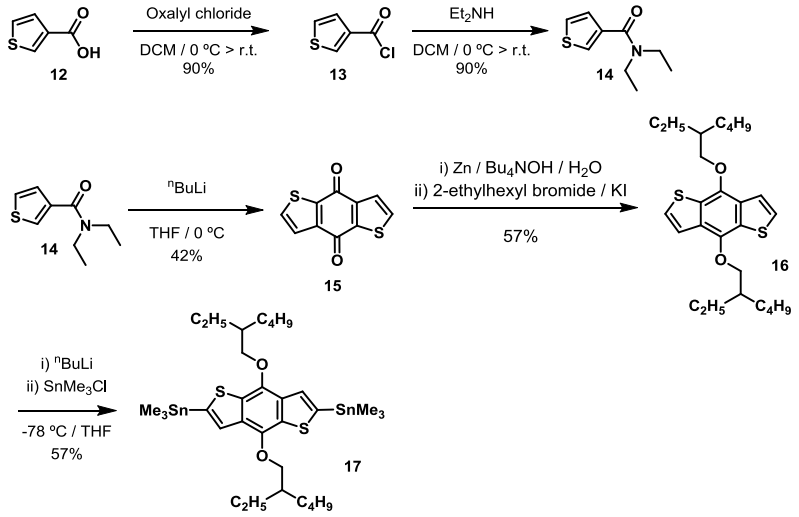

Scheme 1. Synthetic route for the preparation of the BDT central core.

The synthesis of the electron accepting fragment was carried out in parallel from diamine **18** (Scheme 2). 5-Bromobenzo[*c*][1,2,5]thiadiazole (**19**) (BTD) was synthesized following Parmisano's *et al.*[60] procedure, where 4-bromo-1,2-diaminobenzene (**18**) was treated with thionyl chloride in the presence of triethylamine (Et_3N).

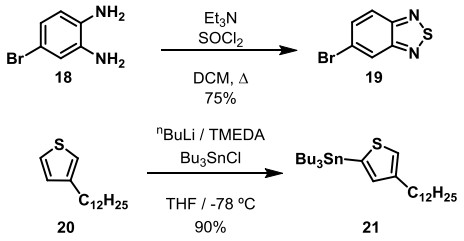

Scheme 2. Synthesis of BTD **19** and stannyl derivative of thiophene **21**.

The build-up of the thiophene bridge was achieved by sequential addition of organotin derivative **21** to **19**. Commercially available 3-dodecylthiophene (**20**) was treated with n-butyllithium followed by the addition of tributyltin chloride (Scheme 2), providing **21**.[61] Stille palladium cross-coupling reaction of **19** and

[60] M. Pagliaro, R.Ciriminna, G.Parmisano, *ChemSusChem* **2008**, *1*, 880−891.

[61] B. Fu, J. Baltazar, Z. Hu, A.-T. Chien, S. Kumar, C. L. Henderson, D.M. Collard, E. Reichmanis, *Chem. Mater.* **2012**, *24*, 4123−4133.

21 using tris(dibenzylideneacetone)dipalladium (Pd_2dba_3) and triphenylphospine (PPh_3) as catalyst gave **22** as a yellow solid. Bromination of this product with NBS provided compound **23** with very good yield. Sequences of cross-coupling/bromination reactions were performed in order to increase the number of 3-dodecylthiophene units, affording compounds **25** and **27** as depicted in Scheme 3.

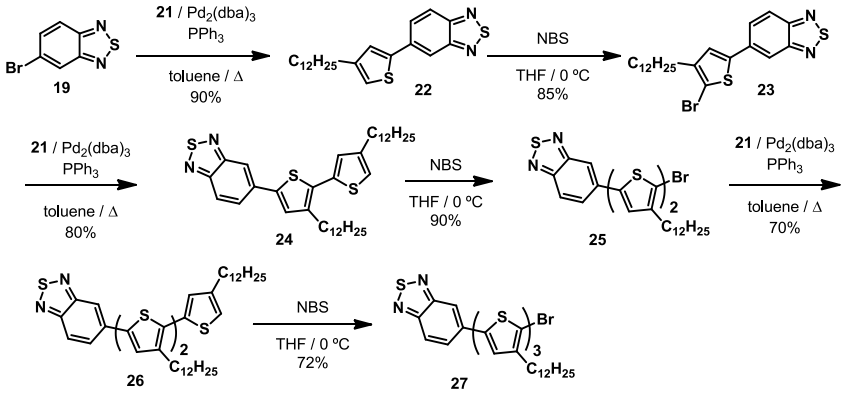

Scheme 3. Synthetic route for the preparation of brominated compounds **23**, **25** and **27**.

Target molecules **28**−**31** were obtained by Stille reaction of donor BDT core **17** with the corresponding brominated acceptor fragment (Scheme 4). Compound **28** was obtained with good yield as an orange solid. In contrast, its increasing size analogues were obtained with moderate to low yields as dark red or maroon solids. All obtained compounds were characterized by the conventional spectroscopic techniques.

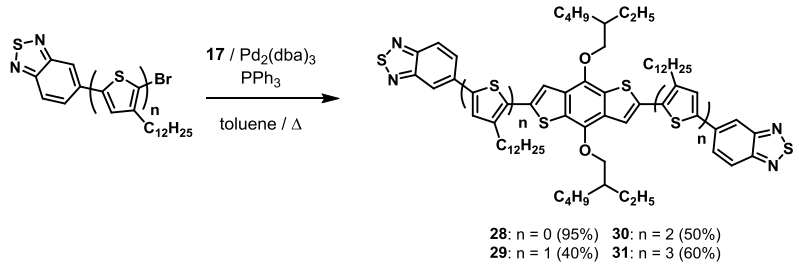

Scheme 4. Synthesis of A−D−A derivatives **28**−**31**.

^{1}H NMR features of compound **25** may serve as representative example of the acceptor fragments (Figure 21). The presence of the BTD moiety is always

evidenced in these compounds by the archetypical down field (8.20−7.80 ppm) small doublet, doublet, double doublet signal pattern. The proton in the C6 position of the molecule (highlighted in blue) shows up at 7.87 ppm as a double doublet, with a ^{3}J coupling of 9.2 Hz with its C7-H neighbor (denoted in purple, and showing itself as a doublet), and a long distance ^{4}J = 1.8 Hz coupling with the proton in C4 (marked in green, being itself a "small" doublet).

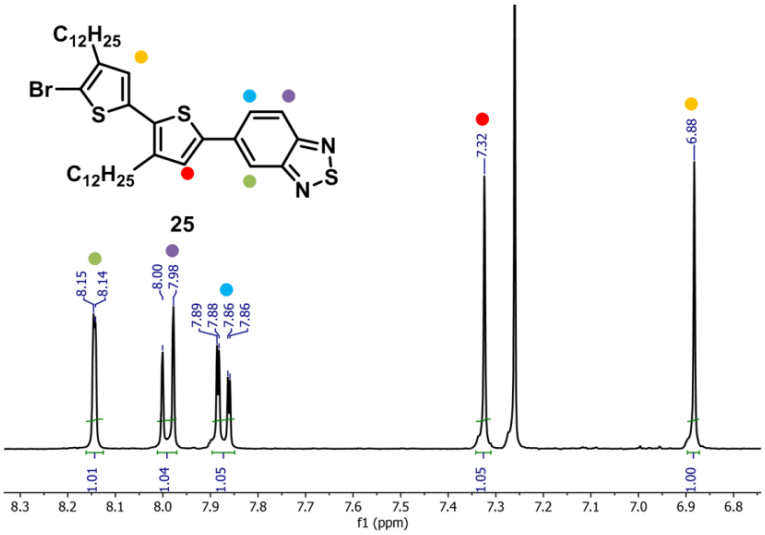

Figure 21. ^{1}H NMR spectrum (400 MHz, $CDCl_3$) of **25** centered on the aromatic region.

In contrast, the signals of the thiophenes protons appear as singlets at higher field (7.32 and 6.88 ppm), with that closer to the BTD (red dot) shifted to down field due to the strong electron deshielding provoked by this electron poor group. Comparison of final product **30** with its **25** precursor evidences a new set of signals belonging to the BDT fragment, i.e. singlet at 7.42 ppm (see Figure 22). It is also characteristic of these compounds the *pseudo* doublet at 4.24 ppm (orange triangle), belonging to the O-CH_2 protons, this signal it is usually confused with a doublet in the literature, neglecting the influence of its chiral neighboring carbon. Finally, also characteristic are the Ar-CH_2 signals (2.87 ppm, blue triangle), belonging to the solubilizing alkyl chains linked to the thiophene rings; interestingly, the signals for both Ar-CH_2 are not isochronous, quite likely due to the electron withdrawing influence exerted by the BTD unit over its neighboring thiophene ring.

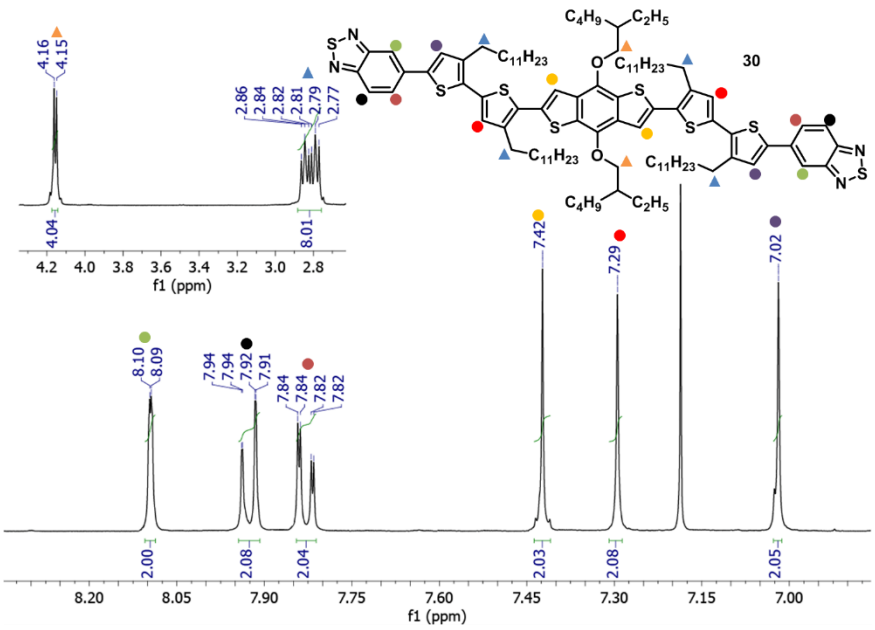

Figure 22. Partial ^{1}H NMR spectrum (400 MHz, $CDCl_3$) of final product **30** focusing on the aromatic region; aliphatic region zoom inset.

Optical properties

Absorption experiments in DCM solution showed that all final products **28**-**31** present a broad band in the 400−500 nm region peaking around 450 nm (Figure 23 top). As the thiophene bridge increases in length, higher-energy bands decrease in intensity to finally virtually disappear or merge with the lower energy absorption band. In a way that might seem counterintuitive, this band experiences a hypsochromic shift (from 456 nm for **28** to 443, 445 and 447 nm for **29**, **30** and **31**, respectively) as longer thiophene linkers are introduced in between BDT and BTD units. This behavior might be attributed to the steric hindrance induced by the dodecyl side-chains linked to the thiophene spacers (*vide infra*), as it is observed when used to disrupt electronic communication in π-conjugated systems.[62] Despite the latter, a significant broadening of the

[62] H. Li, A. S. Batsanov, K. C. Moss, H. L. Vaughan, F. B. Dias,K. T. Kamtekar, M. R. Bryce, A. P. Monkman, *Chem. Commun.* **2010**, *46*, 4812–4814.

absorption is observed for **29**–**31** with onsets (taken as linear extrapolation of the absorption feature when Abs = 0) going up to 532 nm.

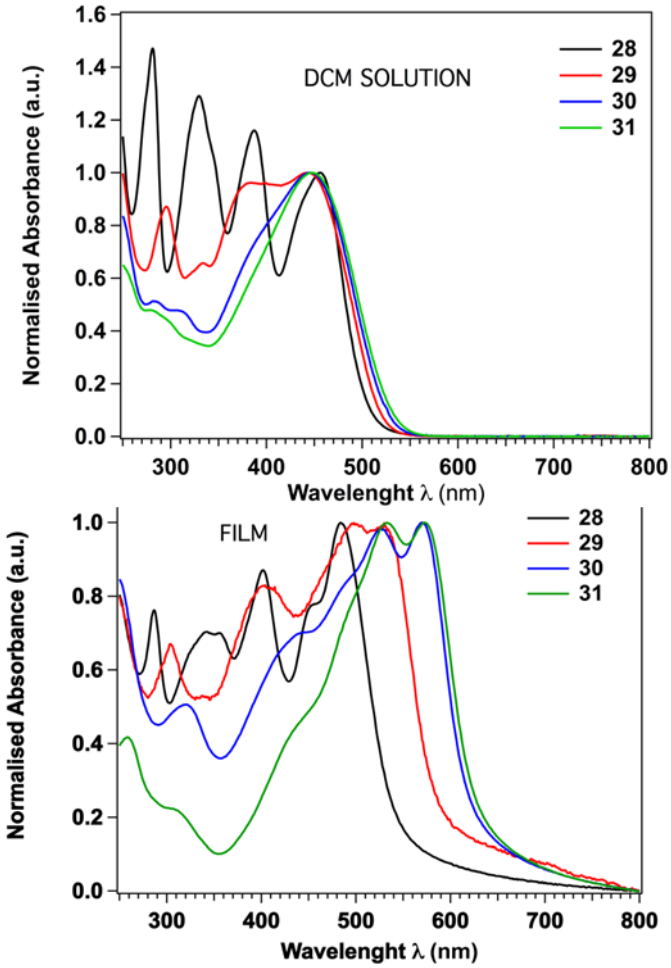

Figure 23. UV-vis absorption spectra of compounds **28**–**31**: (below) DCM solutions, (top) thin-films spin-coated from DCM solutions.

A completely different pattern is obtained when measuring the absorption of thin-films (Figure 23 bottom). In the case of **28**, a 30 nm red-shift takes place compared with DCM solution. This red-shift is ascribed to the planarization of the structure, induced by the solid-state packing of the molecules in thin films. More important changes and the expected shift to longer wavelengths are observed in the spectra as additional thiophene rings are introduced into the π-

conjugated bridge. For **29**−**31** molecules, with increasing length of the thiophene bridges, the thin-films spectra are dominated by a broad absorption ranging from 360 to 800 nm. This band shows the characteristic vibronic structure featuring two peaks indicative of effective π-π interactions between different molecule backbones.[63] Molar absorptions (ε) of the compounds are observed to increase from *ca.* 0.5 to 1.0 × 10^5 M^{-1} cm^{-1} as longer thiophene bridges are inserted in between D and A. The increase of the thiophene spacer implies extending the π-conjugation of the system, which ultimately means an increase of the oscillator's strength. Detailed absorption data are summarized in Table 1.

Table 1. Summarized data from UV-vis spectra of compounds **28**–**31.**

Compound	λ_{max} [nm][a]	λ_{onset} [nm][a]	λ_{max} [nm][b]	λ_{onset} [nm][b]	ε 10^4 [$M^{-1}cm^{-1}$][c]
28	456	502	484	545	4.97
29	443	519	530	590	5.13
30	445	522	570	622	6.84
31	447	532	572	631	9.91

[a] In CH_2Cl_2 solution. [b] In thin films. [c] Molar absorption of the lower energy band in CH_2Cl_2 solution.

Electrochemical properties

The electrochemical behavior of target compounds **28**−**31** was studied by CV. As expected for A−D−A systems, samples showed both oxidation and reduction processes (Figure 24 and Table 2). All molecules experience a single reversible reduction process around −1.62 V with apparently negligible effect of the thiophene bridge size. On the contrary, molecules show a much more complicated behavior upon oxidation, anodically shifting their oxidation potentials as the molecules bear more thiophene units. Compounds **28** and **29** show two reversible oxidation processes, whereas **30** and **31** show many irreversible oxidation processes presumably due to the mixture of states from the oligothiophene bridge and the BDT donor core.

[63] J. Zhou, Y. Zuo, X. Wan, G. Long, Q. Zhang, W. Ni, Y. Liu, Z. Li, G. He, C. Li, B. Kan, M. Li, Y. Chen, *J. Am. Chem. Soc.* **2013**, *135*, 8484−8487.

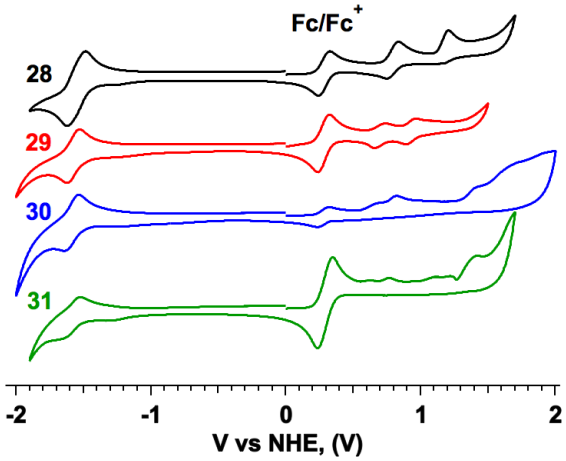

Figure 24. Cyclic voltammograms of compounds **28**–**31** were recorded from 0.1 M DCM deaerated solutions with Bu_4NPF_6 (0.1 M) as supporting electrolyte at 100 mV s^{-1}, employing glassy carbon as working electrode, Pt wire as counter electrode, and $Ag/AgNO_3$ as reference electrode. Fc/Fc^+ internal standard ($E_{1/2}^{ox}$ = 0.28 V) was added after each measurement.

Frontier orbital energies and electrochemical gaps were estimated from the redox potential onsets (Table 2), using the following equations:

Equation 4. $E_{gap}^{opt} = \lambda_{onset} / 1240$

Equation 5. $E_{gap}^{cv} = E_{ox}^{onset} - E_{red}^{onset}$

Equation 6. $E_{HOMO} = -[E_{onset}^{ox} + 4.4]$

Equation 7. $E_{LUMO} = E_{HOMO} + E_{gap}$

A rise of the HOMO energy is obtained as more thiophene units are introduced into the bridge, ranging from −5.24 to −5.04 eV. The energies calculated for the LUMO by using either optical or electrochemical gaps show good agreement and, as expected, are negligibly affected by the bridge size. Empirically calculated gaps between 1.96 and 2.05 eV for **30** and **31** are considered moderate-low band gaps and may potentially be used for OPV.

Table 2. Electrochemical data and estimated HOMO/LUMO energies for compounds **28**–**31.**

Compound	E_{red}^{onset} [V]	E_{ox}^{onset} [V]	E_{gap}^{cv} [eV]	E_{gap}^{opt} [eV]	E_{HOMO} [eV]	E_{LUMO}^{cv} [eV]	E_{LUMO}^{opt} [eV]
28	–1.452	0.729	2.18	2.27	–5.24	–3.06	–2.97
29	–1.499	0.629	2.12	2.10	–5.14	–3.02	–3.04
30	–1.500	0.552	2.05	1.99	–5.07	–3.02	–3.08
31	–1.499	0.529	2.02	1.96	–5.04	–3.02	–3.08

Photovoltaic properties

In collaboration with Prof. Dyakonov (Würzburg University), materials **28**–**31** were tested as donors in BHJ-OSC using $PC_{61}BM$ as acceptor. Built devices, with Glass/ITO/PEDOT:PSS/Active layer/Ca/Al architecture, showed poor photovoltaic performances (PCE < 1%). The best performing material was **31**. Cells based on it showed a maximum efficiency o PCE = 0.72%, with very low short-circuit current (J_{SC} = 1.9 mA cm^{-2}), and a fill factor of 44% (see Figure 25).

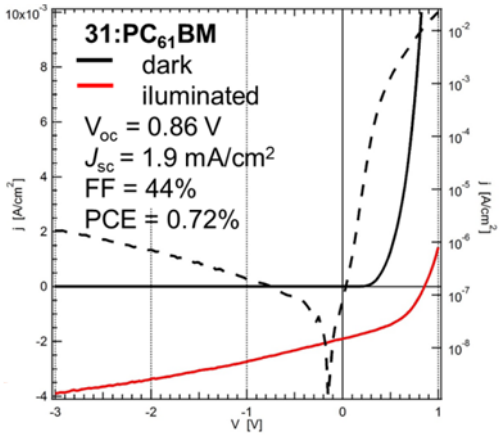

Figure 25. *J-V* curve for BHJ OSC of **31** blended with $PC_{61}BM$, with photovoltaic parameters inset.

Despite the poor PV performance, the relatively high open circuit value of 0.86 V is indicative of charges being photogenerated. Analysis of the *J*/*V* curve shape indicates that the device is not able to fully extract the generated charges, probably due to strong recombination processes.

DFT Computational Study

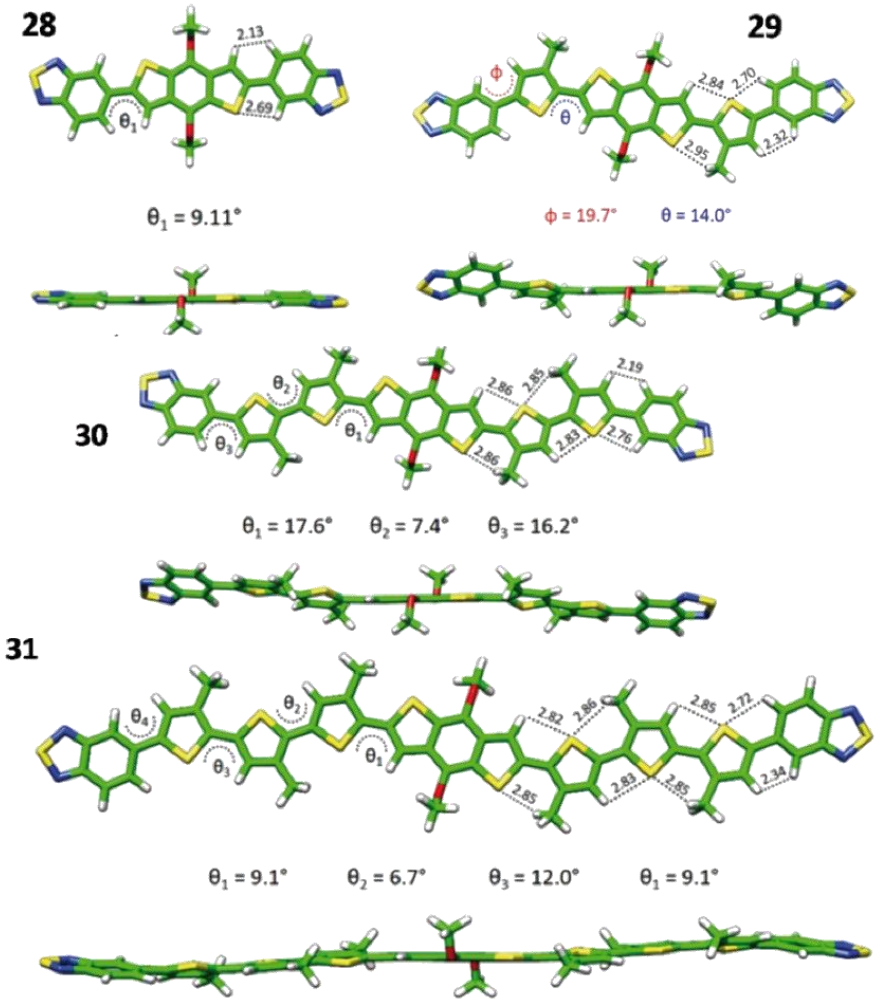

Figure 26. Top and side views of the minimum-energy geometry calculated for compounds **28**–**31**, including the values of dihedral angles Φ and θ and relevant inter-ring short contacts (in Å). Aliphatic chains linked to BDT core and thiophene rings were switched by methyl groups to mitigate the computational cost.

The unexpected underperformance of the built BHJ OSCs compared with analogue molecules,[64] compelled us to delve into the electronic properties of the molecules. Therefore, in collaboration with Prof. Ortí at Universidad de Valencia, theoretical calculations within the density functional theory (DFT) framework were performed to shed light on the optical and spectroscopic properties of **28**−**31** derivatives.

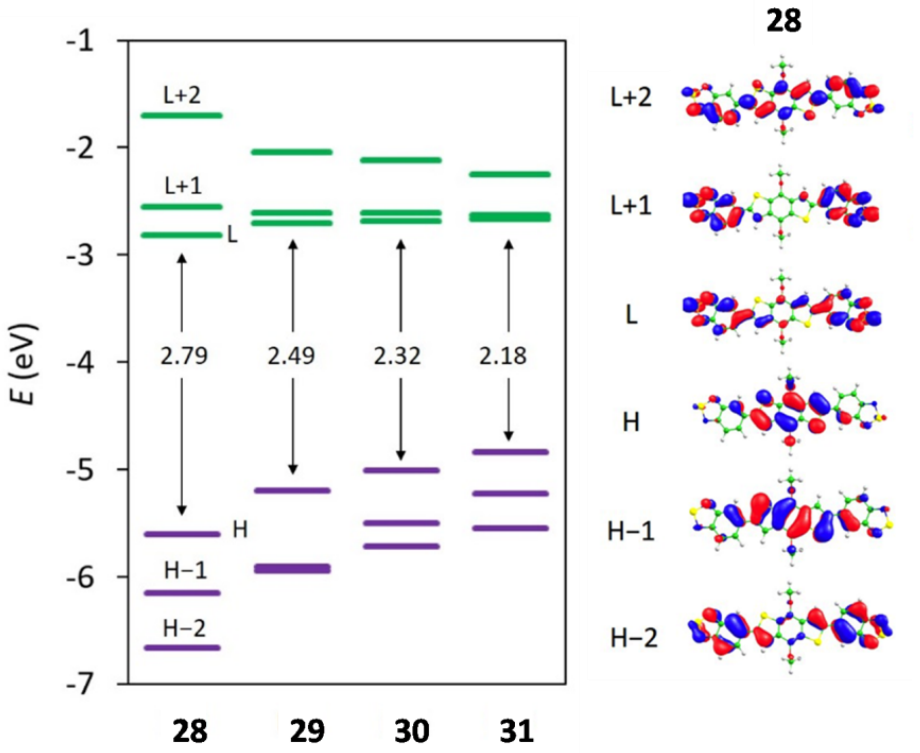

Figure 27. Frontier molecular orbitals diagram including the HOMO–LUMO gap (left), and the isovalue contours (±0.03 a.u.) calculated for the derivative **28** (right). H and L denote HOMO and LUMO, respectively.

Geometry optimizations at the B3LYP/cc-pVDZ level indicate that the minimum-energy structures of the A–D–A derivatives are mainly planar,

[64] a) L. Liang, J.-T. Wang, X. Xiang, J. Ling, F.-G. Zhao, W.-S. Li, *J. Mater. Chem. A* **2014**, *2*, 15396–15405; b) J. Du, A. Fortney, K. E. Washington, C. Bulumulla, P. Huang, D. Dissanayake, M. C. Biewer, T. Kowalewski, M. C. Stefan, *ACS Appl. Mater. Interfaces* **2016**, *8*, 33025−33033.

showing small twisting angles (< 20º) between adjacent rings due to short H···H (2.3 Å) and H···S (2.7–2.9 Å) contacts (Figure 26). Figure 27 shows the frontier molecular orbitals (MOs) energy diagrams calculated for **28**–**31**, along with a representative example of their topology for compound **28**. The HOMO and the HOMO−1 are localized over the electron-donor BDT unit with some contribution from the thiophene π-conjugated bridge, whereas the HOMO−2 mainly spreads over the bridge.

By contrast, the LUMO and the LUMO+1 are fully located over the electron-acceptor BTD moieties, whereas the LUMO+2 spreads over the whole molecule. The description of the frontier MOs is maintained in compounds **29**, **30** and **31**, although the nature of HOMO−1 and HOMO−2 is predicted to swap in **30** and **31**. This swap stems from the larger increase in energy the orbital located over the thiophene spacer experiences upon increasing its length, compared to the orbital localized over the BDT core (Figure 27). The HOMO energy systematically increases in energy going from **28** (−5.60 eV) to **31** (−4.84 eV) upon increasing the number of thiophene rings in the π-conjugated bridge. This trend is in good agreement with the experimentally recorded anodic shift of E_{ox} (Table 2). In contrast, the LUMO and LUMO+1 are predicted to remain practically unaltered at ~ −2.7 eV, regardless the size of the thiophene π-spacer, due to the localization of these orbitals over the electron-acceptor BTD units. This is also in good agreement with the CV experiments. As expected, the energy difference between the LUMO and LUMO+1 decreases as the electron-acceptor moieties get more separated, reaching practically the degeneracy for **31** (Figure 27). The HOMO–LUMO gap is predicted to significantly narrow from 2.79 eV in **28** to 2.18 eV in **31**.

The theoretical trends calculated for the HOMO–LUMO gap and the HOMO and LUMO energies for compounds **28**–**31** are in good agreement with the experimental trends obtained from optical and electrochemical data displayed in Table 2. Time-dependent DFT (TD-DFT) calculations of the singlet excited states (S_n) were also conducted to fully rationalize the nature and trends experimentally recorded for the low-lying absorption bands of **28**–**31**. Theoretical calculations at the TD-B3LYP/cc-pVDZ level predict for **28** two intense electronic transitions to the low-lying excited states S_1 and S_3 at 2.50 and 2.97 eV with oscillator strengths of f = 0.590 and 0.485, respectively (Table 3). The $S_0 \rightarrow S_1$ and $S_0 \rightarrow S_3$ transitions are best described by one-electron

promotions from the HOMO and HOMO−1 to the LUMO, respectively, that mainly implies a CT from the electron-donor BDT moiety to the electron-acceptor BTD units, and give rise to the experimental bands recorded at 456 and 387 nm in DCM for **28** (Figure 23). Moving to higher energies, the electronic transitions to S_5 and S_{10}, predicted at 3.52 and 3.95 eV, respectively, with relatively high oscillator strength (f > 0.35), lead to the peak experimentally recorded at 329 nm (Figure 23), and are mostly centered over the BDT unit (Table 3 and Figure 27). A large number of high-energy electronic states calculated at energies higher than 5.0 eV explain the spectroscopic features recorded below 300 nm for **28**.

Table 3. Lowest-lying singlet excited states calculated for **28**–**31** at the TD-B3LYP/cc-pVDZ level. Vertical excitation energies (*E*), oscillator strengths (*f*), description in terms of mono excitations (contributions within parentheses), and nature of the excited state are summarized. Only the most relevant S_1 and S_3 states are included for **28**–**31**.

	State	*E* [eV]	*E* [nm]	*f*	Description	(%)	Nature
28	S_1	2.502	496	0.5896	H → L	(96)	CT
	S_2	2.719	456	0.0000	H → L+1	(97)	CT
	S_3	2.968	418	0.4849	H−1 → L	(95)	CT
	S_5	3.515	353	0.3641	H → L+2	(96)	donor
	S_{10}	3.950	314	0.3978	H−1 → L+2	(87)	donor
29	S_1	2.215	560	0.9674	H → L	(99)	CT
	S_3	2.860	434	1.0985	H → L+2	(95)	donor (CT)
30	S_1	2.069	599	1.7438	H → L	(98)	CT
	S_3	2.600	477	1.3371	H → L+2	(80)	donor (CT)
31	S_1	1.942	639	2.0687	H → L	(94)	CT
	S_3	2.316	535	1.7056	H → L+2	(86)	donor (CT)

Moving from **28** to **29**–**31**, TD-DFT calculations predict a significant increase in the oscillator strength of the electronic transitions associated to the bright lowest-lying S_1 and S_3 states (Table 3) due to the extension of the thiophene π-conjugated bridge. These electronic transitions, which are computed with a large CT nature, are predicted to undergo a significant red-shift to longer wavelengths (lower energies) upon lengthening the thiophene bridge. The $S_0 \rightarrow S_1$ HOMO→LUMO transition goes from 2.50 eV in **28** to 1.94 eV in **31** in accordance with the HOMO–LUMO gap evolution (Figure 27) and the electrochemical data (Table 2).

However, the trend observed for the E_{gap} is in contradiction with the experimentally recorded hypsochromic shift in DCM solution (Figure 23 top) as longer thiophene linkers are introduced in between the BDT and BTD units. This inconsistency might, in principle, arise from the high twist angles between aromatic rings exerted by the steric hindrance of the dodecyl side-chains attached to the thiophene spacers. To further confirm this, theoretical calculations were performed in order to analyze the effect the inter-ring twist angles between thiophene rings and BTD units may have over the absorption features in the low-energy range. Figure 28 represents the calculated lowest-lying S_1 excited state energy as a function of Φ and θ twist angles that characterize the rotational isomerism of compound **29**.

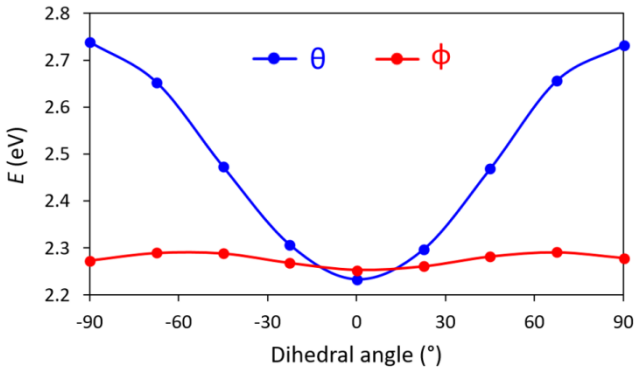

Figure 28. Evolution of the energy calculated for lowest-lying singlet excited state S_1 of **29** as a function of the inter-ring Φ and θ twist angles. See Figure 26 for the definition of Φ and θ.

These theoretical calculations ran at the B3LYP/cc-pVDZ level indicate that the internal rotation of the first thiophene ring with respect to the BTD unit (Φ

angle) hardly impacts on the lowest-lying S_1 energy. Conversely, the variation of θ angle between the thiophene units induces the CT S_1 state to significantly shift to higher energies, from 2.19 eV (530 nm) at 0º to 2.68 eV (460 nm) at 90º. Similar studies were performed for **28**, **30** and **31** and led to consider that the long aliphatic chains can lead to large distortions from planarity in solution; the theoretical red-shift (0.56 eV from **28** to **31**) predicted for S_1 upon increasing the spacer length might be counterbalanced by the blue-shift resulting from the non-planarity of the bridge (up to 0.49 eV in **29**). This would explain the spectroscopic features observed for the lowest-lying absorption band in solution (Figure 23 top). Whereas in thin-films, the effective π–π intermolecular interactions induce the planarization of the π-conjugated spacer, therefore causing this band to undergo the expected red-shift of ~ 0.4 eV moving from **28** to **31** (Figure 23 bottom).

Table 4. Reorganization energies (λ, in eV) related to the transport of holes (λ_{hole}) and electrons ($\lambda_{electron}$) calculated at the B3LYP/cc-pVDZ level of theory.

	28	**29**	**30**	**31**
λ_{hole} [eV]	0.235	0.278	0.252	0.216
$\lambda_{electron}$ [eV]	0.162	0.173	0.138	0.115

Theoretical estimation of the molecules reorganization energies (λ) may help explaining the low photocurrents observed for the fabricated OSCs, by giving an insight into their hole and electron transport ability. Calculations at the B3LYP/cc-pVDZ (Table 4) indicate that hole reorganization energies (λ_{hole}) for compounds **28**–**31** are above 0.20 eV, suggesting limited hole transport capabilities. In contrast, electron reorganization energies ($\lambda_{electron}$) are predicted in the range of 0.11–0.17 eV. These $\lambda_{electron}$ values are as small as that obtained for fullerene C_{60} (0.129 eV) at the same level of theory (reported value of 0.13 eV).[65] These findings point out that BDT-BTD based derivatives **28**–**30** might perform well as efficient electron-transporting materials. It is predicted that both λ_{hole} and $\lambda_{electron}$ diminish as the π-conjugated spacer is extended, suggesting an improvement of the transport properties from **29** to **31**. It is worth mentioning that thiophene bridges are involved in the formation of both cationic and anionic species. For instance, oxidation of **31** to $\mathbf{31}^+$ extracts 0.63e

[65] J. J. Kwiatkowski, J. M. Frost, J. Nelson, *Nano Lett.* **2009**, *9*, 1085–1090.

from the terthiophene bridge; similarly, 0.44e are introduced into the bridge upon reduction to **31**$^{-}$. Notwithstanding, charge carrier mobilities will ultimately be determined by the supramolecular arrangement of the derivatives in the films.

Charge transport study

Charge transport properties study was performed in collaboration with Prof. Seki at Kyoto University. Time-resolved microwave conductivity (TRMC) measurements, performed with spin-coated films of pristine derivatives **28**–**31** by excitation at 355 nm (Figure 29), revealed direct dependence of the photoconductivity over the thiophene bridge length (Table 5), maximizing for **30**.

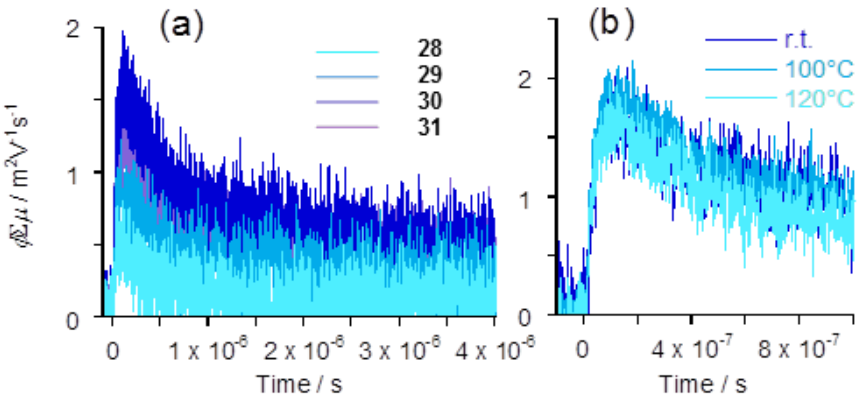

Figure 29. (a) Kinetic traces of transient conductivity ($\varphi\Sigma\mu$; product of photo-carrier generation yield (φ) and the sum of mobilities ($\Sigma\mu$)) observed for the series of compounds **28**–**31** under 355 nm excitation after annealing at 120 ºC. (b) Kinetic traces observed for compound **30** before and after thermal annealing.

Noteworthy, observed kinetic traces for all compounds of the series seem to almost overlap, meaning almost negligible effect of the thiophene bridge size, observing no significant acceleration in the case of the shortest bridged compound (**28**). Altogether, it is suggestive that observed kinetics are due to bulk recombination of the photogenerated free charge carriers. Photoconductivity was also examined after thermal annealing of the films (100 and 120 ºC for 1 h), showing no significant change of conductivity before/after the annealing processes.

Table 5. Observed products of photo-carrier generation yield (φ) and the sum of mobilities ($\Sigma\mu$) for the series of compounds **28**–**31** under 355 nm excitation after annealing at different temperatures.

Compound	$\varphi\Sigma\mu$ [10^{-9} m^2 $V^{-1}s^{-1}$]		
	r.t.	100 ºC	120 ºC
28	1.0	0.7	0.6
29	1.3	1.5	0.9
30	1.8	2.0	1.6
31	1.3	1.5	1.3

The X-ray diffraction (XRD) patterns of the thin-films (Figure 30) reveal that molecule **30** forms well-ordered crystalline structures as cast, experiencing negligible structural changes even after thermal annealing at temperatures up to 120 ºC for 1 h. This structural thermal stability parallels with the $\varphi\Sigma\mu$ steady values obtained for the annealed films. Conversely, films made of **28**, **29** and **31** experienced noticeable structural changes upon thermal annealing.

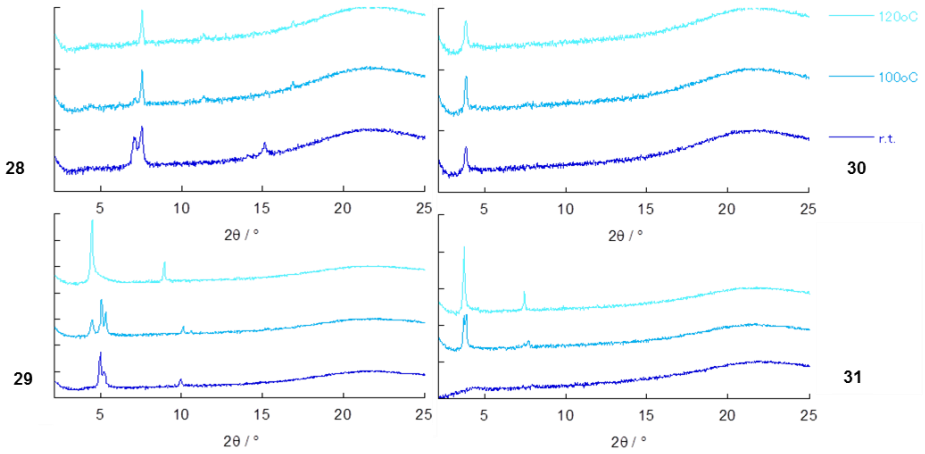

Figure 30. X-ray diffractograms for **28** (bottom left corner), **29** (top left corner), **30** (bottom right corner), **31** (top right corner) films before (blue) and after annealing at 100 °C (turquoise) and 120 °C (sky blue) for 1 h.

Such changes are evidenced for **28** and **29** by the disappearance of the "as cast" diffraction features and the surge of new ones for the thermally annealed films, evidencing a complete rearrangement of their crystalline structures; as for **31**, the "as cast" film showing no diffraction patterns, seem to crystallize after the

thermal annealing processes. These rearrangements observed after the thermal treatment do not provide any meaningful improvement to the conduction properties for **28**, **29** and **31** as shown in Table 5.

Based on the revealing results obtained from the theoretical calculations and the good film-forming property of marked compound **30**, its quantitative separate contributions of positive and negative charge carriers to the semiconducting nature was examined by TRMC@interfaces. With a simple metal-insulator semiconductor device, positive and negative charge carriers are separately injected through ultra-thin electrodes by an applied modulated bias, and accumulated at the semiconductor-insulator interface. The local motion of the selectively injected charge carriers was traced by non-contact 9 GHz microwave probes, directly providing the product of number (n) and mobility (μ) of the injected charge carriers.

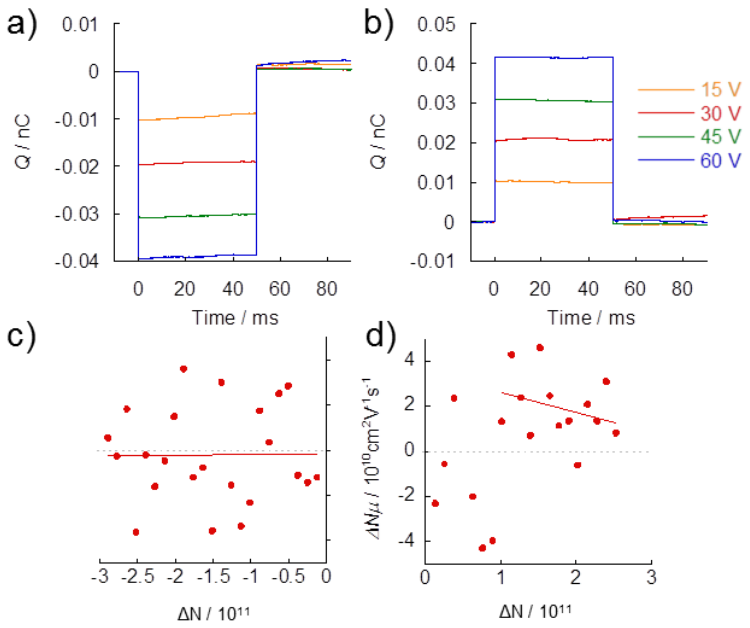

Figure 31. Charge-discharge processes monitored by integration of current to the devices made of **30** (a, b). Correlation between the pseudo electrical conductivity $\Delta N\mu$ and the density of injected charge carriers ΔN (capacitance = 0.672 nF) for hole injection (negative bias, c) electron injection (positive bias, d).

Figure 31 shows the observed pseudo electrical conductivity ($\Delta N\mu$) *vs.* the density of injected charge carriers (ΔN) of holes (Figure 31c) and electrons (Figure 31d). It is noteworthy that the device is completely silent for hole injections as high as ~0.05 nC, although active for electron injection. These observations are in agreement with the theoretically predicted low $\lambda_{electron}$ values (significantly smaller than λ_{hole}, Table 4) and it is coherent with n-type semiconducting nature of the compound. The measured electron mobility (μ_e) is in the range of ~0.1 $cm^2 V^{-1} s^{-1}$.

Altogether, predicted reorganization energies and the charge transport properties measured for **28**−**31**, the poor performance observed for the BHJ built devices employing these materials as p-type organic semiconductors is fully justified. Despite charges being successfully generated within the active layer, the device is unable to efficiently extract them due to the unwillingness of **28**−**31** to transport holes. As a matter of fact, considering that most organic semiconducting materials often exhibit one to two orders of magnitude lower electron mobilities, compound **30** is an excellent candidate to be used as non-fullerenic acceptor for OSCs.

1.3.2. D−A−D Small molecules based on rhodanine acceptors.

Aside from some disperse examples, D−A−D architectures are not as abundantly found as their A−D−A counterparts. Finding no obvious reason to this observation, it is compelling trying to fill this apparent gap. Keeping this aim in mind, the obvious challenge was finding a suitable acceptor core. Rhodanine molecule was chosen to fulfill this role due to the excellent PV performances that molecules bearing it as A unit have demonstrated.[54–56] In order to accommodate the Rh fragment into the D−A−D architecture, it was necessary to find a molecule synthetically compatible with the Rh chemical nature. Fluorenone's ketone group offered the ideal candidate for condensation with Rh *via* Knoevenagel reaction. The incorporation of different arylamine donors has allowed exploring this new A core optical properties and its performance in OSCs.

1.3.2.1. *1st Generation D−A−D small molecules*

As first approximation we explored the optical and electronic properties of systems based in the combination of two different rhodanines (*i.e. N*-(2-ethylhexyl)rhodanine –denoted RhEH henceforth– and *N*-hexyl-2-(1,1-

dicyanomethylene)rhodanine –denoted RhCN henceforth) with two different triarylamine donors (*i.e.* triphenylamine and diphenylaminothiophene). The resulting products combine D and A units of varying strength, thus enabling a fine-tuning of the frontier orbitals and the optical band gap.

Synthesis

Rhodanine precursors were synthesized following slight modifications to previously reported methods. The preparation of novel RhCN derivative **35** was achieved in a single synthetic step by reaction of commercially available *n*-hexylisothiocyanate (**32**) with malononitrile (**33**) and ethyl 2-bromoacetate (**34**), mediated by the addition of 1,8-diazabicyclo[5.4.0]undec-7-ene (DBU) as base (Scheme 5).[66]

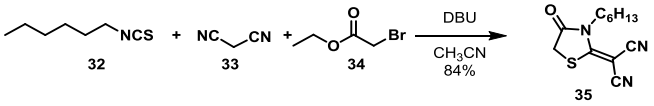

Scheme 5. Synthesis of precursor RhCN (**35**).

The synthesis of RhEH was carried out in good yields following the procedure described by Saji *et al.*,[67] where bis(carboxymethyl)trithiocarbonate (**36**) and 2-ethylhexylamine (**37**) were refluxed in an *iso*-propanol solution using Et_3N as reagent (Scheme 6).

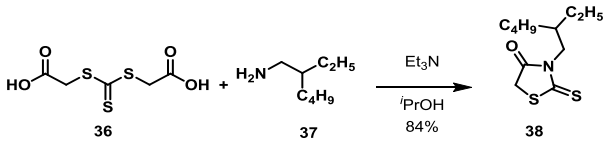

Scheme 6. Synthesis of precursor of RhEH (**38**)**.**

The synthesis of the fluorene core was carried out in parallel, as shown in Scheme 7, following a two steps synthesis reported by Langeveld and collaborators.[68] The bromination of commercially available 9,10-

[66] J. Mao, N. He, Z. Ning, Q. Zhang, F. Guo, L. Chen, W. Wu, J. Hua, H. Tian, *Angew. Chem. Int. Ed.* **2012**, *51*, 9873–9876.

[67] M. Ono, S. Hayashi, K. Matsumura, H. Kimura, Y. Okamoto, M. Ihara, R. Takahashi, H. Mori, H. Saji, *ACS Chem Neurosci*. **2011**, *2*, 269−275.

[68] K. Brunner, A. van Dijken, H. Börner, J. J. A. M. Bastiaansen, N. M. M. Kiggen, B. M. W. Langeveld, *J. Am. Chem. Soc*. **2004**, *126, 6035−6042.*

phenanthrenequinone (**39**) with Br_2 in the presence of benzoyl peroxide (**40**) and under W-lamp irradiation allowed to achieve its 3,6-dibrominated product (**41**). Further treatment with potassium hydroxide and potassium permanganate provided 3,6-dibromofluorenone (**42**) by oxidative ring-contraction decarbonylation.

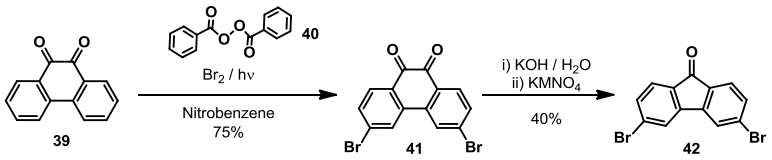

Scheme 7. Preparation of fluorenone derivative **42**.

The synthetic route followed to obtain the triarylamine donating fragments is shown in Scheme 8. Buchwald-Hartwig C-N coupling of 1-bromo-4-butylbenzene (**43**) with 4-butylaniline (**44**) using $Pd_2(dba)_3$ and 2-dicyclohexylphosphino-2′,4′,6′-triisopropylbiphenyl (XPhos) as catalysts provided diphenylamine **45** with excellent yield.[69] The coupling of **45** with commercially available 2-bromothiophene (**46**) by a second Buchwald-Hartwig reaction yielded diphenylaminothiophene (DPAT) derivative **47**. Finally, lithiation at low temperature of **47**, followed by addition of trimethyltin chloride provided organotin derivative **48**; due to stability issues, this type of organotin derivatives are never purified by column chromatography in silica gel, but directly used in the next step without further purification.

[69] K. C. Moss, K. N. Bourdakos, V. Bhalla, K. T. Kamtekar, M. R. Bryce, M. A. Fox, H. L. Vaughan, F. B. Dias, A. P. Monkman, *J. Org. Chem.* **2010**, *75*, 6771–6781.

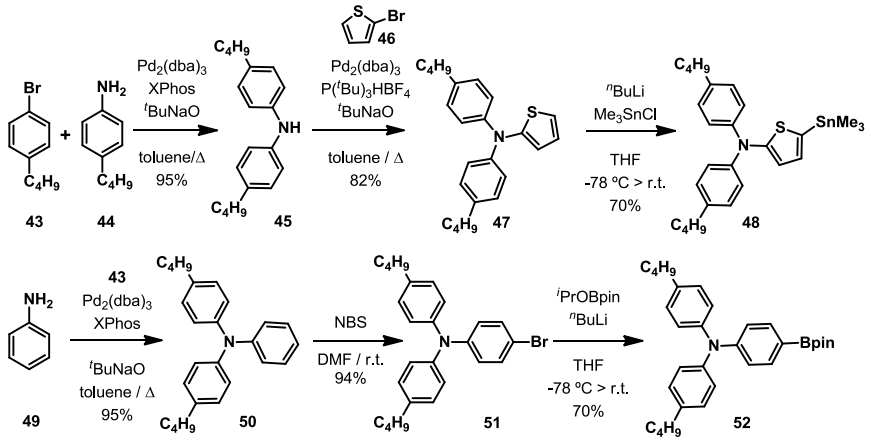

Scheme 8. Preparation of donor fragments **48** and **52**.

Triphenylamine (TPA) donor fragment was similarly prepared following subtle modifications to a previously described procedure.[70] Palladium mediated C-N cross-coupling of aniline (**49**) with two equivalents of bromophenyl derivative **43** provided triphenylamine derivative **50** in high yield. Further bromination employing NBS gave halogenated derivative **51** almost quantitatively. Thereafter, its low temperature lithiation followed by quenching with isopropoxypinacol borate allowed obtaining boron pinacolate derivative **52**.[71] The synthesis of compound **53** was achieved by Suzuki-Miyaura reaction between **42** and **52**, using $Pd_2(dba)_3$ and tri(*o*-tolyl)phosphine (P(*o*-tol)$_3$) to *in situ* generate the Pd catalyst and 3 M K_3PO_4 as base, in moderate-low yield. In contrast, compound **54** was synthesized *via* Stille cross-coupling reaction between **42** and **48**, employing the same $Pd_2(dba)_3$/P(*o*-tol)$_3$ catalyst, in this case in good yield (Scheme 9).

[70] V. Maurel, M. Jouni, P. Baran, N. Onofrio, S. Gambarelli, J.-M. Mouesca, D. Djurado, L. Dubois, J.-F. Jacquot, G. Desfondsa, I. Kulszewicz-Bajer, *Phys. Chem. Chem. Phys.* **2012**, *14*, 1399−1407.

[71] V. Maurel, L. Skorka, N. Onofrio, E. Szewczyk, D. Djurado, L. Dubois, J.-M. Mouesca, I. Kulszewicz-Bajer, *J. Phys. Chem. B* **2014**, *118*, 7657−7667.

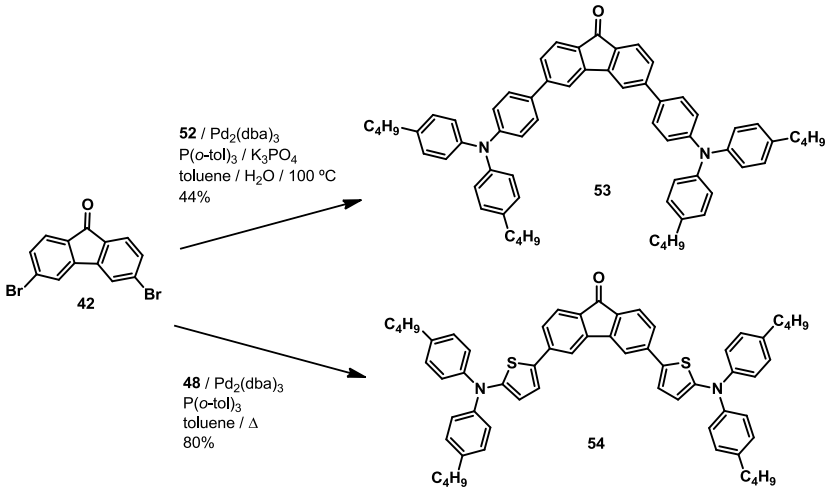

Scheme 9. Synthetic pathway to **53** and **54**.

As shown in Scheme 10 target molecules **55**−**58** were obtained by Knoevenagel condensation of precursors **53** and **54** with rhodanines **35** and **38** in an acetic acid solution containing ammonium acetate (NH_4OAc) as catalyst. These reactions proceeded with moderate to low yields (30−56%), the starting materials were easily recovered and set again until their full conversion. Noteworthy, test reactions of Rh **38** with fluorenone proceeded with high yields (>96%) in less than 2 h, compared to the 24 h required for **55**−**58**. This reactivity decrease is likely due to the presence of the triarylamine strong electron donating groups, which effectively reduce the electrophilicity of the fluorenone's ketone group.

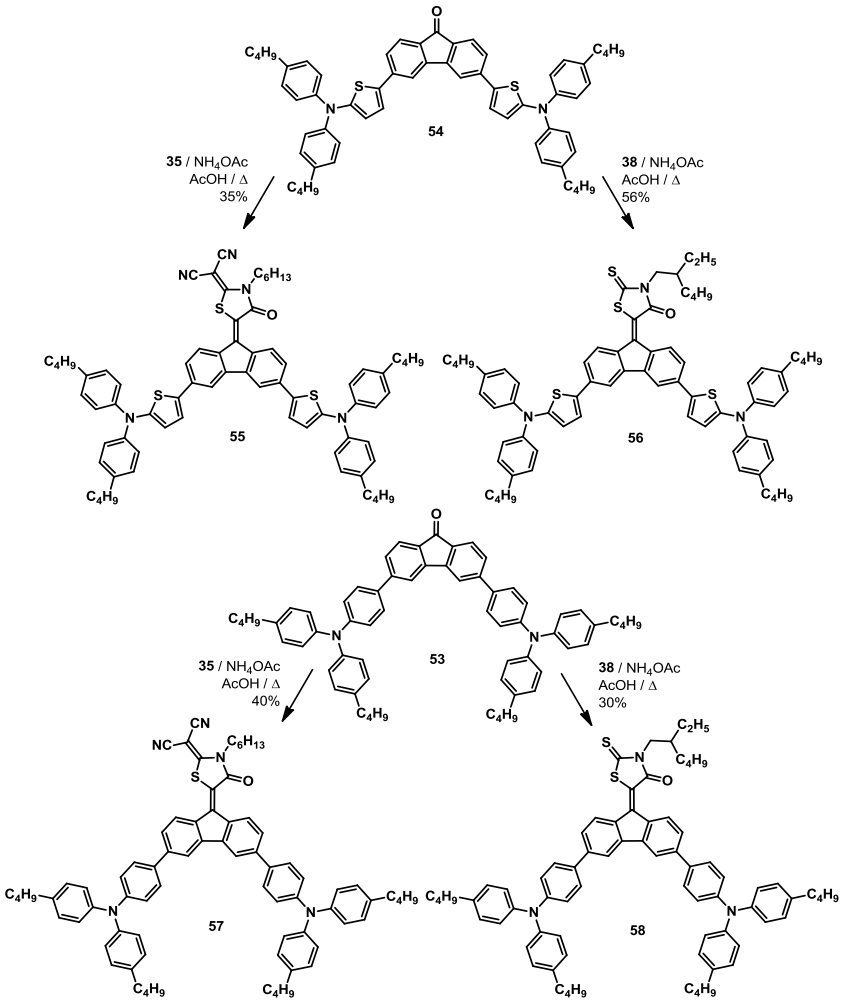

Scheme 10. Synthetic pathway for the preparation of target compounds **55**–**58**.

To the date, all previously described small molecules bearing rhodanine units were obtained by Knoevenagel condensation with an aldehyde pending group, resulting in structures with free rotation between the Rh fragment and the donor aromatic-backbone. To the best of our knowledge, these molecules are the first example of a Rh moiety bind to a fluorene molecule through its C9 position. The resulting Rh-Fl core provides extra planarity and enhanced conjugation, properties that may render into good light absorption properties and better solid state aggregation.

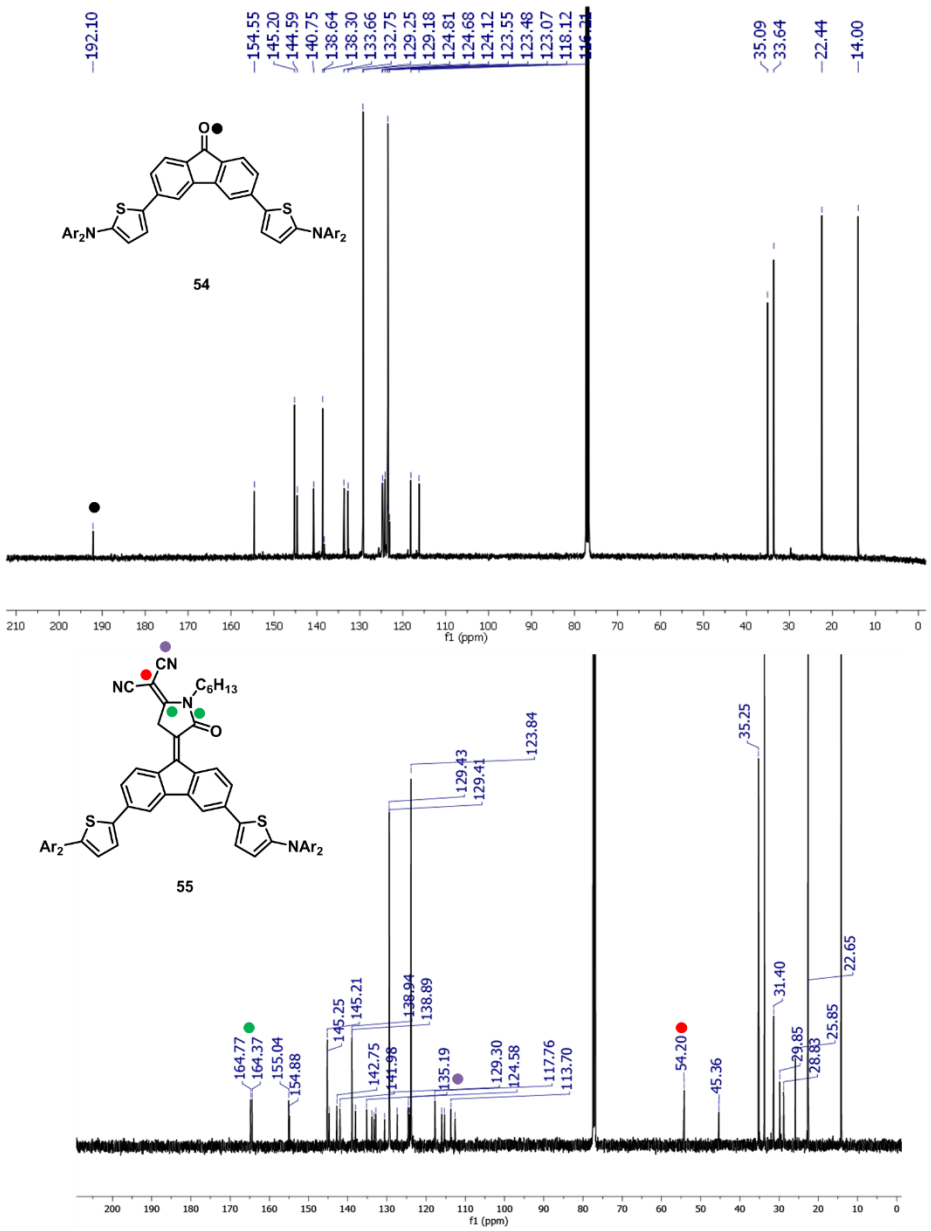

Figure 32. ^{13}C NMR spectra of (101 MHz, $CDCl_3$) **54** (top) and **55** (bottom).

All obtained compounds were characterized by standard spectroscopic techniques. It is interesting to observe how complicated the NMR features of **55**–**58** final products are, compared to the relatively simple features of **53** and

54 precursors. This can be easily visualized in Figure 32, compound **54** (top) relatively simple signal patterning becomes much more complicated upon the insertion of the asymmetric RhCN moiety in **55** (bottom), with almost every aromatic signal split into two. It also can be noted that 192.4 ppm carbonyl signal of **54** is gone for **55**, instead two high field signals are found *ca.* 164 ppm, assigned to the carbons denoted with the green dot. Also characteristic of this derivative is the nitrile carbons signal around 113 ppm (purple dot).

Photophysical study

All compounds show strong absorption in the visible range of the spectrum (Figure 33 top).

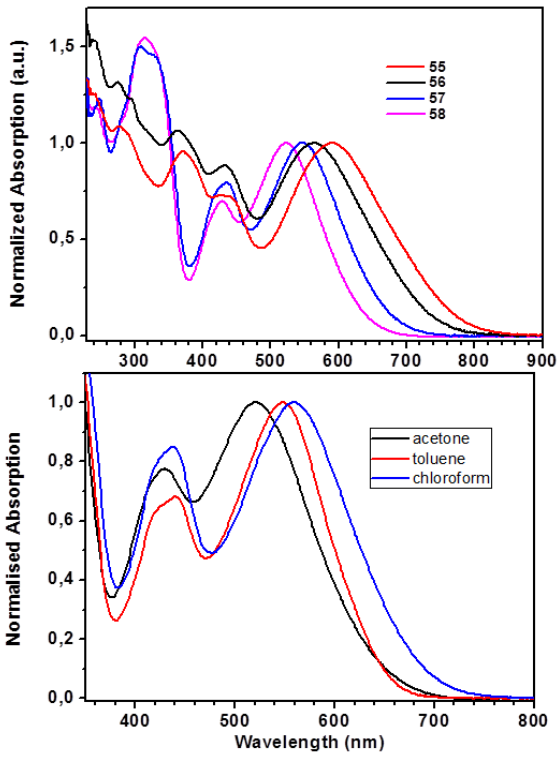

Figure 33. Normalized UV-vis absorption spectra of compounds **55**–**58** recorded in DCM solution (top). Absorption spectra of **57** in different solvents evidences significant solvatochromism over the lower energy band (bottom).

Within this range molecules show two bands, a high energy band peaking around 433 nm for all compounds, and lower energy absorption that strongly shifts depending on the D/A relative strengths. For molecules **57** and **58**, bearing the same triphenylamine donor, the absorption maxima lie at 545 and 523 nm, respectively. The 20 nm observed red-shift is caused by the use of the stronger electron acceptor RhCN in **57**, it is also noteworthy that the absorption onset red-shifts about 40 nm (from 653 to 692 nm, respectively for **58** and **57**).

On the other hand, more dramatic bathochromic shifts are observed when system bears diphenylaminothiophene as D (**55** and **56**). Along with this red-shift of 40 and 70 nm (respectively for **55** and **56**) regarding the absorption of **58**, the lower energy absorption experiences a meaningful broadening, absorbing up to 800 nm. This band shows quite large molar absorption coefficients (1.6–2.3 × 10^4 M^{-1} cm^{-1}) for all compounds. Changes operated in the lower lying energy transition upon modification of the relative D/A strengths are suggestive of a photoinduced internal charge transfer process. Summarized optical data are displayed in Table 6.

Table 6. Photophysical properties of compounds **55**–**58** measured in CH_2Cl_2 solutions.

Compound	λ_{max} [nm][a]	λ_{onset} [nm][a]	$\varepsilon \times 10^4$ [M^{-1} cm^{-1}][b]	λ_{em}^{max} [nm]	$E_{0\text{-}0}$ [eV][b]	Φ_{em}[c]
55	590	786	2,34	1036	1.65	0.010
56	565	748	1,93	1013	1.71	0.011
57	545	692	2,34	1043	1.73	0.006
58	523	653	1,64	1019	1.79	0.008

[a] Estimated extrapolation from the absorption feature edge to $A = 0$. [b] Uncertainty ± 5%. [c] Emission quantum yields relative to $[Os(phen)_3]^{2+}$ standard (Φ_{em} = 0.021 in acetonitrile). Uncertainty ± 20%.

Suggested ICT nature of the lower energy absorption peak was probed in **57** by solvatochromic experiments. Solution in solvents of different polarity showed to noticeably shift lower energy band maxima (Figure 33 bottom), thus providing extra evidence of its ICT nature. In addition, the significant broadening of this absorption band experienced by compounds **55** and **56** is

noteworthy. As discussed below, based on theoretical calculations, this effect was attributed to the larger conjugation between the DPAT units and the fluorene core provided by the thiophene rings.

Photoluminescence (PL) of compounds **55**–**58** is dominated by a very broad emission band between 800 and 1400 nm (Figure 34). Very characteristic of these materials is their remarkably high Stokes' shift, measured to be between 450–500 nm (2.5–2.7 eV). Such huge shifts are usually found when complex internal conversions of the excited state are involved, caused by intersystem crossings from the local excited singlet to the CT and then slow non-radiative decay.[72] On the other hand, the low emission quantum yields determined for all the compounds (1% or below) reflect the little importance the radiative processes have in depopulating the excited state compared with other non-radiative deactivation pathways.

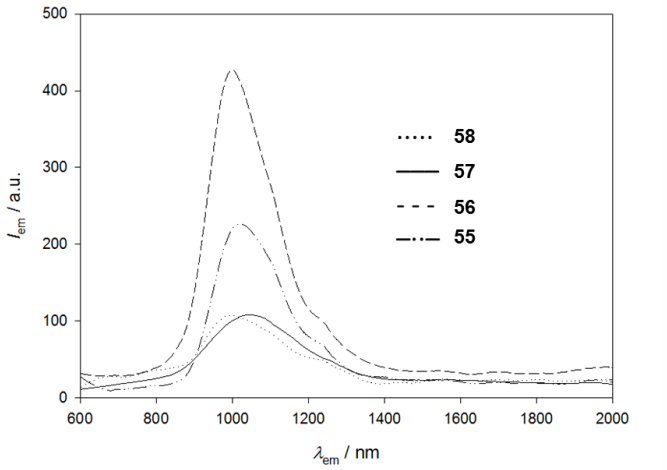

Figure 34. Emission spectra for dyes **55**–**58** recorded in DCM solution (λ_{exc} = 580 nm).

Electrochemical properties

The electrochemical properties of compounds **55**–**58** were studied by CV. All molecules show an amphoteric redox behavior, presenting one oxidation and

[72] F. B. Dias, J. Santos, D. R. Graves, P. Data, R. S. Nobuyasu, M. A. Fox, A. S. Batsanov, T. Palmeira, M. N. Berberan-Santos, M. R. Bryce, A. P. Monkman, *Adv. Sci.* **2016**, *3*, *1600080*.

two reduction processes (Figure 35 and Table 7). For **58** and **57**, both bearing the triphenylamine donor, the oxidation potential is identical (1.05 V). However, a significant 100 mV anodic shift is observed for the first reduction potential when moving from **58** (–0.61 V) to **57** (–0.51 V) due to the effect of the stronger RhCN electron-accepting group. Similarly, the second reduction potential experiences a moderate 50 mV anodic shift. When the stronger DPAT donor is used (**56** and **55**), the oxidation potential experiences a 130 and 110 mV cathodic shift, respectively.

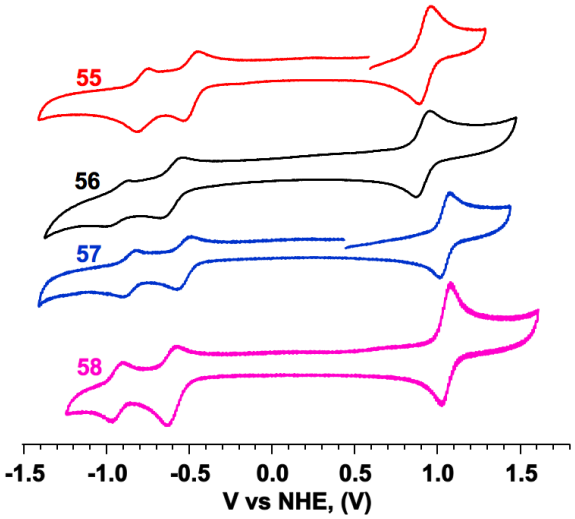

Figure 35. Cyclic voltammograms of compounds **55**–**58**, recorded in 0.1 M DCM deaerated solutions with Bu_4NPF_6 (0.1 M) as supporting electrolyte at 100 mV s^{-1}, employing glassy carbon as working electrode, Pt wire counter and reference electrodes. Fc/Fc^+ internal standard ($E_{1/2}^{ox}$ = 0.28 V) was added, its oxidation potential referenced at 0.7 V vs. NHE. and compounds oxidation potential were recalculated in reference to NHE.

In the case of **56**, with the same Rh acceptor as **58**, there is no change for the first reduction potential (–0.61 V). However, **55**, bearing the stronger RhCN acceptor, shows a 30 mV anodic shift compared to **57** and presents the smallest reduction potential (–0.46 V), this difference is ascribed to experimental uncertainty. The calculated electrochemical gaps range from 1.66 to 1.44 eV, diminishing from **58** to **55**, which is in good agreement with the trend inferred from the spectroscopic data (Table 6). Frontier orbitals energy and electrochemical gaps were estimated from redox half-wave potentials (Table 7)

using Equations 5−7. A rise of the HOMO energy stems from replacing TPA by stronger donor DPAT moiety, ranging from −5.45 to −5.32 eV. Conversely, the opposite trend is observed in the LUMO energies when stronger electron-accepting **35** moiety is introduced**,** ranging from −3.79 to −3.94 eV. From the performed PL experiments, it was possible to calculate the redox potentials of the molecules excited state (Table 7). It was observed that, while the excited state oxidation process has a similar potential for all the dyes, the reduction process seems to be slightly less favored in the case of **56**, compound lacking the TPA (less coplanar / less electronically coupled donor, *vide infra*) and RhCN (stronger acceptor) moieties.

Table 7. Electrochemical data for ground and excited states and estimated HOMO/LUMO energies for compounds **55**–**58**.

Compound	$E_{1/2}^{ox}$ [V][a]	$E_{1/2}^{red}$ [V][a]	E_{gap}^{cv} [V]	E_{HOMO}/E_{LUMO} [eV]	E^{ox*} [V][b]	E^{red*} [V][b]
55	0.94	-0.46	1.42	-5.34/-3.92	-0.74	1.19
56	0.92	-0.61	1.53	-5.32/-3.79	-0.68	1.22
57	1.05	-0.51	1.56	-5.45/-3.89	-0.74	1.10
58	1.05	-0.61	1.66	-5.45/-3.79	-0.71	1.18

[a] Referenced against NHE. [b] Excited state redox potentials, 5% uncertainty.

DFT Computational Study

In order to gain insight into the optical and electronic properties of compounds **55**–**58**, theoretical calculations were performed within the DFT framework. Minimum-energy optimized geometries calculated at the B3LYP/cc-pVDZ level in CH_2Cl_2 indicate that the rhodanine moiety remains coplanar with the fluorene core in all four compounds, constituting both moieties the central acceptor unit of the D−A−D architecture (Figure 36). For **55** and **56**, the thiophene rings bridging the donor diphenylamino groups to the acceptor moiety are calculated almost coplanar with the A core, with largest dihedral angles of 8.9°. In contrast, the phenyl rings bridging the diphenylamine units in **57** and **58** stand 30–32° out of the plane of the A core due to the steric hindrance caused by short H···H contacts (Figure 36). Finally, both TPA and DPTA moieties are calculated to show the typical mill sails shape.

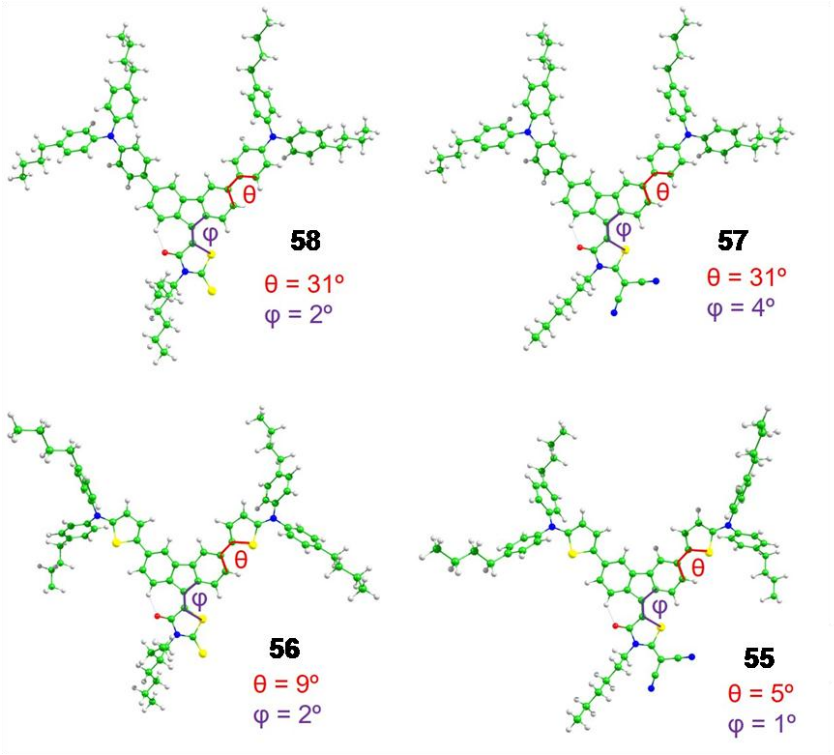

Figure 36. Minimum-energy optimized structures calculated for compounds **55**–**58** at the B3LYP/cc-pVDZ level of theory in DCM. Characteristic dihedral angles are indicated.

The HOMO and HOMO-1 are predicted nearly degenerate and are localized over the two electron-donor fragments (Figure 37). The higher conjugation and more planar structure promoted by the less-aromatic thiophene rings in **55** and **56** determines that the HOMO of these compounds is computed higher in energy (–5.04 and –5.02 eV, respectively) than the HOMO of **57** and **58** (–5.13 and –5.11 eV, respectively), and produces a certain splitting (0.07 eV) between the HOMO and HOMO-1. The increase of ~0.1 eV in the HOMO energy confirms DPTA groups as better donors than TPA and is in good accord with the lower oxidation potentials recorded for **55** and **56** (Table 7).

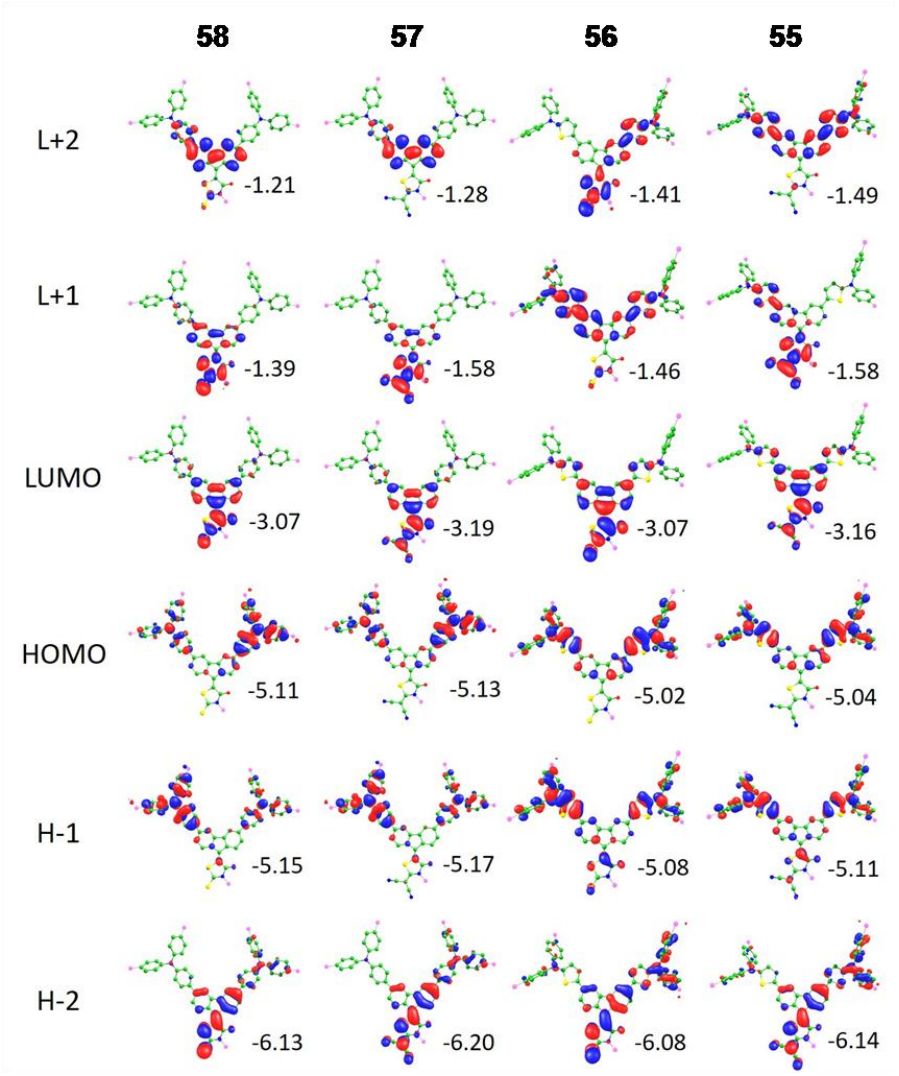

Figure 37. Isovalue contours (±0.025a.u.) computed for the frontier molecular orbitals of compounds **55**–**58** at the B3LYP/cc-pVDZ level in DCM. Orbital energies are indicated in eV. Alkyl chains and hydrogen atoms are omitted for better viewing.

The LUMO is located over the A central core in all four compounds. The LUMO is calculated at –3.07 eV for **56** and **58**, and it is computed ~0.1 eV lower in energy for **57** and **55** due to the presence of the stronger electron-accepting RhCN moiety. This result supports the less negative reduction

potentials recorded for **55** and **57**.

Photovoltaic properties

In collaboration with Prof. Dyakonov, materials **55**–**58** were tested as donors blended with either $PC_{61}BM$ or $PC_{71}BM$ in BHJ-OSC. Built devices, with Glass/ITO/PEDOT:PSS/Active layer/Ca/Al architecture, showed poor photovoltaic performances (PCE < 1%). The best performing material resulted to be **58**, its J/V curves showed in Figure 38. Fullerenic material was blended in a 1.5:1 **58**/fullerene proportion. Cells using $PC_{61}BM$ showed worse performance (Voc = 1.04 V; J_{SC} = 0.17 mA cm^{-2}; FF = 25%; PCE = 0.05%) than the ones making use of $PC_{71}BM$ (Voc = 1.11 V; J_{SC} = 0.82 mA cm^{-2}; FF = 27%; PCE = 0.25%), probably due to its better optical properties.

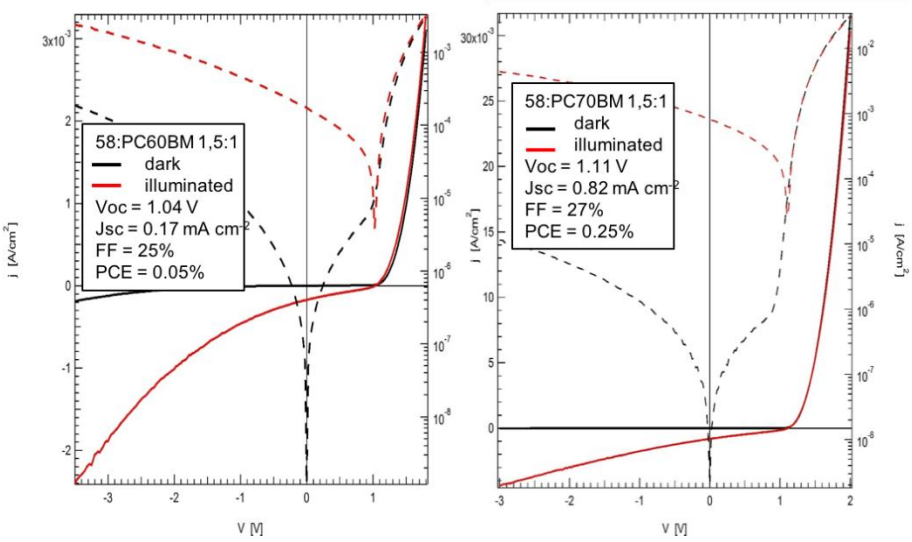

Figure 38. *J-V* curves for BHJ OSC of **58** blended with $PC_{61}BM$ (left) and $PC_{71}BM$ (right) with their corresponding photovoltaic parameters inset.

Despite the displayed poor PV performance, devices made of **58** exhibited V_{OC} > 1.00 V, which is indicative of strong charges photogeneration. Analysis of the *J*/*V* curve shape indicates that the devices are not able to fully extract the generated charges, probably due to strong recombination processes. Suspecting that morphological issues might be concurring in the devices' active layer, a new set of devices was fabricated by thermal annealing at 80 ºC and by solvent vapor annealing, exploring different D/A ratios. As observed from Figure 39

left, annealing processes exerted no significant influence over the cells performance.

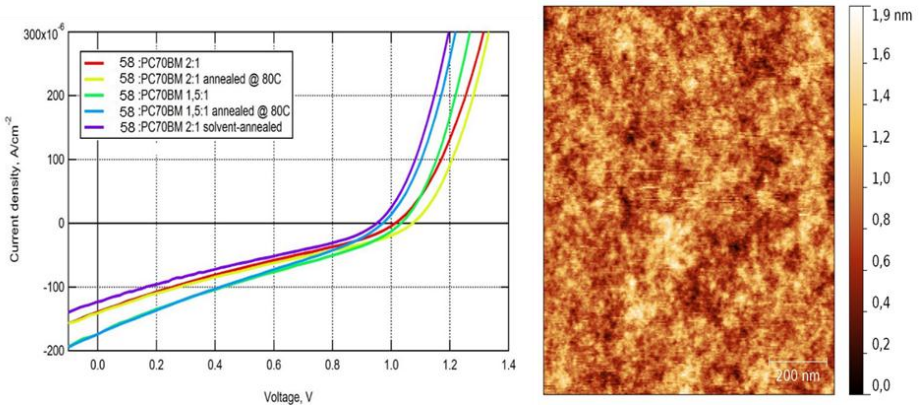

Figure 39. *J-V* curves for BHJ OSC of **58** employing different annealing processing (left). AFM image of **58**/$PC_{71}BM$ blend film (right).

Surface survey by atomic force microscopy (AFM) allowed a close insight into the morphology of the **58**/$PC_{71}BM$ films. All surveyed films exhibited very smooth surfaces (Figure 39 right), lacking the typically observed granulation when percolative pathways of D and A are formed. The poor performance of the fabricated devices is caused by the strong recombination of the generated charges due to the lack of percolative pathways to the electrodes. In term, the observed smoothness is attributed to an effective intermixing of D materials with the fullerenic material, which might be caused by the excess of solubilizing side-chains in the D molecules.

1.3.2.2. *2nd Generation D−A−D small molecules*

Regarding the low photovoltaic performance, the first generation compounds provided, attributed to their inability to segregate from the $PC_{71}BM$, a new generation of derivatives was developed. Keeping the same active features (*i.e.* rhodanine acceptor, triphenylamine donor), the butyl side-chains linked to the triarylamines were removed. Instead, substituents able to modify the donor's strength were employed. With this aim, triphenylamine (TPA-H), bis(4-methylphenyl)aminophenyl (TPA-Me), bis(4-methoxyphenyl)amine (DPA-OMe), and bis(4-methoxyphenyl)aminophenyl (TPA-OMe) donor moieties were chosen.

Synthesis

Taking advantage of the knowledge acquired for the first generation materials, different triarylamine derivatives were designed (Scheme 11).

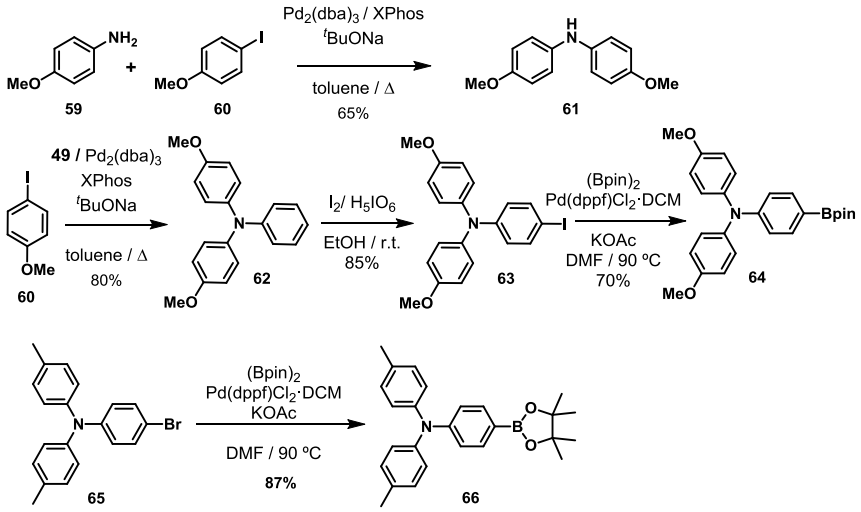

Scheme 11. Donor fragments synthetic pathways.

Donor fragment **61** (DPA-OMe) was obtained *via* Buchwald-Hartwig reaction between commercially available *p*-anisidine (**59**) and 4-iodoanisole (**60**) using Pd_2dba_3 and (XPhos) as catalyst and sodium *tert*-butoxide as base, as reported by Hill and collaborators.[73] Similarly, triphenylamine derivative **62** was synthesized by a Buchwald-Hartwig between **60** and aniline.[74] Resulting product was iodinated by treatment with iodine and periodic acid in ethanol.[75] Boronate **64** was obtained by Miyaura borylation reaction of **63** with bispinacolatediboron, employing [1,1′-bis(diphenylphosphino)ferrocene]dichloropalladium (II) complex with

[73] L. L. Hill, L. R. Moore, R. Huang, R. Craciun, A. J. Vincent, D. A. Dixon, J. Chou, C. J. Woltermann, K. H. Shaughnessy, *J. Org. Chem.* **2006**, *71*, 5117−5125.

[74] A. C. Hernandez-Perez, A. Caron, S. K. Collins, *Chem. Eur. J.* **2015**, *21*, 16673−16678.

[75] L. Cai, T. Moehl, S.-J. Moon, J.-D. Decopet, R. Humphry-Baker, Z. Xue, L. Bin, S. M Zakeeruddin, M. Grätzel, *Org. Lett.* **2014**, *16*, 106−109.

dichloromethane as catalyst and potassium acetate as base.[76] The same reaction over commercially available 4-bromo-*N*,*N*-di-*p*-tolylaniline (**65**) yielded donor fragment bearing TPA-Me (**66**).[77]

Suzuki-Miyaura cross-coupling of the corresponding triphenylamine [including commercially available 4-(diphenylamino)phenylboronic acid] with 3,6-dibromofluorenone (**42**) provided intermediates **67**–**69**. Diphenylamine derivative was obtained by Buchwald-Hartwig reaction between **42** and **61** in good yield (Scheme 12).

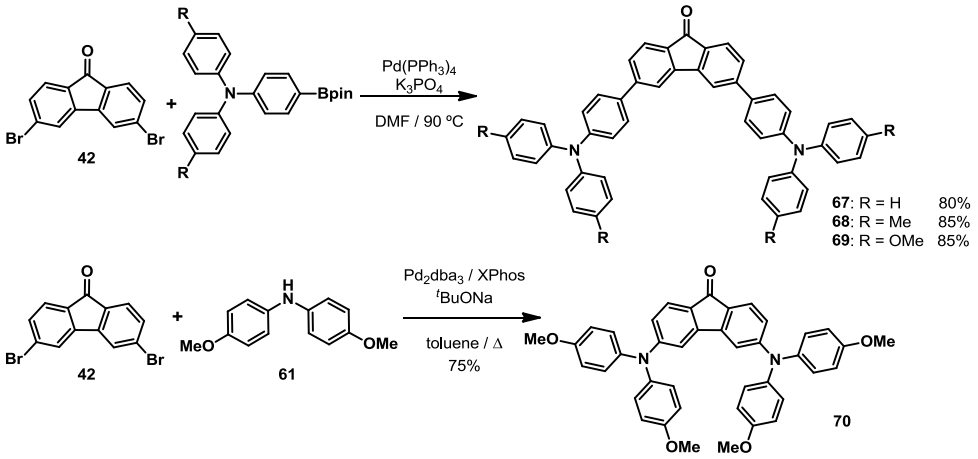

Scheme 12. Synthetic pathway for the preparation of compounds **67**–**70**.

Finally, intending to improve the low to moderate yields obtained for **55**–**58** in the synthesis of final products **71**–**74**, ammonium acetate was substituted by *β*-alanine as some authors have earlier reported (Scheme 13).[78] Unfortunately, despite this modification on the catalyst employed, reaction's yield was not meaningfully affected. Here again, starting materials were easily recovered and

[76] K. Rakstys, A. Abate, M. I. Dar, P. Gao, V. Jankauskas ,G. Jacopin , E. Kamarauskas, S. Kazim, S. Ahmad, M. Grätzel, M. K. Nazeeruddin, *J. Am. Chem. Soc.* **2015**, *137*, 16172−16178.

[77] R. Anémian, D.C. Cupertino, P.R. Mackie, S.G. Yeates, *Tetrahedron Letters* **2005**, *46*, 6717−6721.

[78] K. Harada, H. Kubo, J. Abe, M. Haneta, A. Conception, S. Inoue, S. Okada, K. Nishioka, *Bioorg. Med. Chem.* **2012**, *20*, 3242–3254.

set again until fully consumed.

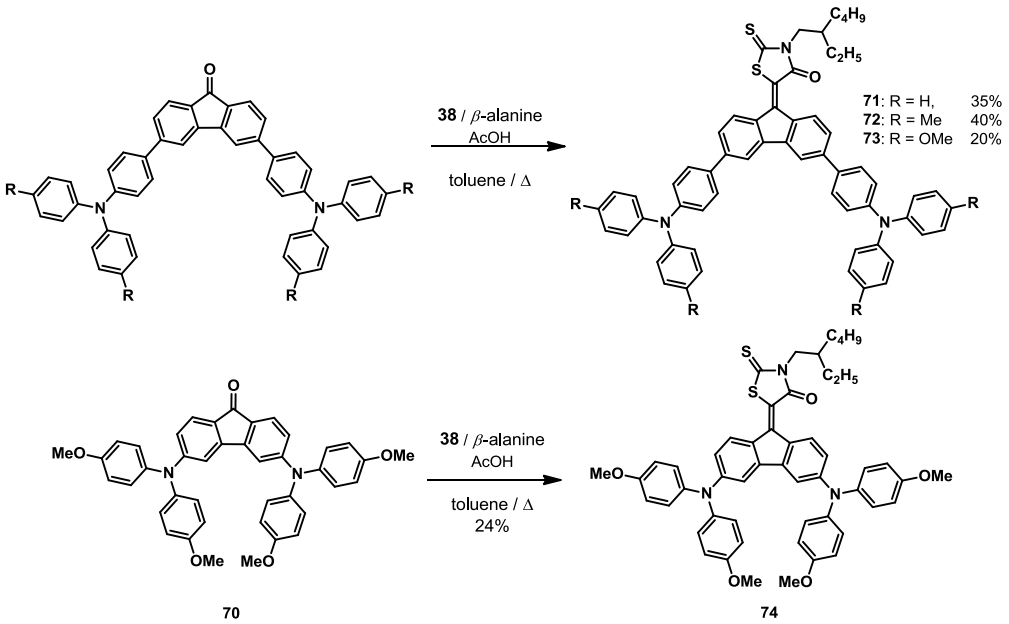

Scheme 13. Synthesis of target compounds **71**–**74**.

All obtained compounds were characterized by conventional spectroscopic techniques. Precursor **68** may serve as representative example to illustrate how symmetry elements produce very simple ^{1}H-NMR features (Figure 40), compared to asymmetric **72** (Figure 41). Fluorene core, shows a down field signal as a small doublet assigned to C4 and C5 at 8.01 ppm (yellow mark) with a long distance ^{4}J = 1.2 Hz coupling with its C2-H and C7-H neighbors (red mark), being itself a double doublet (7.55 ppm) with a ^{3}J coupling of 7.8 Hz with its C8-H and C1-H neighbors (their 7.62 ppm signal being isochronous with some of the arylamine signals, black mark).

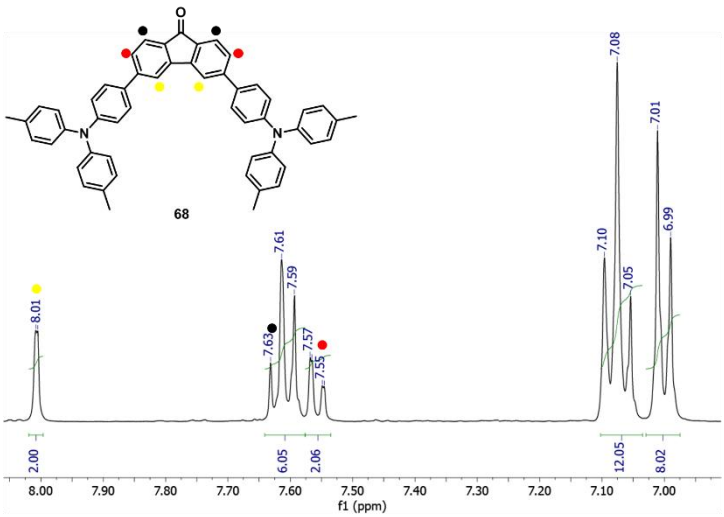

Figure 40. ^{1}H NMR spectrum (400 MHz, THF-d^{8}) of **68** centered on its aromatic region.

Final product **72**, on the other hand, evidences a new set of aliphatic signals belonging to the Rh fragment side-chain (Figure 41 bottom), with a pseudo doublet at 4.10 ppm (green triangle) belonging to the N-CH_2 protons, and a multiplet at 2.14 ppm belonging to the proton bound to the asymmetric carbon (orange triangle). In the literature N-CH_2 protons signal is usually incorrectly assigned as a doublet, neglecting its protons different coupling with their chiral neighbor. The insertion of the non-symmetric Rh moiety gives rise to the split of all fluorene signals (Figure 41 top). C1 and C8 protons (green dot marks) showing up at 9.39 and 7.90 ppm as doublets, couple with ^{3}J = 8.5 and 8.3 Hz, respectively, with their neighboring C2 and C7 protons (highlighted in purple). These two protons also split into two double doublets at 7.60 and 7.54 ppm, with a long distance ^{4}J coupling of 1.8 and 1.9 Hz, respectively, with C4 and C5 protons (marked in pink). These two last protons show up as doublets (at 8.10 and 8.07 ppm).

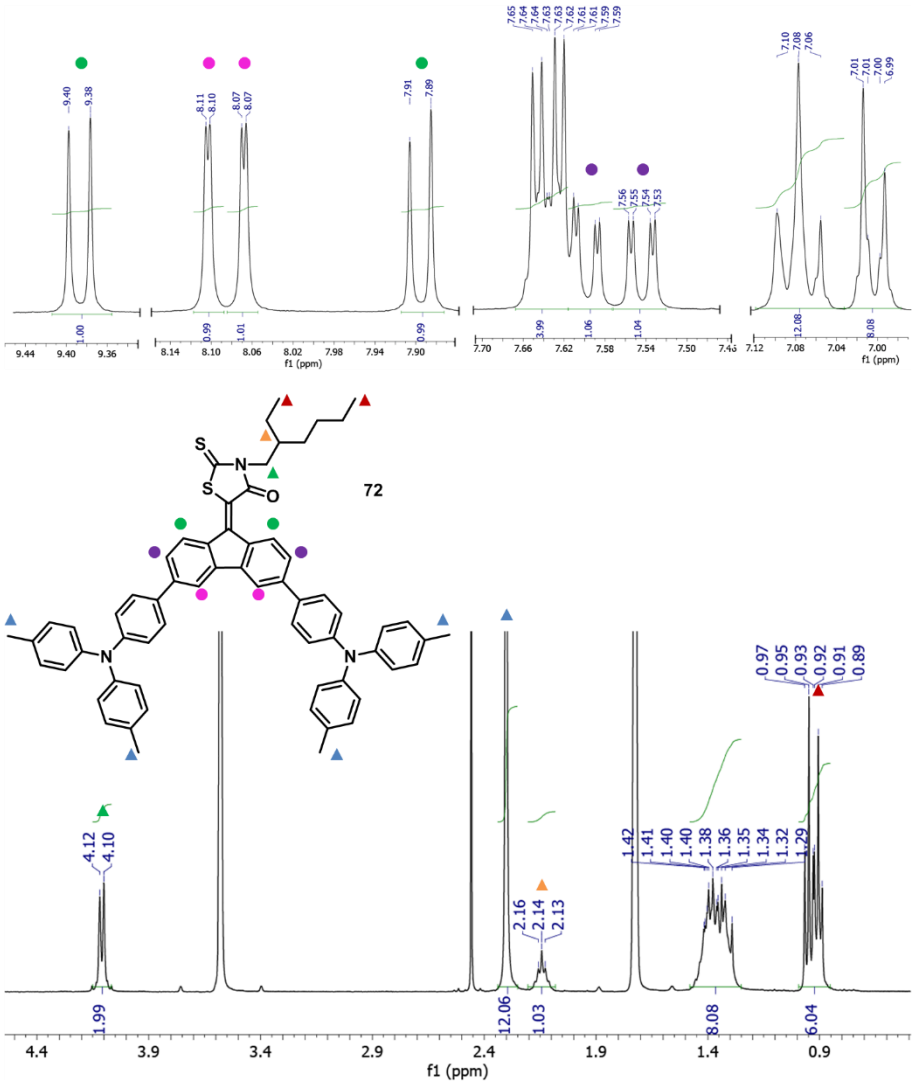

Figure 41. ^{1}H NMR spectrum (400 MHz, THF-d^{8}) of target compound **72**, with its aromatic zone (top) and its aliphatic zone (bottom).

Optical properties

Similarly to the first generation materials (**55**–**58**), these new dyes absorption spectra are dominated by a strong (4.4−5.9 × 10^{4} M^{-1} cm^{-1}) broad band covering most of the visible range (Figure 42 and Table 8). In analogy with their preceding generation materials, the low energy band is attributed an ICT process. Accordingly, absorption maxima experience sensitive bathochromic

shifts as stronger donors are used (TPA-H > TPA-Me > TPA-OMe). For compound **71**, bearing the weakest TPA-H donor, the ICT band peaks at 504 nm (onset at 640 nm); as stronger donors are employed it is observed *ca.* 20 and 40 nm red-shifts (onsets at 652 and 690 nm) for **72** and **73**, respectively. As for the case of derivative **74** (bearing DPA-OMe donor), it shows the largest red-shift, peaking at 541 nm (onset at 702 nm).

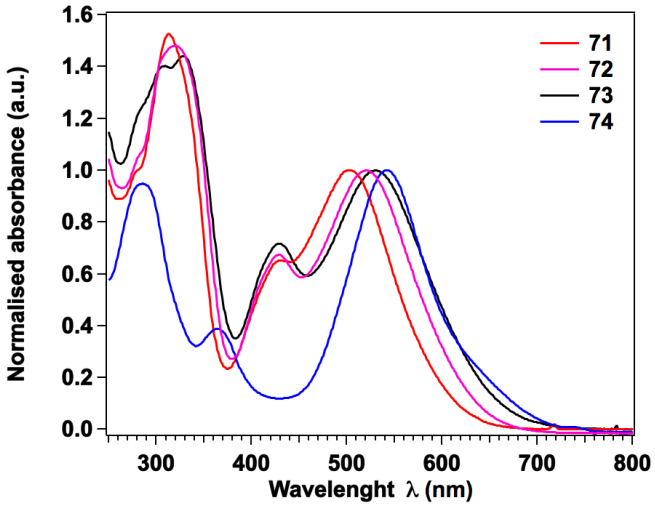

Figure 42. UV-vis absorption spectra (DCM) of compounds **71**–**74**.

Table 8. UV-vis data of compounds **71**–**74**.

Compound	λ_{max} [nm][a]	λ_{onset} [nm][a]	E_g^{opt} [eV]	ε 10^4 [M^{-1} cm^{-1}]
71	504	640	1.93	4.38
72	521	652	1.90	4.43
73	531	690	1.80	4.37
74	541	702	1.76	5.87

[a] Recorded in DCM solution.

Electrochemical properties

From the voltammograms of compounds **71**−**74** showed in Figure 43, it is evident the ambipolar behavior of these D−A−D materials. In the anodic zone, compounds **71**−**73** show two reversible waves attributed to the reduction of the

Rh moiety. As for **74**, the molecule seems to experience three non-reversible reductions. The first reduction potential of all four compounds seem to slowly decrease from **71** to **73**, with a larger *ca.* 100 mV shift for **74**, as stronger donors are used in the systems. Scanning the cathodic zone, compounds **71**−**73** exhibit a single reversible oxidation process related with the triphenylamine group oxidation. With the increase of donor strength from TPA-H > TPA-Me > TPA-OMe there is a noticeable 270 mV cathodic shift in the oxidation potential from **71** (1.18 V) to **73** (0.89 V)**.** Compound **74**, on the other hand, exhibits two oxidation processes (at 0.93 and 1.04 V), tentatively attributed to the sequential oxidation of the two diphenylamine groups. As show in Table 9 A rise of the HOMO energy is observed as more electron-donating strength substituents are introduced within triphenylamine group ranging from −5.56 to −5.36 eV.

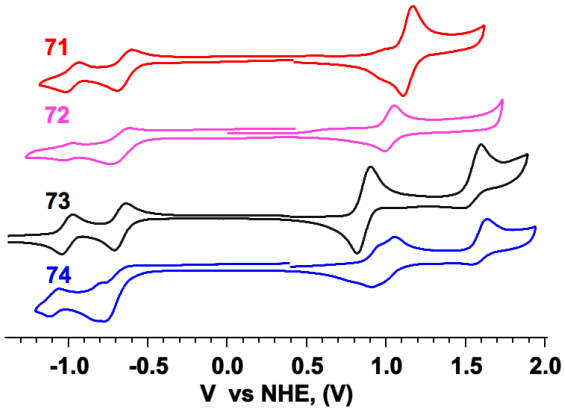

Figure 43. Cyclic voltammetry of compounds **71**–**74** were recorded at a scan rate of 100 mV s^{-1} using an air-tight single compartment three-electrode cell, employing glassy carbon as working electrode and platinum wires as counter and reference electrodes. Ferrocene was added as internal standard, its oxidation potential in DCM positioned at 0.7 V vs. NHE and compounds' oxidation potentials were accordingly recalculated.

The LUMO energies were calculated from the electrochemical gaps of the molecules. As expected, LUMO shows negligible variation from **71**–**73** lying around 3.7 eV, whereas product **74** displays its LUMO 0.1 eV higher in energy. Conversely, the HOMO energies experience an energy rise as stronger D are attached to the molecules from **71** to **74**.

Table 9. Electrochemical data and calculated HOMO/LUMO energies of compounds **71**–**74**.

Compound	$E_{1/2}^{ox}$ [V]	$E_{1/2}^{red}$ [V]	E_{gap}^{cv} [V]	E_{HOMO}/E_{LUMO} [eV]
71	1.16	-0.67	1.85	-5.56/-3.73
72	1.02	-0.71	1.76	-5.42/-3.69
73	0.90	-0.69	1.62	-5.36/-3.71
74	0.96	-0.80	1.79	-5.33/-3.60

Photovoltaic properties

A new set of BHJ-OSC devices was fabricated with compounds **71**–**74** blended with $PC_{71}BM$ as acceptor. Out of all four dyes, **72** blended in a 1:3 D/A ratio showed to provide the best performing OSCs. In order to further optimize devices employing **72**, a new set of them exploring different active layer thicknesses was fabricated (see Figure 44).

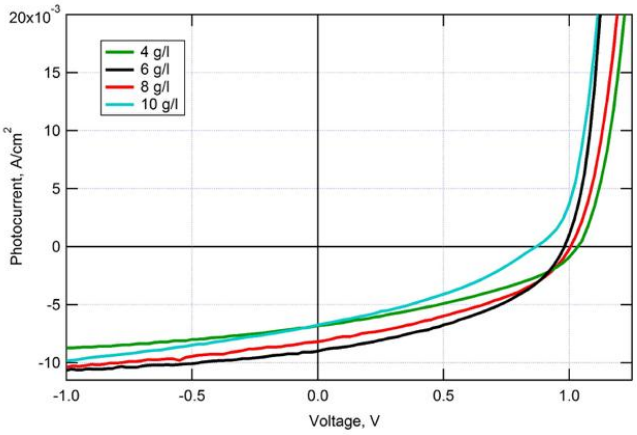

Figure 44. Current-voltage curves showing the effect of thickness within active layer over photovoltaic performance of **72**–devices.

Device performance is strongly affected by active layer thickness, usually its increase results in a more efficient light harvesting by the active layer. However, this benefit finds its limit when the maximum exciton diffusion length is exceeded, resulting in a trade-off between light harvesting and

recombination processes. Films from 42 to 80 nm thick were prepared (data summarized in Table 10). From 42 nm to 57 nm efficiency seems to benefit from the increased light gathering ability. Thereafter, further increase of active layer thickness results detrimental to the device's performance. Device **B** resulted to be the optimal configuration. Featuring a 57 nm thick active layer, it exhibits a high open circuit voltage of 0.98 V, a J_{sc} = 9.0 mA cm^{-2} and a fill factor of 42%, resulting in an overall PCE of 3.7%.

Table 10. Photovoltaic characteristics of **72** based devices with different configurations based on the modification of the active layer thickness.

Device	Conc. [g/L]	Thickness [nm]	V_{OC} [V]	J_{SC} [mA cm^{-2}]	*FF* [%]	PCE [%]
A	4	42	1.04	6.8	38	2.7
B	6	57	0.98	9.0	42	3.7
C	8	70	1.01	8.2	40	3.3
D	10	80	0.87	6.8	35	2.1

1.4. Conclusions

1.4. CONCLUSIONS

In the light of the results presented in this Chapter, the following conclusions have been reached:

1.4.1. A-D-A Small molecules based on BDT-BTD

- A series of D/A small molecules containing electron-rich BDT and electron-deficient BTD featuring A-D-A structure have been synthesized.
- Optical, electrochemical and computational studies revealed their electroactive nature and the ability to form well-ordered thin films with broad visible absorptions (360–800 nm) and low band gaps (*ca.* 2.0 eV).
- Photovoltaic studies showed the poor photovoltaic performance of these materials when blended with fullerenes as acceptors, reaching a PCE of 0.72 % in the case of **31**.
- Time resolved microwave conductivity (TRMC) studies unveiled unexpected n-type charge transport, displaying remarkable high electron mobilities of around 0.1 cm^2 V^{-1} s^{-1} comparable with those obtained for fullerene derivatives. This fact accounts for the bad results obtained for the OSC built with these materials.
- Consequently, these molecules could be potential candidates for their use in BHJ OSC as non-fullerenic acceptors.

1.4.2. D-A-D Small molecules based on rhodanine acceptors

1.4.2.1. *1st Generation D−A−D small molecules*

- A series of D-A-D small molecules bearing rhodanines as acceptor moieties along with butyltriarylamine groups as donor groups have been synthesized and characterized. Condensation between rhodanine and fluorene has been achieved for the first time, providing a more rigid and planar structure which is pivotal for enhancing electronic conjugation and promoting intermolecular π–π stacking.
- These novel dyes show the ability to absorb in the entire optical range of the spectrum (between 400 and 800 nm).
- DPAT donor fragment has demonstrated providing a more effective

coupling with the acceptor due to the reduced dihedral angle allowed by the thiophene ring. Combination of DPAT with strong RhCN electron acceptor gave rise to a bandgap of 1.42 eV (**52**).

- OSC with different materials were built, showing poor photovoltaic performance, the best PCE was reached by 58/PC71BM with a value of 0.25%. The results were lower when PC61BM was used instead. Although butyl side chains help with processability, AFM studies revealed that the morphology of the 58/PC71BM films was smooth, lacking the typical granulation needed to form percolative pathways to the electrodes.
- The next logical step was to avoid the solubility with shorter alkyl chains.

1.4.2.2. *2nd Generation D−A−D small molecules*

- Keeping the same active features as for the first generation materials, butyl side-chains linked to the triarylamines were removed from the donor groups. Instead, as donors, triphenylamine with different donating strength (TPA-H, TPA-Me, TPA-OMe) and a bis(4-methoxyphenyl)amine have been used.
- Optical and electrochemical studies revealed that similarly to the first generation, these new small molecules show wide absorption bands covering most of the visible region of the spectrum (400–702 nm) with electrochemical bandgaps between 1.62−1.85 eV.
- Photovoltaic studies evidenced that the best performing OSC was reached by blending **72** with $PC_{71}BM$ in a 1:3 ratio. Different active layer thicknesses were explored to optimize the device performance. Active layers of 57 nm thick maximized operation, exhibiting a V_{oc} of 0.98 V, J_{sc} of 9.00 mA cm^{-2} and a FF of 42%, resulting in an overall PCE of 3.7%.
- The results obtained demonstrate that D−A−D architectures are equally feasible for PV purposes. Despite the moderate-low performance obtained, the type of systems presented herein has the potential to achieve higher PV outputs by further extending the conjugation with the insertion of spacers between the D and A units.

1.5. Experimental section

1.5. EXPERIMENTAL SECTION

General methods. Chemicals and reagents were purchased from commercial suppliers and used as received. All solvents were dried according to standard procedures. Air-sensitive reactions were carried out under nitrogen atmosphere. Flash chromatography was performed using silica gel (Fluorochem, Silicagel 60A, 40-63 micron). Analytical thin layer chromatography (TLC) was performed using aluminum coated Merck Kiesegel 60 F254 plates. NMR spectra were recorded on a Bruker Advance 400 (^{1}H: 400 MHz; ^{13}C: 101 MHz) spectrometer at 298 K using partially deuterated solvents as internal standards. Coupling constants (*J*) are denoted in Hz and chemical shifts (δ) in ppm. UV-Vis spectra were recorded in a Varian Cary 50 spectrophotometer. FT-IR spectra were recorded in a Bruker Tensor 27 (ATR device) spectrophotometer. Emission spectra were recorded in the fluorescence equipment Fluorolog-3 Horiba. Matrix-assisted laser desorption ionization (coupled to a time-of-flight analyzer) (MALDI-TOF/TOF) mass spectra were recorded on a Bruker ULTRAFLEX III spectrometer. Thermogravimetric analysis (TGA) was performed using a TA instrument TGAQ500 with a ramp of 10 °C/min under N_2 from 100 to 1000 °C. DSC was performed on a Discovery DSC from TA instrument; three cycles were recorded under nitrogen, heating (until 400 °C) and cooling (50 °C) at 20 °C/min of scanning rate. Melting points were determined with Sanyo Gallenkamp.

1.5.1. Synthesis of A-D-A small molecules based on BDT-BTD

Thiophene-3-carbonyl chloride (13).

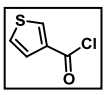

Thiophene-3-carboxylic acid (**12**) (5.08 g, 39.6 mmol) was added into a 100mL 2-neck round bottom flask containing dry DCM (10 mL) and with nitrogen blanket. The resulting mixture was cooled to 0°C, and then oxalyl chloride (10.0 g, 79.3 mmol) was added in one portion. After 5 min the reaction was allowed to warm to room temperature and then was stirred overnight. After removal of the solvent and unreacted oxalyl under reduced pressure, the resulting compound was obtained (5.24, 90%) as colorless solid, and used in the next step without further purification.

N,N-Diethylthiophene-3-carboxamide (14).[79]

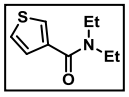

Inside a 100 mL 2-neck round bottom flask filled with nitrogen, diethylamine (8.27 mL, 79.3 mmol) was dissolved in dry DCM (50 mL). Upon cooling to 0 ºC, a solution of **13** (5.80 g, 39.6 mmol) in dry DCM (10 mL) was added dropwise. Thereafter reaction mixture was stirred at room temperature for 30 min. After quenching the reaction with water (50 mL) organic layer was washed with water (3 × 50 mL) and dried over anhydrous Na_2SO_4. After removing the solvent under reduced pressure, the resulting residue was purified by distillation under vacuum providing a pale-yellow oil (6.47 g, 90%).

^{1}H NMR ($CDCl_3$, 400 MHz) δ: 7.47 (s, 1H), 7.33−7.31 (m, 1H), 7.18 (d, *J* = 4.0 Hz, 1H), 3.51−3.29 (m, 4H), 1.23–1.17 (m, 6H) (ppm).

Benzo[1,2-b:4,5-b']dithiophene-4,8-dione (BDT) (15).[79]

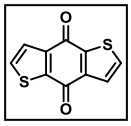

Into a 100 mL flame-dried round bottom flask **14** (6.46 g, 34.6 mmol) was dissolved in dry THF (50 mL) under nitrogen atmosphere. The mixture was cooled to 0 °C and *n*-butyllithium (2.5 M in hexane, 13.9 mL, 34.6 mmol) was added dropwise within 30 min. After stirring at room temperature for 30 min, the reaction was poured into a 150 mL ice/water mixture and stirred for several hours. After filtration, the resulting yellow precipitate was sequentially washed with H_2O (100 mL), MeOH (25 mL) and hexane (25 mL). Desired product was obtained as a yellow powder (3.02 g, 42%).

^{1}H NMR ($CDCl_3$, 400 MHz) δ: 7.69 (d, *J* = 4.2 Hz, 2 H), 7.65 (d, *J* = 4.2 Hz, 2 H) ppm.

4,8-bis((2-ethylhexyl)oxy)benzo[1,2-b:4,5-b']dithiophene (16).

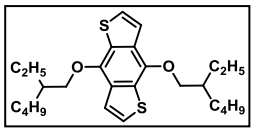

Compound **15** (3.25 g, 14.5 mmol) and Zn (2.90 g, 44.3 mmol) were added to a stirring solution of Bu_4NOH (50 mL, 40% w/w) in water (50 mL), the mixture was degassed for 15 min and refluxed for 2 h, during this period the reaction acquired an intense dark-red color. Upon addition of 2-

[79] Y. Ma, T. Leng, G. Lai, Z. Li, X. Xu, J. Zou, Y. Shen, C. Wang, *Tetrahedron* **2016**, *72*, 2219−2225.

ethylhexyl bromide (7.90 mL, 44.3 mmol) and a catalytic amount of KI, the reaction was refluxed further 8 h. After cooling to room temperature, the mixture was quenched with H_2O (100 mL) and then extracted with DCM (3 × 50 mL). After drying the organic layer over anhydrous Na_2SO_4, the solvent was filtered and then removed under reduced pressure. Reaction crude was purified by flash chromatography on silica gel (hexane/dichloromethane 9:1) yielding a colorless oil (3.74 g, 57%).

^{1}H RMN (400 MHz, $CDCl_3$) δ: 7.48 (d, *J* = 5.5 Hz, 2H), 7.36 (d, *J* = 5.5 Hz, 2H), 4.18 (d, *J* = 5.4 Hz, 4H), 1.84−1.78 (m, 2H), 1.73−1.47 (m, 8H), 1.41−1.38 (m, 8H), 1.02 (t, *J* = 7.4 Hz, 6H), 0.94 (t, *J* = 7.0 Hz, 6H) ppm.

Compound 17.[59]

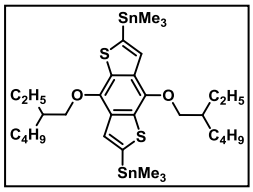

Into a 100 mL flame-dried round bottom flask **16** (500 mg, 1.12 mmol) was added and dissolved in dry THF (40 mL) under nitrogen atmosphere. After cooling to −78 °C, *n*-butyllithium (2.5 M in hexane, 1.20 mL, 3.00 mmol) was added dropwise and the mixture stirred at this same temperature for 30 min. Reaction was allowed to warm to room temperature for 5 min and then cooled again to −78 °C before adding trimethyltinchloride (1.0 M in hexane, 3.40 mL, 3.40 mmol) dropwise. Reaction allowed to warm to room temperature and stirred overnight. Dilution with H_2O (40 mL) was followed by extraction with hexane (3 × 20 mL). The combined organic extracts were dried over anhydrous Na_2SO_4, filtered and the solvent vacuum removed. The resulting crude was purified by recrystallization from EtOH as white flakes (452 mg, 57%).

^{1}H RMN (400 MHz, $CDCl_3$) δ: 7.52 (s, 2H), 4.20 (d, *J* = 5.4 Hz, 4H), 1.85−1.79 (m, 2H), 1.73−1.49 (m, 8H), 1.45−1.38 (m, 8H), 1.03 (t, *J* = 7.4 Hz, 6H), 0.95 (t, *J* = 6.8 Hz, 6H), 0.45 (s, 18H) ppm.

5-bromobenzo[c][1,2,5]thiadiazole (19).[80]

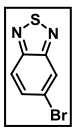

To a dry DCM (100 mL) solution of 4-bromo-1,2-diaminobenzene (**18**) (3.38 g, 18.0mmol) and Et_3N (7.35 g, 72.3 mmol), thionyl chloride (1.37 g, 36.1 mmol) was added dropwise and the mixture stirred at reflux for 2 h. After cooling to room temperature the solvent was

[80] Q. Zou, H. Tian, *Sensors and Actuators B* **2010**, *149*, 20−27.

removed under reduced pressure. The crude was purified by flash chromatography (silica gel, hexane) yielding a white solid (2.90 g, 75%).

^{1}H RMN (400 MHz, $CDCl_3$) δ: 8.23 (dd, *J* = 1.9 Hz, *J* = 0.5 Hz, 1H), 7.88 (dd, *J* = 9.3, *J* = 0.5 Hz, 1H), 7.67 (dd, *J* = 9.3, *J* = 1.9 Hz, 1H) ppm.

Tributyl(4-dodecylthiophen-2-yl)stannane (21).[61]

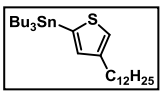

4-Dodecylthiophene (**20**) (5.00 g, 19.8 mmol,) and TMEDA (3.54 mL, 23.7 mmol) were dissolved in dry THF (35 mL) under nitrogen atmosphere and *n*-butyllithium (2.5 M in hexane, 9.50 mL, 23.8 mmol) was dropwise added to the mixture at −78 °C. After being stirred at −78 °C for 40 min, reaction was further stirred at room temperature for 1.5 h. The resulting light-yellow mixture was again cooled to −78 °C, tributyltinchloride (6.72 mL, 24.7 mmol) was then added dropwise. After stirring at room temperature for 8 h, it was poured over H_2O (50 mL),extracted with DCM (3 × 30 mL), washed with brine (2x 30 mL), dried over anhydrous Na_2SO_4, filtered and the solvent was removed under reduced pressure. Thus obtained yellow oil (9.64 g, 90%) was employed without further purification.

^{1}H NMR (400 MHz, CDCl3) δ: 7.19 (s, 1H), 6.97 (s, 1H), 2.65 (t, *J* = 8.0 Hz, 2H), 1.65–1.61 (m, 2H), 1.59–1.50 (m, 6H) 1.41–1.20 (m, 24H), 1.14–1.05 (m, 6H), 0.91–0.88 (m, 12H) ppm.

Compound 22.

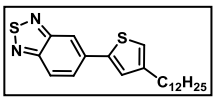

Into a 100 mL flame-dried 2-neck round bottom flask equipped with a condenser **21** (4.40 g, 8.13 mmol), **19** (1.16 g, 5.42mmol), $Pd_2(dba)_3$ (250 mg, 0.27 mmol) and PPh_3 (284 mg, 1.07 mmol) were added and dissolved in dry toluene (15 mL) under nitrogen atmosphere. The mixture was degassed for 30 min and stirred at 110 °C for 18 h. On cooling to room temperature, the solvent was removed under reduced pressure. The crude was purified by flash chromatography (silica gel, hexane/DCM 7:3) giving a light yellow solid (1.33 g, 90%).

^{1}H RMN (400 MHz, $CDCl_3$) δ: 8.16 (dd, *J* = 1.6 Hz, 0.7 Hz, 1H), 7.98 (dd, *J* = 9.2 Hz, *J* = 0.7 Hz, 1H), 7.89 (dd, *J* = 9.2 Hz, 1.6 Hz, 1H), 7.34 (d, *J* = 1.3 Hz, 1H), 7.00 (d, *J* = 1.3 Hz, 1H), 2.65 (t, *J* = 7.6 Hz, 2H), 1.71-1.63 (m, 2H), 1.39–1.26 (m, 18H), 0.88 (t, *J* = 6.8 Hz, 3H) ppm.

^{13}C RMN (100 MHz, $CDCl_3$) δ: 155.5, 154.3, 145.0, 142.3, 136.0, 129.1, 126.6, 121.7, 121.6, 116.2, 32.1, 30.7, 30.6, 29.9, 29.8, 29.7, 29.6, 29.5, 29.4, 22.8, 14.3 ppm.

MS (ESI, CH_3OH): *m/z* = 387.1902 ($M+1^+$).

Compound 23.

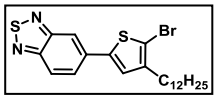

Inside a 50 mL 2-neck round bottom flask **22** (1.15 g, 2.97 mmol) was dissolved in dry THF (20 mL) under nitrogen atmosphere. NBS (580 mg, 3.25 mmol) was added in one portion at 0 ºC and stirred for 10 min, then mixture was stirred at room temperature overnight. The solvent was removed under reduced pressure and the crude was purified by flash chromatography (silica gel, hexane/chloroform 7:3) yielding a yellow solid (1.17 g, 85%).

^{1}H NMR (400 MHz, $CDCl_3$) δ: 8.14 (d, *J* = 0.6 Hz, 1H), 8.05 (d, *J* = 9.1 Hz, 1H), 7.87 (d, *J* = 9.2 Hz, 1H), 7.33 (s, 1H), 2.60 (t, *J* = 7.7 Hz, 2H), 1.69–1.59 (m, 2H), 1.50–1.27(m, 18H), 0.87 (t, *J* = 6.5 Hz, 3H) ppm.

^{13}C NMR (101 MHz, $CDCl_3$) δ: 155.3 154.2, 143.8, 141.8, 134.9, 128.3, 126.0, 121.8, 116.1, 110.4, 31.9, 29.7, 29.68, 29.66, 29.5, 29.4, 29.36, 29.2, 22.7, 14.1 ppm.

MS (ESI, CH_3OH): *m/z* = 465.1028 ($M+1^+$).

Compound 24.

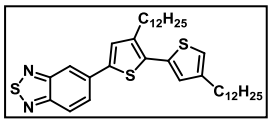

Into a 100 mL flame-dried 2-neck round bottom flask equipped with a condenser **21** (1.05 g, 1.95 mmol), **23** (608 mg, 1.30 mmol), $Pd_2(dba)_3$ (65 mg, 0.06 mmol) and PPh_3 (70.0 mg, 0.26 mmol) were added and dissolved in dry toluene (15 mL) under nitrogen atmosphere. The mixture was degassed for 30 min and stirred at 110 °C for 18 h. On cooling to room temperature, the solvent was removed under reduced pressure. The crude was purified by flash chromatography (silica gel, hexane/DCM 1:1) giving a light yellow solid (660 mg, 80%).

^{1}H NMR (400 MHz, $CDCl_3$) δ: 8.15 (d, *J* = 1.7 Hz, 1H), 7.98 (d, *J* = 9.2 Hz, 1H), 7.89 (dd, *J* = 9.2, 1.7 Hz, 1H), 7.34 (s, 1H), 7.03 (d, *J* = 1.1 Hz, 1H), 6.94

(d, *J* = 1.1 Hz), 2.79 (m, *J* = 7.7 Hz, 2H), 2.63 (t, *J* = 7.7 Hz, 2H), 1.72–1.64 (m,4H), 1.47–1.19 (m, 36H), 0.88 (t, *J* = 6.7 Hz, 6H) ppm.

^{13}C NMR (101 MHz, $CDCl_3$) δ: 155.4, 154.2, 143.8, 140.7, 139.5, 135.4, 135.3, 132.8, 128.6, 128.1, 127.6, 121.6, 120.5, 115.9, 31.9, 30.6, 30.5, 30.4, 29.7, 29.67, 29.6, 29.56, 29.5, 29.47, 29.45, 29.4, 29.36, 22.7, 14.1 ppm.

HRMS (MALDI-TOF): *m/z* calculated for $C_{38}H_{56}N_2S_3$: 636.3609, found: 636.3600.

Compound 25.

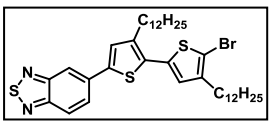

Inside a 50 mL 2-neck round bottom flask **24** (1.24 g, 1.94 mmol) was dissolved in dry THF (20 mL) under nitrogen atmosphere. NBS (380 mg, 2.13 mmol) was added in one portion at 0 ºC and stirred for 10 min, then mixture was stirred at room temperature overnight. The solvent was removed under reduced pressure and the crude was purified by flash chromatography (silica gel, hexane/chloroform 3:1) providing a yellow solid (1.24 g, 90%).

^{1}H NMR (400 MHz, $CDCl_3$) δ: 8.14 (dd, *J* = 1.7, 0.7 Hz, 1H), 7.99 (dd, *J* = 9.2, 0.7 Hz, 1H), 7.87 (dd, *J* = 9.2, 1.7 Hz, 1H), 7.32 (s, 1H), 6.88 (s, 1H), 2.75 (t, *J* = 7.7 Hz, 2H), 2.58 (t, *J* = 7.5 Hz, 2H), 1.73–1.58 (m, 4H), 1.46–1.18 (m, 36H), 0.87 (t, *J* = 6.8 Hz, 6H) ppm.

^{13}C NMR (101 MHz, $CDCl_3$) δ: 153.5, 152.4, 140.8, 139.4, 138.2, 133.3, 133.27, 129.9, 126.7, 126.2, 125.3, 119.8, 114.2, 107.4, 30.1, 29.1, 28.8, 27.9, 27.86, 27.8, 27.7, 27.70, 27.63, 27.62, 27.6, 27.4, 20.9, 12.3 ppm.

HRMS (MALDI-TOF): *m/z* calculated for $C_{38}H_{55}BrN_2S_3$: 714.2705, found: 714.2716.

Compound 26.

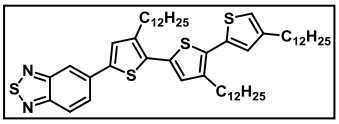

Into a 100 mL flame-dried 2-neck round bottom flask equipped with a condenser **21** (1.18 g, 2.17 mmol), **25** (1.04 g, 1.45 mmol), $Pd_2(dba)_3$ (66.0 mg, 0.07 mmol) and PPh_3 (76.0 mg, 0.29 mmol) were added and dissolved in dry toluene (20 mL) under nitrogen atmosphere. The mixture was degassed for 30 min and stirred at 110 °C for 18 h. On cooling to room temperature, the solvent was removed under reduced pressure. The crude was purified by flash

chromatography (silica gel, hexane/DCM 2:1) giving a light-orange solid (927 mg, 70%).

^{1}H NMR (400 MHz, $CDCl_3$) δ: 8.15 (dd, *J* = 1.7, 0.7 Hz, 1H), 7.99 (dd, *J* = 9.2, 0.7 Hz, 1H), 7.89 (dd, *J* = 9.2, 1.8 Hz, 1H), 7.34 (s, 1H), 7.02 (s, 1H), 6.99 (d, *J* = 1.4 Hz, 1H), 6.91 (d, *J* = 1.3 Hz, 1H), 2.82 (t, *J* = 7.7 Hz, 2H), 2.77 (t, *J* = 7.7 Hz, 2H), 2.62 (t, *J* = 7.6 Hz, 2H), 1.77–1.59 (m, 6H), 1.48–1.18 (m, 54H), 0.92–0.83 (m, 9H) ppm.

^{13}C NMR (101 MHz, $CDCl_3$) δ: 155.4, 154.2, 143.7, 140.8, 139.7, 139.5, 135.3, 135.26, 133.2, 132.4, 131.6, 128.9, 128.6 128.2, 127.3, 121.6, 120.2, 115.9, 31.9, 30.6, 30.57, 30.5, 30.46, 29.7, 29.65, 29.6, 29.5, 29.4, 29.3, 22.7, 14.1 ppm.

HRMS (MALDI-TOF): *m/z* calculated for $C_{54}H_{82}N_2S_4$: 886.5337, found: 886.5355.

Compound 27.

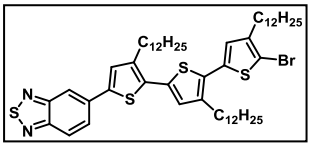

Inside a 50 mL 2-neck round bottom flask **26** (800 mg, 0.563 mmol) was dissolved in dry DCM (20 mL) under nitrogen atmosphere. NBS (115 mg, 0.619 mmol) was dissolved in dry DCM (5 mL) and added dropwise at 0 ºC. After stirring for 10 min at that same temperature, the mixture was stirred at room temperature overnight. The solvent was removed under reduced pressure and the crude was purified by flash chromatography (silica gel, hexane/chloroform 2:1) providing a bright orange solid (400 mg, 72%).

^{1}H NMR (400 MHz, $CDCl_3$) δ: 8.15 (dd, *J* = 1.7, 0.7 Hz, 1H), 7.99 (dd, *J* = 9.2, 0.7 Hz, 1H), 7.89 (dd, *J* = 9.2, 1.8 Hz, 1H), 7.34 (s, 1H), 7.01 (s, 1H), 6.84 (s, 1H), 2.81 (t, *J* = 7.6 Hz, 2H), 2.73 (t, *J* = 7.7 Hz, 2H), 2.58 (t, *J* = 7.5 Hz, 2H), 1.76–1.57 (m, 6H), 1.48–1.19 (m, 54H), 0.92–0.83 (m, 9H) ppm.

^{13}C NMR (101 MHz, $CDCl_3$) δ:155.4, 154.2, 154.15, 142.6, 141.0, 140.3, 139.8, 135.2, 133.8, 132.1, 130.5, 128.9, 128.6, 128.2, 126.8, 121.6, 115.9, 108.8, 31.9, 30.6, 29.7, 29.6, 29.56, 29.5, 29.4, 29.38, 29.3, 22.7, 14.1 ppm.

HRMS (MALDI-TOF): *m/z* calculated for $C_{54}H_{81}BrN_2S_4$: 964.4460, found: 964.4452.

Compound 28.

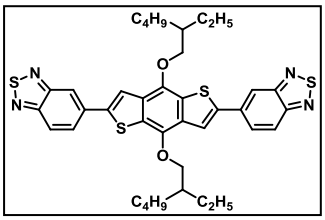

Into a 100 mL flame-dried 2-neck round bottom flask fitted with a condenser, 5-bromobenzo[*c*][1,2,5]thiadiazole (**19**) (174 mg, 0.81 mmol), **17** (300 mg, 0.38 mmol), and $Pd(PPh_3)_4$ (22.0 mg, 0.02 mmol) were dissolved in dry toluene (15 mL) under nitrogen atmosphere. Resulting mixture was degassed for 30 min and stirred at 110 °C for 18 h. Upon cooling to room temperature, reaction mixture was diluted with chloroform (50 mL) and washed with H_2O (3 × 25 mL), organic layer was dried over anhydrous Na_2SO_4, filtered and solvent eliminated under reduced pressure. Reaction crude was purified by flash chromatography (silica gel, hexane/DCM 1:2), obtaining an orange-red solid (323 mg, 95%).

^{1}H RMN (400 MHz, $CDCl_3$) δ: 8.28 (s, 2H), 8.08–7.99 (m, 4H), 7.84 (s, 2H), 4.27 (m, 4H), 1.95–1.85 (m, 2H), 1.82–1.53 (m, 8H), 1.53–1.40 (m, 8H), 1.07 (t, *J* = 7.4 Hz, 6H), 0.99 (t, *J* = 6.9 Hz, 6H) ppm.

^{13}C RMN (101 MHz, $CDCl_3$) δ: 155.3, 154.7, 144.9, 142.2, 135.5, 133.2, 129.78 128.6, 121.9, 118.4, 118.1, 76.4, 40.9, 30.6, 29.4, 24.1, 23.3, 14.4, 11.5 ppm.

HRMS (MALDI-TOF): *m/z* calculated for $C_{38}H_{42}N_4O_2S_4$: 714.2185, found: 714.2195.

FTIR (neat): 2956, 2925, 2863, 1606, 1544, 1516, 1461, 1369, 1269 1177, 1141, 1044, 959, 899, 848, 810, 750, 630 cm^{-1}.

UV-visible (DCM): 456 (49750), 387 (57712), 329 (64179), 280 (73083) nm ($M^{-1}cm^{-1}$).

Compound 29.

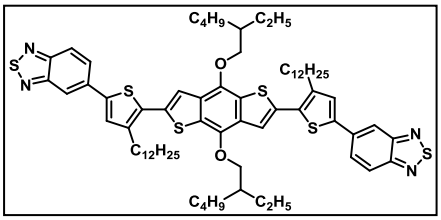

Into a 100 mL flame-dried 2-neck round bottom flask fitted with a condenser, **23** (397 mg, 0.85 mmol), **17** (300 mg, 0.38 mmol), and $Pd(PPh_3)_4$ (19.0 mg, 0.02 mmol) were dissolved in dry toluene (15 mL) under nitrogen atmosphere. Resulting mixture was degassed for 30 min and stirred at 110 °C for 18 h.

Upon cooling to room temperature, reaction mixture was diluted with chloroform (50 mL) and washed with H_2O (3 × 25 mL), organic layer was dried over anhydrous Na_2SO_4, filtered and solvent eliminated under reduced pressure. Reaction crude was purified by flash chromatography (silica gel, hexane/DCM 6:4), followed by a second column (silica, hexane/EtOAc 17:1) to finally yield a maroon solid (184 mg, 40%).

^{1}H RMN (400 MHz, $CDCl_3$) δ: 8.14 (dd, J = 1.8 Hz, 0.6 Hz, 2H), 7.95 (dd, *J* = 9.2 Hz, 0.6 Hz, 2H), 7.86 (dd, *J* = 9.2 Hz, 1,8 Hz, 2H), 7.48 (s, 2H), 7.34 (s, 2H), 4.18 (m, 4H), 2.98–2.90 (m, 4H), 1.84–1.76 (m, 2H), 1.73–1.54 (m, 8H), 1.45–1.32 (m, 8H), 1.50–1.26 (m, 40H), 1.00 (t, *J* = 7.4 Hz, 6H), 0.90 (t, *J* = 7.0 Hz, 6H), 0.79 (t, *J* = 6.8 Hz, 6H) ppm.

^{13}C NMR (101 MHz, $CDCl_3$) δ: 155.3, 154.2, 144.2, 144.1, 142.2, 140.9, 135.4, 135.0, 132.4, 131.9, 129.7, 128.5, 128.3, 121.63, 118.51, 116.1, 76.0, 40.7, 31.9, 30.7, 30.6, 29.9, 29.7, 29.7, 29.6, 29.4, 29.3, 23.9, 23.2, 22.7, 14.3, 14.26, 14.1, 11.4 ppm.

HRMS (MALDI-TOF): *m/z* calculated for $C_{70}H_{94}N_4O_2S_6$: 1214.5696, found: 1214.5708.

FTIR (neat): 2923, 2855, 1732, 1605, 1516, 1460, 1367, 1273, 1175, 1045, 848, 813, 726, 667, 629 cm^{-1}.

UV-visible (DCM): 444 (51277), 384 (49457), 334 (33761), 295 (44778) nm ($M^{-1}cm^{-1}$).

Compound 30.

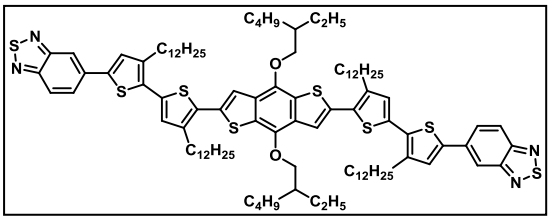

Into a 100 mL flame-dried 2-neck round bottom flask fitted with a condenser, **25** (142 mg, 0.20 mmol), **17** (70.0 mg, 0.09 mmol), Pd_2dba_3 (9.00 mg, 0.01 mmol) and PPh_3 (10.0 mg, 0.04 mmol) were dissolved in dry toluene (15 mL) under nitrogen atmosphere. Resulting mixture was degassed for 30 min and stirred at 110 °C for 18 h. Upon cooling to room temperature, reaction mixture was diluted with chloroform (50 mL) and washed with H_2O (3 × 25 mL), organic layer was dried over anhydrous Na_2SO_4, filtered and solvent eliminated under reduced

pressure. Reaction crude was purified by flash chromatography (silica gel, hexane/DCM 4:3) to yield a dark red solid (77.0 mg, 50%).

^{1}H NMR (400 MHz, $CDCl_3$) δ: 8.18 (dd, *J* = 1.7, 0.7 Hz, 2H), 8.01 (dd, *J* = 9.2, 0.7 Hz, 2H), 7.91 (dd, *J* = 9.2, 1.7 Hz, 2H), 7.50 (s, 2H), 7.37 (s, 2H), 7.10 (s, 2H), 4.23 (m, 4H), 2.95–2.84 (m, 8H), 1.89–1.81 (m, 2H), 1.80–1.70 (m, 12H), 1.69–1.59 (m, 4H), 1.50–1.24 (m, 80H), 1.06 (t, *J* = 7.4 Hz, 6H), 0.96 (t, *J* = 7.0 Hz, 6H), 0.90–0.82 (m, 12H) ppm.

^{13}C NMR (101 MHz, $CDCl_3$) δ: 155.40, 154.3, 144.0, 141.4, 141.2, 139.9, 135.4, 135.2, 134.8, 132.1, 132.0, 131.2, 129.8, 129.2, 128.6, 128.3, 121.7, 118.3, 116.0, 76.0, 40.7, 31.9, 30.7, 30.6, 30.55, 29.7, 29.68, 29.6, 29.5, 29.4, 29.3, 23.9, 23.2, 22.7, 14.2, 14.1, 11.4 ppm.

HRMS (MALDI-TOF): *m/z* calculated for $C_{102}H_{146}N_4O_2S_8$: 1714.9206, found: 1714.9243.

FTIR (neat): 2922, 2853, 1650, 1605, 1514, 1459, 1428, 1370, 1269 1185, 1043, 845, 813, 724, 666, 624 cm^{-1}.

UV-visible (DCM): 444 (68403), 309 (32494), 285 (35191) nm ($M^{-1}cm^{-1}$).

Compound 31.

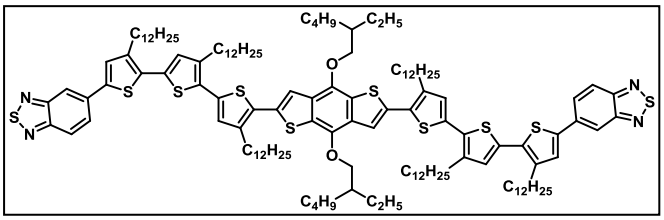

Into a 100 mL flame-dried 2-neck round bottom flask fitted with a condenser, **27** (366 mg, 0.37 mmol), **17** (132 mg, 0.17 mmol), Pd_2dba_3 (18.0 mg, 0.02 mmol) and PPh_3 (20.0 mg, 0.08 mmol) were dissolved in dry toluene (15 mL) under nitrogen atmosphere. Resulting mixture was degassed for 30 min and stirred at 110 °C for 18 h. Upon cooling to room temperature, reaction mixture was diluted with chloroform (50 mL) and washed with H_2O (3 × 25 mL), organic layer was dried over anhydrous Na_2SO_4, filtered and solvent eliminated under reduced pressure. Reaction crude was purified by flash chromatography (silica gel, hexane/DCM 2:1) to yield a dark red solid (228 mg, 60%).

^{1}H NMR (400 MHz, $CDCl_3$) δ: 8.17 (d, *J* = 1.6 Hz, 2H), 8.00 (d, *J* = 9.2 Hz, 2H), 7.90 (dd, *J* = 9.2, 1.6 Hz, 2H), 7.49 (s, 2H), 7.36 (s, 2H), 7.06 (s, 2H),

7.05 (s, 2H), 4.23 (m, 4H), 2.94–2.89 (m, 4H), 2.88–2.81 (m, 8H), 1.91–1.81 (m, 2H), 1.78–1.70 (m, 12H), 1.67–1.59 (m, 4H), 1.48–1.23 (m, 120H),1.06 (t, J = 6.2 Hz, 6H), 0.96 (t, J = 7.0 Hz, 6H), 0.89–0.83 (m, 18H) ppm.

^{13}C NMR (101 MHz, $CDCl_3$) δ: 155.4, 154.3, 144.0, 141.3, 141.00, 140.3, 139.7, 135.5, 135.2, 134.9, 133.70, 132.3, 131.9, 130.8, 129.8, 129.1, 128.9, 128.6, 128.3, 121.6, 118.2, 116.0, 76.0, 40.7, 31.9, 30.8, 30.6, 29.7, 29.6, 29.7, 29.6, 29.5, 29.52, 29.4, 29.3, 23.4, 23.2, 22.7, 14.2, 14.1, 11.4 ppm.

HRMS (MALDI-TOF): *m/z* calculated for $C_{134}H_{198}N_4O_2S_{10}$: 2215.2716, found: 2215.2657.

FTIR (neat): 2922, 2853, 1604, 1516, 1460, 1366, 1272, 1176, 1043, 814, 724, 624 cm^{-1}.

UV-visible (DCM): 448 (99276), 278 (47638) nm ($M^{-1}cm^{-1}$).

1.5.2. Synthesis of D−A−D Small molecules based on rhodanine acceptors

1.5.2.1. *1st Generation D−A−D small molecules*

2-(3-Hexyl-4-oxothiazolidin-2-ylidene)malononitrile (35).

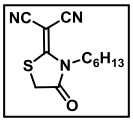

To an acetonitrile solution (70 mL) of hexyl isothiocyanate (**32**) (3.40 mL, 22.0 mmol) and malononitrile (**33**) (1.32 g, 20.0 mmol), DBU (3.00 mL, 20.0 mL) was added at room temperature. After stirring for 30 min, ethyl 2-bromoacetate (**34**) (3.80 mL, 34.0 mmol) was added. Reaction was stirred at room temperature for 1 h and then stirred further 3 h at reflux. Upon completion, reaction was quenched with 2 M hydrochloric acid aqueous solution and extracted with DCM (3 × 50 mL), dried over Na_2SO_4, filtered and evaporated under vacuum. Purification was carried out by column chromatography (silica gel, hexane/DCM 1:3) yielding a tan solid (4.19 g, 84%). Further purification may be carried out by recrystallization from minimal amount of methanol at -20 °C.

^{1}H NMR (400 MHz, $CDCl_3$) δ: 4.10–4.06 (m, 2H), 3.99 (s, 2H), 1.72–1.64 (m, 2H), 1.40–1.30 (m, 6H), 0.89 (t, J = 7.0 Hz, 3H) ppm.

^{13}C NMR (101 MHz, $CDCl_3$) δ: 171.7, 142.9, 113.0, 111.8, 56.8, 45.5, 32.4, 31.3, 28.6, 25.7, 22.5, 14.0 ppm.

FTIR (neat): 2933, 2860, 2218, 1746, 1522, 1460, 1384, 1335, 1278, 1171, 1126, 1052, 893, 785 cm^{-1}.

HRMS (MALDI-TOF): *m/z* calculated for $C_{12}H_{15}N_3OS$: 249.0936, found: 249.0941.

***N*-(2-Ethylhexyl)rhodanine (38).[67]**

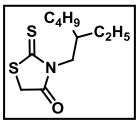

To a suspension of bis(carboxymethyl)trithiocarbonate (**36**) (5.00 g, 22.09 mmol) in isopropanol (50 mL), 2-ethylhexylamine (**37**) (3.60 mL, 22.1 mmol) and trimethylamine (13.5 mL, 22.5 mmol) were added. The resulting mixture was stirred and refluxed for 1 h. After cooling to room temperature, solvent was evaporated under reduced pressure. The resulting oily crude was purified by flash chromatography (silica gel, hexane/DCM 1:1), providing title compound as a colorless oil (4.56 g, 84%).

^{1}H NMR (400 MHz, $CDCl_3$) δ: 3.97 (s, 2H), 3.90 (d, *J* = 7.4 Hz, 2H), 2.04−1.93 (m, 1H), 1.37−1.21 (m, 8H), 0.89 (t, *J* = 7.5 Hz, 3H), 0.88 (t, *J* = 6.8 Hz, 3H) ppm.

3,6-dibromophenanthrene-9,10-dione (41).[68]

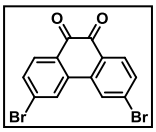

To a suspension of phenanthrenequinone (**39**) (12.8 g, 61.8 mmol) and benzoyl peroxide (**40**) (50.0 mg, 0.20 mmol) in nitrobenzene (100 mL, 0.97 mmol), bromine (19.5 mL, 370 mmol) was added dropwise. Reaction mixture was heated at 110 °C for 1 h under W-lamp irradiation. Upon cooling to room temperature, the resulting dark precipitate was filtered off and washed with abundant hexane to give rise to bright yellow solid (15.7 g, 75%). Resulting product was used without further purification.

^{1}H NMR (400 MHz, $CDCl_3$) δ: 8.13 (d, *J* = 1.8 Hz, 2H), 8.08 (d, *J* = 8.3 Hz, 2H), 7.67 (dd, *J* = 8.3, 1.8 Hz, 2H) ppm.

3,6-dibromo-9*H*-fluoren-9-one (42).[68]

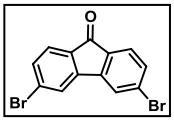

Into a KOH (21.5 g, 384mmol) solution in H_2O (200 mL) at 85 °C, **41** (5.00 g, 13.7 mmol) was added. After stirring at 85 °C for 12 h, $KMnO_4$ (11.5 g, 70.5 mmol) was added over 30 min. Resulting dark suspension was then refluxed for 2 h. After cooling to room temperature, the suspension was diluted with H_2O (200 mL) and the precipitate filtered off and washed with abundant water to provide a dark green solid. Obtained solid was suspended in H_2O (250 mL) at 50 ºC and Na_2HSO_3 portions

were added until dark color faded away. Upon cooling to room temperature the precipitate was collected by filtration as a pale yellow solid (1.84 g, 40%).

1H NMR (400 MHz, DMSO-d^6) δ: 8.25 (d, *J* = 1.3 Hz, 2H), 7.65 (dd, *J* = 7.9, 1.5 Hz, 2H), 7.59 (d, *J* = 7.9 Hz, 2H) ppm.

Bis(4-butylphenyl)amine (45).

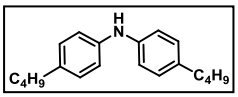

1-Bromo-4-butylbenzene (**43**) (1.24 g, 5.86 mmol), 4-butylaniline (**44**) (0.92 mL, 5.86 mmol), $Pd_2(dba)_3$ (133 mg, 0.14 mmol) and XPhos (138 mg, 0.29 mmol) were dissolved in dry Toluene (20 mL) under nitrogen atmosphere. The mixture was degassed for 30 minutes before adding NaO^{t}Bu (560 mg, 5.86 mmol) in one portion, and then stirred at 100 °C for 18 h. Upon completion, the reaction was quenched with H_2O (20 mL) and extracted with CH_2Cl_2 (3 × 10 mL). Combined organic extracts were dried over anhydrous Na_2SO_4, filtered, and evaporated by rotary evaporation. Obtained crude was purified by column chromatography (silica gel, hexane/DCM 4:1) yielding a colorless thick oil (3.60 g, 95%).

^{1}H NMR (400 MHz, $CDCl_3$) δ: 7.07 (d, *J* = 8.2 Hz, 4H), 6.97 (d, *J* = 8.1 Hz, 4H), 5.54 (s, 1H), 2.55 (t, *J* = 7.6 Hz, 4H), 1.65–1.53 (m, 4H), 1.42–1.32 (m, 4H), 0.93 (t, *J* = 7.3 Hz, 6H) ppm.

***N*,*N*-Bis(4-butylphenyl)thiophen-2-amine (47).**[81]

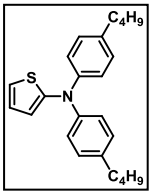

Into a 100 mL 2-neck round flask 2-bromothiophene (**46**) (240 mg, 1.50 mmol), bis(4-butylphenyl)amine (**45**) (420 mg, 1.50 mmol), $Pd_2(dba)_3$ (18.0 mg, 0.04 mmol), and P(^{t}Bu)$_3$HBF$_4$ (44.0 mg, 0.15 mmol) were added. After purging the air with nitrogen, dry toluene (20 mL) was introduced, and the resulting mixture was degassed by bubbling nitrogen into the solvent over 30 minutes. Then, NaO^{t}Bu (430 mg, 4.50 mmol) was added in one portion into the mixture, and degassed for further 10 min. Reaction was stirred at reflux for 18 h. After cooling to room temperature, the mixture was diluted with toluene (100 mL) and washed with H_2O. Separated organic extracts were dried over anhydrous Na_2SO_4, filtered, and dried under reduced pressure. Product was purified by

[81] S. Ohira, I. Rudra, K. Schmidt, S. Barlow, S.-J. Chung, Q. Zhang, J. Matichak, S. R. Marder, J.-L. Brédas, *Chem. Eur. J*. **2008**, *14*, 11082−11091.

flash chromatography (silica gel, hexane/DCM 10:1) obtaining a yellow oil (440 mg, 82%).

^{1}H NMR (400 MHz, $CDCl_3$) δ: 7.10–6.99 (m, 8H), 6.93 (d, *J* = 5.6 Hz, 1H), 6.85 (dd, *J* = 5.5, 3.7 Hz, 1H), 6.66 (d, *J* = 3.6 Hz, 1H), 2.58–2.53 (m, 4H), 1.58 (m, 4H), 1.36 (m, 4H), 0.93 (t, *J* = 7.3 Hz, 6H) ppm.

_N_,_N_-bis(4-butylphenyl)-5-(trimethylstannyl)thiophen-2-amine (48).

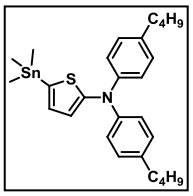

Inside a 100 mL flame-dried 2-neck round flask with nitrogen atmosphere *N*,*N*-bis(4-butylphenyl)thiophen-2-amine (**47**) (700 mg, 1.92 mmol) was dissolved in dry THF (20 mL). After cooling to –78 °C, *n*-butyllithium (2.5 M in hexane,1.15 mL, 2.90 mmol) was added dropwise over 10 min. The resulting mixture was warmed to 0 °C and stirred for 1 h. Then, trimethyltinchloride (1.0 M in hexane, 3.85 mL, 3.85 mmol) was added in one portion and the mixture was allowed to warm to room temperature and stirred overnight. Saturated ammonium chloride solution (20 mL) was added to the reaction mixture and the product was extracted with diethyl ether (3 × 20 mL). Combined organic extracts were dried over anhydrous Na_2SO_4, filtered, and solvent removed under reduced pressure. Title product was obtained as an oil (700 mg, 70%) and used in the next synthetic step without further purification.

^{1}H NMR (400 MHz, $CDCl_3$) δ: 7.04 (d, *J* = 1.6 Hz, 8H), 6.93 (d, *J* = 3.4 Hz, 1H), 6.72 (d, *J* = 3.4 Hz, 1H), 2.59–2.52 (m, 4H), 1.64–1.55 (m, 4H), 1.36 (m, 4H), 0.93 (t, *J* = 7.3 Hz, 6H), 0.32 (s, 9H) ppm.

4-butyl-_N_-(4-butylphenyl)-_N_-phenylaniline (50).

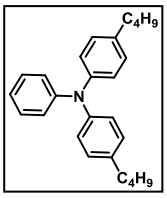

A dry toluene (20 mL) solution of 1-bromo-4-butylbenzene (**43**) (4.79 g, 22.4 mmol), aniline (**49**) (0.98 mL, 10.7 mmol), $Pd_2(dba)_3$ (491 mg, 0.53 mmol), and XPhos (505 mg, 1.06 mmol) was degassed over 30 minutes by bubbling nitrogen directly into it. NaO^{t}Bu (3.13 g, 32.2 mmol) was added thereafter in one portion, and the resulting mixture was stirred at 100 °C for 18 h. After cooling to room temperature, the reaction was quenched with H_2O (20 mL), extracted with DCM (3 × 10 mL), the organic layers dried over anhydrous Na_2SO_4, filtered, and finally the solvent removed under reduced pressure. Reaction crude was purified by flash chromatography (silica gel, hexane/DCM 4:1) providing a colorless viscous oil (3.60 g, 95%).

^{1}H NMR (300 MHz, $CDCl_3$,) δ:7.27 (d, *J*= 8.2 Hz, 2H), 7.14–6.98 (m, 11H), 2.62 (t, *J* = 7.7 Hz, 4H), 1.65 (m, 4H), 1.45 (m, 4H), 1.00 (t, *J*= 7.2 Hz, 6H) ppm.

4-bromo-*N*,*N*-bis(4-butylphenyl)aniline (51).

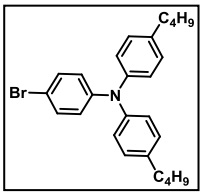

Compound **50** (2.00 g, 5.60 mmol) was dissolved in dry DMF (10 mL) under nitrogen atmosphere. To the stirring solution at 0 °C a solution of NBS (1.00 g, 5.60 mmol) in dry DMF (10 mL) was added dropwise over 30 min. Upon completion, the mixture was allowed to stir at room temperature overnight. Saturated NH_4Cl aqueous solution (25 mL) was added to the reaction mixture and the product extracted with Et_2O (3 × 20 mL). The combined organic extracts were dried over anhydrous Na_2SO_4, filtered and the solvent removed under reduced pressure. Purification was carried out by flash chromatography (silica gel, hexane) yielding a colorless viscous oil (2.33 g, 94%).

^{1}H NMR (400 MHz, C_6D_6) δ: 7.12 (d, *J* = 8.8 Hz, 2H), 7.04–7.01 (m, 4H), 6.94–6.92 (m, 4H), 6.79 (d, *J* = 9.2 Hz, 2H), 2.42 (t, *J* = 7.8 Hz, 4H), 1.50–1.43 (m, 4H), 1.29–1.20 (m, 4H), 0.83 (t, *J* = 7.2 Hz, 6H) ppm.

***N*,*N*-di(4'-butylphenyl)-4-(1,2,3-dioxaborolan-2-yl)aniline (52).[71]**

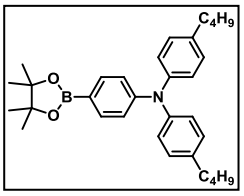

Compound **51** (2.33 g, 5.31 mmol) was dissolved in dry THF (10 mL) under nitrogen atmosphere. To the stirring solution at -78 °C *n*-butyllithium (2.5 M in hexane, 4.24 mL, 10.6 mmol) was added dropwise. The mixture was stirred at this temperature for 30 minutes followed by the addition of isopropyl pinacol borate (2.10 g, 11.1 mmol). Saturated NH_4Cl aqueous solution (25 mL) was added to the reaction mixture and the product extracted with Et_2O (3 x 20 mL). The combined organic extracts were dried over anhydrous Na_2SO_4, filtered and the solvent removed under reduced pressure. Purification was carried out by flash chromatography (silica gel, hexane/DCM 2:1) yielding a colorless viscous liquid (788 mg, 70%).

^{1}HNMR (400 MHz, $CDCl_3$) δ: 7.63 (d, *J* = 8.8 Hz, 2H), 7.07–6.97 (m, 10H), 2.57 (t, *J* = 7.8 Hz, 4H), 1.64–1.55 (m, 4H), 1.44–1.33 (m, 4H), 1.32 (s, 12H), 0.94 (t, *J* = 7.2 Hz, 6H) ppm.

Compound 53.

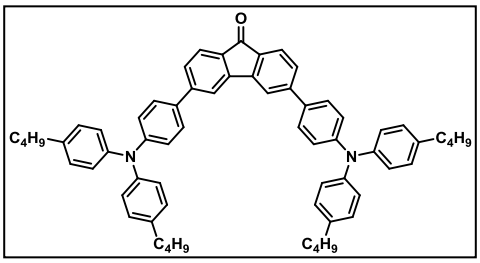

Into a 100 mL 2-neck round flask filled with dry toluene (20 mL) and nitrogen, 4-butyl-*N*-(4-butylphenyl)-*N*-(4-(4,4,5,5-tetramethyl-1,3,2-dioxaborolan-2-yl)phenyl)aniline (**52**) (680 mg, 1.40 mmol), 3,6-dibromo-9*H*-fluoren-9-one (**42**) (240 mg, 0.70 mmol), $Pd_2(dba)_3$ (16.0 mg, 0.02 mmol), and P(*o*-tolyl)$_3$ (21.0 mg, 0.07 mmol) were dissolved. The mixture was degassed for 30 minutes. Then, a previously degassed K_3PO_4 (4.40 g, 21.0mmol) DI water solution (7 mL) was added. The resulting mixture was stirred at 100 °C for 18 h. The mixture was cooled to room temperature and washed with water (3 ×25 mL). After extraction with DCM (3 × 15 mL), combined organic extracts were dried over anhydrous Na_2SO_4, filtered, and evaporated. The resulting crude was purified by flash chromatography (silica gel, hexane/DCM 1:2) giving rise to an orange solid (300 mg, 44%).

^{1}H NMR (400 MHz, $CDCl_3$) δ: 7.75 (s, 2H), 7.69 (d, *J* = 7.7 Hz, 2H), 7.52 (d, *J* = 8.7 Hz, 4H), 7.47 (dd, *J* = 7.8, 1.3 Hz, 2H), 7.15–7.06 (m, 20H), 2.65–2.58 (m, 8H), 1.69–1.59 (m, 8H), 1.48–1.36 (m, 8H), 0.98 (t, *J* = 7.4 Hz, 12H) ppm.

^{13}C NMR (101 MHz, $CDCl_3$) δ: 193.0, 148.8, 147.2, 145.0, 144.9, 138.2, 133.0, 132.5, 129.3, 127.8, 126.9, 125.0, 124.6, 122.1, 122.0, 118.3,35.1, 33.7, 22.5, 14.0 ppm.

HRMS (MALDI-TOF): *m/z* calculated for $C_{65}H_{66}N_2O$: 890.5163, found: 890.5170.

FTIR (neat): 3025, 2955, 2925, 2858, 1702, 1604, 1504, 1455, 1370, 1295, 1108, 914, 730 cm^{-1}.

Compound 54.

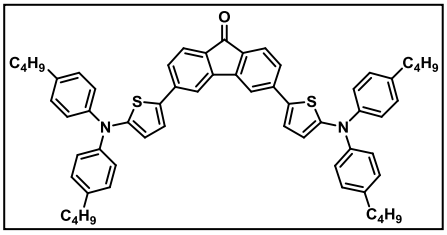

Into a 100 mL 2-neck round bottom flask equipped with a condenser, **48** (700 mg, 1.34 mmol), **42** (200 mg, 0.60 mmol), $Pd_2(dba)_3$ (14.0 mg, 0.01 mmol), and P(*o*-tolyl)$_3$ (18.0 mg, 0.06

mmol) were added to dry toluene (15 mL) under nitrogen atmosphere. The reaction mixture was degassed for 30 min, and then stirred and refluxed for 18 h. Upon cooling, Et_2O (50 mL) was added and then washed with H_2O (3 × 50 mL). The organic layer was extracted, dried over anhydrous Na_2SO_4, filtered, and evaporated to dryness. Purification by column chromatography (silica gel, hexane/DCM 1:2) gave rise to a dark red solid (440 mg, 80%).

^{1}H NMR (400 MHz, $CDCl_3$) δ: 7.62 (d, *J* = 1.1 Hz, 2H), 7.58 (d, *J* = 7.8 Hz, 2H), 7.39 (dd, *J* = 7.8, 1.5 Hz, 2H), 7.27 (d, *J* = 4.0 Hz, 2H), 7.17 (m, 16H), 6.55 (d, *J* = 4.0 Hz, 2H), 2.63–2.55 (m, 8H), 1.66–1.56 (m, 8H), 1.44–1.32 (m, 8H), 0.94 (t, *J* = 7.3 Hz, 12H) ppm.

^{13}C NMR (101 MHz, $CDCl_3$) δ: 192.1, 154.5, 145.2, 144.6, 140.7, 138.6, 133.7, 132.7, 129.2, 129.2, 124.8, 124.7, 124.1, 123.5, 123.5, 123.1, 118.1, 116.2, 35.1, 33.6, 22.4, 14.0 ppm.

HRMS (MALDI-TOF): *m/z* calculated for $C_{61}H_{62}N_2O_1S_2$: 902.4298, found: 902.4295.

FTIR (neat): 3052, 2955, 2926, 2859, 1707, 1596, 1508, 1473, 1435, 1318, 1280, 1183, 828, 743, 694 cm^{-1}.

Compound 55.

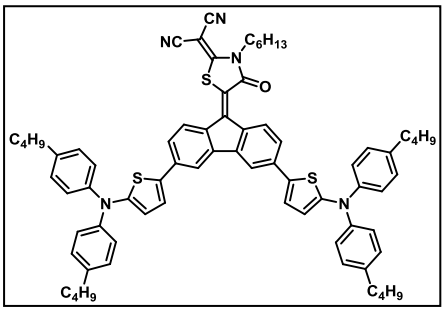

Compounds **54** (180 mg, 0.20 mmol), **35** (270 mg, 1.02 mmol), and NH_4OAc (110 mg, 1.43 mmol) were dissolved in glacial acetic acid (10 mL). The mixture was stirred at 118 °C for 24 h. After cooling to room temperature, the reaction was diluted with chloroform and repeatedly washed with a $NaHCO_3$ saturated solution until no CO_2 generation was observed. Organic extracts were dried over anhydrous Na_2SO_4, filtered, and dried. Purification was carried out by flash chromatography (silica gel, hexane/DCM 1:2) to give a deep blue solid (80.0 mg, 35%).

^{1}H NMR (400 MHz, $CDCl_3$) δ: 9.09 (d, *J* = 8.6 Hz, 1H), 7.72 (d, *J* = 8.4 Hz, 1H), 7.68 (d, *J* = 1.8 Hz, 1H), 7.66 (d, *J* = 1.9 Hz, 1H), 7.42 (dd, *J* = 8.4, 1.8 Hz, 1H), 7.37 (dd, *J* = 8.6, 1.9 Hz, 1H), 7.29 (d, *J* = 4.1 Hz, 1H), 7.28 (d, *J* =

4.1 Hz, 1H),7.18–7.10 (m, 16H), 6.56 (d, *J* = 4.1 Hz, 1H), 6.55 (d, *J* = 4.1 Hz, 1H),4.26–4.20 (m, 2H), 2.63–2.56 (m, 8H), 1.82–1.71 (m, 2H), 1.67–1.56 (m, 8H), 1.49–1.44 (m, 2H), 1.43–1.32 (m, 12H), 0.94 (t, *J* = 7.3 Hz, 12H), 0.90 (t, *J* = 7.1 Hz, 3H) ppm.

^{13}C NMR (126 MHz, $CDCl_3$) δ: 164.7, 164.3, 154.9, 154.8, 145.1, 145.0, 144.6, 142.6, 141.9, 138.8, 138.8, 137.9, 135.1, 133.7, 133.2, 132.7, 130.5, 129.3, 129.3, 129.2, 127.3, 124.5, 124.2, 124.0, 123.7, 123.6, 117.6, 115.9, 115.2, 113.6, 113.5, 112.5, 54.2, 45.2, 35.1, 33.6, 31.3, 29.7, 28.7, 25.7, 22.5, 22.4, 14.0 ppm.

HRMS (MALDI-TOF): *m/z* calculated for $C_{73}H_{75}N_5O_1S_3$: 1133.5128, found: 1133.5116.

FTIR (neat): 2923, 2854, 2215, 1714, 1651, 1604, 1545, 1510, 1454, 1375, 1275, 755 cm^{-1}.

Compound 56.

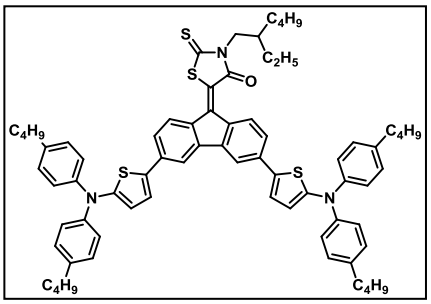

Compounds **54** (100 mg, 0.11 mmol), **38** (140 mg, 0.35 mmol), and NH_4OAc (60 mg, 0.77 mmol) were dissolved in glacial acetic acid (10 mL). The mixture was stirred at 118 °C for 24 h. After cooling to room temperature, the reaction was diluted with chloroform and repeatedly washed with a $NaHCO_3$ saturated solution until no CO_2 generation is observed. Organic extracts were dried over anhydrous Na_2SO_4, filtered, and dried. Purification was carried out by flash chromatography (silica gel, pentane/DCM10:1) to yield a dark green solid (70.0 mg, 56%).

^{1}H NMR (400 MHz, $CDCl_3$) δ: 9.11 (d, *J* = 8.5 Hz, 1H), 7.59–7.54 (m, 3H), 7.31 (d, *J* = 8.7 Hz, 1H), 7.28 (dd, *J* = 8.4, 1.6 Hz, 1H), 7.22 (d, *J* = 3.9 Hz, 1H), 7.21 (d, *J* = 3.9 Hz, 1H), 7.18–7.06 (m, 16H), 6.54 (d, *J* = 3.9 Hz, 2H), 4.00 (d, *J* = 7.4 Hz, 2H), 2.62–2.59 (m, 8H), 2.10–2.04 (m, 1H), 1.66–1.59 (m, 8H), 1.45–1.28 (m, 16H), 0.96 (t, *J* = 7.3 Hz, 12H), 0.94–0.88 (m, 6H) ppm.

^{13}C NMR (101 MHz, $CDCl_3$) δ: 191.4, 166.5, 154.1, 153.7, 145.3, 145.3, 142.6, 142.1, 140.7, 138.5, 138.4, 137.2, 137.0, 136.1, 134.3, 133.9, 130.1,

129.3, 129.2, 127.5, 124.3, 123.8, 123.7, 123.5, 123.3, 121.0, 118.8, 118.4, 115.9, 115.5, 48.7, 37.2, 35.1, 33.7, 30.6, 28.5, 24.0, 23.1, 22.5, 14.1, 14.0, 10.7 ppm.

HRMS (MALDI-TOF): *m/z* calculated for $C_{72}H_{79}N_3O_1S_4$: 1129.5100, found: 1129.5071.

FTIR (neat): 3030, 2956, 2925, 2857, 1702, 1655, 1605, 1507, 1457, 1371, 1292, 1192, 1128, 828, 791 cm^{-1}.

Compound 57.

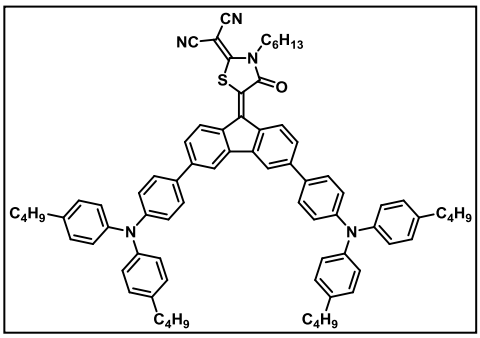

Compounds **53** (140 mg, 0.16 mmol), **35** (210 mg, 0.78 mmol), and NH_4OAc (86.0 mg, 1.12 mmol) were dissolved in glacial acetic acid (10 mL). The mixture was stirred at 118 °C for 24 h. After cooling to room temperature, the reaction was diluted with chloroform and repeatedly washed with a $NaHCO_3$ saturated solution until no CO_2 generation is observed. Organic extracts were dried over anhydrous Na_2SO_4, filtered, and dried. Purification was carried out by flash chromatography (silica gel, hexane/DCM 1:2) to give a dark purple solid (70.0 mg, 40%).

^{1}H NMR (400 MHz, $CDCl_3$) δ: 9.21 (d, *J* = 8.5 Hz, 1H), 7.87–7.83 (m, 3H), 7.55–7.49 (m, 6H), 7.12–7.06 (m, 20H), 4.28–4.25 (m, 2H), 2.59 (t, *J* = 7.6 Hz, 8H), 1.83–1.76 (m, 2H), 1.65–1.58 (m, 8H), 1.49–1.45 (m, 2H), 1.43–1.34 (m, 12H), 0.95 (t, *J* = 7.3 Hz, 12H), 0.91–0.88 (m, 3H) ppm.

^{13}C NMR (101 MHz, $CDCl_3$) δ: 164.8, 164.4, 149.0, 148.8, 145.2, 145.0, 144.9, 144.1, 144.0, 143.0, 142.2, 138.4, 138.2, 135.6, 134.1, 131.6, 131.2, 130.6, 129.4, 129.3, 127.5, 127.4, 125.2, 125.1, 121.9, 121.7, 117.8, 117.1, 114.7, 113.4, 112.3, 54.5, 45.3, 35.2, 33.7, 31.2, 29.7, 28.6, 25.8, 22.5, 14.0 ppm.

HRMS (MALDI-TOF): *m/z* calculated for $C_{77}H_{79}N_5OS$: 1121.6003, found: 1121.6000.

FTIR (neat): 3030, 2924, 2855, 2215, 1713, 1595, 1539, 1509, 1470, 1451, 1321, 1279, 1101, 826 cm^{-1}.

Compound 58.

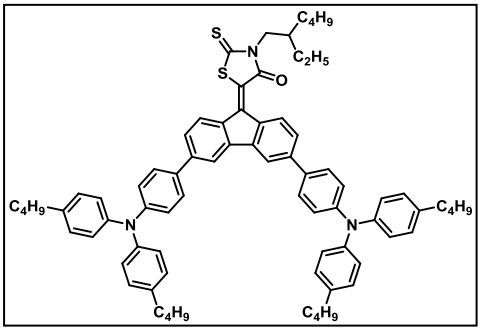

Compounds **53** (120 mg, 0.14 mmol), **38** (170 mg, 0.70 mmol), and NH_4OAc (75.0 mg, 0.9 mmol) were dissolved in glacial acetic acid (10 mL). The mixture was stirred at 118 °C for 24 h. After cooling to room temperature, the reaction was diluted with chloroform and repeatedly washed with a $NaHCO_3$ saturated solution until no CO_2 generation is observed. Organic extracts were dried over anhydrous Na_2SO_4, filtered, and dried. Purification was carried out by flash chromatography (silica gel, hexane/DCM 1:2) to give a dark purple solid (40.0 mg, 30%).

^{1}H NMR (400 MHz, $CDCl_3$) δ: 9.31 (d, *J* = 8.4 Hz, 1H), 7.88–7.79 (m, 3H), 7.55 (dd, *J* = 8.2, 6.3 Hz, 4H), 7.52–7.48 (m, 2H), 7.13–7.05 (m, 20H), 4.10 (d, *J* = 7.5 Hz, 2H), 2.63–2.55 (m, 8H), 2.14–2.11 (m, 1H), 1.67–1.58 (m, 10H), 1.44–1.35 (m, 14H), 0.96 (t, *J* = 7.3 Hz, 12H), 0.92–0.89 (m, 6H) ppm.

^{13}C NMR (101 MHz, $CDCl_3$) δ: 191.8, 148.6, 148.4, 145.1, 145.0, 143.7, 143.1, 142.6, 141.6, 138.2, 138.1, 136.7, 134.7, 132.7, 132.3, 130.1, 129.3, 129.3, 127.6, 127.5, 124.9, 124.9, 122.2, 122.1, 48.8, 37.2, 35.1, 33.7, 29.7, 28.5, 24.0, 23.1, 22.4, 14.1, 14.0, 10.7 ppm.

HRMS (MALDI-TOF): *m/z* calculated for $C_{76}H_{83}N_3O_1S_2$: 1117.5972, found: 1117.5955

FTIR (neat): 2924, 2855, 2218, 1735, 1599, 1510, 1460, 1374, 1261, 1093, 1022, 801 cm^{-1}.

1.5.2.2. *2nd Generation D−A−D small molecules*

Bis(4-methoxyphenyl)amine (61).[73]

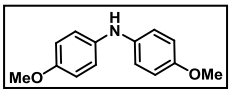

A solution of p-anisidine (**59**) (1.00 g, 8.12 mmol), 4-iodoanisole (**60**) (2.02 g, 8.54 mmol), $Pd_2(dba)_3$ (186 mg,

0.20 mmol) and XPhos (194 mg, 0.41 mmol) in dry toluene (20 mL) under nitrogen atmosphere was degassed for 30min. After addition of NaO^{t}Bu (2.20 g, 22.7 mmol) in one portion, the mixture was stirred at 110 °C for 3 h. Upon cooling to room temperature the mixture was diluted with $CHCl_3$ (50 mL) and washed with H_2O (3 × 40 mL). The organic layer was dried over anhydrous Na_2SO_4, filtered and dried by rotary evaporation. The resulting residue was purified by column chromatography (silica gel, hexane/DCM 1:2), providing a white solid (1.21 g, 65%).

^{1}H NMR (400 MHz, DMSO-d^6) δ: 7.50 (s, 1H), 6.91 (d, *J* = 8.9 Hz, 4H), 6.80 (d, *J* = 8.9 Hz, 4H), 3.68 (s, 6H) ppm.

4-methoxy-*N*-(4-methoxyphenyl)-*N*-phenylaniline (62).

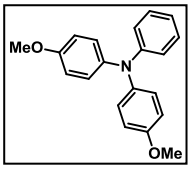

A solution of 4-iodoanisole (**60**) (5.27 g, 22.5 mmol), aniline (**49**) (0.98 mL, 10.7 mmol), $Pd_2(dba)_3$ (245 mg, 0.27 mmol) and XPhos (511 mg, 1.07mmol) in dry toluene (20 mL) under nitrogen atmosphere was degassed for 30 min. After addition of NaO^{t}Bu (3.01 g, 32.2 mmol) in one portion, the mixture was stirred at 110 °C for 18 h. Upon cooling to room temperature, the mixture was diluted with $CHCl_3$ (50 mL) and washed with H_2O (3 × 40 mL). The organic layer was dried over anhydrous Na_2SO_4, filtered and dried by rotary evaporation. The resulting residue was purified by column chromatography (silica gel, hexane/DCM 4:1), providing a white solid (2.61 g, 80%).

^{1}H NMR (400 MHz, $CDCl_3$) δ: 7.19–7.14 (m, 2H), 7.07–7.02 (m, 4H), 6.94 (dd, *J* = 8.6, 0.9 Hz, 2H), 6.86 (dd, *J* = 11.8, 4.5 Hz, 2H), 6.85–6.77 (m, 4H), 3.79 (s, 6H) ppm.

4-iodo-*N*,*N*-bis(4-methoxyphenyl)aniline (63).[75]

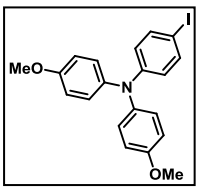

Into a 50mL round bottom flask containing EtOH (25 mL), **62** (1.09 g, 3.56 mmol), H_5IO_6 (162 mg, 0.71 mmol) and I_2 (362 mg, 1.43 mmol) were added under nitrogen atmosphere. After stirring at room temperature overnight, a saturated sodium bisulfite aqueous solution (20 mL) was added to the mixture and thereafter extracted with $CHCl_3$ (3 × 20 mL). The combined organic extracts were dried over anhydrous Na_2SO_4, filtered and evaporated by rotary evaporation. The resulting residue was purified by

column chromatography (silica gel, hexane/DCM 2:1) as a white solid (1.30 g, 85%).

^{1}H NMR (400 MHz, DMSO-d^6) δ: 7.78 (d, *J* = 8.9 Hz, 2H), 7.42–7.33 (m, 4H), 7.28–7.23 (m, 4H), 6.88 (d, *J* = 8.9 Hz, 2H), 4.08 (s, 6H) pp

4-methoxy-*N*-(4-methoxyphenyl)-*N*-(4-(4,4,5,5-tetramethyl-1,3,2-dioxaborolan-2-yl)phenyl)aniline (64).[76]

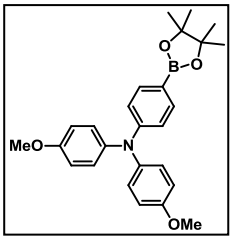

Into a 100mL 2-neck round bottom flask equipped with a condenser, **63** (980 mg, 2.22 mmol), bis(pinacolato)diboron (866 mg, 3.41 mmol) and $Pd_2(Cl_2(dppf)_2)\cdot CH_2Cl_2$ (185 mg, 0.22 mmol) were added and dissolved in dry DMF (20 mL) under nitrogen atmosphere, after degassing for 30 min, KOAc (668 mg, 6.81 mmol) was added in one portion and the reaction stirred at 90 °C for 18 h. After quenching with H_2O (30 mL) the reaction was extracted with CH_2Cl_2 (3 × 15 mL). Combined organic extracts were dried over anhydrous Na_2SO_4, filtered and evaporated under reduced pressure. Purification was carried out by column chromatography (silica gel, hexane/ethyl acetate 8:1) to give rise to a white solid (670 mg, 70%).

^{1}H NMR (400 MHz, DMSO-d^6) δ: 7.44 (d, *J* = 8.7 Hz, 2H), 7.08−7.02 (m, 4H), 6.94 (t, *J* = 6.2 Hz, 4H), 6.67 (d, *J* = 8.7 Hz, 2H), 3.74 (s, 6H), 1.25 (s, 12H) ppm.

4-methyl-*N*-(4-(4,4,5,5-tetramethyl-1,3,2-dioxaborolan-2-yl)phenyl)-*N*-(*p*-tolyl)aniline (66).[77]

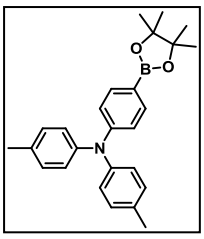

4-Bromo-*N*,*N*-di-*p*-tolylaniline (**65**) (813 mg, 2.30 mmol), bis(pinacolato)diboron (880 mg, 3.46 mmol) and $Pd_2(Cl_2(dppf)_2)\cdot CH_2Cl_2$ (187 mg, 0.23 mmol) were dissolved in dry DMF (20 mL) under nitrogen atmosphere. After purging with nitrogen for 30 min, KOAc (677 mg, 7.00 mmol) was added in one portion and the mixture was stirred at 90 °C for 18 h. After quenching with H_2O (30 mL) the reaction was extracted with DCM (3 × 15 mL). Combined organic extracts were dried over anhydrous Na_2SO_4, filtered and evaporated under reduced pressure. Purification was carried out by column chromatography (silica gel, hexane/DCM 1:1) to give rise to a colorless oil (800 mg, 87%).

^{1}H NMR ($CDCl_3$) δ: 7.60 (m, 2), 7.01 (m, 10H), 2.30 (s, 6H), 1.32 (s, 12H) ppm.

Compound 67.

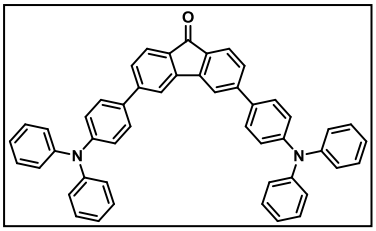

Into a 100 mL 2-neck round flask filled with dry DMF (20 mL) and nitrogen, **42** (300 mg, 0.88 mmol), (4-(diphenylamino)phenyl)boronic acid (540 mg, 1.86 mmol) and $Pd(PPh_3)_4$ (101 mg, 0.09 mmol) were added. The mixture was degassed for 30 minutes. Then, K_3PO_4 (3.00 g, 14.0 mmol) was added in one portion. The resulting mixture was stirred at 90 °C for 6 h. The mixture was cooled to room temperature and washed with H_2O (30 mL). After extraction with DCM (3× 15 mL), combined organic extracts were dried over anhydrous Na_2SO_4, filtered, and evaporated. The resulting crude was purified by flash chromatography (silica gel, hexane/DCM 1:4) yielding an orange solid (480 mg, 80%).

^{1}H NMR (400 MHz, THF- d^8) δ: 8.01 (s, 2H), 7.67–7.61 (m, 6H), 7.57 (dd, *J* = 7.8, 1.4 Hz, 2H), 7.29–7.23 (m, 8H), 7.16–7.09 (m, 12H), 7.05–7.00 (m, 4H) ppm.

^{13}C NMR (101 MHz, THF-d^8) δ: 192.4, 149.6, 148.7, 148.0, 146.1, 134.9, 134.3, 130.3, 128.9, 128.0, 126.1, 125.7, 125.1, 124.4, 119.6 ppm.

HRMS (MALDI-TOF): *m/z* calculated for $C_{49}H_{34}N_2O_1$: 666.2666, found: 666.2694.

Compound 68.

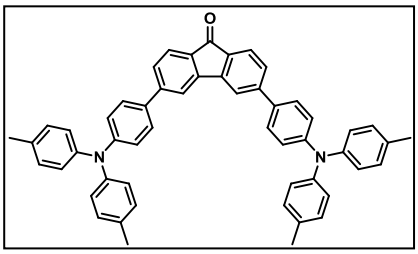

Into a 100mL 2-neck round flask filled with dry DMF (20 mL) and nitrogen, **42** (338 mg, 1.00 mmol), **66** (800 mg, 2.00 mmol) and $Pd(PPh_3)_4$ (115 mg, 0.10 mmol) were added. The mixture was degassed for 30 minutes. Then, a K_3PO_4 (3.00 g, 14.0 mmol) was added in one portion. The resulting mixture was stirred at 90 °C for 6 h. The mixture was cooled to room temperature and washed with H_2O (30 mL). After extraction

with DCM (3 × 15 mL), combined organic extracts were dried over anhydrous Na_2SO_4, filtered, and evaporated. The resulting crude was purified by flash chromatography (silica gel, hexane/DCM 1:8) yielding a light orange solid (615 mg, 85%).

^{1}H NMR (400 MHz, THF-d^8) δ: 8.01 (d, *J* = 2H, 1.2 Hz), 7.66–7.59 (m, 6H), 7.56 (dd, *J* = 7.8, 1.2 Hz, 2H), 7.29–7.05 (m, 12H), 7.04–6.97 (m, 8H), 2.30 (s, 12H) ppm.

^{13}C NMR (101 MHz, THF-d^8) δ: 192.4, 149.9, 148.1, 146.2, 146.1, 134.1, 134.0, 133.8, 130.9, 128.8, 127.8, 125.9, 125.0, 123.1, 119.4, 21.0 ppm.

HRMS (MALDI-TOF): *m/z* calculated for $C_{53}H_{42}N_2O_1$: 722.3292, found: 722.3289.

Compound 69.

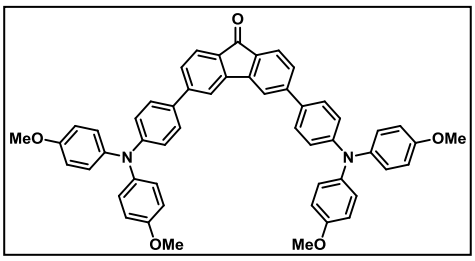

Into a 100mL 2-neck round flask filled with dry DMF (20 mL) and nitrogen, **42** (300 mg, 0.88 mmol), **64** (650 mg, 1.86 mmol) and $Pd(PPh_3)_4$ (101 mg, 0.09 mmol) (20 mL) were added. The mixture was degassed for 30 minutes. Then, K_3PO_4 (3.00 g, 14.0 mmol) was added in one portion. The resulting mixture was stirred at 90 °C for 6 h. The mixture was cooled to room temperature and washed with H_2O (30 mL). After extraction with DCM (3×15 mL), combined organic extracts were dried over anhydrous Na_2SO_4, filtered, and evaporated. The resulting crude was purified by flash chromatography (silica gel, hexane/DCM 1:8) yielding a red-orange solid (590 mg, 85%).

^{1}H NMR (400 MHz, $CDCl_3$) δ: 7.73 (s, 2H), 7.68 (d, *J* = 7.7 Hz, 2H), 7.46 (d, *J* = 7.3 Hz, 6H), 7.03–6.92 (m, 12H), 6.87 (d, *J* = 7.8 Hz, 8H), 3.82 (s, 12H) ppm.

^{13}C NMR (101 MHz, $CDCl_3$) δ: 193.0, 156.2, 149.2, 147.3, 144.9, 140.4, 132.9, 131.5, 127.7, 126.9, 126.8, 124.6, 120.1, 118.1, 114.8, 55.5 ppm.

HRMS (MALDI-TOF): *m/z* calculated for $C_{53}H_{42}N_2O_5$: 786.3088, found: 786.3089.

Compound 70.

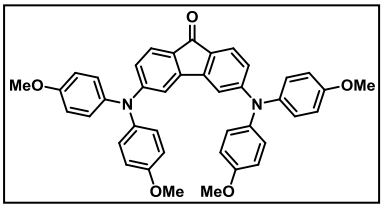

A solution of **42** (192 mg, 0.57 mmol), **61** (288 mg, 1.27 mmol), $Pd_2(dba)_3$ (21 mg, 0.02 mmol) and XPhos (33.0 mg, 0.06 mmol) in dry toluene (20 mL) was deaerated by bubbling nitrogen during 30min. Then NaO^tBu (165 mg, 1.72 mmol) was added in one portion and the resulting mixture was stirred at 110 °C for 18 h. Upon cooling to room temperature, the mixture was quenched with H_2O (20 mL) and extracted with $CHCl_3$ (3 × 15 mL). Combined organic extracts were dried over anhydrous Na_2SO_4, filtered, and evaporated. The product was purified by flash chromatography (silica gel, hexane/DCM 1:1) yielding a red-orange powder (272 mg, 75%).

^{1}H NMR (400 MHz, THF-d^8) δ: 7.29 (d, *J* = 8.2 Hz, 2H), 7.07–7.01 (m, 8H), 6.91 (d, *J* = 2.1 Hz, 2H), 6.88–6.83 (m, 8H), 6.59 (dd, *J* = 8.2, 2.0 Hz, 2H), 3.75 (s, 12H) ppm.

^{13}C NMR (101 MHz, THF-d^8) δ: 189.9, 158.2, 155.1, 146.2, 140.9, 128.3, 125.2, 120.6, 119.3, 115.8, 111.6, 55.8 ppm.

Compound 71.

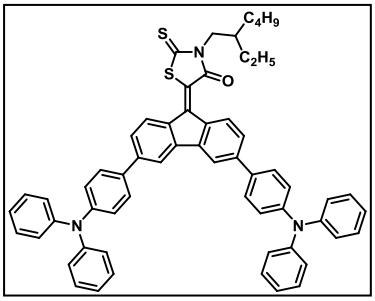

Compounds **67** (300 mg, 0.45 mmol), **38** (165 mg, 0.67 mmol) and *β*-alanine (80.0 mg, 0.90 mmol) were dissolved in a mixture of glacial acetic acid (10 mL) and toluene (10 mL) and stirred at 118 °C for 18 h. Upon cooling to room temperature, the mixture was diluted with water (100 mL) and extracted with $CHCl_3$ (3 × 15 mL), the organic extracts were washed with $NaHCO_3$ saturated solution until no gas development was observed, dried over anhydrous Na_2SO_4, filtered, and evaporated. The remaining residue was purified by flash chromatography (silica gel, hexane/DCM 1:4), giving a red-brown solid (141 mg, 35%).

^{1}H NMR (400 MHz, Acetone-d^6) δ: 9.18 (d, *J* = 8.4 Hz, 1H), 8.05 (d, *J* = 1.5 Hz, 1H), 8.03 (d, *J* = 1.3 Hz, 1H), 7.70–7.61 (m, 5H), 7.51 (d, *J* = 8.4, 1.5 Hz, 1H), 7.45 (dd, *J* = 8.5, 1.5 Hz, 1H), 7.37–7.28 (m, 8H), 7.15–7.04 (m, 16H),

4.00 (d, *J* = 7.4 Hz, 2H), 2.14–2.09 (m, 1H), 1.42–1.24 (m, 8H), 0.93 (t, *J* = 7.4 Hz, 3H), 0.88 (t, *J* = 6.9 Hz, 3H) ppm.

^{13}C NMR (101 MHz, THF-d^8) δ: 192.9, 167.9, 149.4, 149.3, 148.8, 148.7, 144.5, 144.3, 143.9, 141.4, 137.8, 135.9, 135.0, 134.6, 131.2, 130.3, 130.3, 128.9, 128.7, 127.1, 126.8, 125.7, 125.6, 124.5, 124.4, 124.3, 124.2, 123.6, 119.3, 118.7, 49.5, 38.4, 31.7, 29.6, 24.1, 14.6, 11.2 ppm.

HRMS (MALDI-TOF): *m/z* calculated for $C_{60}H_{51}N_3OS_2$: 893.3488, found: 893.3468.

FTIR (neat): 3035, 2957, 2926, 2857, 1701, 1591, 1530, 1514, 1492, 1444, 1392, 1329, 1313, 1280, 1196, 1179, 1135, 1075, 1027, 876, 822, 753, 696, 620 cm^{-1}.

Compound 72.

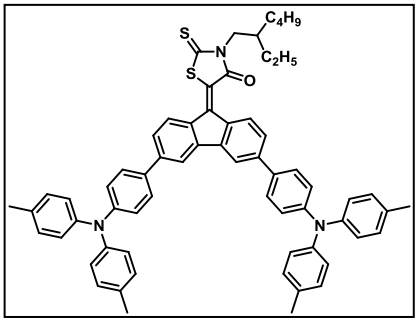

Compounds **68** (470 mg, 0.65 mmol), **38** (240 mg, 0.98 mmol), *β*-alanine (110 mg, 1.31 mmol) were dissolved in a mixture of glacial acetic acid (10 mL) and toluene (10 mL) and stirred at 118 °C for 18 h. Upon cooling to room temperature, the mixture was diluted with water (100 mL) and extracted with $CHCl_3$ (3 × 15 mL), the organic extracts were washed with $NaHCO_3$ saturated solution until no gas development was observed, dried over anhydrous Na_2SO_4, filtered, and evaporated. The remaining residue was purified by flash chromatography (silica gel, hexane/toluene 1:3), giving a dark brown solid (250 mg, 40%).

^{1}H NMR (400 MHz, THF-d^8) δ: 9.39 (d, *J* = 8.5 Hz, 1H), 8.10 (d, *J* = 1.6 Hz, 1H), 8.07 (d, *J* = 1.7 Hz, 1H), 7.90 (d, *J* = 8.3 Hz, 1H), 7.66–7.62 (m, 4H), 7.60 (dd, *J* = 8.3, 1.8 Hz, 1H), 7.54 (dd, *J* = 8.5, 1.9 Hz, 1H), 7.07 (dd, *J* = 12.0, 5.1 Hz, 12H), 7.03–6.99 (m, 8H), 4.11 (d, *J* = 7.3 Hz, 2H), 2.30 (s, 12H), 2.20–2.10 (m, 1H), 1.46–1.28 (m, 8H), 0.95 (t, *J* = 7.4 Hz, 3H), 0.91 (t, *J* = 7.1 Hz, 3H) ppm.

^{13}C NMR (101 MHz, THF-d^8) δ: 192.9, 167.8, 149.7, 149.6, 146.3, 146.2, 144.6, 144.4, 144.3, 143.9, 141.5, 137.6, 135.7, 134.0, 133.9, 133.8, 133.6,

130.9, 128.6, 128.5, 126.6, 125.9, 125.9, 123.3, 123.2, 119.1, 118.6, 49.5, 38.4, 31.7, 29.6, 24.1, 21.1, 14.6, 11.2 ppm.

HRMS (MALDI-TOF): *m/z* calculated for $C_{64}H_{59}N_3OS_2$:949.4094, found: 949.4078.

FTIR (neat): 3026, 2956, 2922, 2857, 1701, 1597, 1529, 1506, 1478.56, 1445, 1392, 1320, 1292, 1277, 1195, 1134, 1074, 1020, 876, 814, 766, 737 cm^{-1}.

Compound 73.

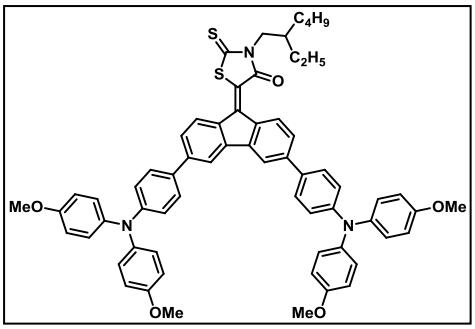

Compounds **69** (410 mg, 0.52 mmol), **38** (190 mg, 0.78 mmol), *β*-alanine (93.0 mg, 1.04 mmol) were dissolved in a mixture of glacial acetic acid (10 mL) and toluene (10 mL) and stirred at 118 °C for 18 h. Upon cooling to room temperature, the mixture was diluted with water (100 mL) and extracted with $CHCl_3$ (3 × 15 mL), the organic extracts were washed with $NaHCO_3$ saturated solution until no gas development was observed, dried over anhydrous Na_2SO_4, filtered, and evaporated. The remaining residue was purified by flash chromatography (silica gel, hexane/DCM 1:4), giving a dark brown solid (100 mg, 20%).

^{1}H NMR (400 MHz, Acetone-d^6) δ: 9.01 (d, *J* = 8.4 Hz, 1H), 7.76 (d, *J* = 1.2 Hz, 1H), 7.74 (d, *J* = 1.4 Hz, 1H), 7.50–7.41 (m, 4H), 7.39 (d, *J* = 8.3 Hz, 1H), 7.28 (dd, *J* = 8.3, 1.6 Hz, 1H), 7.24 (dd, *J* = 8.5, 1.7 Hz, 1H), 7.06–7.01 (m, 8H), 6.94–6.88 (m, 8H), 6.85 (t, *J* = 8.6 Hz, 4H), 3.89 (d, *J* = 7.5 Hz, 2H), 3.79 (s, *J* = 1.3 Hz, 12H), 2.09–2.07 (m, 1H), 1.38–1.26 (m, 8H), 0.90 (t, *J* = 7.3 Hz, 3H), 0.86 (t, *J* = 6.9 Hz, 3H) ppm.

^{13}C NMR (101 MHz, Acetone-d^6) δ: 192.5, 167.0, 157.4, 157.4, 149.8, 149.7, 143.8, 143.7, 143.5, 143.4, 141.6, 141.2, 141.1, 136.8, 134.9, 132.0, 131.5, 130.8, 128.4, 128.3, 127.9, 127.9, 126.2, 125.8, 121.9, 120.3, 120.2, 118.4, 117.9, 115.7, 55.8, 49.3, 38.0, 31.4, 24.8, 23.8, 14.4, 11.1 ppm.

HRMS (MALDI-TOF): *m/z* calculated for $C_{64}H_{59}N_3O_5S_2$: 1013.3903, found: 1013.3891

FTIR (neat): 3037, 2996, 2953, 2928, 2855, 2833, 1670, 1597, 1505, 1479, 1463, 1443, 1392, 1318, 1281, 1240, 1195, 1134, 1106, 1074, 1035, 976, 876, 824, 781, 766, 728, 597, 578 cm^{-1}.

Compound 74.

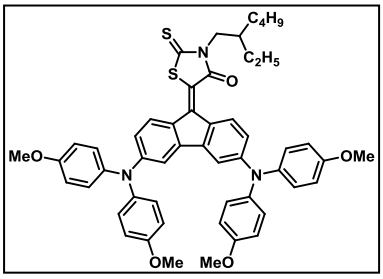

Compounds **70** (272 mg, 0.43 mmol), **38** (105 mg, 0.42 mmol), *β*-alanine (38.0 mg, 0.42 mmol) were dissolved in a mixture of glacial acetic acid (10 mL) and toluene (10mL) and stirred at 118 °C for 18 h. Upon cooling to room temperature, the mixture was diluted with water (100 mL) and extracted with $CHCl_3$ (3 ×15 mL), the organic extracts were washed with $NaHCO_3$ saturated solution until no gas development was observed, dried over anhydrous Na_2SO_4, filtered, and evaporated. The remaining residue was purified by flash chromatography (silica gel, hexane/ethyl acetate 4:1), giving a dark brown solid (90 mg, 24%).

^{1}H NMR (400 MHz, Acetone-d^6) δ: 9.11 (d, *J* = 8.9 Hz, 1H), 7.60 (d, *J* = 8.8 Hz, 1H), 7.14–7.08 (m, 8H), 6.94–6.90 (m, 9H), 6.88 (d, *J* = 2.4 Hz, 1H), 6.66 (dd, *J* = 8.8, 2.4 Hz, 1H), 6.59 (dd, *J* = 8.9, 2.4 Hz, 1H), 4.05 (d, *J* = 7.4 Hz, 2H), 3.81 (s, 12H), 2.16–2.07 (m, 1H), 1.41–1.30 (m, 8H), 0.92 (t, *J* = 7.4 Hz, 3H), 0.87 (t, *J* = 7.1 Hz, 3H) ppm.

^{13}C NMR (101 MHz, Acetone-d^6) δ: 192.6, 167.3, 158.2, 158.1, 152.7, 152.5, 144.5, 144.3, 142.6, 140.3, 140.1, 131.8, 130.3, 129.2, 128.9, 128.7, 128.6, 117.8, 117.7, 115.8, 115.8, 110.4, 110.1, 55.8, 49.1, 37.9, 31.4, 24.8, 23.7, 14.3, 11.0 ppm.

HRMS (MALDI-TOF): *m/z* calculated for $C_{52}H_{51}N_3O_5S_2$: 861.3265, found: 861.3264.

FTIR (neat): 2955, 2929, 2856, 2834, 1691, 1599, 1559, 1504, 1484, 1453, 1393, 1354, 1330, 1275, 1241, 1184, 1130, 1070, 1035, 828 cm^{-1}.

Chapter 2.

Small molecules as hole transporting materials for perovskite SCs.

2.1. Background

2.1. BACKGROUND

As stated in the introduction, the past six years have witnessed the unprecedented rapid emergence of a brand new class of solar cells based on mixed organic–inorganic halide perovskites.

Originally discovered by Gustav Rose in 1839 and named after the Russian mineralogist Lev Perovski, naturally occurring perovskite mineral consists in $CaTiO_3$. Perovskite also lends its name to the crystal family sharing its same crystallographic structure.

2.1.1. Structure

Perovskites are materials described by the formula ABX_3, where X is the anion bonding cations A and B (A being larger than B). Ordered in an ideal cubic-symmetry structure where cation B occupies the center of an octahedron defined by X and A fitting within the resulting cuboctahedron (see Figure 45); occupying lattice parameters (0,0,0) for A, (1/2,1/2,1/2) for B and (1/2,1/2,0) for X of the idealized cubic cell, the structure stability is very sensitive to relative ion size variations. Thus subtle ion size variations result in lattice distortion to lower symmetry arrangements (typically orthorhombic or tetragonal).

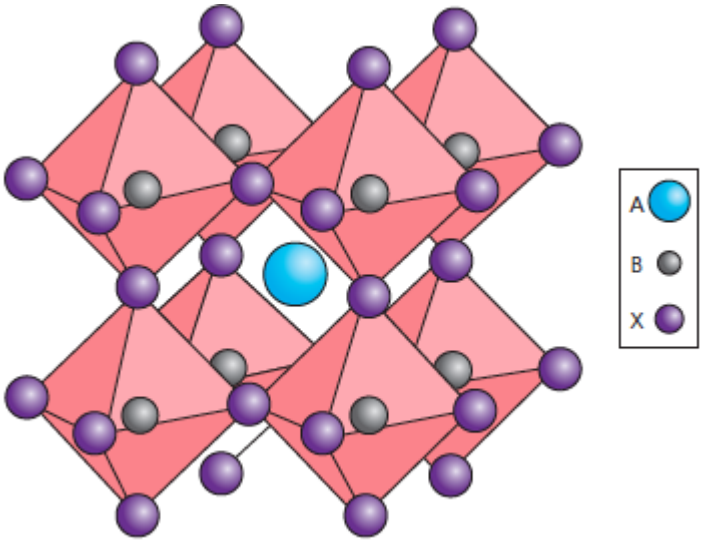

Figure 45. General crystal structure of perovskites.

Perovskites used as absorbers for solar cells typically make use of an organic cation as A component, either methylammonium (MA) ($CH_3NH_3^+$) [82,83] or formamidine (FA) ($HC(NH_2)_2^+$);[84,85] as for B, it is a divalent metal cation usually Pb^{2+} and more seldom Sn^{2+}; finally, X consist of an halide (I^-, Br^-, Cl^-).[86]

2.1.2. Brief history of perovskites

Early interest on this type of materials was focused on their photo-ionic conductivity and semiconducting properties applied to organic-light-emitting diodes (OLED) and thin film transistors (TFT).[87,88] However, it was not until 2009 when organometal halide perovskites ($CH_3NH_3PbX_3$; X: I, Br) were first employed as visible-light sensitizers in a typical liquid-electrolyte-based DSSC photovoltaic cell.[89] The PCE of the obtained devices was less than 4% and their stability in liquid electrolyte configuration was poor. Subsequently, in 2011, Park *et al.* used $CH_3NH_3PbI_3$ nanocrystals sized *ca.* 2–3 nm in a DSSC cell using iodide redox shuttle, which resulted in a 6.54% PCE under 1 sun illumination.[90]

---

[82] H.-S. Kim, C.-R. Lee, J.-H. Im, K.-B. Lee, T. Moehl, A. Marchioro, S.-J. Moon, R. Humphry-Baker, J.-H. Yum, J. E. Moser, M. Grätzel, N.-G. Park, *Sci. Rep*. **2012**, *2*, 591.

[83] M. M. Lee, J. Teuscher, T. Miyasaka, T. N. Murakami, H. J. Snaith, *Science* **2012**, *338*, 643.

[84] G. E. Eperon, S. D. Stranks, C. Menelaou, M. B. Johnston, L. M. Herz, H. J. Snaith, *Energy Environ. Sci*. **2014**, *7*, 982−988.

[85] J.-W. Lee, D.-J. Seol, A.-N. Cho , N.-G. Park , *Adv. Mater*. **2014**, *26*, 4991−4998.

[86] F. Hao, C. C. Stoumpos, D. H. Cao, R. P. H. Chang, M. G. Kanatzidis, *Nat. Photonics* **2014**, *8*, 489−494.

[87] C. R. Kagan, D. B. Mitzi, C. D. Dimitrakopoulos, *Science* **1999**, *286*, 945−947.

[88] T. Hattori, T. Taira, M. Era, T. Tsuitsui, S. Saito, *Chem. Phys. Lett*. **1996**, *254*, 103−108.

[89] A. Kojima, K. Teshima, Y. Shirai, T. Miyasaka, *J. Am. Chem. Soc*. **2009**, *131*, 6050−6051.

[90] J. H. Im, C. R. Lee, J. W. Lee, S. W. Park and N. G. Park, *Nanoscale* **2011**, *3*, 4088−4093.

The next breakthrough was achieved in 2012 by Grätzel and co-workers with the replacement of the liquid electrolyte by a solid-state hole transport material. The combination of $MAPbI_3$ with the solid hole conductor 2,2',7,7',-tetrakis-(N,N-dimethoxyphenyl-amine)-9,9'-spirobifluorene (spiro-OMeTAD) on mesoporous TiO_2 (m-TiO_2) [91] favored a dramatic enhancement of the efficiency, obtaining a PCE of 9.7% (see Figure 46).[92]

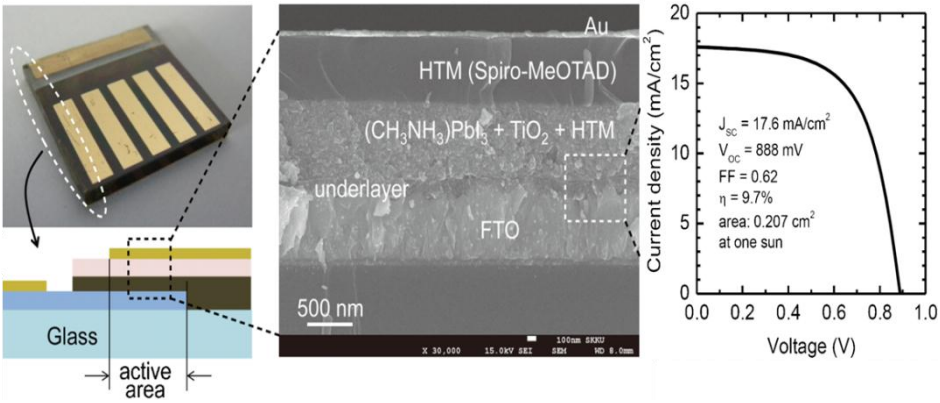

Figure 46. Real solid-state device (top left). Graphic depiction of the device architecture (bottom left). Cross-sectional structure of the device (middle). *J*/*V* curve (right) with photovoltaic parameters (inset).

Shortly after, H. Snaith in collaboration with T. Miyasaka achieved a major milestone when they demonstrated that in "meso-supersutructured" solar cells the n-type mesoporous oxide could be replaced by an inert framework such as Al_2O_3 onto which mixed-halide perovskite ($CH_3NH_3PbI_2Cl_2$) and (spiro-OMeTAD) were coated.[93] The use of Al_2O_3 generates increased V_{oc} with a value of 1.13 V and a PCE of 10.9%. Furthermore, perovskite material is relatively versatile and its electronic properties can be widely tuned by cationic or anionic substitution. As an example, Snaith and coworkers investigated the

[91] U. Bach, D. Lupo, P. Comte, J. E. Moser, F. Weissortel, J. Salbeck, H. Spreitzer, M. Grätzel, *Nature* **1998**, *395*, 583−585.

[92] H. S. Kim, C. R. Lee, J. H. Im, K. B. Lee, T. Moehl, A. Marchioro, S. J. Moon, R. Humphry-Baker, J. H. Yum, J. E. Moser, M. Grätzel, N. G. Park, *Sci. Rep*. **2012**, *2*, 591.

[93] M. M. Lee, J. Teuscher, T. Miyasaka, T. N. Murakami, H. J. Snaith, *Science* **2012**, *338*, 643−647.

effect of changing the size of the A cation in the organolead trihalide perovskite structure, and found out that they were able to tune the bandgap in this manner. They showed that replacing methylammonium by formamidinium narrowed the bandgap (see Figure 47).[94]

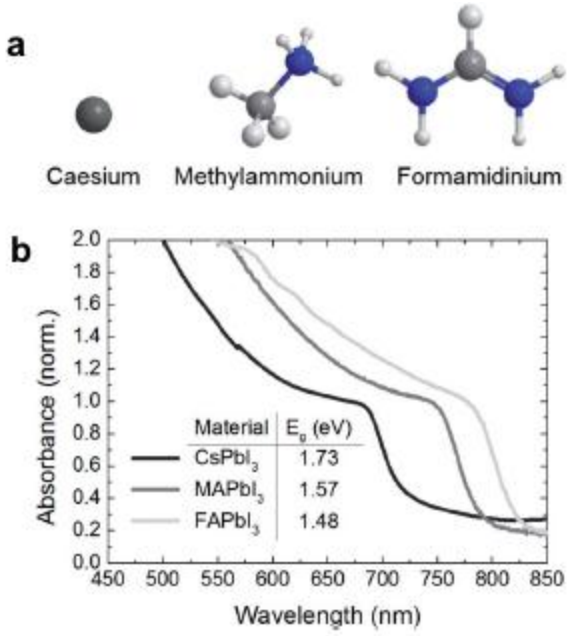

Figure 47. Tuning perovskite bandgap by replacing the A cation. a) The atomic structure of the three A site cations explored. b) UV Vis spectra for the $APbI_3$ perovskites formed, where A is either caesium (Cs), methylammonium (MA) or formamidinium (FA).

Manipulation of the ABX_3 structure by substitution of the B metal cation (Pb>Sn) shows how the band gap may be narrowed (see Figure 48). The increase of the covalent character of the B–X bond is evidenced when shifting from Pb^{2+} to Sn^{2+} by a substantial band gap narrowing. The most dramatic

[94] G. E. Eperon, S. D. Stranks, C. Menelaou, M. B. Johnston, L. M. Herz, H. J. Snaith, *Energy Environ. Sci*. **2014**, *7*, 982−988.

effect is observed for $MASnI_3$ offering a band gap of 1.20 eV, whereas $MAPbI_3$ and $FAPbI_3$ show 1.52 and 1.48 eV respectively.[95]

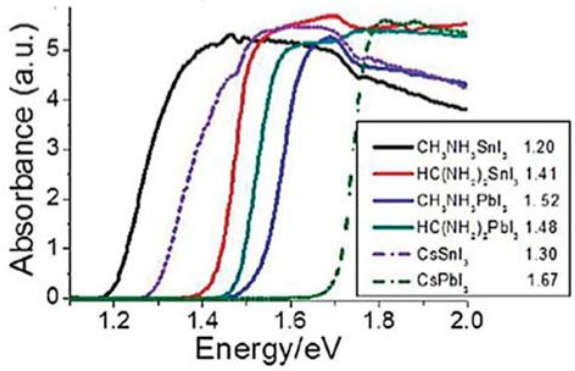

Figure 48. Tuning perovskite bandgap by replacing the M cation (Sn^{2+}, Pb^{2+}).

Further band gap manipulation can be achieved by substitution of the halide anion. The lattice changes induced by increasing size halides (Cl<Br<I) result in a spectral shift towards longer wavelengths.[96] This effect can be appreciated in the work by Seok et al. where they synthesized perovskites with varying proportion of bromide. $MAPb(I_{1-x}Br_x)_3$ perovskites are an excellent example of band gap engineering (Figure 49).[97]

[95] C. C. Stoumpos, C. D. Malliakas, M. G. Kanatzidis, *Inorg. Chem*. **2013**, *52*, 9019−9038.

[96] a) J. Calabrese, N. L. Jones, R. L. Harlow, N. Herron, D. L. Thorn, Y. Wang, *J. Am. Chem. Soc.*, **1991**, *113*, 2328−2330; b) A. Kojima, K. Teshima, Y. Shirai, T. Miyasaka**,** *J. Am. Chem. Soc.* **2009**, *131*, 6050−6051.

[97] J. H. Noh, S. H. Im, J. H. Heo, T. N. Mandal, S. I. Seok, *Nano Lett*. **2013**, *13*, 1764−1769.

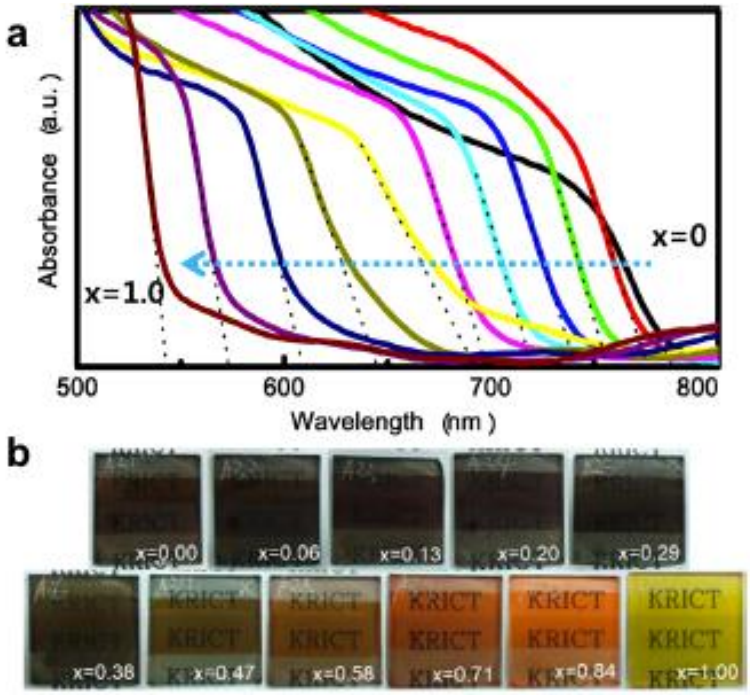

Figure 49. a) UV-vis absorption spectra of FTO/c-TiO2/m-TiO2/MAPb($I_{1-x}Br_x$)$_3$/Au cells measured using an integral sphere. b) Photographs of 3D TiO2/MAPb($I_{1-x}Br_x$)$_3$ bilayer nanocomposites on FTO glass substrates.

Another example by Seok's group of compositional engineering of the perovskite was achieved by incorporation of $MAPbBr_3$ into $FAPbI_3$. Relatively unstable formamidinium idodide perovskite stabilizes with the addition of a $MAPbBr_3$ phase. Optimum composition was observed for $(FAPbI3)_{0.85}(MAPbBr_3)_{0.15}$ with an average PCE of 18% under a standard illumination of 100 mW/cm^2.[98]

2.1.3. Charge transporting layers

An unavoidable requisite of perovskite SCs to yield high photovoltaic performances is the presence of charge transport interlayers. As above mentioned in this section, early perovskite devices bearing no charge transport

[98] N. J. Jeon, J. H. Noh, W. S. Yang, Y. C. Kim, S. Ryu, J. Seo, S. I. Seok, *Nature* **2015**, *517*, 476−480.

layer exhibited low photovoltaic response.[99] It was not until Snaith introduced a HTM based on spiro-OMeTAD, when this sort of SC demonstrated their potential.[100] The ambipolar behavior of perovskites allows their use in either n–i–p (regular) or p–i–n (inverted) configurations (Figure 50), depending on the position of the electron transporting (ETMs) or hole transporting (HTMs) materials in front of incident light. These interface layers are essential for transporting and blocking the charges.

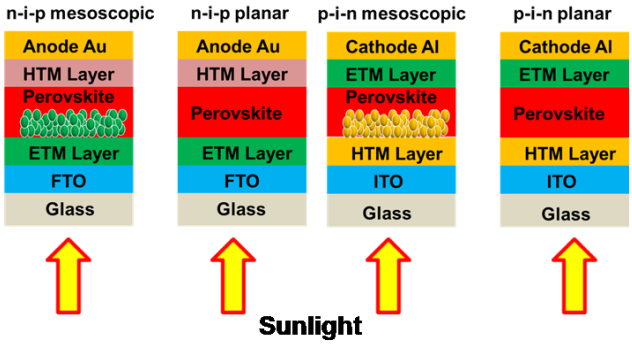

Figure 50. Different architectures of perovskite solar cells.

2.1.4. Perovskite solar cell functioning mechanism

As shown in Figure 51, the working principle of a perovskite solar cell involves: 1) electron and hole generation upon irradiation in the perovskite layer, 2) transfer of the excited electrons and holes into the conduction band and valence band of the semi-conductor, 3) transfer of holes and electrons on the perovskite into HTM and ETM layers, respectively, and 4) injection of holes and electrons into metal electrode and ITO/FTO, respectively.

[99] L. Etgar, P. Gao, Z. Xue, Q. Peng, A. K. Chandiran, B. Liu, M. K. Nazeeruddin, M. Gratzel, *J. Am. Chem. Soc*. **2012**, *134*, 17396−17399.

[100] A. Abrusci, S. D. Stranks, P. Docampo, H.-L. Yip, A. K.-Y. Jen, H. J. Snaith, *Nano Lett.* **2013**, *13*, 3124–3128.

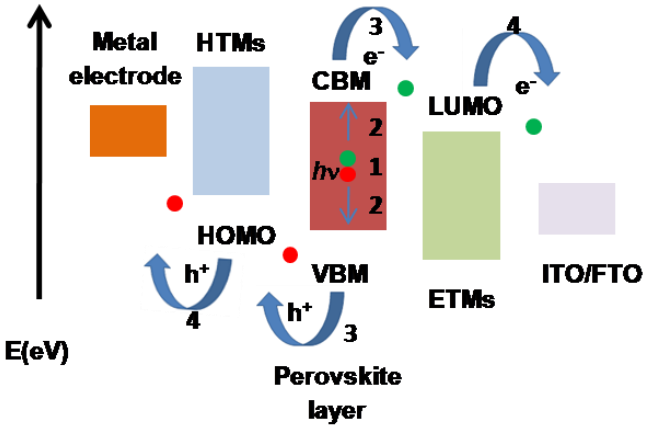

Figure 51. Mechanism of a typical perovskite solar cell.

2.1.5. A brief survey of HTMs

A broad variety of HTMs have been synthesized and investigated in recent years. The main requisite for a functional HTM is to electronically match the HOMO level of the perovskite; in addition, the material should be easy to process and provide well-ordered structures that, in turn, enable an efficient charge transport. In this sense, employed materials range from semiconducting polymers to small molecules. Other desirable properties are to exhibit excellent thermal and photochemical stability. In a perovskite SC all the PV process is carried out by the active layer (*i.e.* the perovskite), having itself excellent visible light absorption properties. However, it is not necessary for the HTM to complement the absorption as some authors earlier suggested.[101] So far, it can be deduced that arylamines are present in almost every HTM reported to date. This extensive use it is only explained by their nearly perfect electronic matching with the perovskite active layer.[102]

Since their early development stage, the addition of dopants has demonstrated to be beneficial for the HTM performance. These dopants (typically consisting in bis(trifluoromethane)sulfonimide lithium salt, tertbutylpyridine, cobalt(III)

[101] S. S. Reddy, K. Gunasekar, J. H. Heo, S. H. Im, C. S. Kim, D.-H. Kim, J. H. Moon, J. Y. Lee, M. Song, S.-H. Jin, *Adv. Energy Mater*. **2016**, *28*, 686−693.

[102] J. Wang, K. Liu, L. Ma, X. Zhan, *Chem. Rev.* **2016**, *116*, 14675−14725.

complexes such as FK209) play the role of partially oxidizing the HTM.[103] Despite being widely used, their use tends to accelerate the cell degradation. For this reason, much effort has been directed to develop dopant-free HTMs.[104]

Spiro-based small molecules. Along the last 4 years a large number of HTMs have been tested in PSC. Among all, spiro-OMeTAD (2,2',7,7'-tetrakis(*N*,*N*-di-*p*-

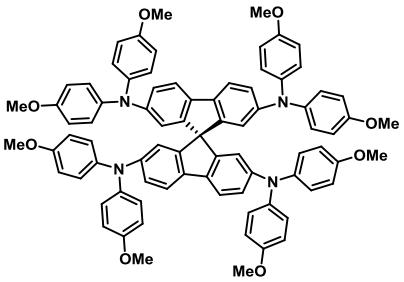

Figure 52. Chemical structure of Spiro-OMeTAD.

methoxyphenylamine)-9,9'-spirobifluorene) (see Figure 52) is by far the most employed one, due, not only to its outstanding performance, but also to its processability and durability. This is the reason because many efforts have been directed into the development of analogues that explore different substitution patterning or structural changes.

Seok *et al.* have studied the influence of the methoxy group position in a series of spirobifluorene compounds.[105] As shown in Figure 53, three compounds were synthesized, varying the position of one of the methoxy substituents from *ortho* (**75**), to *para* (**76**), to *meta* (**77**); while the other one kept its *para* substitution. *Ortho* substituted derivative **75** demonstrated to clearly outperform the other two analogues with a 16.7% PCE, while **76** and **77** yielded 14.9 and 13.9% respectively.

[103] H. Zhou, Q. Chen, G. Li, S. Luo, T.-b. Song, H.-S. Duan, Z. Hong, J. You, Y. Liu, Y. Yang, *Science* **2014**, *345*, 542−546.

[104] C. Huang, W. Fu, C.-Z. Li, Z. Zhang, W. Qiu, M. Shi, P. Heremans, A. K.-Y. Jen, H. Chen, *J. Am. Chem. Soc*. **2016**, *138*, 2528−2531.

[105] N. J. Jeon, H. G. Lee, Y. C. Kim, J. Seo, J. H. Noh, J. Lee, S. I. Seok, *J. Am. Chem. Soc*. **2014**, *136*, 7837−7840.

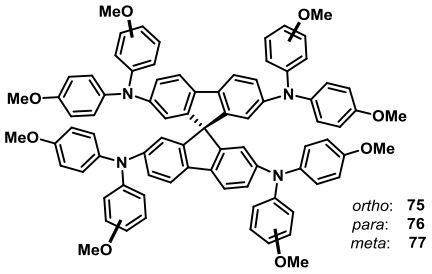

Figure 53. Chemical structures of compounds **75**-**77**.

Recently, a new series of spirobifluorenes have been synthesized by Wei Huang and coworkers.[106] In this work, the authors explored replacing the heteroatom of the –OMe substituent by S (**78**), N (**79**), and C (**80**) (Figure 54).

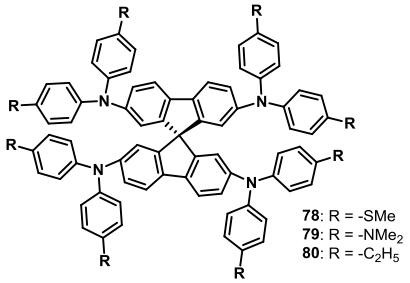

Figure 54. Chemical structures of compounds **78**-**80**.

Compared with spiro-OMeTAD, molecules making use of S and C (**78** and **80**, respectively) showed better match the perovskite HOMO level, therefore providing enhanced PCEs of 15.9 and 15.7%, respectively (where spiro-OMeTAD gave 11.5%).

[106] Z. Hu, W. Fu, L. Yan, J. Miao, H. Yu, Y. He, O. Goto, H. Meng, H. Chen, W. Huang, *Chem. Sci*. **2016**, *7*, 5007−5012.

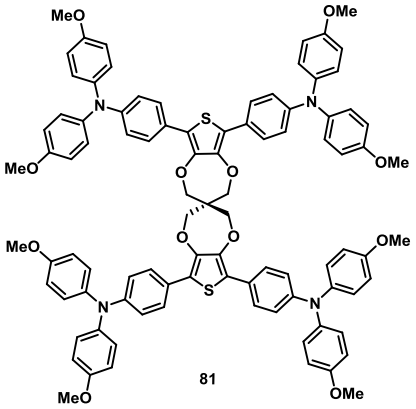

Figure 55. Chemical structure of compound **81**.

In the search for materials inspired on spiro-OMeTAD, Nazeeruddin and coworkers designed a new spiro-like derivative (**81**) based on 3,4-propylenedioxythiophene moieties that also carry *p*-methoxy-substituted triarylamine groups (Figure 55). The new material showed to work better than the standard spiro-OMeTAD (13.44 *vs.* 12.2% PCE). More interestingly, **81** devices fabricated using no FK209 dopant performed almost as efficiently (12.7% PCE) as the doped one (whereas spiro-OMeTAD dramatically dropped to 9.60%).[107]

Following with the idea of developing this type of HTMs, Grätzel *et al*. substituted the spiro-bifluorene scaffold by the sulfur containing cyclopentadithiophene one in compound **82** (see Figure 56). Here again, this material showed a better performance than spiro-OMeTAD when used without any dopant (13.4% *vs.* 7.20% PCE). It is noteworthy that when dopants are used (TBP/Li/FK209), the efficiency of **82** dropped to 6.00% while spiro-OMeTAD was 15.0%.[108]

[107] P. Ganesan, K. Fu, P. Gao, I. Raabe, K. Schenk, R. Scopelliti, J. Luo, L. H. Wong, M. Grätzel, M. K. Nazeeruddin, *Energy Environ. Sci*. **2015**, *8*, 1986−1991.

[108] M. Franckevicius, A. Mishra, F. Kreuzer, J. Luo, S. M. Zakeeruddin, M. Grätzel, *Mater. Horiz.* **2015**, *2*, 613−618.

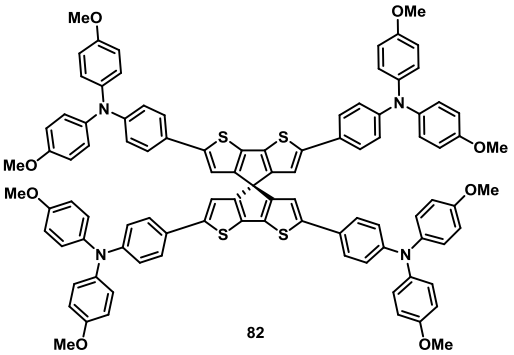

Figure 56. Chemical structure of compound **82**.

The search for alternative HTMs not only explored symmetric spiro-like molecules. Asymmetric spiro structures have also demonstrated their ability to efficiently operate as HTMs. Hagfeldt and coworkers reported a spiro fluorene/xanthene molecule (**83**, Figure 57) that reached an impressive PCE of 19.8% (20.8% obtained for spiro-OMeTAD), making use of additives.[109] Liao *et al.* synthesized another spiro compound inspired in a fluorene/acridine core (**84**, Figure 57); in this case **84** remarkably improved the performance both doped (16.7%) and undoped (12.4%), with respect of spiro-OMeTAD (14.8 and 5.90% for the doped and undoped devices respectively).[110] Recently, Nazeeruddin and coworkers presented a small molecule with a simple dissymmetric fluorene/cyclopentadithiophene core bearing methoxydiphenylamines as donor groups (**85**, Figure 57); compared with spiro-OMeTAD, **85** shows the distinctive advantage of being soluble in the more environmentally friendly toluene instead of chlorobenzene. Compound **85** was tested with mixed perovskites, yielding a PCE value of 20.2% (19.7% for spiro-OMeTAD), which makes it a potential replacement for spiro-OMeTAD.[111]

[109] D. Bi, B. Xu, P. Gao, L. Sun, M. Grätzel, A. Hagfeldt, *Nano Energy* **2016**, *23*, 138−144.

[110] Y.-K. Wang, Z.-C. Yuan, G.-Z. Shi, Y.-X. Li, Q. Li, F. Hui, B.-Q. Sun, Z.-Q. Jiang, L.-S. Liao, *Adv. Funct. Mater*. **2016**, *26*, 1375−1381.

[111] M. Saliba, S. Orlandi, T. Matsui, S. Aghazada, M. Cavazzini, J.-P. Correa-Baena, P. Gao, R. Scopelliti, E. Mosconi, K. H. Dahmen, F. De Angelis, A. Abate, A. Hagfeldt, G. Pozzi, M. Grätzel, M. K. Nazeeruddin, *Nature Energy* **2016**, *1*, 15017.

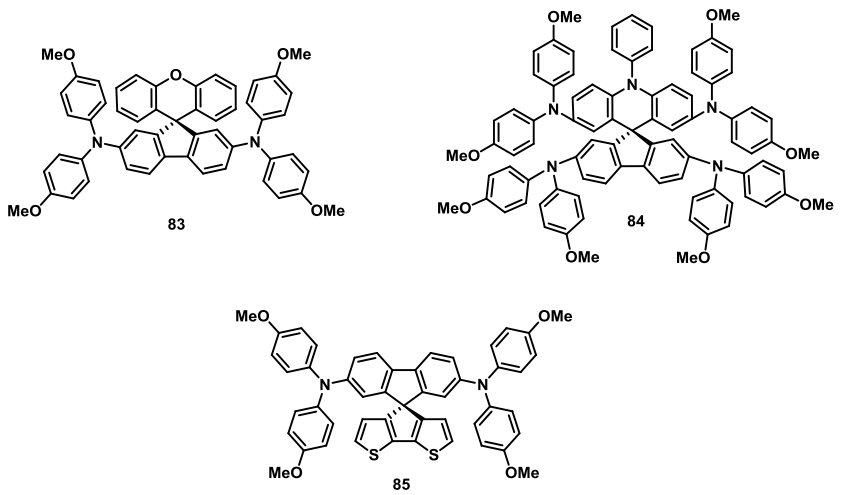

Figure 57. Chemical structures of compounds **83-85**.

Planar small molecules. Not only spiro-like structures have been tested as HTM. In order to promote the crystallinity of the hole transporting layer, many authors have employed highly planar cores. Triazatruxene based star-shaped molecules **86**–**89** were used with mixed $(FAPbI_3)_{0.85}$ $(MAPbBr_3)_{0.15}$ perovskite (Figure 58). While reference spiro-OMeTAD devices obtained 17.1% PCE, these triazatruxene derivatives showed 17.7, 8.9, 11.5, and 15.8%, respectively for **86**–**89**.[76]

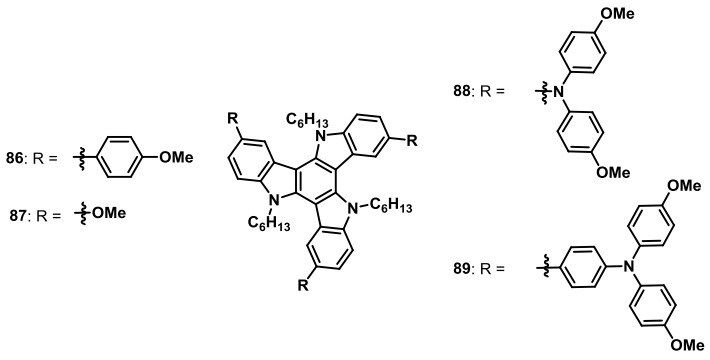

Figure 58. Chemical structures of compounds **86-89**.

Against this background, in collaboration with Prof. Nazeeruddin, our research group has developed several HTMs bearing planar central cores. The series of star-shaped benzotrithiophene-based HTMs depicted in Figure 59, showed remarkable high performances of 17 and 16% for **90** and **92**, respectively. As for the case of **91**, PCE values above 18% were observed, attributed to the high hole mobility exhibited by the compound and its excellent band alignment with the $MAPbI_3$ perovskite.[112]

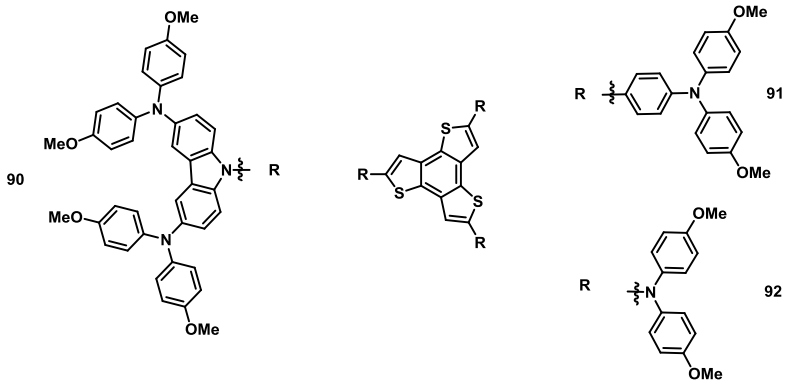

Figure 59. Chemical structures of compounds **90**-**92**.

Further extension of the central core aromatic surface was obtained with compounds **93**−**96**.[113] In this work, as depicted in Figure 60, the effect of attaching solubilizing alkyl side-chains of increasing length to the tetrathiophene fused anthracene core was studied. Despite the great solubility improvement observed when attaching long alkyl chains to the triarylamines, the device performance significantly decreased from 18.1% to 9.67% when moving from **93** to **96**. These results evidenced the strong impact that the lenght of the alkyl chains have on the efficiency of the perovskite SC.

[112] A. Molina-Ontoria, I. Zimmermann, I. Garcia-Benito, P. Gratia, C. Roldan-Carmona, S. Aghazada, M. Grätzel, M. K. Nazeeruddin, N. Martín, *Angew. Chem. Int. Ed*. **2016**, *55*, 6270−6274.

[113] I. Zimmermann, J. Urieta-Mora, P. Gratia, J. Aragó, G. Grancini, A. Molina-Ontoria, E. Ortí, N. Martín, M. K.Nazeeruddin, *Adv. Energy Mater*. **2016**, 1601674.

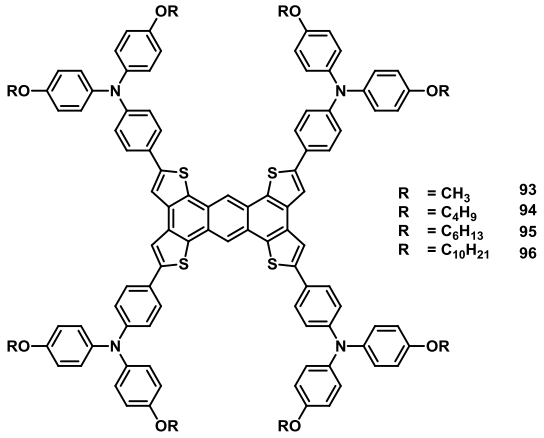

Figure 60. Chemical structures of compounds **93-96**.

2.2. Objectives

2.2. OBJECTIVES

As can be inferred from HTMs literature, most of the reported structures present a central core decorated with electron donating groups (*i.e.* triphenylamine, diphenylamine). The role of these arylamine groups is to provide HOMO levels of the appropriate energy to match perovskite's valence band, so that efficient charge extraction from the active layer may be achieved. With the aim of developing new HTMs with enhanced charge extraction properties, four different approaches have been observed within this Chapter.

For that purpose, we have split the Chapter in four parts. The first one is dedicated to HTMs similar to spiro-OMeTAD (reference one). The second one is dedicated to a planar central core based on dibenzothiophene (DBT) bearing diphenylamines, triphenylamines or phenothiazine. The third part is dedicated to a planar HTM based on anthradithiophene (ADT) and, finally, the last part is dedicated to BDT and the change of central ring by a pyrrole forming a DTP core, all of them decorated with four triphenylamine moieties.

2.2.1. Hemi-spiro HTMs

As spiro-OMeTAD represents the benchmark material as hole transporting layer, much attention has been drawn into preparing new analogues that reproduce its most structural motif: the spiranic carbon binding both fluorene moieties. Herein, the synthesis of three molecules (Figure 61) mimicking spiro-OMeTAD is proposed. The interest of the proposed structures is their synthetic ease when compared to spiro-OMeTAD as well as cost production.

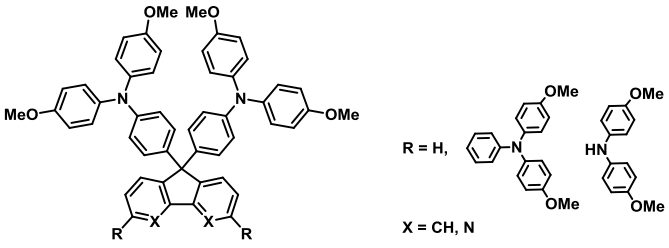

Figure 61. Series of hemi-spiro HTMs synthesized in this study.

2.2.2. HTMs with different electron donor strength based on dibenzothiophene

A series of small molecules based on planar dibenzothiophene as central core and incorporating different electron rich substituents are proposed (Figure 62). Employing electron donors of slightly different strengths allows fine tuning the HOMO energy of the HTM so that the right energy alignment with the perovskite may be achieved.

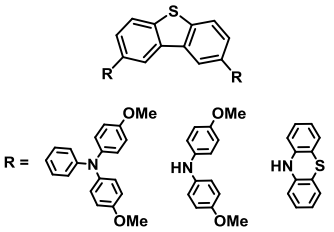

Figure 62. Series of HTMs based on dibenzothiophene.

2.2.3. HTMs with planar central cores based on anthradithiophene

In order to provide an efficient charge transport, it is of key importance having highly ordered transport layers. Central cores that make use of fused polyheterocycles have the potential to obtain this objective by inducing strong and effective intermolecular interactions. In this sense, anthra[1,9-*bc*:5,10-*b'c'*]dithiophene (ADT) was chosen to play this role. Our interest in this scaffold lied in the rarity of its use despite its synthetic readiness. This considered, two molecules bearing arylamines as electron-rich units were proposed (Figure 63).

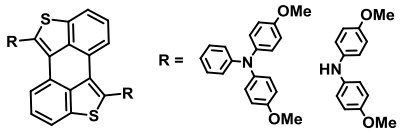

Figure 63. Series of HTMs based on anthradithiophene.

2.2.4. HTMs bearing four donor groups

The final approach considered within this Chapter was the use of central planar cores able to carry four arylamine units, thus increasing the density of donor

units per molecule. The flat central cores we have studied are BDT and DTP, both presenting different electron-donor strength (Figure 64).

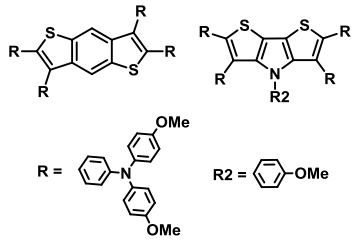

Figure 64. Series of HTMs bearing four donor groups.

2.3. Results and discussion

2.3. RESULTS AND DISCUSSION

2.3.1. Hemi-spiro HTMs

Given the excellent performance showed by spiro-OMeTAD molecule (in terms of efficiency, durability, and reproducibility), it is difficult to find new molecules that may outperform it. However, the need to employ dopants that partially oxidize spiro-OMeTAD to yield its optimum performance (which has a detrimental effect over the medium term stability of the devices), along with its elevated production cost, has encouraged the scientific community to search for more stable and cheaper analogues. In this sense, within this section, new analogues featuring *hemi-spiro* structure are presented. The synthesized molecules are so-called hemi-spiro due to the removal of one of the C-C bonds linking the two phenyl rings of one of the fluorene moieties.

Synthesis

Making use of fluorenone **42** as main scaffold, its condensation with triarylamine **62**, facilitated by Eaton's reagent (7.7 wt.% P_2O_5 in methanesulfonic acid), provided hemi-spiro dihalogenated derivative **97** (Scheme 14).

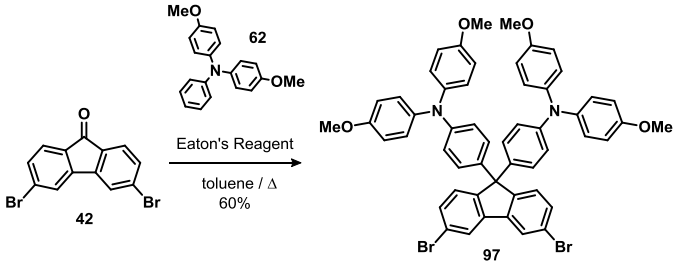

Scheme 14. Synthetic pathway for the preparation of hemi-spiro precursor **97**.

Dihalogenated derivative **97** served as precursor for target molecules **98** and **99** as shown in Scheme 15. Buchwald-Hartwig reaction with diphenylamine **61** gave rise to hemi-spiro compound **98**. On the other hand, double Suzuki-Miyaura coupling with **64** provided the other hemi-spiro derivative (**99**) that features four triphenylamine moieties.

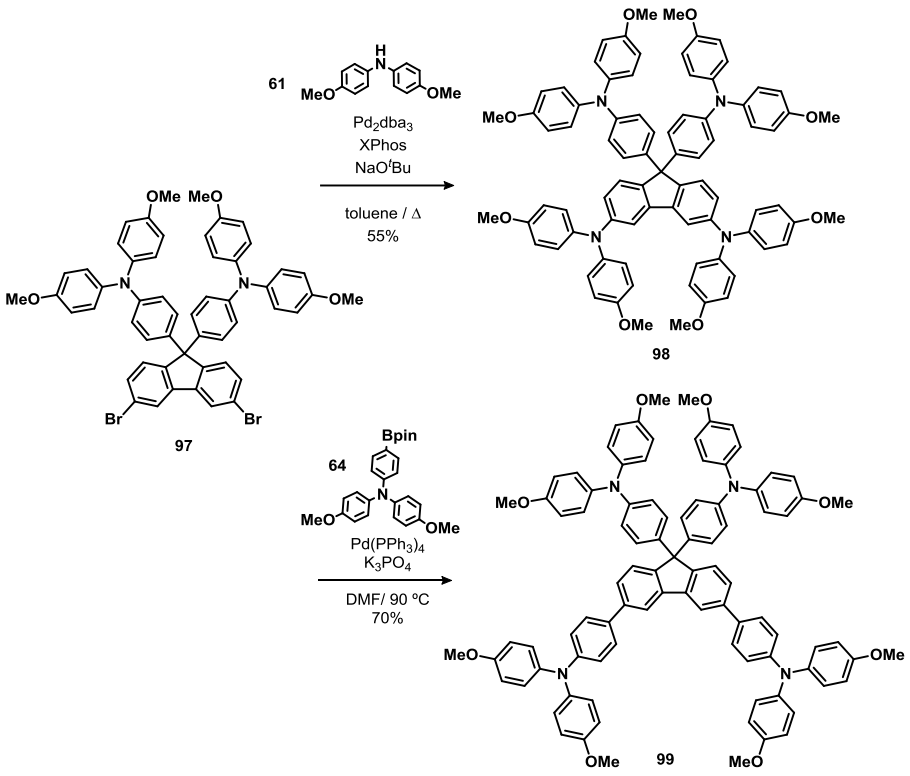

Scheme 15. Synthetic pathway for the preparation of target compounds **98** and **99**.

In addition to hemi-spiro fluorene based compounds, another product now based on the 4,5-diazafluorene scaffold was prepared (Scheme 16). Treatment of commercially available 4,5-diazafluorenone (**100**) with Eaton's reagent in the presence of triphenylamine **62** yielded hemi-spiro product **101**. In contrast to fluorene based products (**98** and **99**), the condensation step with electron poor 4,5-diazafluorenone was carried out in mild conditions (DCM reflux *vs.* toluene reflux), evidencing the detrimental effect the arylamine electron-donating groups exert over this nucleophilic attack reaction.

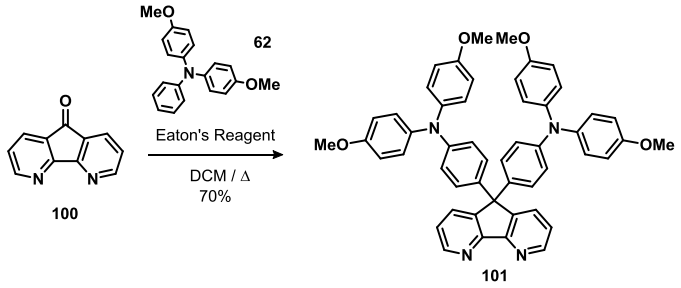

Scheme 16. Synthesis of target compound **101**.

All obtained compounds were characterized by the conventional spectroscopic techniques. The archetypical down-field (between 7.82−7.27 ppm) small doublet, double doublet, and doublet signal pattern denotes the 3,6-disubstituted fluorene core of **97** (Figure 65). The protons linked to fluorene's C4 and C5 atoms (highlighted with red dot) show up at 7.82 ppm as a small doublet, with a ^{4}J = 1.7 Hz coupling with the protons linked to C2 and C7 (marked with black dot). These two protons appear as a double doublet at 7.40 ppm with a ^{3}J coupling of 8.2 Hz with its C1-H and C8-H neighbors (denoted with purple dot).

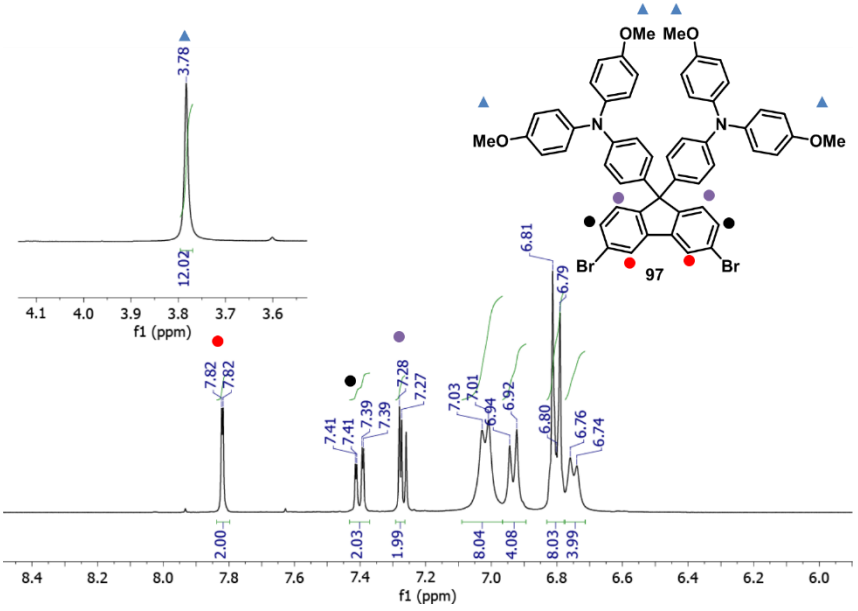

Figure 65. ^{1}H NMR (400 MHz, $CDCl_3$) spectrum of **97** centered on the aromatic region. Aliphatic region inset.

With the introduction of the diphenylamine groups, new signals arise in the aromatic region of the ^{1}H NMR spectrum of **98** (see Figure 66). This target compound exhibits a small doublet at 7.21 ppm (red dot) with a long distance ^{4}J coupling of 2.1 Hz with the protons linked to C2 and C7 (green dot). The doublet signal at 7.17 ppm corresponds to C1-H and C8-H protons (purple dot) and shows a ^{3}J = 8.3 Hz coupling with its neighbors marked in green (these protons' signal appears merged with the multiplet of the arylamine protons between 7.01 and 6.96 ppm). Moving to the aliphatic region, there are two singlet signals at 3.72 and 3.71 ppm that belong to the CH_3-O protons.

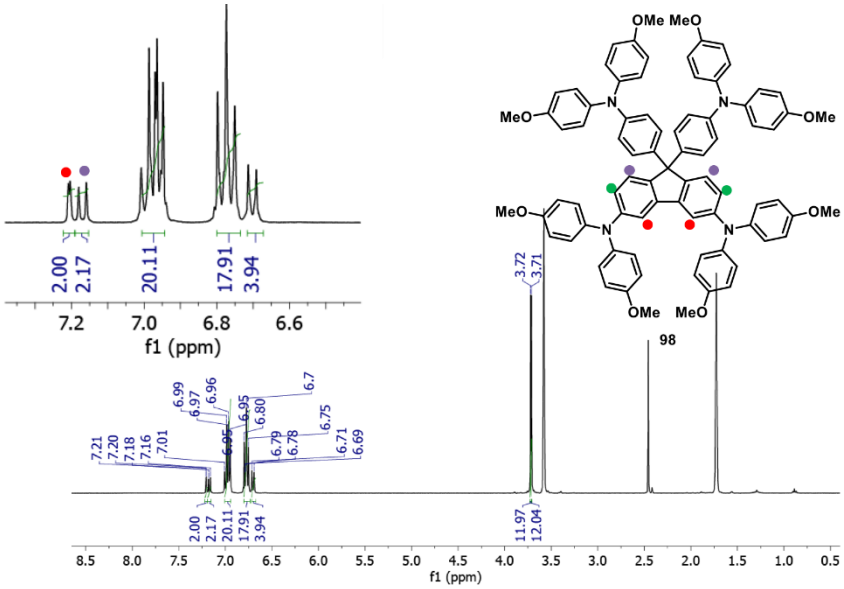

Figure 66. ^{1}H NMR (400 MHz, THF-d^{8}) spectrum of final product **98**, aromatic region inset.

Spectroscopic properties

Absorption spectra of final compounds **98**, **99** and **101** recorded in DCM solution are dominated by a band that maximizes *ca.* 308 nm (Figure 67). For **98** and **101** this band is well defined (**98** exhibiting a small high frequency vibronic shoulder) and ranges from 250 to 360 nm. On the other hand, the absorption band of **99** is broader (260−390 nm) and presents two well defined maxima at 307 and 343 nm. All of them exhibit high extinction coefficients that range from 7.9−11.4 10^{4} M^{-1} cm^{-1} (see Table 11). Both **98**

and **99** show similar emission features that mirror the lowest energy absorption band. The emission bands are broad (spanning 150 nm) and peak at 450 and 457 nm, for **98** and **99** respectively (Stokes shift of *ca.* 150 nm). Compound **101** presents a different emission behavior, with a very broad emission centered at 584 nm. The large Stokes shift involved (275 nm) might be indicative of complex excited states dynamics.

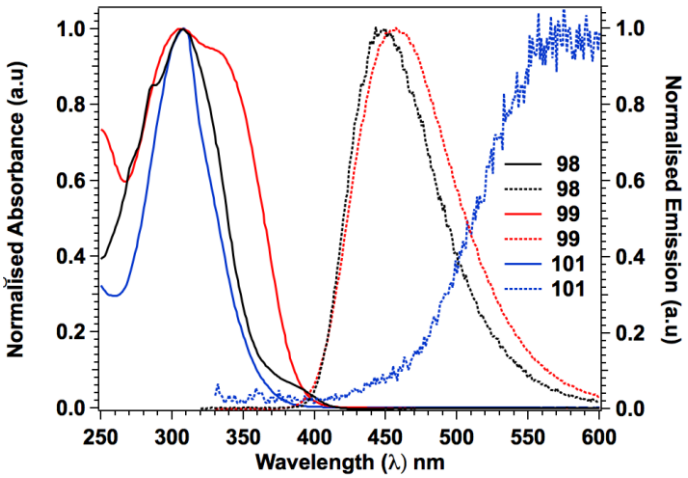

Figure 67. Normalized absorption (straight line) and emission (dotted line) of compounds **98**, **99** and **101** recorded in DCM solution.

Table 11. Summarized data of UV-vis spectra shown in Figure 67.

Compound	λ_{max}^{abs} [nm]	ε 10^4 [M^{-1} cm^{-1}]	λ_{max}^{ems} [nm]	$E_{0\text{-}0}$[a] [eV]
98	308	11.0	450	3.11
99	307	7.90	457	3.13
101	309	11.4	584	3.29

[a] $E_{0\text{-}0}$ = intersection point between absorption and emission spectra.

Electrochemical properties

The electrochemical behavior of target compounds **98**, **99** and **101** was measured by CV at a scan rate of 100 mV s^{-1}, using 0.1 M deaerated solutions in DCM that contained 0.1 M Bu_4NPF_6 as supporting electrolyte, as working

electrode glassy carbon was used, and platinum wires as a counter and reference electrodes. Ferrocene was added as internal standard after every measurement. All oxidation potentials were corrected referencing the Fc/Fc^+ process at 0.7 V *vs.* NHE. All compounds presented a single quasi reversible oxidation process in the cathodic zone, which may be attributed to the oxidation of the arylamine moieties (Figure 68 and Table 12). Looking at the values of the oxidation potential of all compounds, a moderate 40 mV cathodic shift is observed when replacing the central fluorene core of **98** by the diazafluorene one of **101**. Comparing the oxidation potential of compounds **98** and **99**, a negligible effect in bearing diphenylamine or triphenylamine as electron-donating groups was found.

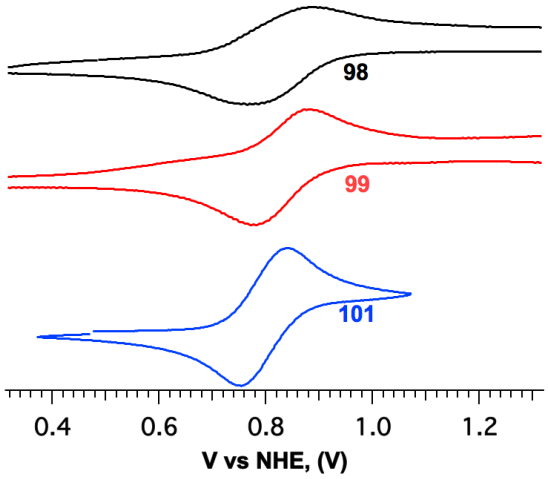

Figure 68. Cyclic voltammograms of **98**, **99** and **101** recorded in DCM solution.

Frontier orbital energies and electrochemical gaps were estimated from the half-wave oxidation potentials (Table 12), using the following equations:

Equation 8. $E_{0\text{-}0} = \lambda_{intersection}/1240$

Equation 9. $E_{HOMO} = -[E_{1/2}^{ox} + 4.4]$

Equation 10. $E_{LUMO} = E_{HOMO} + E_{0\text{-}0}$

The HOMO energy level of these compounds is determined by the energy of the parent arylamine groups, thus being the differences between compounds negligible. Compounds **98** and **99** exhibit a HOMO of –5.28 eV whereas

compound **101** shows a HOMO of –5.24 eV, which is slightly lower than that of spiro-OMeTAD (–5.16 eV).[114] Therefore, these new molecules present an excellent alignment between their HOMO and the valence band of the perovskite (–5.40) eV.

Table 12. Electrochemical data and HOMO-LUMO energy levels of compounds **98**, **99** and **101**.

Compound	$E_{1/2}^{ox}$ [V]	E_{HOMO}/E_{LUMO} [eV]
98	0.88	−5.28/−2.17
99	0.87	−5.28/−2.15
101	0.84	−5.24/−1.95

Thermal properties

Relevant insights into the thermal properties of final compounds **98**, **99** and **101** were provided by thermogravimetric analysis (TGA) and differential scanning calorimetry (DSC). As depicted in Figure 69, TGA reveals that all compounds exhibit good thermal stability. Compounds **98** and **99** start decomposing at temperatures of around 410 °C. As for compound **101**, it seems being less temperature resistant, starting to decompose at 365 °C.

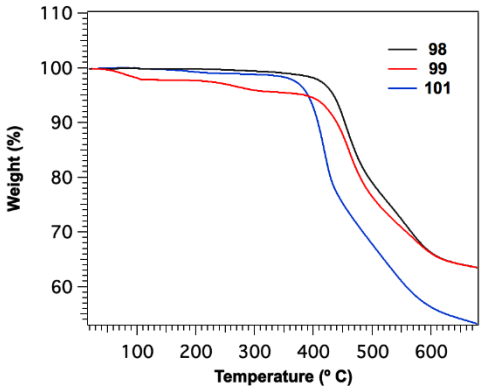

Figure 69. TGA of compounds **98**, **99** and **101** at scan rate of 10 °C/min.

[114] K. Rakstys, M. Saliba, P. Gao, P. Gratia, E. Kamarauskas, S. Paek, V. Jankauskas, M. K. Nazeeruddin, *Angew. Chem. Int. Ed*. **2016**, *55*, 7464−7468.

DSC analyses show that the materials remain stable within the operating temperature range of the cells (Figure 70).[115] For compounds **98** and **99** a glass transition was found at *ca.* 140 ºC. In contrast, derivative **101** exhibited a crystallization process at 214.6 ºC and a melting point of 284.0 ºC. In comparison, spiro-OMeTAD experiences a crystallization process at 173.3 ºC and a melting point of 247.5 ºC in the first heating cycle, when a second and third cycle are applied it just also shows a glass transition at *ca.* 113 ºC. Compound **101** presents both crystalline and amorphous nature, as observed for reference spiro-OMeTAD (Figure 70d). In contrast, the results obtained for compounds **98** and **99** reveal their amorphous nature.

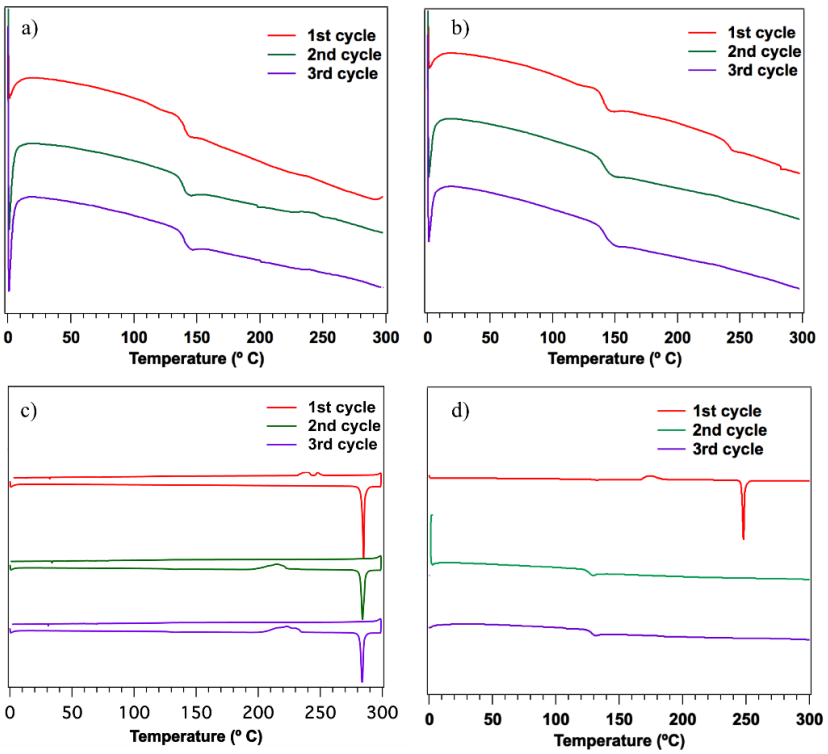

Figure 70. DSCs of target compounds a) **98**. b) **99**. c) **101**. d) spiro-OMeTAD , using a scan rate of 20 °C/min.

[115] a) M. C. Alonso García, J. L. Balenzategui, *Renewable Energy* **2004**, *29*, 1997−2010; b) H. Zhang, X. Qiao, Y. Shen, M. Wang, J. *Energy Chem*. **2015**, *24*, 729–735.

Photovoltaic performance

In collaboration with Prof. Nazeeruddin at Ecole Polytechnique Fédérale de Lausanne (EPFL) in Switzerland, compounds **98**, **99** and **101** were tested as HTMs in perovskite SCs. The cell architecture of the fabricated devices can be appreciated from the high-resolution scanning electron microscopy (SEM) cross-sectional images displayed in Figure 71. The anode, coated over a transparent glass substrate, consists in a fluorine-doped tin oxide (FTO) layer. On top of this layer, serving as the electron collector, compact and mesoporous TiO_2 is grafted. On the other end, the cathode consists on a thermally evaporated gold layer, directly deposited over the HTM layer. The photoactive $MAPbI_3$ material is sandwiched in between these layers.

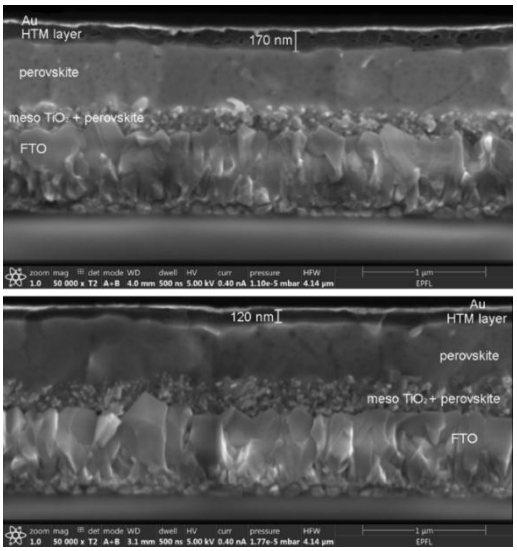

Figure 71. Cross sectional images of devices fabricated with **98** (top), **99** (bottom) HTMs, employing $MAPbI_3$ perovskite as active layer.

All fabricated devices showed meaningful hysteresis that depended on the bias scanning direction of the *J*/*V* curves (Figure 72 and Table 13). Devices fabricated out of **98** showed a maximum PCE of 13.5% measuring in reverse mode (from positive to negative potentials). In contrast, forward scanning diminished PCE to 11.1%. All measurements were performed under standard AM 1.5 G illumination. In the case of HTM **99**, the *J*/*V* curves exhibited a less pronounced hysteresis (<11%) and enhanced PV performance with 14.6% PCE

(reverse mode), despite **98**'s better FF (73.7 *vs.* 71.1%), compound **99** produced higher photocurrent (19.9 *vs.* 15.8 mA cm^{-2}). Given the observed results, it may be concluded that the structural modification introduced into the hemi-spiro materials is detrimental to the performance of the HTMs, compared to spiro-OMeTAD.

Table 13. PV parameters of perovskite cells using compounds **98**, **99**, and spiro-OMeTAD as HTM.

Compound		V_{oc} [V]	J_{sc} [mA cm^{-2}]	FF [%]	PCE [%]
98	Forward	0.98	18.3	61.8	11.1
	Reverse	0.99	18.5	73.7	13.5
99	Forward	1.02	19.6	65.3	13.1
	Reverse	1.03	19.9	71.1	14.6
spiro-OMeTAD	Forward	1.12	21.3	74.4	17.8
	Reverse	1.12	21.2	73.8	17.4

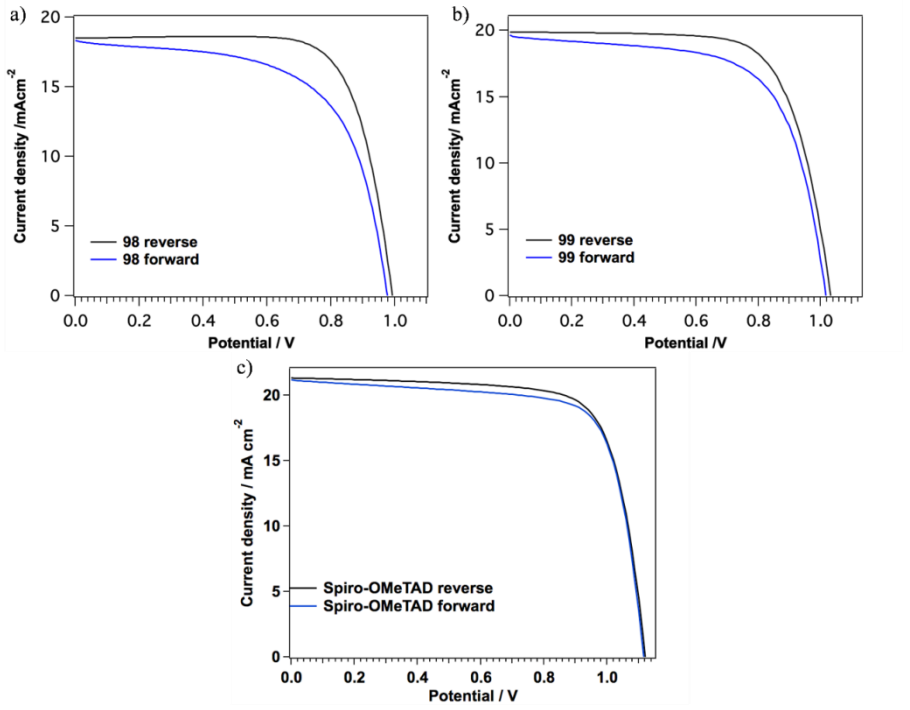

Figure 72. a) *J*/*V* curves of a **98**:$MAPbI_3$ perovskite device. b) **99**:$MAPbI_3$ perovskite measured at 10 mV s^{-1} scan rate. c) spiro-OMeTAD:$MAPbI_3$ device was prepared as reference.

Attempts to fabricate cells with compound **101** resulted in failure. Upon preparation of the HTM solution, it was observed that the addition of dopant FK209 induced the precipitation of **101**. After different solubility tests, it was concluded that **101** bipyridine-like structure was prone to chelate the cobalt contained in FK209, resulting in an insoluble thus unprocessable solid.

2.3.2. HTMs based on dibenzothiophene (DBT)

In parallel with the study of structures mimicking the spiranic structure of spiro-OMeTAD, structures bearing different central cores were also explored. In this case, a series of molecules making use of dibenzothiophene (DBT) as central core was prepared. Within the series, different electron donors were employed (*i.e.* diphenylamine, triphenylamine, and phenothiazine).

Synthesis

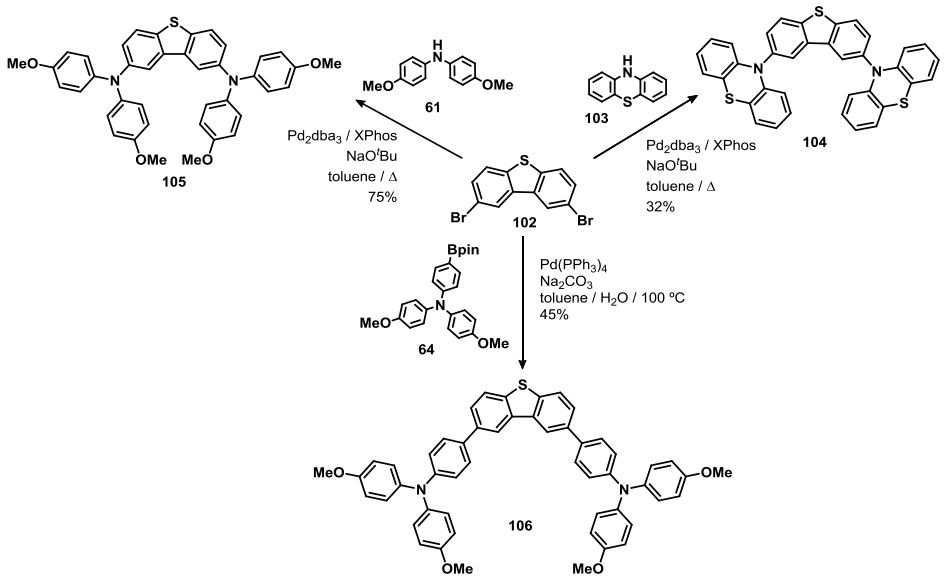

Scheme 17. Synthetic pathway for the preparation of target compounds **104**−**106**.

The synthesis of the central core starts with the treatment of dibenzothiophene with bromine to halogenate its C2 and C8 positions.[116] As shown in Scheme 17, resulting 2,8-dibromodibenzothiophene (**102**) served as scaffold for the

[116] J. Korang, W. R. Grither, R. D. McCulla, *J. Am. Chem. Soc.* **2010**, *132*, 4466–4476.

synthesis of final products **104**−**106**. Palladium mediated C-N cross-coupling with phenothiazine (**103**), using $Pd_2(dba)_3$/XPhos as catalyst and sodium *tert*-butoxide as base, yielded final product **104** in moderate-low yield. The same methodology allowed obtaining product **105** from diphenylamine **61** this time in good yield. Finally, biphasic (toluene/water) Suzuki-Miyaura reaction of dibrominated compound **102** with pinacolboronate **64**, using $Pd(PPh_3)_4$ as catalyst and 2 M sodium carbonate as base, rendered final compound **106** in moderate-low yield.

Characterization by standard spectroscopic technics was coherent with the structure of final products **104**−**106**. ^{1}H NMR features of compound **104** may serve as representative example of target compounds (Figure 73). The presence of 2,8 disubstituted DBT core always evidences itself as a down field "small" doublet, doublet and double doublet signal pattern. The C3 and C7 protons (black dot) show up at 7.60 ppm as a double doublet with a vicinal 8.5 Hz coupling with the doublet at 8.24 ppm (purple dot, C4 and C6 protons) and long distance 2.0 Hz coupling with the "small" doublet at 8.47 ppm (red dot).

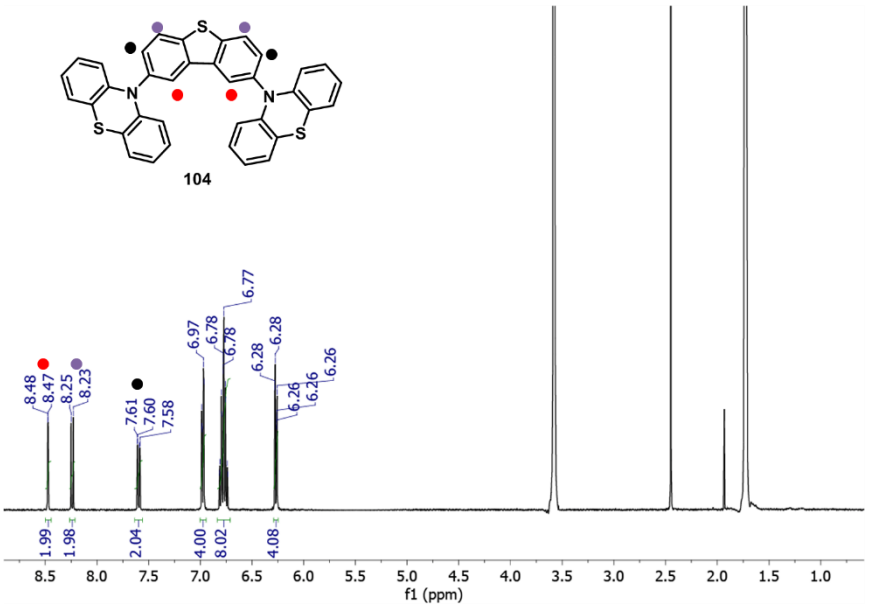

Figure 73. ^{1}H NMR (400 MHz, THF-d^8) spectrum of **104**.

Optical properties

The UV-vis absorption spectra features of molecules **104** and **106** recorded in DCM solution can be considered as the combination of the individual absorption spectra of their constituting moieties, with the high energy band *ca.* 260 nm arising from transitions from the DBT core (see Figure 74 and Table 14).[117] Along with this high energy band, molecule **104** shows the characteristic features of phenothiazine with a low intensity broad band centered at 320 nm. The exhibited features are very consistent with the DBT core and the phenothiazine moieties been electronically decoupled due to high twist angles between them, as demonstrated for similar systems where phenothiazine and the central core planes displayed nearly orthogonal.[118]

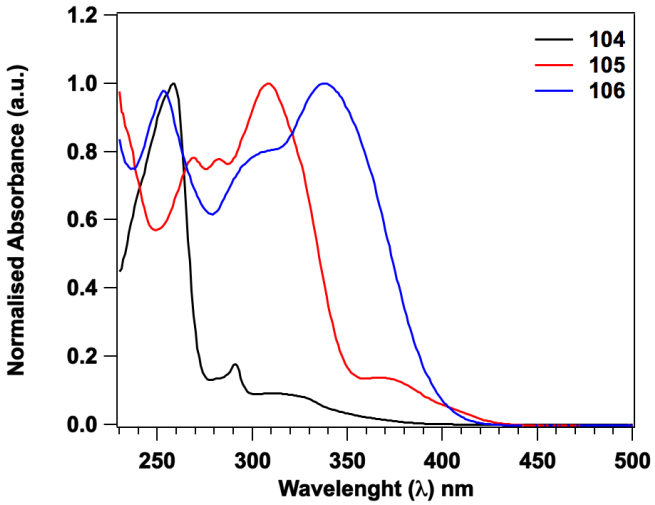

Figure 74. Normalized UV-vis absorption spectra of compounds **104**–**106** in DCM solution.

In the case of **105**, the absorption is dominated by a strong peak at 308 nm featuring two high frequency shoulders. These features resemble the

[117] S. H. Jeong, J. Y. Lee, *J. Mater. Chem.* **2011**, *21*, 14604–14609.

[118] M. K. Etherington, F. Franchello, J. Gibson, T. Northey, J. Santos, J. S. Ward, H. F. Higginbotham, P. Data, A. Kurowska, P. Lays Dos Santos, D. R. Graves, A. S. Batsanov, F. B. Dias, M. R. Bryce, T. J. Penfold, A. P. Monkman, *Nat. Commun.* **2017**, *8*, 14987.

combination of DPA and DBT spectra,[119] with the high frequency shoulders probably arising from the DBT core (in this case core's absorption is red-shifted due to the rise of the HOMO energy caused by the direct link with the N from the DPAs). Final product **106** low energy absorption (λ_{max} = 339 nm) arises from the TPA moiety, showing around 30 nm red-shifted with respect to **105** due to the extended conjugation the system presents.

Table 14. Summarized optical data of compounds **104**−**106**.

Compound	λ_{max} [nm]	ε 10^4 [M^{-1} cm^{-1}]
104	325	2.2
105	371	1.1
106	339	1.8

Electrochemical properties

As shown in Figure 75 these dibenzothiophene based HTMs just show redox activity under oxidizing conditions, within the solvent's scan window. Compounds **104** and **106**, bearing phenothiazine and triphenylamine respectively, exhibit a single quasireversible oxidation at 0.96 V for **104** and at 0.88 V for **106**. This 80 mV cathodic shift is attributed to the stronger reducing power of the TPA-OMe moieties compared to that of phenothiazine. In contrast, compound **105** experiences two oxidation processes, as observed for compound **74**. As for this compound, DPA bearing system shows stronger reducing power (0.83 V for **105**) than that bearing TPA, because of the mixing of states from the DPA and the central core.

[119] T.-H. Huang, W.-T. Whang, J. Y. Shen, J. T. Lin, H. Zheng, *J. Mater. Chem.* **2005**, *15*, 3233–3240.

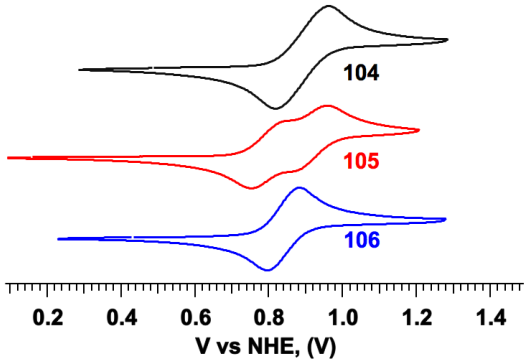

Figure 75. Cyclic voltammograms of **104**−**106** in DCM solution.

As shown in Table 15, frontier orbital energies were estimated according to Equation 9 and 10 from the half-wave oxidation potentials. Calculated HOMO energies increase in energy following the trend **105**>**106**>**104**, reflecting the order of electron-donating strength of the substituents (DPA-OMe>TPA-OMe>phenothiazine). In the case of compounds **105** and **106** the HOMO values are −5.23 and −5.28 eV respectively, slightly lower than spiro-OMeTAD (−5.16 eV), whereas for compound **104** this difference is more pronounced (−5.36 eV) due to the use of less electron-donating phenothiazine group. Presented values show that compounds **105** and **106** HOMO levels have an offset of 0.17 and 0.12 eV, respectively, with the valence band of the perovskite, whereas derivative **104** has a perfect electronic match.

Table 15. Electrochemical data of compounds **104**−**106**.

Compound	$E_{1/2}^{ox}$ [V]	E_{HOMO} [eV]
104	0.96	−5.36
105	0.83	−5.23
106	0.88	−5.28

Thermal properties

To gain insight into the thermal properties of the final compounds **104**−**106** TGA and DSC analyses were performed. As depicted in Figure 76 compounds **104**−**106** exhibited good thermal stability. Compound **104** bearing phenothiazine donors experienced an initial 6% weight loss at *ca.* 150 ºC,

remaining stable until decomposition at 323 ºC. As for compounds **105** and **106**, they showed to be very stable until decomposing at 280 and 330 ºC, respectively.

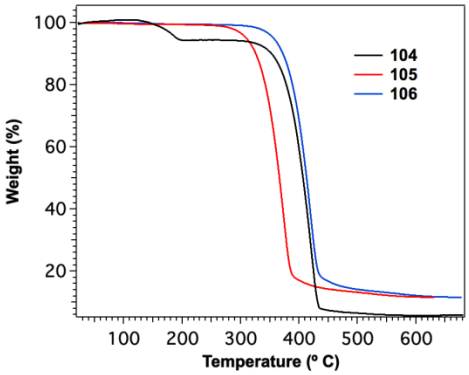

Figure 76. TGA of compounds **104**–**106** at a scan rate of 10 °C/min.

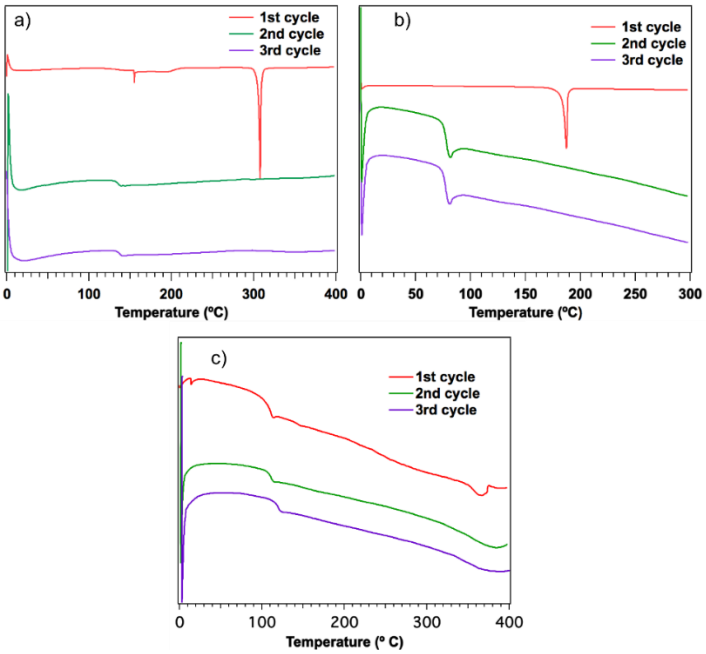

Figure 77. DSC (heating flow) of compound a) **104**. b) **105**. c) **106** with scan rate of 20° C/min.

As shown in Figure 77, DSC analysis of **104** showed a small glass transition at 191 ºC prior melting at 307.9 ºC in the first heating cycle; second and third cycles evidenced a marked glass transition around 135 ºC. Compound **105** showed a similar trend showing a melting point at 187.1 °C during the first heating cycle, the second and third cycles evidencing a glass transition *ca.* 76.0 °C. Finally, compound **106** presents just a single glass transition around 109 ºC, which is indicative of its amorphous nature. None of them showed crystalline structure as in the case of spiro-OMeTAD.

Photovoltaic properties

As shown in Figure 78 and Table 16 the performance of the perovskite devices employing **104**−**106** as HTMs was measured under standard illumination conditions of 1 sun 1.5 AMG (100 mW cm^{-2}). Out of the three tested materials, compound decorated with phenothiazines (**103**) showed very low overall performance (PCE = 4.0%, V_{OC} = 0.65 V, J_{SC} = 12.5 mA cm^{-2}), in contrast to what would have been expected from its good electronic alignment with the perovskite. Conversely, molecules decorated with arylamines (**105** and **106**) showed moderate PV response.

Table 16. Photovoltaic parameters for compounds **104**−**106**.

Compound	V_{oc} [V]	J_{sc} [mA cm^{-2}]	FF [%]	PCE [%]
104	0.65	12.5	48.9	4.0
105	1.01	15.6	74.3	11.7
106	1.03	18.9	63.8	12.7

Best performing one, **106**, exhibited a PCE of 12.7%, while **105** slightly underperformed with a 11.7%. Paradoxically, **105** exhibited a much better FF (16% higher) than **106** (compensated with a 18% loss of photocurrent) (see Table 16).

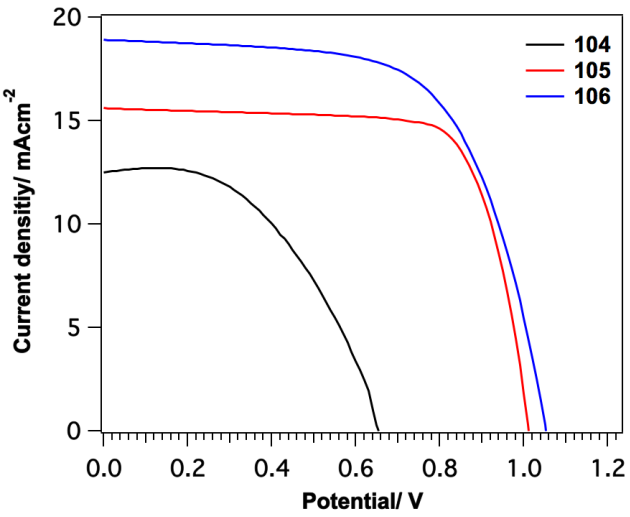

Figure 78. Current-voltage curves of compounds **104**−**106** recorded at a scanning rate of 20 mV s^{-1}.

2.3.3. HTMs based on anthradithiophene

In this section anthra[1,9-*bc*:5,10-*b'c'*]dithiophene (ADT) is employed as central core with either DPA or TPA units as donors. ADT molecule interests lies not only on its increased number of fused aromatic rings, but on having been rarely employed as building block.

Synthesis

The synthesis of 1,6-dibrominated ADT was performed following an experimental procedure described by C. Brown *et al.* from Plextronics, Inc.,[120] where starting from cheap (100 g <> €119.00) commercially available 1,5-dichloroanthracene-9,10-dione (**107**) ADT was obtained with 75% yield in two steps (Scheme 18) as follows: Reaction of **107** with mercaptoacetic acid (**108**) in the presence of sodium ethoxide, manganese (II) oxide, and 15-crown-ether yielded dicarboxylate **109**. Reflux of the obtained dicarboxylate in acetic anhydride induced intramolecular cyclization giving rise to ADT (**110**). Chemical modification of ADT was attained by reaction with a large excess of

[120] S. Sundarraj, C. Eickhoff, S. Bahulayan, R. Send, Y. Nishimae, H. Reichelt, J. Tanabe, P. Erk, WO 2015/024848 A l, 26.02.2015.

NBS in hot DMF (80 ºC) in less than 1 hour, providing a pale yellow solid consistent with the structure of 1,6-dibrominated ADT **111**.

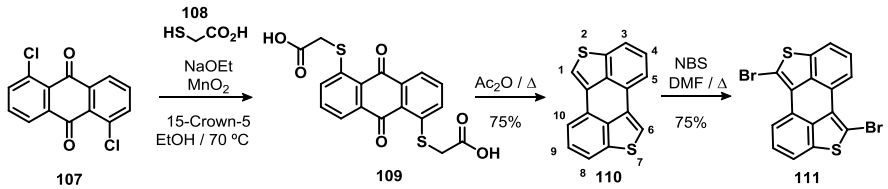

Scheme 18. Synthetic pathway for the preparation of core **111** (Substitution numbering for ADT compounds is shown for compound **110**).

Making use of ADT **111** as building-block, it was possible to obtain final products **112** and **113** by palladium mediated cross-couplings (Scheme 19). In the case of **112**, featuring two DPA subunits, the reaction was performed by Buchwald-Hartwig coupling with DPA **61**, using a palladium (0) catalytic system employing tri-*tert*-butylphosphine as ligand and sodium *tert*-butoxide as base, with moderate yield. As for analogue **113**, decorated with two TPA subunits, nearly quantitative conversion was obtained by Suzuki-Miyaura reaction employing $Pd(PPh_3)_4$ as catalyst and potassium phosphate as base.

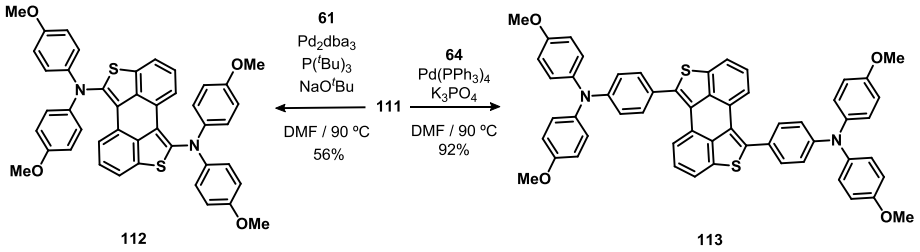

Scheme 19. Synthesis of ADT based molecules **112** and **113**.

The symmetry elements of ADT **128** give rise to a very simple ^{1}H-NMR spectrum featuring just three signals (Figure 79 top). Anthradithiophene core exhibits a signal at 7.59 ppm resembling a triplet but that actually is a double doublet corresponding to the C4-H and C9-H protons (black dot). These protons, in turn, couple with the signal at 7.97 ppm with 7.9 Hz, and with that at 8.66 ppm with 7.7 Hz; as a result of the small difference between the coupling constants the dd signal merges in a triplet. Tentatively, C5-H and C10-H protons (red dot) were assigned to the higher frequency signal at 8.66

ppm in analogy with anthracene derivatives, where these protons in *peri* positions normally appear quite deshielded. Therefore, the doublet at 7.97 ppm was assigned to protons at C3 and C8 positions (purple dot). ^{1}H-NMR spectrum of final compound **112** ^{1}H-NMR spectrum differentiates from parent molecule **111** in showing a new set of signals that belong to the diphenylamine groups (Figure 79 bottom). As a consequence of attaching these electron donor moieties, the signals of the ADT central core experience a noticeable shielding (0.9 ppm for C5,10-H signals and *ca.* 0.5 ppm for C4,9-H and C3,8-H). The dd signal shows up merged with the AA'BB' signal (*para* substituted phenyl ring) of the DPA.

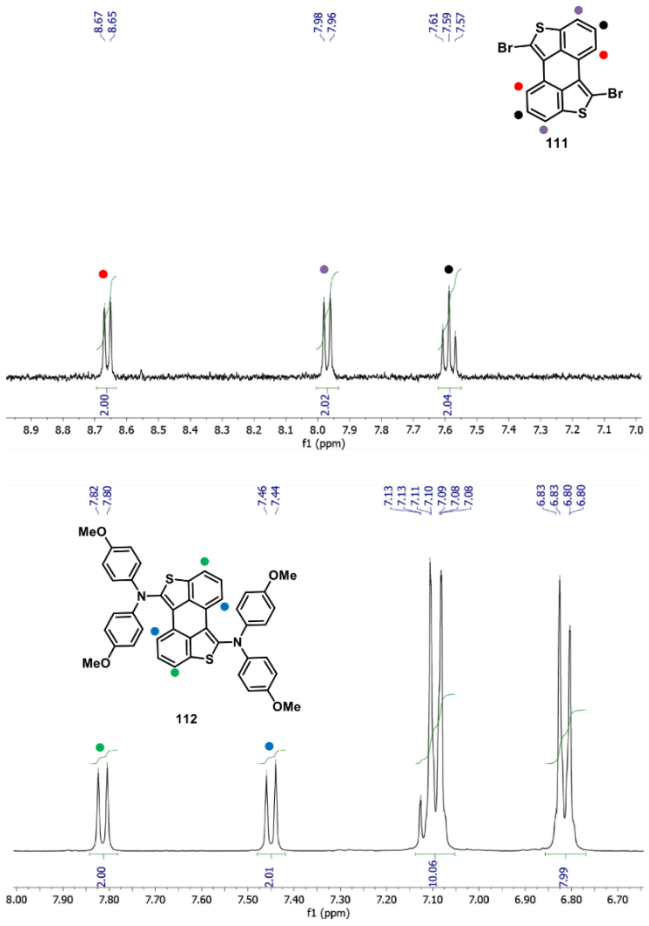

Figure 79. ^{1}H NMR (400 MHz, DMSO-d^{6}) spectra of **111** (top) and ^{1}H NMR (400 MHz, THF-d^{8}) of **112**(bottom), centered in the aromatic region.

Optical properties

Conversely to that observed for compounds **104**−**106**, where their absorption features resulted from the combination of the DBT and the donor moieties spectra, compounds **112** and **113** spectra have their own personality (Figure 80 and Table 17). Connectivity of the arylamines to the ADT core through its thiophene rings allows enhanced conjugation which, in turn, results in a significant broadening and red-shift of the lower energy bands. While TPA and ADT absorption features lie below 400 nm, the absorption of the arylamine-ADT conjugated systems is much red-shifted. In the case of the derivative bearing TPA (**113**) λ_{max} = 413 nm, whereas for the DPA bearing one (**112**) λ_{max} is 18 nm red-shifted, maintaining the trend observed for all TPA/DPA bearing materials. Both materials present an emission band mirroring the lower energy absorption band. For **112** the observed fluorescence band is very broad (between 450 and 725 nm) with the maximum at 547 nm. As for **113**, it emits between 420 and 650 nm, with the maximum at 476 nm.

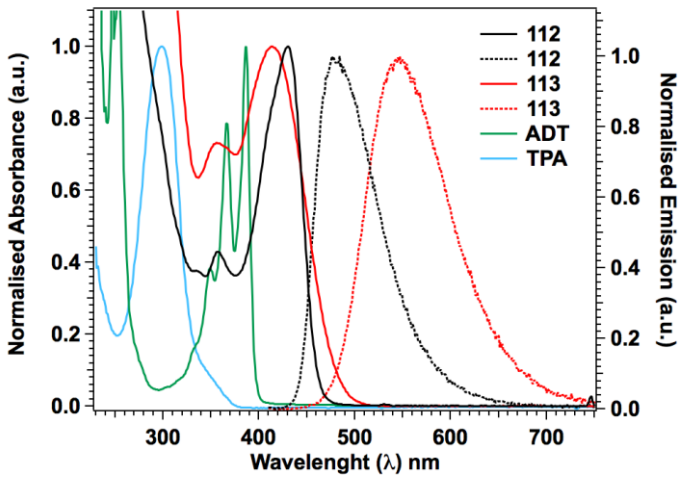

Figure 80. Normalized absorption (straight line) and emission (dotted line) of compounds **112** and **113** recorded in DCM solution. Overlay of ADT and TPA absorption features does not seem to match **112** and **113** absorption spectra.

Table 17. Summarized data from UV-vis spectra of compounds **112** and **113**.

Compound	λ_{ems}^{max} [nm]	ε 10^4 [M^{-1} cm^{-1}]	λ_{ems}^{max} [nm]	$E_{0\text{-}0}$ [eV]
112	431	3.0	476	2.74
113	413	3.3	547	2.58

Electrochemical properties

As for all previously presented DPA bearing systems, cyclic voltammetry of compound **112** revealed two quasireversible oxidation processes at 0.74 and 0.85 V, which are attributed to the sequential oxidation of the diphenylamine moieties (Figure 81). In contrast, compound **113** bearing triphenylamine groups displayed a single quasireversible oxidation wave at 0.92 V. The meaningful 180 mV anodic shift observed for the oxidation potential of **113** compared to **112** is, again, attributed to the mixing of the DPA states with those of the ADT central core (as above explained, the mixing of states is due to the direct linkage of the N atom of the DPA to the ADT core). In the case of TPA moieties, the mixing cannot be as marked due to the free rotation of the intermediating phenyl rings. As a result of the states being mixed, the HOMO energy of **112** rises (lying at −5.15 eV) with respect of **113** (−5.33 eV) as summarized in Table 18.

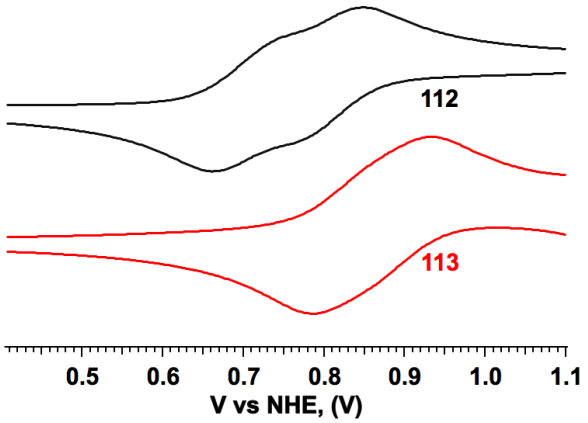

Figure 81. Cyclic voltammograms of **112** and **113** recorded in DCM solution.

Table 18. Electrochemical data and HOMO-LUMO energy levels for compounds **112** and **113**.

Compound	$E_{1/2}^{ox}$ [V]	E_{HOMO}/E_{LUMO} [eV]
112	0.74	−5.15/−2.41
113	0.93	−5.33/−2.75

Thermal properties

To shed light into the thermal properties of the final compounds **112** and **113** TGA and DSC were performed. Molecule **113** shows excellent stability against temperature, decomposing just at the high temperature of 387 ºC (Figure 82). Compound **112** shows also good thermal stability only decomposing over 327 ºC. This compound shows a 5% weight loss at 160 ºC which is attributed to solvent allegedly occluded within the sample.

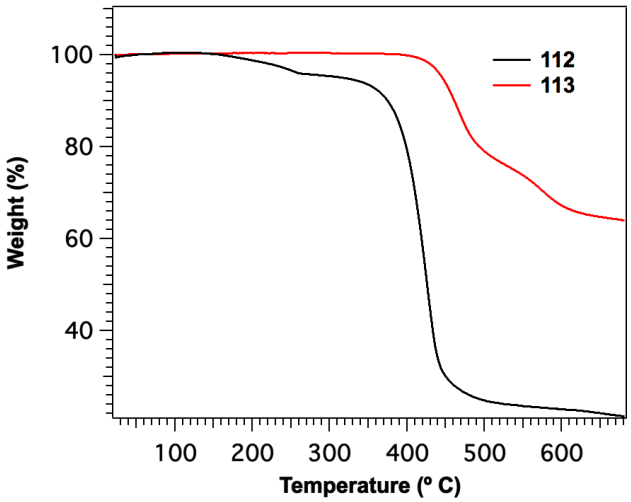

Figure 82. TGA of compounds **112** and **113** at a scan rate of 10° C/min.

The first melting cycle applied to **112** shows a melting point at 262.1 °C. This phase change is no longer observed in the second and third heating cycles, instead a glass transition occurring between 116.7 and 101.4 °C seems to give rise to an amorphous phase (Figure 83a). In the case of compound **113**, it

shows similar behavior with a melting point at 250.1 °C during the first cycle, and a glass transition between 131.7 and 134.9 °C over the second and third cycles (Figure 83b) also suggestive of its amorphous nature.

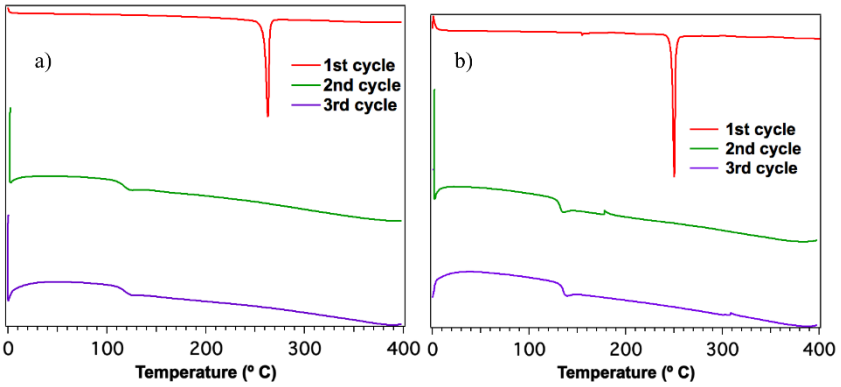

Figure 83. a) DSC (heating flow) of compound **112** and b) **113** with a scan rate of 20 °C/min.

Photovoltaic properties

The photovoltaic performance of **112** and **113** as HTMs was tested in $MAPbI_3$ perovskite solar cells (Figure 84). Devices employing DPA based HTM (**112**) with a PCE of 12.8% (measured in reverse mode), showed sensible hysteresis depending on the measuring mode: in forward mode the FF was of 67.2%, sensibly lower than the 71.4% observed for the reverse mode. On the other hand, TPA based (**113**) devices produced little hysteresis (FF difference <1%) with an excellent performance (PCE = 17.6%; V_{oc} =1.06 V; J_{sc} = 22.3 mA cm^{-2}; FF =74.3%) which is pretty similar to that obtained for the reference devices using spiro-OMeTAD as HTM (see Table 19). The cells maintain nearly 80% EQE over all the absorption range of the perovskite, showing an integrated current density of 21.1 mA cm^{-2} which is in good agreement with the value observed from the *J*/*V* curves.

Table 19. PV parameters of perovskite cells using compounds **112**, **113**, and spiro-OMeTAD as HTM.

Compound		V_{oc} [V]	J_{sc} [mA cm^{-2}]	FF [%]	PCE [%]
112	Forward	0.96	18.1	67.2	11.7
	Reverse	0.98	18.2	71.4	12.8
113	Forward	1.04	22.2	73.6	17.0
	Reverse	1.06	22.3	74.3	17.6
spiro-OMeTAD	Reverse	1.04	22.9	76.0	18.2

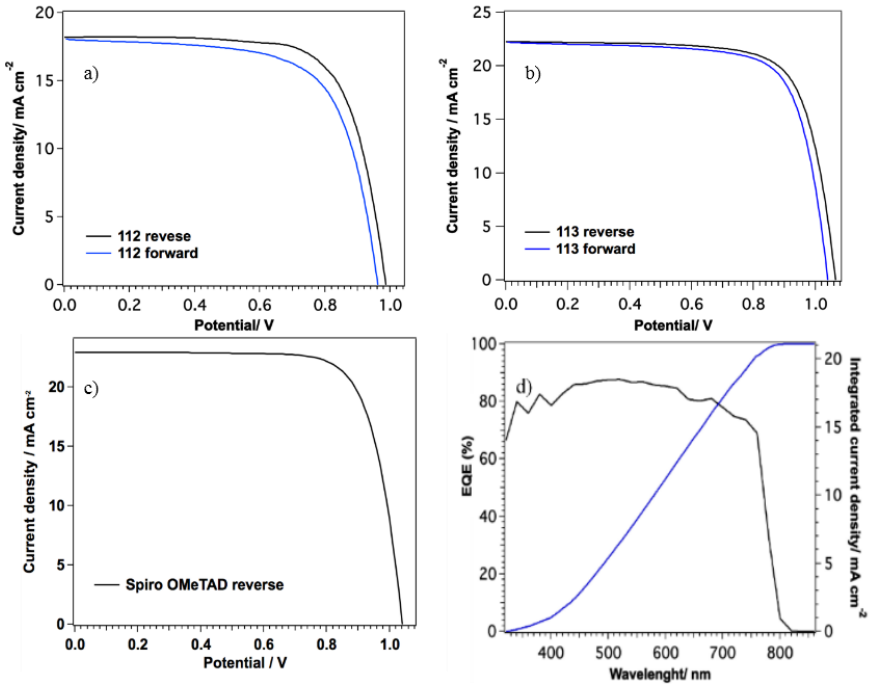

Figure 84. a) *J*/*V* curves of a **112**:$MAPbI_3$ perovskite device, b) and of **113**:$MAPbI_3$ perovskite measured at 10 mV s^{-1} scan rate. c) spiro-OMeTAD:$MAPbI_3$ device was prepared as reference. d) EQE spectrum and the integrated current density of **113**:$MAPbI_3$ device.

2.3.4. HTMs bearing four donor groups

To this point, the explored modifications of the HTM have included spiranic analogues of spiro-OMeTAD and employment of different central core scaffolds. One last approach taken into consideration within this Thesis is to increase the number of triarylamine electron-rich moieties. With this aim, two different scaffolds prone to undergo four-fold substitution reactions in order to introduce multiple TPA subunits were employed.

Synthesis

The first example of molecule susceptible to host four TPA moieties is offered by benzodithiophene. The fused thiophene rings of BDT provide four positions prone to be brominated. Polybromination of BDT (**114**) was easily achieved by treatment with excess of bromine in chloroform. This reaction provided a white solid consistent with 2,3,6,7-tetrabromobenzodithiophene (**115**) structure (the product shows a single ^{1}H-NMR signal at 8.34 ppm). Target compound **116** with BDT central core was achieved by four-fold Suzuki-Miyaura cross-coupling between **64** and **115** as pale yellow solid in good yield (Scheme 20).

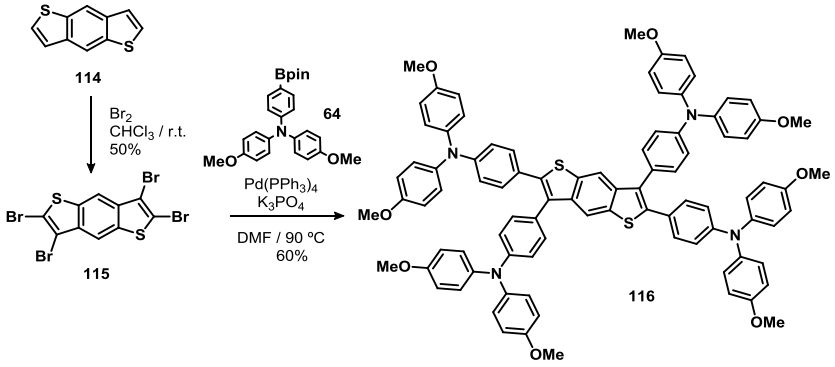

Scheme 20. Synthetic pathway for the preparation of target compound **116** with BDT central core.

On the other hand, exploiting again thiophene's ring ability to brominate in positions C2 and C3, dithienopyrrole (featuring two thiophene rings) provided the second central core. The DTP core was obtained following a modification

of the procedure described by Wong and collaborators,[121] according to which it was quite straightforward obtained from the palladium cross-coupling of 3,3'-dibromo-2,2'-bithiophene (**117**) with *p*-anisidine (**59**) employing BINAP as ligand. Polybromination of DTP **118** was possible in a one-pot two-step reaction; bromination of thiophene C2 position was performed under mild conditions by using NBS. Further bromination of the C3 positions of the thiophene rings required heating and the use of bromine for 48 h to yield **119**. Finally, four-fold Suzuki-Miyaura reaction with TPA **64** gave rise to the DTP molecule decorated with four TPA donor units **120** in good yield (Scheme 21).

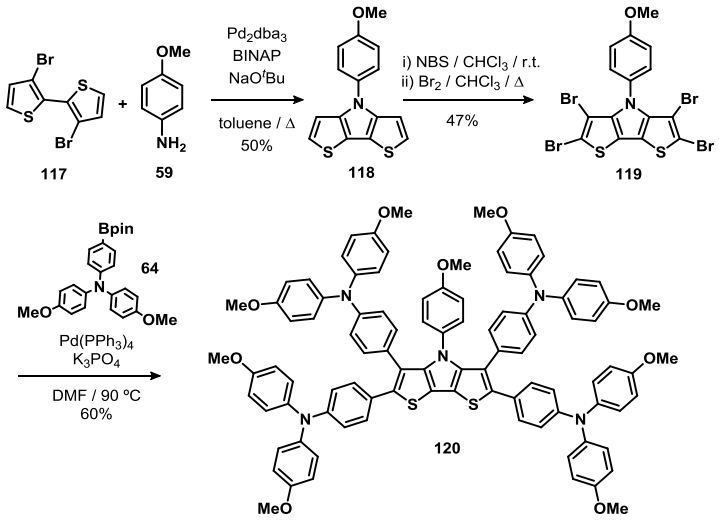

Scheme 21. Synthetic pathway for the preparation of compound **120** with DTP central core.

Optical properties

Final compounds **116** and **120** showed strong absorption features below 470 nm (Figure 85 and Table 20). Despite the different central cores they possess, the absorption profile of both molecules is very similar. Both systems exhibit a high energy band that maximizes at 310 nm, along with a broad absorption between 350 and 470 nm that peaks ca. 407 nm (6.5 and 8.9 10^4 $M^{-1}cm^{-1}$ for **116** and **120**, respectively). Both **116** and **120** emission features mirror their

[121] H.-L. Wong, C.-C. Ko, W. H. Lam, N. Zhu, V. W.-W. Yam, *Chem. Eur. J.* **2009**, *15*, 10005−10009.

lowest energy absorption band. The emission bands are broad (between 420 and 700 nm) and peak at 506 and 501 nm, for **116** and **120**, respectively.

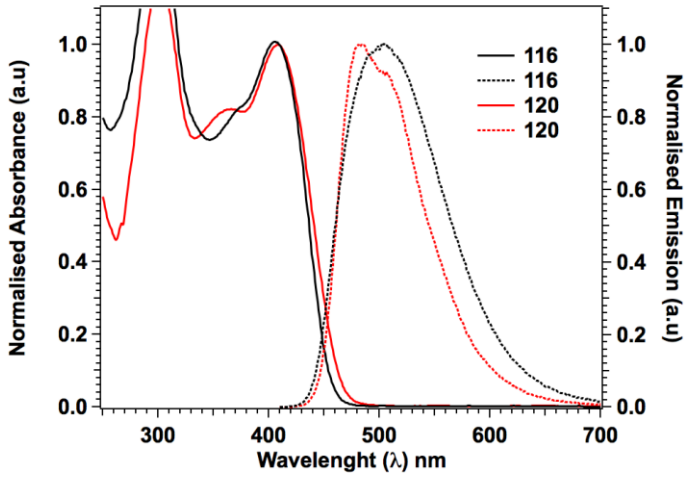

Figure 85. UV-vis absorption spectra of final compounds **116** and **120**, and parent BDT (**114**) and DPT (**119**) central cores recorded in DCM solutions.

Table 20. Optical data of compounds **116** and **120**.

Compound	λ_{abs}^{max} [nm]	ε 10^4 [$M^{-1}cm^{-1}$]	λ_{ems}^{max} [nm]	$E_{0\text{-}0}$ [eV]
116	407	6.5	506	2.76
120	408	8.9	501	2.73

Electrochemical properties

The electrochemical properties of target compounds **116** and **120** studied by CV showed significantly different oxidation behavior (Figure 86 and Table 21). Both compounds only present redox activity in the anodic part of the voltammograms. In the case of compound **116**, it exhibited a single quasireversible oxidation wave ($E_{1/2}^{ox}$ = 0.94 V). This oxidation wave shows a subtle shoulder which is rationalized as the sequential oxidation of the two TPA moieties fully conjugated with the core (linked to the BDT through the 2 and 2' positions), followed by the oxidation of the TPAs linked to the 3 and 3' positions. This apparent subtlety makes the 2,2' TPAs being stronger donors due to the effective conjugation with the BDT core. As for compound **120**, four

quasireversible oxidation waves ($E_{1/2}^{ox}$ = 0.57, 0.74, 0.95, 1.22 V) were visible. In this case, the first oxidation process is attributed to the one electron oxidation of the strong electron-donating DTP core (0.57 V oxidation), and the following processes being the oxidations of the TPA units. The third oxidation wave (0.95 V) seems to be more intense and probably arises from the TPA moieties attached to the DTP through 3,3' positions, which, as for **116**, cannot experience effective conjugation with the core. This difference in donating strength is reflected in the HOMO energies of the materials, observing −5.34 eV for **116** and −4.97 eV for **120**. Comparison of these values with the *ca.* −5.40 eV of $MAPbI_3$ suggests that compound **120** may not have the right energy alignment.

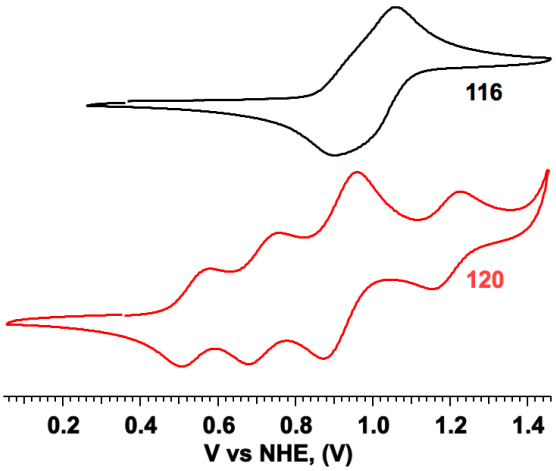

Figure 86. Cyclic voltammograms of **116** and **120** in DCM solution.

Table 21. Electrochemical data and HOMO-LUMO energy levels of compounds **116** and **120**.

Compound	$E_{1/2}^{ox1}$ [V]	E_{HOMO}/E_{LUMO} [eV]
116	0.94	−5.34/−2.58
120	0.57	−4.97/−2.24

Thermal properties

The thermal behaviour of the HTMs determined by TGA and DSC showed good thermal stability for both compounds (Figure 87). Both **116** and **120** show a platteau of stability until 411.7 and 424.7 °C, respectively, when they started decomposing. Upon heating, BDT based compound **116** shows a glass transition at 164.3 ºC prior to experience a crystallization process at 218.3 ºC, and eventually melting at 282.5 ºC during the first heating cycle. Second and third cycles just showed a lower temperature glass transition around 138.5 ºC.

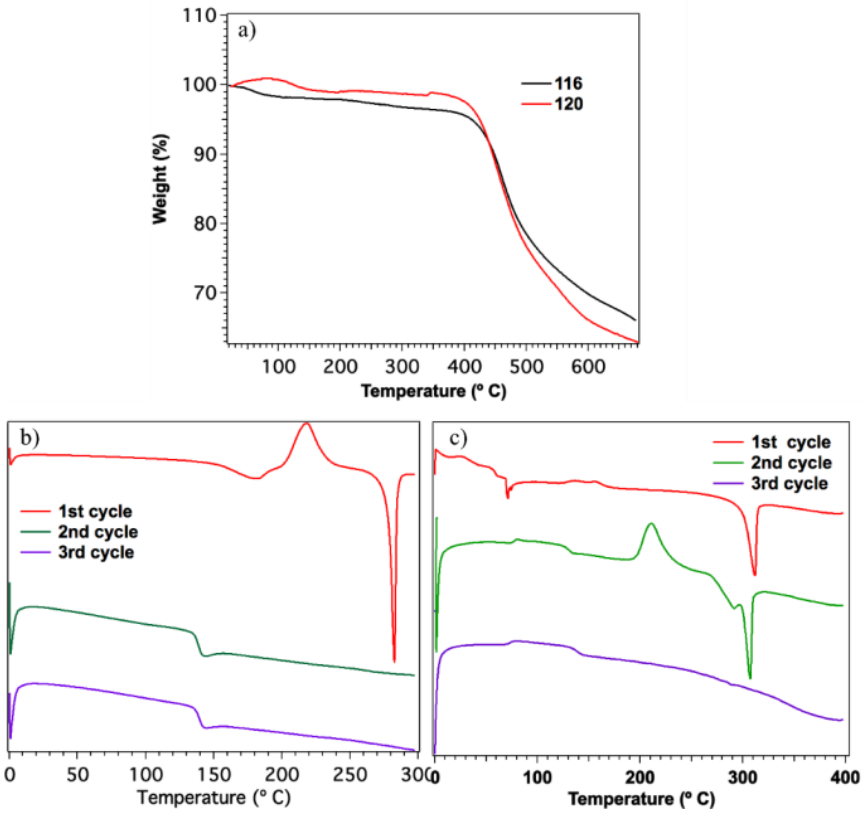

Figure 87. a) TGA of compounds **112** and **113** at scan rate of 10° C/min. b) DSC (heating flow) of compound **116** with scan rate of 20° C/min. c) DSC (heating flow) of compound **120** with scan rate of 20° C/min c).

The DTP based material **120** experienced a glass transition at 71.1 ºC, followed by two crystallization processes at 105.3 and 156.1 ºC and a final melt at 311.5 ºC, during the first heating cycle. In the second cycle, the material underwent a

glass transition at 112.8 ºC, further crystallizing at 211.1 ºC and melting at 306.9 ºC. In the third cycle, the compound only exhibited a glass transition at 120.3 ºC. The DSC analyses unveil that both **116** and **120** may exist in both crystalline and amorphous state.

Photovoltaic properties

Devices fabricated with a 100 nm layer of **116** as HTM (Figure 88) showed little hysteresis, exhibiting a PCE of 18.1% (17.2% in the forward mode), with a FF of 73.6%, a J_{sc} of 23.0 mA cm^{-2}, and a V_{oc} of 1.07 V under AM 1.5 G illumination (Figure 89a, Table 22). The PCE value obtained for **116** is slightly higher than that of spiro-OMeTAD (17.7 %) measured in the same conditions (Figure 89c, Table 22). Therefore, **116** could be a potential candidate for replacing spiro-OMeTAD as HTM. The external quantum efficiency (EQE) of the cell reflects efficient and homogeneous current photogeneration all over the absorption range of the perovskite, showing spectral response up to approximately 820 nm; the integrated current density obtained from the EQE (21.8 mA cm^{-2}) shows good agreement with the value obtained from the *J*/*V* curve (23.0 mA cm^{-2}) (Figure 90 left).

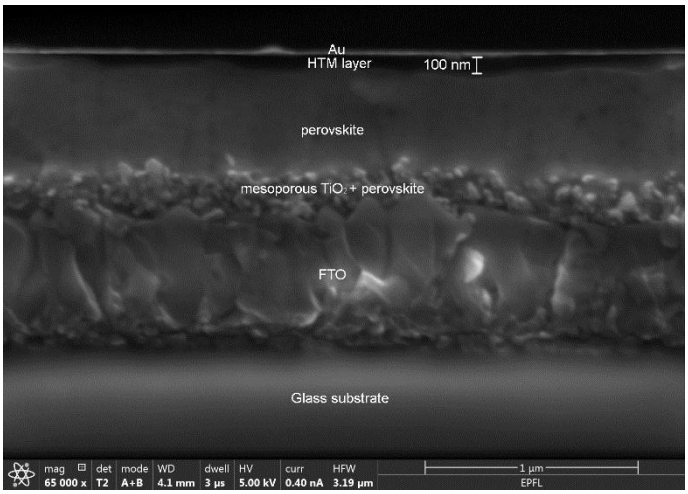

Figure 88. Cross sectional images of a $MAPbI_3$ perovskite device using **116** as HTM.

Devices built with **120** as HTM showed large hysteresis (with a difference in FF >18%) with a PCE of 15.6 % (12.8 % in the forward mode), with a FF of

65.8%, a J_{sc} of 22.2 mA cm^{-2}, and a V_{oc} of 1.06 V (Figure 89b, Table 22). As depicted in Figure 90 right, the integrated short-circuit current density obtained from the EQE (J_{sc} = 16.8 mA cm^{-2}) significantly differs from the value obtained from the *J*/*V* curve (22.0 mA cm^{-2}).

Table 22. PV parameters of perovskite cells using compounds **116**, **120**, and spiro-OMeTAD as HTM.

Compound		V_{oc} [V]	J_{sc} [mA cm^{-2}]	FF [%]	PCE [%]
116	reverse	1.07	23.0	73.6	18.1
	forward	1.06	23.0	70.4	17.2
120	reverse	1.07	22.0	65.8	15.6
	forward	1.06	22.0	53.7	12.8
spiro-OMeTAD	reverse	1.10	22.2	72.5	17.7
	forward	1.09	22.2	72.4	17.6

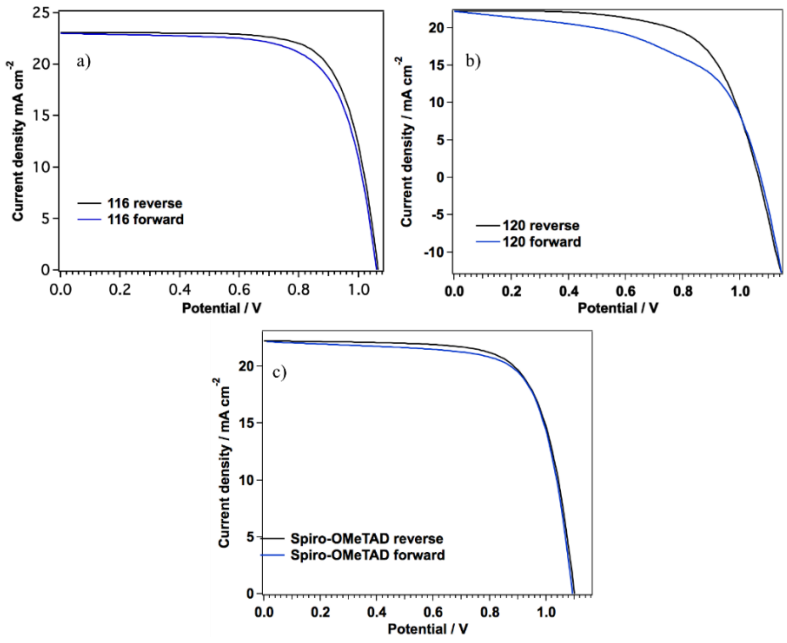

Figure 89. a) *J*/*V* curves of a **116**:$MAPbI_3$ perovskite device, b) and of **120**:$MAPbI_3$ perovskite measured at 10 mV s^{-1} scan rate. c) Spiro-OMeTAD:$MAPbI_3$ device was prepared as reference.

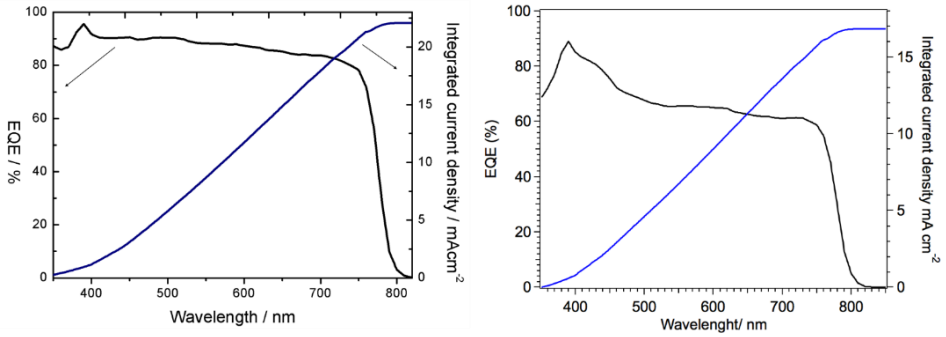

Figure 90. EQE spectrum and integrated current density of **116** (left) and **120** (right) cells.

2.4. Conclusions

2.4. CONCLUSIONS

In the light of the results presented in this Chapter, the following conclusions have been reached:

2.4.1. Hemi-spiro HTMs

- A series of new hemi-spiro HTMs (**98**, **99** and **101**) mimicking the spiranic structure of spiro-OMeTAD have been synthesized. Spectroscopic and electrochemical characterizations revealed suitable HOMO values for their use as HTM in perovskite solar cells. The obtained materials show good thermal stability within the temperature operating range of the devices.
- The fabricated perovskite solar cells revealed *J*/*V* curves with pronounced hysteresis depending on the bias scanning direction. Devices built with **98** reached 13.5% of PCE. Conversely, compound **99** allowed achieving 14.6% PCE. Comparing these results with spiro-OMeTAD (17.8%), it may be deduced that the introduced structural modification is detrimental to the performance of the HTM.
- Material **101** resulted to be unprocessable due to the lack of solubility in the presence of the necessary additives to cast the hole transporting layer.

2.4.2. HTMs based on dibenzothiophene (DBT)

- Three new HTMs using DBT as central core and decorated with electron donors of different strength (phenothiazine, DPA-OMe, and TPA-OMe) have been synthesized (**104**, **105** and **106**). The obtained materials show good thermal stability within the temperature operating range of the devices.
- Calculated HOMO energies are −5.23, −5.28, −5.36 eV for **105**, **106** and **104**, respectively, following the trend of decreasing electron-donating strength of the substituent groups (DPA-OMe > TPA-OMe > phenothiazine). Compared to the value of spiro-OMeTAD (-5.16 eV), target compounds **105** and **106** present slightly lower values, whereas, for **104** this difference is more remarkable. Compound **104** has an optimal electronic match with the valence band of the perovskite.
- The perovskite SCs fabricated with these compounds as HTM showed

moderate to poor performances. Devices using arylamines as pendant groups (**105** and **106**) exhibited the best performances, 12.7% PCE for the material bearing TPA (**106**) and 11.7% for **105**.

- Despite having a HOMO level that nearly matches that of the valence band of the perovskite, the material bearing phenothiazine donors (**104**) produced very low PCE (4%). Tentatively, we attribute this underperformance to the crystalline microstructure of the HTM layer that might not be correctly ordered to produce good charge transport.

2.4.3. HTMs based on anthradithiophene (ADT)

- Two new HTMs based on ADT as central core and featuring either DPA or TPA as donors have been synthesized. The obtained materials show good thermal stability within the temperature operating range of the devices.
- An estimated HOMO energy of −5.33 eV for TPA bearing **113** allows predicting good HTM performance due to its good energy alignment with the perovskite.
- As expected from its good band alignment, TPA bearing **113** allows a PCE of 17.6 % (presenting little hysteresis), comparable with that obtained for the spiro-OMeTAD employed as reference. On the other hand, devices fabricated with **112** as HTM achieved the moderate PCE of 12.8%. Compound **113** could be a potential candidate to replace spiro-OMeTAD in perovskite SCs.
- From the experience drawn so far, the HTMs with central cores bearing TPA as electron-rich moiety seem to outperform those bearing DPA.

2.4.4. HTMs bearing four donor groups.

- In this section, we have synthesized two derivatives bearing four TPAs as donor units, one making use of BDT as central core, the other one employing DTP. The obtained materials show good thermal stability within the temperature operating range of the devices.
- The calculated HOMO energy (4.97 eV) of **120** suggests a mismatch with the valence band of the perovskite. On the other hand, compound **116** with −5.34 eV shows a much better alignment (as in the case of compound

104).

- Perovskite SCs fabricated with these HTMs showed moderate to high performances. Devices fabricated with **120** provided a PCE of 15.6%, whereas the ones using **116** showed a PCE of 18.1%. This value is slightly higher than that of spiro-OMeTAD (17.7 %) measured under the same conditions. Therefore, **116** could be a potential candidate for replacing spiro-OMeTAD as HTM.

2.5. Experimental section

2.5. EXPERIMENTAL SECTION

2.5.1. Synthesis of Hemi-spiro HTMs

4,4'-(3,6-Dibromo-9*H*-fluorene-9,9-diyl)bis(*N*,*N*-bis(4-methoxyphenyl) aniline) (97).

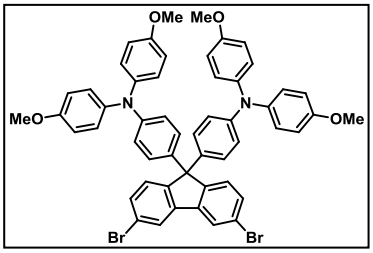

Into a 100 mL 2-neck round bottom flask fitted with a condenser, 3,6-dibromo-9*H*-fluoren-9-one **42** (750 mg, 2.24 mmol), **62** (1.71 g, 5.59 mmol) were dissolved in dry toluene (20 mL), under nitrogen atmosphere. The resulting mixture was heated up to 110 °C, then Eaton's reagent (0.67 mL, 8.87 mmol) was added dropwise and the reaction stirred for 18 h. After cooling to room temperature, the mixture was quenched with saturated ammonium chloride solution (20 mL) and extracted with diethyl ether (3 × 15 mL). Combined organic extracts were dried over anhydrous Na_2SO_4, filtered and solvent removed under reduced pressure. Reaction crude was purified by flash chromatography (silica gel, hexane/DCM 1:7) yielding a white solid (1.25 g, 60%).

^{1}H NMR (400 MHz, $CDCl_3$) δ: 7.82 (d, *J* = 1.7 Hz, 2H), 7.40 (dd, *J* = 8.2, 1.8 Hz, 2H), 7.27 (d, *J* = 8.2 Hz, 2H), 7.02 (d, *J* = 7.7 Hz, 8H), 6.93 (d, *J* = 8.5 Hz, 4H), 6.80 (d, *J* = 8.9 Hz, 8H), 6.75 (d, *J* = 8.1 Hz, 4H), 3.78 (s, 12H) ppm.

^{13}C NMR (101 MHz, $CDCl_3$) δ: 156.0, 151.3, 147.7, 140.9, 136.1, 131.2, 128.5, 127.9, 126.8, 123.6, 121.5, 119.9, 114.8, 64.1, 55.6 ppm.

HRMS (MALDI-TOF): *m/z* calculated for $C_{53}H_{42}Br_2N_2O_4$: 930.1455, found: 928.1487.

FTIR (KBr): 3734, 3618, 3035, 2937, 2831, 1740, 1600, 1495, 1461, 1318.61, 1273, 1233, 1169, 1102, 1028, 873, 815, 758, 718, 665, 631, 571 cm^{-1}.

m.p.: 279.0−281.0 °C.

Compound 98.

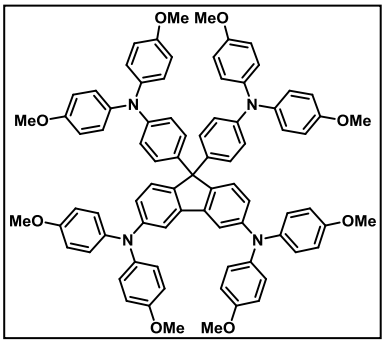

Into a 100 mL 2-neck round bottom flask fitted with a condenser, **97** (1.03 g, 1.10 mmol), **61** (558 mg, 2.43 mmol), $Pd_2(dba)_3$ (25.0 mg, 0.03 mmol), XPhos (52.0 mg, 0.11 mmol) were dissolved in dry toluene (20 mL) under nitrogen atmosphere. The mixture was degassed for 30 min. Then NaO^tBu (317 mg, 3.30 mmol) was added in one portion and the resulting mixture was stirred at 110 °C for 18 h. Upon cooling to room temperature, the mixture was quenched with H_2O (15 mL) and extracted with Et_2O (3 × 10 mL). Combined organic extracts were dried over anhydrous Na_2SO_4, filtered and evaporated under reduced pressure. Reaction crude was purified by flash chromatography (silica gel, DCM/ethyl acetate 20:1) yielding a white powder (742 mg, 55%).

^{1}H NMR (400 MHz, THF-d^8) δ: 7.21 (d, *J* = 2.1 Hz, 2H), 7.17 (d, *J* = 8.3 Hz, 2H), 7.01–6.93 (m, 20H), 6.81–6.74 (m, 18H), 6.70 (d, *J* = 8.7 Hz, 4H), 3.72 (s, 12H), 3.71 (s, 12H) ppm.

^{13}C NMR (101 MHz, THF-d^8) δ: 157.3, 156.9, 149.4, 148.2, 146.5, 142.6, 142.1, 142.06, 139.5, 129.6, 127.6, 127.4, 126.7, 122.8, 120.5, 115.53, 115.5, 114.4, 64.1, 55.72, 55.7 ppm.

HRMS (MALDI-TOF): *m/z* calculated for $C_{81}H_{70}N_4O_8$: 1226.5166, found: 1226.5188.

FTIR (neat): 3034, 2998, 2948, 2834, 1743, 1607, 1502, 1453, 1239, 1175, 1106, 1035, 824, 731, 580 cm^{-1}.

m.p.: 165.1−167.1 °C.

Compound 99.

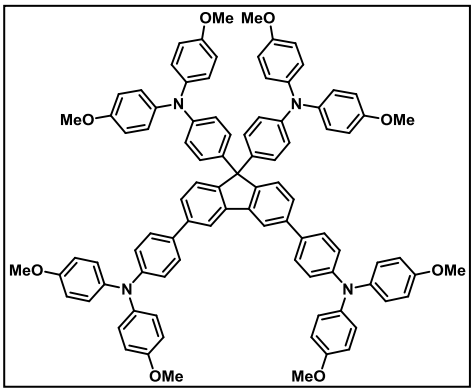

Into a 100 mL 2-neck round bottom flask fitted with a condenser, **97** (173 mg, 0.12 mmol), **64** (176 mg, 0.41 mmol) and $Pd(PPh_3)_4$ (22.0 mg, 0.02 mmol) were dissolved in dry DMF (20 mL) under nitrogen atmosphere, the mixture was then degassed for 30 min. Thereafter, K_3PO_4 (631 mg, 2.97 mmol) was added in one portion and the mixture was stirred at 90 °C for 18 h. Upon cooling to room temperature, the mixture was quenched with H_2O (30 mL). The resulting precipitate was filtered off and washed with water. After vacuum drying the remaining moisture, the crude was purified by flash chromatography (silica gel using ethyl DCM/acetate 17:1) yielding a white powder (180 mg, 70%).

^{1}H NMR (400 MHz, THF-d^8) δ: 7.50 (d, *J* = 8.4 Hz, 4H), 7.47–7.39 (m, 4H), 7.10–7.01 (m, 12H), 6.96 (d, *J* = 8.5 Hz, 14H), 6.84 (d, *J* = 8.6 Hz, 8H), 6.77 (d, *J* = 8.7 Hz, 8H), 6.72 (d, *J* = 8.4 Hz, 4H), 3.75 (s, 12H), 3.71 (s, 12H) ppm.

^{13}C NMR (101 MHz, THF-d^8) δ: 157.44, 157.4, 157.2, 151.7, 149.4, 148.4, 142.1, 142.0, 141.8, 141.4, 139.0, 134.4, 129.7, 128.5, 127.6, 127.5, 126.9, 121.6, 120.8, 119.1, 115.6, 115.5, 65.0, 55.8, 55.7 ppm.

HRMS (MALDI-TOF): *m/z* calculated for $C_{93}H_{78}N_4O_8$: 1378.5814, found: 1378.5831.

FTIR (neat): 3037, 2925, 2837, 1740, 1606, 1503, 1318, 1274, 1298, 1174, 1106, 1035, 822, 728, 605, 576 cm^{-1}.

m.p.: 215.3−217.3 °C.

4,4'-(5*H*-Cyclopenta[1,2-b:5,4-b']dipyridine-5,5-diyl)bis(*N*,*N*-bis(4-methoxyphenyl)aniline) (101).

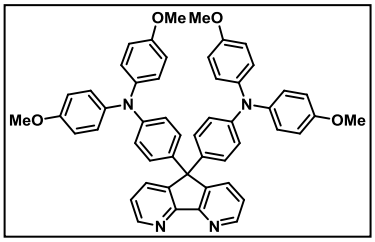

Into a 100 mL 2-neck round bottom flask fitted with a condenser, 4,5-diazafluoren-9-one **100** (154 mg, 0.85 mmol), **62** (650 mg, 2.12 mmol) were dissolved in dry DCM (15 mL), under nitrogen atmosphere. After warming up to 40 °C, Eaton's reagent (0.27 mL, 3.36 mmol) was added dropwise and the reaction stirred for 4 h. Upon cooling to room temperature, the reaction was quenched with H_2O (10 mL) and extracted with DCM (2 × 15 mL). Combined organic extracts were dried over anhydrous Na_2SO_4, filtered and solvent removed under reduced pressure. Reaction crude was purified by flash chromatography (silica gel, DCM/ethyl acetate 2:1) yielding a white solid (460 mg, 70%).

^{1}H NMR (400 MHz, THF-d^8) δ: 8.62 (dd, *J* = 4.8, 1.5 Hz, 2H), 7.80 (dd, *J* = 7.8, 1.5 Hz, 2H), 7.23 (dd, *J* = 7.8, 4.8 Hz, 2H), 6.99–6.92 (m, 12H), 6.81–6.76 (m, 8H), 6.73–6.68 (m, 4H), 3.72 (s, 12H) ppm.

^{13}C NMR (101 MHz, THF-d^8) δ: 159.1, 157.5, 150.7, 149.0, 147.6, 141.7, 136.6, 134.3, 129.4, 127.7, 123.8, 120.5, 115.6, 61.1, 55.7 ppm.

HRMS (MALDI-TOF): *m/z* calculated for $C_{51}H_{42}N_4O_4$: 774.3201, found: 774.3199.

FTIR (KBr): 3855, 3736, 2930, 2834, 1739, 1608, 1565, 1500, 1463 1398, 1324, 1278, 1235, 1171, 1102, 1034, 912, 828, 782 753, 725 623, 575 cm^{-1}.

m.p.: 258.2−260.2 °C.

2.5.2. Synthesis of HTMs based on dibenzothiophene (DBT)

2,8-Dibromodibenzothiophene (102).[116]

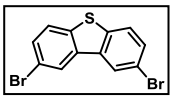

Dibenzothiophene (2.00 g, 10.9 mmol) was dissolved in chloroform (60 mL) and the solution cooled to 0 °C. Bromine (1.56 mL, 30.3 mmol) was dropwise added. The resulting mixture was stirred for 3 days at room temperature. The obtained precipitate was filtered off and washed with methanol. The product was purified by recrystallization from chloroform as a white solid (3.20 g, 85%).

^{1}H NMR (400 MHz, $CDCl_3$) δ: 8.24 (d, *J* = 1.8 Hz, 2H), 7.71 (d, *J* = 8.5 Hz, 2H), 7.58 (dd, *J* = 8.5 Hz, 1.8 Hz, 2H) ppm.

Compound 104.

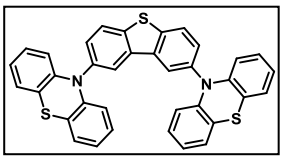

Into a 100 mL 2-neck round bottom flask fitted with a condenser, **102** (473 mg, 1.38 mmol), **103** (830 mg, 4.14 mmol), $Pd_2(dba)_3$ (32.0 mg, 0.03 mmol), and XPhos (70.0 mg, 0.14 mmol) were dissolved in dry toluene (30 mL) under nitrogen atmosphere. The solution was degassed for 30 min. Then NaO^tBu (400 mg, 4.16 mmol) was added in one portion and the resulting mixture was stirred at 110 °C for 18 h. Upon cooling to room temperature, the reaction was quenched with H_2O (20 mL) and extracted with DCM (3 × 10 mL). Combined organic extracts were dried over anhydrous Na_2SO_4, filtered and the solvent removed under reduced pressure. Reaction crude was purified by flash chromatography (silica gel, hexane/DCM 2:1) giving rise to a light-yellow solid (250 mg, 32%).

^{1}H NMR (400 MHz, THF-d^8) δ: 8.47 (d, *J* = 1.7 Hz, 2H), 8.24 (d, *J* = 8.5 Hz, 2H), 7.60 (dd, *J* = 8.5, 2.0 Hz, 2H), 7.02–6.93 (m, 4H), 6.84–6.69 (m, 8H), 6.33–6.20 (m, 4H) ppm.

^{13}C NMR (101 MHz, THF-d^8) δ: 145.6, 141.0, 139.5, 139.1, 131.4, 127.8, 127.5, 126.2, 126.1, 123.4, 121.5, 117.2 ppm.

HRMS (MALDI-TOF): *m/z* calculated for $C_{36}H_{22}N_2S_3$: 578.0940, found: 578.0914.

FTIR (neat): 3929, 3062, 2924, 2852, 1710, 1583, 1462, 1435, 1307, 1239, 1160, 1130, 1074, 1044, 925, 819, 742, 650, 626, 568 cm^{-1}.

m.p.: 278.0−280.0 °C.

Compound 105.

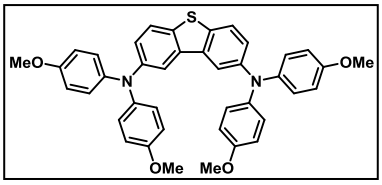

Into a 100 mL 2-neck round bottom flask fitted with a condenser **102** (250 mg, 0.73 mmol), **61** (420 mg, 1.85 mmol), $Pd_2(dba)_3$ (17.0 mg, 0.02 mmol), and XPhos (34.0 mg, 0.08 mmol) were dissolved in dry toluene (30 mL) under nitrogen atmosphere. The mixture was degassed for 30 min. Then NaO^tBu (210 mg, 2.20 mmol) was added in one portion and the resulting mixture was stirred at 110 °C for 18 h. Upon cooling to room temperature, the reaction was quenched with H_2O (30 mL) and extracted with Et_2O (3 × 10 mL). Combined organic extracts were dried over anhydrous Na_2SO_4, filtered and the solvent removed under reduced pressure. Reaction crude was purified by flash chromatography (silica gel, hexane/DCM 1:8) giving rise to a light-yellow powder (350 mg, 75%).

^{1}H NMR (400 MHz, THF-d^8) δ: 7.63 (d, *J* = 8.7 Hz, 2H), 7.60 (d, *J* = 2.1 Hz, 2H), 7.05 (dd, *J* = 8.6, 2.3 Hz, 2H), 6.98–6.93 (m, 8H), 6.80–6.75 (m, 8H), 3.73 (s, 12H) ppm.

^{13}C NMR (101 MHz, $CDCl_3$) δ: 156.9, 147.4, 142.7, 137.6, 134.3, 126.4, 124.3, 124.2, 116.5, 115.5, 55.7 ppm.

HRMS (MALDI-TOF): *m/z* calculated for $C_{40}H_{34}N_2O_4S$: 638.2234, found: 638.2205.

FTIR (neat): 3043, 2997, 2928, 2835, 1599, 1547, 1505, 1468, 1441, 1239, 1176, 1107, 1036, 824, 712, 645, 591 cm^{-1}.

m.p.: 161.2−163.2 °C.

Compound 106.

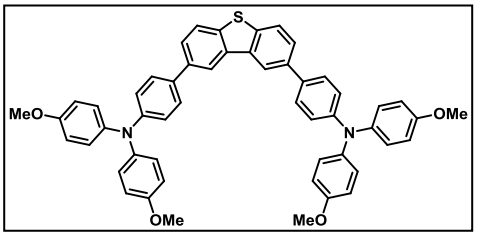

Into a 100 mL 2-neck round bottom flask fitted with a condenser, **102** (260 mg, 0.76 mmol), **64** (820 mg, 1.90 mmol), and $Pd(PPh_3)_4$ (26.0 mg, 0.02 mmol) were dissolved in dry toluene (20 mL) under nitrogen atmosphere. The mixture was degassed for 30 min. Then, a previously degassed 2 M Na_2CO_3 DI water solution (8 mL) was added. The resulting

mixture was stirred at 100 °C for 18 h. Upon cooling to room temperature, the reaction was quenched with H_2O (30 mL) and extracted with $CHCl_3$ (3 × 10 mL). Combined organic extracts were dried over anhydrous Na_2SO_4, filtered and the solvent removed under reduced pressure. Reaction was purified by flash chromatography (silica gel, hexane/ethyl acetate 8:1) yielding a light-yellow powder (270 mg, 45%).

^{1}H NMR (400 MHz, THF-d^8) δ: 8.53 (d, *J* = 1.7 Hz, 2H), 7.89 (d, *J* = 8.4 Hz, 2H), 7.71 (dd, *J* = 8.4, 1.7 Hz, 2H), 7.62–7.57 (m, 4H), 7.08–7.03 (m, 8H), 7.03–6.98 (m, 4H), 6.88–6.83 (m, 8H), 3.76 (s, 12H) ppm.

^{13}C NMR (101 MHz, THF-d^8) δ: 157.4, 149.5, 142.0, 139.2, 138.8, 137.5, 134.1, 128.6, 127.4, 126.5, 123.9, 122.0, 120.4, 115.6, 55.8 ppm.

HRMS (MALDI-TOF): *m/z* calculated for $C_{52}H_{42}N_2O_4S$: 790.2860, found: 790.2830.

FTIR (neat): 2924, 2852, 1710, 1606, 1505, 1465, 1321, 1279, 1241, 1174, 1108, 1035, 824, 755, 577 cm^{-1}.

2.5.3. Synthesis of HTMs based on Anthradithiophene (ADT)

Anthra[1,9-*bc*:5,10-*b'c'*]dithiophene (110).[120]

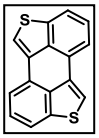

Into a 100 mL 2-neck round bottom flask fitted with a condenser, 1,5-dichloroanthraquinone (**107**) (5.00 g, 18.0 mmol) was dissolved in a sodium ethoxide ethanol solution (43 mL, 21% w/w). Thereafter, mercaptoacetic acid (**108**) (3.64 g, 39.6 mmol) was gradually added at 22 °C, followed by the addition of MnO_2 (0.85 g, 9.85 mmol) and 15-crown-5-ether (85.0 mg, 0.40 mmol). The resulting mixture was stirred at 70 °C for 14 h. Upon cooling to room temperature, the mixture was gradually poured into H_2O (400 mL), stirred mixture was then acidified to pH 3 with 2 M hydrochloric acid. The formed precipitate was collected by filtration, washed with water, and dried under vacuo to give compound **109** as black solid. The black solid was used in the next step without further purification. Compound **109** (6.89 g, 17.5 mmol) was suspended in acetic anhydride (120 mL) and was refluxed for 3 h. Without cooling, the precipitate was collected by filtration and then redissolved in hot n-pentane. After the solvent was removed under reduced pressure and the reaction was purified by flash chromatography (silica gel using hexane/DCM 4:1) yielding a yellow solid (3.62 g, 75%).

^{1}H NMR (400 MHz, $CDCl_3$) δ: 7.70 (dd, *J* = 2.9, 0.7 Hz, 2H), 7.68 (dd, *J* = 3.6, 0.7 Hz, 2H), 7.63 (s, 2H), 7.40–7.35 (m, 2H).

^{13}C NMR (101 MHz, $CDCl_3$) δ: 140.0, 137.5, 132.1, 128.6, 126.1, 121.4, 118.0, 117.3.

MS (MALDI-TOF) *m/z*: 264.0.

1,6-Dibromoanthra[1,9-bc:5,10-b'c']dithiophene (111).[120]

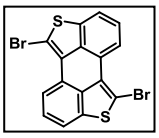

Into a solution of **110** (0.28 g, 1.08 mmol) in dry DMF (35 mL), a solution of NBS (0.67 g, 3.77 mmol) in DMF (6mL) was dropwise added. The resulting mixture was stirred at 110 ºC until totally dissolved. Thereafter, the mixture was cooled down to 80 ºC and further stirred for 1h. Formed precipitate was collected by filtration, washed with acetone, and dried under vacuum to give rise to a pale yellow solid (0.32 g, 75%).

^{1}H NMR (400 MHz, DMSO-d^6) δ: 8.66 (d, *J* = 7.7 Hz, 2H), 7.97 (d, *J* = 7.9 Hz, 2H), 7.59 (dd, *J* = 7.9 Hz, *J* = 7.7 Hz, 2H) ppm.

HRMS (MALDI-TOF): *m/z* calculated for $C_{16}H_6Br_2S_2$: 419.8, found: 419.9.

Compound 112.

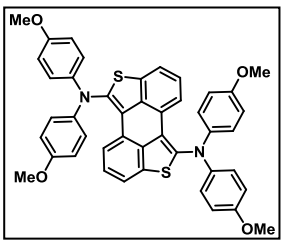

Into a 100 mL 2-neck round bottom flask fitted with a condenser, **111** (120 mg, 0.30 mmol), **61** (150 mg, 0.67 mmol), and Pd_2dba_3 (13.0 mg, 0.01 mmol) were dissolved in dry toluene (25 mL) under nitrogen atmosphere. The mixture was degassed for 30 min. NaO^{t}Bu (84.0 mg, 0.88 mmol) was then added in one portion and the resulting mixture stirred at 110 °C for 5 h. Upon cooling to room temperature, the solvent was removed under reduced pressure and the reaction crude purified by flash chromatography (silica gel, DCM) yielding a yellow solid (120 mg, 56%).

^{1}H NMR (400 MHz, THF-d^8) δ: 7.82 (d, *J* = 7.8 Hz, 2H), 7.44 (d, *J* = 8.0 Hz, 2H), 7.14–7.06 (m, 10H), 6.86–6.77 (m, 8H), 3.72 (s, 12H) ppm.

^{13}C NMR (101 MHz, THF-d^8) δ: 157.3, 144.8, 141.4, 137.8, 137.6, 128.5, 126.7, 124.3, 124.0, 121.5, 121.1, 115.5, 55.7 ppm.

HRMS (MALDI-TOF): *m/z* calculated for $C_{44}H_{34}N_2O_4S_2$: 718.1955, found: 718.1923.

FTIR (neat): 3849, 3726, 3680, 3650, 3620, 2950, 2836, 1741, 1645 1546, 1504, 1462, 1406, 1358, 1242, 1179, 1035, 825, 778 cm^{-1}.

Compound 113.

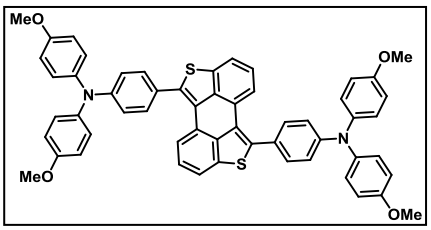

Into a 100 mL 2-neck round bottom flask fitted with a condenser, **111** (200 mg, 0.47 mmol), **64** (510 mg, 1.20 mmol), and $Pd(PPh_3)_4$ (54.0 mg, 0.05 mmol) were dissolved in dry DMF (25 mL) under nitrogen atmosphere. After degassing the mixture for 30 min, K_3PO_4 (1.20 g, 5.68 mmol) was added in one portion and the reaction stirred at 100 °C for 2 h. Upon cooling to room temperature, it was quenched with H_2O (20 mL). Formed precipitate was filtered off and sequentially washed with H_2O and MeOH. Thereafter the precipitate was redissolved in DCM (50 mL). The solvent was removed under reduced pressure and the reaction crude was purified by flash chromatography (silica gel, DCM) to give a pale orange solid (380 mg, 92%).

^{1}H NMR (400 MHz, THF-d^8) δ: 7.58–7.53 (m, 4H), 7.43–7.39 (m, 4H), 7.18–7.14 (m, 8H), 7.12–7.06 (m, 2H), 7.01–6.96 (m, 4H), 6.93–6.88 (m, 8H), 3.77 (s, 12H) ppm.

^{13}C NMR (101 MHz, THF-d^8) δ: 158.0, 150.8, 141.3, 140.1, 139.8, 138.4, 131.2, 130.4, 128.4, 127.2, 126.7, 126.1, 121.1, 120.1, 115.8, 55.8 ppm.

HRMS (MALDI-TOF): *m/z* calculated for $C_{56}H_{42}N_2O_4S_2$: 870.2581, found: 870.2584.

FTIR (KBr): 3008, 2945, 2832, 1605, 1546, 1499, 1464, 1405, 1319, 1288, 1234, 1173, 1100, 1028, 914, 879, 823, 767, 721, 677, 649, 601, 573 cm^{-1}.

m.p.: 220.3−222.3 °C.

2.5.4. Synthesis of HTMs bearing four donor groups

2,3,6,7-tetrabromobenzo[1,2-b:4,5-b']dithiophene (115).

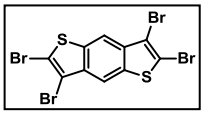

Compound **114** (104 mg, 0.54 mmol) was dissolved in $CHCl_3$ (8 mL). A Br_2 (0.12 mL, 2.45 mmol) solution in $CHCl_3$ (2 mL) was added dropwise at room temperature and the resulting mixture stirred overnight. Sodium hydrogen sulfite solution 40% (15 mL) was added to the mixture resulting in the formation of a white precipitate, which was filtered off, washed with H_2O (20mL), and dried. Obtained off white solid (136 mg, 50%) was used without further purification.

^{1}H NMR (400 MHz, THF-d^8) δ: 8.34 (s, 2H).

^{13}C NMR (175 MHz, THF-d^8) δ: 138.2, 137.1, 118.0, 117.3, 111.5 ppm.

FTIR (neat): 3734, 3651, 3616, 2924, 2851, 1710, 1500, 1465, 1375, 1347, 1269, 1228, 1135, 984, 892, 853, 757, 577 cm^{-1}.

m.p.: 271.4−273.4 °C.

Compound 116.

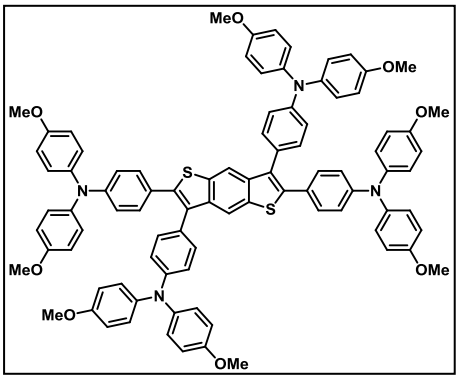

Compounds **115** (101 mg, 0.20 mmol), **64** (362 mg, 0.84 mmol), and $Pd(PPh_3)_4$ (46.0 mg, 0.04 mmol) were dissolved in dry DMF (150 mL) under nitrogen atmosphere. The mixture was degassed for 30 min and K_3PO_4 (1.02 g, 4.80 mmol) was added in one portion. Reaction was stirred at 90 °C for 18 h. Upon cooling to room temperature, quenching with H_2O (50 mL) was followed formation of a precipitate. Formed solid was filtered off, and washed with H_2O (150 mL). Then the precipitate was redissolved in DCM (50 mL). The solvent was removed under reduced pressure. The reaction crude was purified by chromatography (silica gel, DCM/AcOEt 200:1) yielding a pale yellow powder (168 mg, 60%).

^{1}H NMR (400 MHz, THF-d^8) δ: 7.93 (s, 2H), 7.18 (d, *J* = 6.4 Hz, 4H), 7.16 (d, *J* = 6.1 Hz, 4H), 7.13–7.08 (m, 8H), 7.07–7.01 (m, 8H), 6.96 (d, *J* = 8.7 Hz,

4H), 6.88–6.82 (m, 16H), 6.74 (d, *J* = 8.8 Hz, 4H), 3.76 (s, 12H), 3.75 (s, 12H) ppm.

^{13}C NMR (101 MHz, THF-d^{8}) δ: 157.8, 157.6, 149.6, 149.4, 141.8, 141.4, 140.8, 140.4, 136.8, 131.9, 130.7, 128.5, 128.1, 128.0, 127.0, 125.3, 120.8, 119.7, 116.6, 115.7, 55.8 ppm.

m. p: 206.7-208.7 °C.

HRMS (MALDI-TOF): *m/z* calculated for $C_{90}H_{74}N_4O_8S_2$: 1402.4943, found: 1402.4932.

FTIR (neat): 3038, 2999, 2927, 2837, 1741, 1605, 1502, 1463, 1319, 1281, 1239, 1175, 1106, 1034, 826, 729, 603, 575 cm^{-1}.

Compound 118.[121]

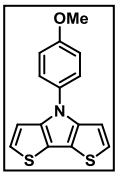

Into a 100 mL 2-neck round bottom flask fitted with a condenser, **117** (2.00 g, 6.20 mmol), **59** (769 mg, 6.2 mmol), Pd_2dba_3 (163 mg, 0.18 mmol), and BINAP (460 mg, 0.74 mmol) were dissolved in dry toluene (20 mL) under nitrogen atmosphere. The mixture was degassed for 30 minutes before adding NaO^{t}Bu (1.80 g, 18.5 mmol) in one portion and then stirred at 110 °C for 18 h. Upon cooling to room temperature, the mixture was quenched with brine (20 mL) and extracted with DCM. Combined organic extracts were dried over anhydrous Na_2SO_4, filtered and evaporated. Resulting residue was purified by flash chromatography (silica gel, hexane/DCM 3:1) giving rise to a white solid (883 mg, 50%).

^{1}H NMR (400 MHz, $CDCl_3$) δ: 7.52–7.47 (m, 2H), 7.16 (d, *J* = 5.3 Hz, 2H), 7.09 (d, *J* = 5.3 Hz, 2H), 7.07–7.03 (m, 2H), 3.88 (s, 3H).

Compound 119.[121]

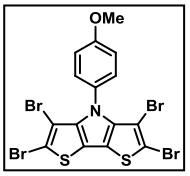

To a stirring solution of **118** (300 mg, 1.05 mmol) in $CHCl_3$ (60 mL) NBS (411 mg, 2.31 mmol) was added. After stirring at room temperature for 3 hours, the reaction was cooled down to 0 °C, and Br_2 (0.18 mL, 3.47 mmol) dissolved in $CHCl_3$ (15 mL) was dropwise added. After stirring for 3 h at 0 ºC, reaction refluxed for 48 h. Resulting dark solution was allowed to cool to room temperature before adding a sodium hydrogen sulfite solution (50 mL, 40%). The mixture was extracted with $CHCl_3$ (3 × 20 mL), and the combined

organic extracts dried over anhydrous Na_2SO_4, filtered and evaporated. Reaction crude was purified by flash chromatography (silica gel, hexane/DCM 3:1) giving a white solid (296 mg, 47%).

^{1}H NMR (400 MHz, $CDCl_3$) δ: 7.34–7.29 (m, 2H), 7.01–6.96 (m, 2H), 3.91 (s, 3H).

Compound 120.

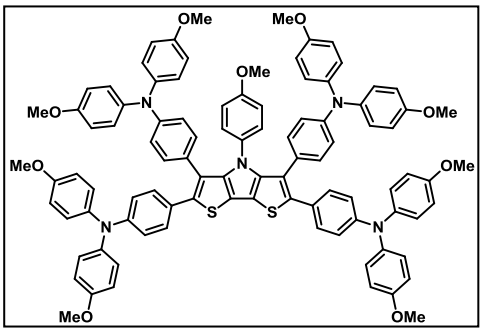

Into a 100 mL 2-neck round bottom flask fitted with a condenser, **119** (174 mg, 0.29 mmol), **64** (626 mg, 1.45 mmol), and $Pd(PPh_3)_4$ (60.0 mg, 0.06 mmol) were dissolved in dry DMF (22 mL) under nitrogen atmosphere. After purging with N_2 for 30 min, K_3PO_4 (1.47 g, 6.96 mmol) was added in one portion and the resulting mixture was stirred at 90 °C for 18 h. Upon cooling to room temperature, the reaction was quenched with a saturated ammonium chloride solution (20 mL) and extracted with DCM (3 × 10 mL). Combined organic extracts were dried over Na_2SO_4, filtered and the solvent removed under reduced pressure. Reaction crude was purified by flash chromatography (silica gel, toluene/ethyl acetate 100:3) yielding an orange solid (390 mg, 60%).

^{1}H NMR (400 MHz, THF-d^8) δ: 7.06–7.03 (m, 4H), 7.02–6.99 (m, 8H), 6.94–6.90 (m, 8H), 6.85–6.79 (m, 16H), 6.72–6.62 (m, 10H), 6.52–6.45 (m, 6H), 3.83 (s, 3H), 3.75 (s, 12H), 3.74 (s, 12H) ppm.

^{13}C NMR (101 MHz, THF-d^8) δ: 159.6, 157.5, 157.2, 148.6, 148.2, 145.4, 141.9, 141.6, 138.0, 131.8, 130.8, 130.0, 128.6, 127.8, 127.4, 125.2, 120.4, 120.2, 115.6, 115.5, 114.2, 113.7, 56.2, 55.7 ppm.

HRMS (MALDI-TOF): *m/z* calculated for $C_{95}H_{79}N_5O_9S_2$: 1497.5314, found: 1497.5259.

FTIR (neat): 2924, 2853, 1718, 1605, 1504, 1464, 1320, 1279, 1240, 1174, 1106, 1034, 827, 728, 575 cm^{-1}.

m.p.: 288.1−290.1 °C.

References

1. G. L. Stephens, J. Li, M. Wild, C. A. Clayson, N. Loeb, S. Kato, T. L'Ecuyer, P. W. Stackhouse Jr, M. Lebsock, T. Andrews, "An update on Earth's energy balance in light of the latest global observations" *Nat. Geoscience* **2012**, *5*, 691−696.
2. Source: International Energy Agency−Photovoltaic Power Systems Programme: www.iea-pvps.org.
3. G. Conibeer, *Materials Today "Third-generation photovoltaics"* **2007**, *10*, 42−50.
4. Source: National Renewable Energy Laboratory (NREL) webpage http://www.nrel.gov.
5. H. Gerischer, M.E. Michel-Beyerle, F. Rebentrost, H. Tributsch, "Sensitization of charge injection into semiconductors with large band gap" *Electrochim. Acta* **1968**, *13*, 1509−1515.
6. B. O'Regan, M. Grätzel, "A low-cost, high-efficiency solar cell based on dye-sensitized colloidal TiO_2 films" *Nature* **1991**, *353*, 737−740.
7. S. Mathew, A. Yella, P. Gao, R. Humphry-Baker, F. E. CurchodBasile, N. Ashari-Astani, I. Tavernelli, U. Rothlisberger, M. K. Nazeeruddin, M. Grätzel, "Dye-sensitized solar cells with 13% efficiency achieved through the molecular engineering of porphyrin sensitizers" *Nat. Chem.* **2014**, *6*, 242−247.
8. A. Kojima, K. Teshima, Y. Shirai, T. Miyasaka, "Organometal halide perovskites as visible-light sensitizers for photovoltaic cells" *J. Am. Chem. Soc*. **2009**, *131*, 6050−6051.
9. a) Y.-C. Hsiao, T. Wu, M. Li, Q. Liu, W. Qin, B. Hu, "Fundamental physics behind high-efficiency organo-metal halide perovskite solar cells" *J. Mater. Chem. A.* **2015**, *3*, 15372−15385. b) J. M. Ball, S. D. Stranks, M. T. Hörantner, S. Hüttner, W. Zhang, E. J.W. Crossland, I. Ramirez, M. Riede, M. B. Johnston, R. H. Friend, H. J. Snaith, "Optical properties and limiting photocurrent of thin-film perovskite solar cells" *Energy Environ. Sci*. **2015**, *8*, 602−609. c) D. Shi, V. Adinolfi, R. Comin, M. Yuan, E. Alarousu, A. Buin, Y. Chen, S. Hoogland, A. Rothenberger, K. Katsiev, Y. Losovyj, X. Zhang, P. A. Dowben, O. F. Mohammed, E. H. Sargent, O. M. Bakr, "Solar cells.

Low trap-state density and long carrier diffusion in organolead trihalide perovskite single crystals" *Science* **2015**, *347*, 519−522.

10. a) A. K. Ghosh, D. L. Morel, T. Feng, R. F. Shaw, C. A. Rowe, "Photovoltaic and rectification properties of Al/Mg phthalocyanine/Ag Schottky-barrier cells" J. *Appl. Phys.* **1974**, *45*, 230−236. b) S. Glenis, G. Tourillon, F. Garnier, "Influence of the doping on the photovoltaic properties of thin films of poly-3-methylthiophene" *Thin Solid Films* **1986**, *139*, 221−231. c) S. Karg, W. Riess, V. Dyakonov, M. Schwoerer, "Electrical and optical characterization of poly(phenylene-vinylene) light emitting diodes" *Synth. Metals* **1993**, *54*, 427−433.

11. a) C. W. Tang, A. C. Albrecht, "Photovoltaic effects of metal–chlorophyll-a–metal sandwich cells" *J. Chem. Phys*. **1975**, *62*, 2139−2149. b) V. Y. Merritt, H. J. Hovel, *Appl. Phys. Lett*. "Organic solar cells of hydroxy squarylium" **1976**, *29*, 414−415. c) F. J. Kampas, M. Gouterman, "Porphyrin films. 3. Photovoltaic properties of octaethylporphine and tetraphenylporphine" *J. Phys. Chem*. **1977**, *81*, 690−695.

12. A. L. Ayzner, C. J. Tassone, S. H. Tolbert, B. J. Schwartz, "Reappraising the Need for Bulk Heterojunctions in Polymer−Fullerene Photovoltaics: The Role of Carrier Transport in All-Solution-Processed P3HT/PCBM Bilayer Solar Cells" *J. Phys. Chem. C* **2009**, *113*, 20050–20060.

13. a) Y. Huang, E. J. Kramer, A. J. Heeger, G. C. Bazan, "Bulk Heterojunction Solar Cells: Morphology and Performance Relationships" *Chem. Rev.* **2014**, *114*, 7006–7043. b) J. L. Delgado, P.-A. Bouit, S. Filippone, M. A. Herranz, N. Martín "Organic photovoltaics: a chemical approach" *Chem. Commun.* **2010**, *46*, 4853–4865. c) A. J. Heeger "25th Anniversary Article: Bulk Heterojunction Solar Cells: Understanding the Mechanism of Operation" *Adv. Mater*. **2014**, *26*, 10–28

14. a) C. J. Brabec, C. Winder, N. S. Sariciftci, J. C. Hummelen, A. Dhanabalan, P. A. van Hal, R. A. J. Janssen "A Low-Bandgap Semiconducting Polymer for Photovoltaic Devices and Infrared Emitting Diodes" *Adv. Funct. Mater*. **2002**, *12*, 709−712. b) P. T.

Boudreault, A. Najari, M. Leclerc "Processable Low-Bandgap Polymers for Photovoltaic Applications" *Chem. Mater*. **2011**, *23*, 456-469. c) J. Hou, H.-Y. Chen, S. Zhang, G. Li, Y. Yang, "Synthesis, Characterization, and Photovoltaic Properties of a Low Band Gap Polymer Based on Silole-Containing Polythiophenes and 2,1,3-Benzothiadiazole" *J. Am. Chem. Soc*. **2008**, *130*, 16144-16145.

15. Y. Liu, C.-C. Chen, Z. Hong, J. Gao, Y. Michael Yang, H. Zhou, L. Dou, G. Li, Y. Yang "Solution-processed small-molecule solar cells: breaking the 10% power conversion efficiency" *Sci. Rep*. **2013**, *3*, 3356.
16. J. You, L. Dou, K. Yoshimura, T. Kato, K. Ohya, T. Moriarty, K. Emery, C.-C. Chen, J. Gao, G. Li, Y. Yang "A polymer tandem solar cell with 10.6% power conversion efficiency" *Nat. Commun*. **2013**, *4*, 1446.
17. J. Frenkel "Some Remarks on the Theory of the Photoelectric Effect" *Phys. Rev*. **1931**, *38*, 309−320.
18. a) S. Yoo, B. Domercq, B. Kippelen "Efficient thin-film organic solar cells based on pentacene/C_{60} heterojunctions" *Appl. Phys. Lett*. **2004**, *85*, 5427−5429. b) Y. Terao, H. Sasabe, C. Adachi, "Correlation of hole mobility, exciton diffusion length, and solar cell characteristics in phthalocyanine/fullerene organic solar cells" *Appl. Phys. Lett*. **2007**, *90*, 103515.
19. T. Förster, Naturwissenschaften **1946**, *33*, 66.
20. B. A. Gregg, J. van de Lagemaat "Solar cells: Folding photons" *Nature Photon*. **2012**, *6*, 278−280.
21. a) X.-Y. Zhu, Q. Yang, M. Muntwiler "Charge-transfer excitons at organic semiconductor surfaces and interfaces" *Acc. Chem. Res*. **2009**, *42*, 1779−1787. b) M. Hallermann, S. Haneder, E. Da Como "Charge-transfer states in conjugated polymer/fullerene blends: Below-gap weakly bound excitons for polymer photovoltaics" *Appl. Phys. Lett*. **2008**, *93*, 053307.
22. H. Bässler, "Charge Transport in Disordered Organic Photoconductors a Monte Carlo Simulation Study" *Phys. Stat. Sol. b* **1993**, *175*, 15−56.

23. L.-M. Chen, Z. Xu, Z. Hong, Y. Yang "Interface investigation and engineering – achieving high performance polymer photovoltaic devices" *J. Mater. Chem.* **2010**, *20*, 2575-2598.
24. L. Onsager "Initial Recombination of Ions" *Phys. Rev.* **1938**, *54*, 554−557.
25. a) W. Tress, A. Merten, M. Furno, M. Hein, K. Leo, M. Riede "Correlation of Absorption Profile and Fill Factor in Organic Solar Cells: The Role of Mobility Imbalance" *Adv. Energy Mater.* **2013**, *3*, 631-638, b) C. M. Proctor, S. Albrecht, M. Kuik, D. Neher, T.-Q. Nguyen "Overcoming Geminate Recombination and Enhancing Extraction in Solution-Processed Small Molecule Solar Cells" *Adv. Energy Mater.* **2014**, *4*, 1400230.
26. D. Credgington, F. C. Jamieson, B. Walker, T. -Q. Nguyen, J. R. Durrant "Quantification of Geminate and Non-Geminate Recombination Losses within a Solution-Processed Small-Molecule Bulk Heterojunction Solar Cell" *Adv. Mater.* **2012**, *24*, 2135−2141.
27. C. G. Shuttle, B. O'Regan, A. M. Ballantyne, J. Nelson, D. D. C. Bradley, J. R. Durrant "Bimolecular recombination losses in polythiophene: Fullerene solar cells" *Phys. Rev. B* **2008**, *78*, 113201.
28. C. Brabec, A. Cravino, D. Meissner, N. Sariciftci, T. Fromherz, M.Rispens, L. Sanchez, J. C. Hummelen "Origin of the Open Circuit Voltage of Plastic Solar Cells" *Adv. Funct. Mater*. **2001**, *11*, 374−380.
29. V. D. Mihailetchi, P. W. M. Blom, J. C. Hummelen, M. T. Rispens "Cathode dependence of the open-circuit voltage of polymer:fullerene bulk heterojunction solar cells" *J. Appl. Phys*. **2003**, *94*, 6849−6854.
30. Q. Peng, K. Park, T. Lin, M. Durstock, L. M. Dai "Donor-π-Acceptor Conjugated Copolymers for Photovoltaic Applications: Tuning the Open-Circuit Voltage by Adjusting the Donor/Acceptor Ratio" J. *Phys. Chem. B* **2008**, *112*, 2801−2808.
31. C.W. Tang "Two-layer organic photovoltaic cell" *Appl. Phys. Lett*. **1986**, *48*, 183−185.
32. N. S. Sariciftci, L. Smilowitz, A. J. Heeger, F. Wudl "Photoinduced electron transfer from a conducting polymer to buckminsterfullerene" *Science* **1992**, *258*, 1474−1476.

33. J. J. M. Halls, C. A. Walsh, N. C. Greenham, E. A. Marseglia, R. H. Friend, S. C. Moratti, A. B. Holmes "Efficient photodiodes from interpenetrating polymer networks" *Nature* **1995**, *376*, 498−500.
34. G. Yu, A. J. Heeger "Charge separation and photovoltaic conversion in polymer composites with internal donor/acceptor heterojunctions" *J. Appl. Phys*. **1995**, *78*, 4510−4515.
35. a) S. E. Shaheen, C. J. Brabec, N. S. Sariciftci, F. Padinger, T. Fromherz, J. C. Hummelen "2.5% efficient organic plastic solar cells" *Appl. Phys. Lett.* **2001**, *78*, 841−843. b) C. J. Brabec, S. E. Shaheen, C. Winder, N. S. Sariciftci *"Effect of LiF/metal electrodes on the performance of plastic solar cells" Appl. Phys. Lett.* **2002**, 80, 1288-1290.
36. a) Y. Kim, S. Cook, S. M. Tuladhar, S. A. Choulis, J. Nelson, J. R. Durrant, D. C. Bradley, M. Giles, I. McCulloch, C.-S. Ha, M. Ree "A strong regioregularity effect in self-organizing conjugated polymer films and high-efficiency polythiophene:fullerene solar cells" *Nature Mater.* **2006**, *5*, 197−203; b) G. Dennler, M. C. Scharber ,C. J. Brabec "Polymer-Fullerene Bulk-Heterojunction Solar Cells" *Adv. Mater.* **2009**, *21*, 1323−1338.
37. a) M. Reyes-Reyes, K. Kim, D. L. Carroll "High-Efficie- ncy Photovoltaic Devices based on Annealed Poly(3-hexyl- thio-phene) and 1-(3-Methoxycarbonyl)- Propyl-1-Phenyl- (6,6) C61 Blends" *Appl. Phys. Lett*. **2005**, *87*, 083506. b) J. Y. Kim, S. H. Kim, H. H. Lee, K. Lee, W. L. Ma, X. Gong, A. J. Heeger "New Architecture for High-Efficiency Polymer Photovoltaic Cells Using Solution-Based Titanium Oxide as an Optical Spacer" *Adv. Mater*. **2006**, *18*, 572−576.
38. A. Sánchez-Díaz, M. Izquierdo, S. Filippone, N. Martín, E. Palomares "The Origin of the High Voltage in DPM12/P3HT Organic Solar Cells" *Adv. Funct. Mater.* **2010**, *20*, 2695−2700.
39. a) J.-L. Brédas, J. E. Norton, J. Cornil, V. Coropceanu "Molecular Understanding of Organic Solar Cells: The Challenges" *Acc. Chem. Res*. **2009**, *42*, 1691−1699. b) H. Zhou, L. Yang, S. Stoneking, W. You "A Weak Donor−Strong Acceptor Strategy to Design Ideal Polymers for Organic Solar Cells" *ACS Appl. Mater. Interfaces* **2010**, *2*, 1377−1383.

40. a) H. Choi, S.-J. Ko, T. Kim, P.-O. Morin, B. Walker, B. H. Lee, M-Leclerc, J. Y. Kim, A. J. Heeger "Small-Bandgap Polymer Solar Cells with Unprecedented Short-Circuit Current Density and High Fill Factor" *Adv. Mater.* **2015**, *27*, 3318−3324. b) J. Huang, J. H. Carpenter, C.-Z. Li, J.-S. Yu, H. Ade, A. K.-Y. Jen "Highly Efficient Organic Solar Cells with Improved Vertical Donor–Acceptor Compositional Gradient Via an Inverted Off-Center Spinning Method" *Adv. Mater.* **2016**, *28*, 967−974.
41. C. B. Nielsen, S. Holliday, H.-Y. Chen, S. J. Cryer, I. McCulloch "Non-Fullerene Electron Acceptors for Use in Organic Solar Cells" *Acc. Chem. Res.* **2015**, *48*, 2803−2812.
42. Q. Wu, D. Zhao, A. M. Schneider, W. Chen, L. Yu "Covalently Bound Clusters of Alpha-Substituted PDI—Rival Electron Acceptors to Fullerene for Organic Solar Cells" *J. Am. Chem. Soc.* **2016**, *138*, 7248−7251.
43. a) B. Verreet, B. P. Rand, D. Cheyns, A. Hadipour, T. Aernouts, P. Heremans, A. Medina, C. G. Claessens, T. Torres "A 4% Efficient Organic Solar Cell Using a Fluorinated Fused Subphthalocyanine Dimer as an Electron Acceptor" *Adv. Energy Mater.* **2011**, *1*, 565–568. b) K. Cnops, B. P. Rand, D. Cheyns, B. Verreet, M. A. Empl, P. Heremans "8.4% efficient fullerene-free organic solar cells exploiting long-range exciton energy transfer" *Nature Commun.* **2014**, *5*, 3406.
44. S. Li, L. Ye, W. Zhao, S. Zhang, S. Mukherjee, H. Ade, J. Hou "Energy-Level Modulation of Small-Molecule Electron Acceptors to Achieve over 12% Efficiency in Polymer Solar Cells" *Adv. Mater.* **2016**, *28*, 9423–9429.
45. B. Kan, M. Li, Q. Zhang, F. Liu, X. Wan, Y. Wang, W. Ni, G. Long, X. Yang, H. Feng, Y. Zuo, M. Zhang, F. Huang, Y. Cao, T. P. Russell, Y. Chen "A Series of Simple Oligomer-like Small Molecules Based on Oligothiophenes for Solution-Processed Solar Cells with High Efficiency" *J. Am. Chem. Soc.* **2015**, *137*, 3886−3893.
46. J.-L. Wang, Q.-R. Yin, J.-S. Miao, Z. Wu, Z.-F. Chang, Y. Cao, R.-B. Zhang, J.-Y. Wang, H.-B. Wu, Y. Cao "Rational Design of Small Molecular Donor for Solution-Processed Organic Photovoltaics with 8.1% Efficiency and High Fill Factor via Multiple Fluorine

Substituents and Thiophene Bridge" *Adv. Funct. Mater.* **2015**, *25*, 3514–3523.

47. J. Du, A. Fortney, K. E. Washington, C. Bulumulla, P. Huang, D. Dissanayake, M. C. Biewer, T. Kowalewski, M. C. Stefan "Systematic Investigation of Benzodithiophene-Benzothiadiazole Isomers for Organic Photovoltaics" *ACS Appl. Mater. Interfaces* **2016**, *8*, 33025−33033.
48. a) G. C. Welch, L. A. Perez, C. V. Hoven, Y. Zhang, X.-D. Dang, A. Sharenko, M. F. Toney, E. J. Kramer, T.-Q. Nguyen, G. C. Bazan "A modular molecular framework for utility in small-molecule solution-processed organic photovoltaic devices" *J. Mater. Chem.* **2011**, *21*, 12700−12709. b) Z. B. Henson, G. C. Welch, T. van der Poll, G. C. Bazan "Pyridalthiadiazole-Based Narrow Band Gap Chromophores" *J. Am. Chem. Soc.* **2012**, *134*, 3766−3779.
49. Y. Sun, G. C. Welch, W. L. Leong, C. J. Takacs, G. C. Bazan, A. J. Heeger "Solution-processed small-molecule solar cells with 6.7% efficiency" *Nat. Mater.* **2012**, *11*, 44−48.
50. T. S. van der Poll, J. A. Love, T. Q. Nguyen, G. C. Bazan "Non-basic high-performance molecules for solution-processed organic solar cells" *Adv. Mater.* **2012**, *24*, 3646−3649.
51. C. D. Wessendorf, G. L. Schulz, A. Mishra, P. Kar, I. Ata, M. Weidelener, M. Urdanpilleta, J. Hanisch, E. Mena-Osteritz, M. Lindén, E. Ahlswede, P. Bäuerle "Efficiency Improvement of Solution-Processed Dithienopyrrole-Based A-D-A Oligothiophene Bulk-Heterojunction Solar Cells by Solvent Vapor Annealing" *Adv. Energy Mater.* **2014**, *4*, 1400266.
52. a) Y. Liu, X. Wan, F. Wang, J. Zhou, G. Long, J. Tian, Y. Chen "High-Performance Solar Cells using a Solution-Processed Small Molecule Containing Benzodithiophene Unit" *Adv. Mater.* **2011**, *23*, 5387–5391. b) J. Zhou, X. Wan, Y. Liu, Y. Zuo, Z. Li, G. He, G. Long, W. Ni, C. Li, X. Su, Y. Chen "Small Molecules Based on Benzo[1,2-b:4,5-b′]dithiophene Unit for High-Performance Solution-Processed Organic Solar Cells" *J. Am. Chem. Soc.* **2012**, *134*, 16345–16351. c) S. Shen, P. Jiang, C. He, J. Zhang, P. Shen, Y. Zhang, Y. Yi, Z. Zhang, Z. Li, Y. Li "Solution-Processable Organic Molecule Photovoltaic Materials with Bithienyl-benzodithiophene Central Unit and Indenedione End

Groups" *Chem. Mater.* **2013**, *25*, 2274−2281. d) B. Kan, Q. Zhang, M. Li, X. Wan, W. Ni, G. Long, Y. Wang, X. Yang, H. Feng, Y. Chen "Solution-Processed Organic Solar Cells Based on Dialkylthiol-Substituted Benzodithiophene Unit with Efficiency near 10%" *J. Am. Chem. Soc*. **2014**, *136*, 15529–15532. e) M. Li, F. Liu, X. Wan, W. Ni, B. Kan, H. Feng, Q. Zhang, X. Yang, Y. Wang, Y. Zhang, Y. Shen, T. P. Russell, Y. Chen "Subtle Balance Between Length Scale of Phase Separation and Domain Purification in Small-Molecule Bulk-Heterojunction Blends under Solvent Vapor Treatment" *Adv. Mater*. **2015**, *27*, 6296–6302.

53. D. Deng, Y. Zhang, J. Zhang, Z. Wang, L. Zhu, J. Fang, B. Xia, Z. Wang, K. Lu, W. Ma, Z. Wei "Fluorination-enabled optimal morphology leads to over 11% efficiency for inverted small-molecule organic solar cells" *Nature Commun.* **2016**, *7*, 13740.
54. a) Z. Li, G. He, X. Wan, Y. Liu, J. Zhou, G. Long, Y. Zuo, M. Zhang, Y. Chen "Solution Processable Rhodanine-Based Small Molecule Organic Photovoltaic Cells with a Power Conversion Efficiency of 6.1%" *Adv. Energy Mater.* **2012**, *2*, 74–77. b) R. Fitzner, E. Mena-Osteritz, A. Mishra, G. Schulz, E. Reinold, M. Weil, C. Körner, H. Ziehlke, C. Elschner, K. Leo, M. Riede, M. Pfeiffer, C. Uhrich, P. Bäuerle "Correlation of π-Conjugated Oligomer Structure with Film Morphology and Organic Solar Cell Performance" *J. Am. Chem. Soc.* **2012**, *134*, 11064–11067, c) G. He, Z. Li, X. Wan, Y. Liu, J. Zhou, G. Long, M. Zhang, Y. Chen "Impact of dye end groups on acceptor–donor–acceptor type molecules for solution-processed photovoltaic cells" *J. Mater. Chem.* **2012**, *22*, 9173-9180.
55. Y. Liu, C.-C. Chen, Z. Hong, J. Gao, Y. (M.) Yang, H. Zhou, L. Dou, G. Li, Y. Yang "Solution-processed small-molecule solar cells: breaking the 10% power conversion efficiency" *Sci. Rep.* **2013**, *3*, 3356.
56. Q. Zhang, B. Kan, F. Liu, G. Long, X. Wan, X. Chen, Y. Zuo, W. Ni, H. Zhang, M. Li, Z. Hu, F. Huang, Y. Cao, Z. Liang, M. Zhang, T. P. Russell, Y. Chen "Small-molecule solar cells with efficiency over 9%" *Nature Photonics* **2015**, *9*, 35-41.

57. H. Yao, L. Ye, H. Zhang, S. Li, S. Zhang, J. Hou "Molecular Design of Benzodithiophene-Based Organic Photovoltaic Materials" *Chem. Rev.*, **2016**, *116*, 7397−7457.
58. J. Hou, M.-H. Park, S. Zhang, Y. Yao, L.-M. Chen, J.-H. Li, Y. Yang "Bandgap and Molecular Energy Level Control of Conjugated Polymer Photovoltaic Materials Based on Benzo[1,2-*b*:4,5-*b′*]dithiophene" *Macromolecules* **2008**, *41*, 6012−6018.
59. K. R. Graham, C. Cabanetos, J. P. Jahnke, M. N. Idso, A. El Labban, G. O. N. Ndjawa, T. Heumueller, K. Vandewal, A. Salleo, B. F. Chmelka, A. Amassian, P. M. Beaujuge, M. D. McGehee "Importance of the Donor:Fullerene Intermolecular Arrangement for High-Efficiency Organic Photovoltaics" *J. Am. Chem. Soc.* **2014**, *136*, 9608−9618.
60. M. Pagliaro, R.Ciriminna, G.Parmisano *"Flexible Solar Cells" ChemSusChem.* **2008**, *1*, 880−891.
61. B. Fu, J. Baltazar, Z. Hu, A.-T. Chien, S. Kumar, C. L. Henderson, D.M. Collard, E. Reichmanis "High Charge Carrier Mobility, Low Band Gap Donor–Acceptor Benzothiadiazole-oligothiophene Based Polymeric Semiconductors" *Chem. Mater.* **2012**, *24*, 4123−4133.
62. H. Li, A. S. Batsanov, K. C. Moss, H. L. Vaughan, F. B. Dias, K. T. Kamtekar, M. R. Bryce, A. P. Monkman "The interplay of conformation and photophysical properties in deep-blue fluorescent oligomers" *Chem. Commun.* **2010**, *46*, 4812–4814.
63. J. Zhou, Y. Zuo, X. Wan, G. Long, Q. Zhang, W. Ni, Y. Liu, Z. Li, G. He, C. Li, B. Kan, M. Li, Y. Chen "Solution-Processed and High-Performance Organic Solar Cells Using Small Molecules with a Benzodithiophene Unit" *J. Am. Chem. Soc.* **2013**, *135*, 8484−8487.
64. a) L. Liang, J.-T. Wang, X. Xiang, J. Ling, F.-G. Zhao, W.-S. Li "Influence of moiety sequence on the performance of small molecular photovoltaic materials" *J. Mater. Chem. A* **2014**, *2*, 15396–15405, b) J. Du, A. Fortney, K. E. Washington, C. Bulumulla, P. Huang, D. Dissanayake, M. C. Biewer, T. Kowalewski, M. C. Stefan "Systematic Investigation of Benzodithiophene-Benzothiadiazole Isomers for Organic Photovoltaics" *ACS Appl. Mater. Interfaces* **2016**, *8*, 33025−33033.

65. J. J. Kwiatkowski, J. M. Frost, J. Nelson "The Effect of Morphology on Electron Field-Effect Mobility in Disordered C60 Thin Films" *Nano Lett.* **2009**, *9*, 1085–1090.
66. J. Mao, N. He, Z. Ning, Q. Zhang, F. Guo, L. Chen, W. Wu, J. Hua, H. Tian "Stable Dyes Containing Double Acceptors without COOH as Anchors for Highly Efficient Dye-Sensitized Solar Cells" *Angew. Chem. Int. Ed.* **2012**, *51*, 9873–9876.
67. M. Ono, S. Hayashi, K. Matsumura, H. Kimura, Y. Okamoto, M. Ihara, R. Takahashi, H. Mori, H. Saji "Rhodanine and Thiohydantoin Derivatives for Detecting Tau Pathology in Alzheimer's Brains" *ACS Chem Neurosci*. **2011**, *2*, 269−275.
68. K. Brunner, A. van Dijken, H. Börner, J. J. A. M. Bastiaansen, N. M. M. Kiggen, B. M. W. Langeveld *"*Carbazole Compounds as Host Materials for Triplet Emitters in Organic Light-Emitting Diodes: Tuning the HOMO Level without Influencing the Triplet Energy in Small Molecules*" J. Am. Chem. Soc*. **2004**, *126*, 6035−6042.
69. K. C. Moss, K. N. Bourdakos, V. Bhalla, K. T. Kamtekar, M. R. Bryce, M. A. Fox, H. L. Vaughan, F. B. Dias, A. P. Monkman "Tuning the Intramolecular Charge Transfer Emission from Deep Blue to Green in Ambipolar Systems Based on Dibenzothiophene *S*,*S*-Dioxide by Manipulation of Conjugation and Strength of the Electron Donor Units" *J. Org. Chem.* **2010**, *75*, 6771–6781.
70. V. Maurel, M. Jouni, P. Baran, N. Onofrio, S. Gambarelli, J.-M. Mouesca, D. Djurado, L. Dubois, J.-F. Jacquot, G. Desfondsa, I. Kulszewicz-Bajer "Magnetic properties of a doped linear polyarylamine bearing a high concentration of coupled spins (S = 1)" *Phys. Chem. Chem. Phys.* **2012**, *14*, 1399−1407.
71. V. Maurel, L. Skorka, N. Onofrio, E. Szewczyk, D. Djurado, L. Dubois, J.-M. Mouesca, I. Kulszewicz-Bajer *"*Ferromagnetic Spin Coupling through the 3,4′-Biphenyl Moiety in Arylamine Oligomers—Experimental and Computational Study*" J. Phys. Chem. B* **2014**, *118*, 7657−7667.
72. F. B. Dias, J. Santos, D. R. Graves, P. Data, R. S. Nobuyasu, M. A. Fox, A. S. Batsanov, T. Palmeira, M. N. Berberan-Santos, M. R. Bryce, A. P. Monkman "The Role of Local Triplet Excited States and

D-A Relative Orientation in Thermally Activated Delayed Fluorescence: Photophysics and Devices" *Adv. Sci.* **2016**, *3*, 1600080.

73. L. L. Hill, L. R. Moore, R. Huang, R. Craciun, A. J. Vincent, D. A. Dixon, J. Chou, C. J. Woltermann, K. H. Shaughnessy "Bulky Alkylphosphines with Neopentyl Substituents as Ligands in the Amination of Aryl Bromides and Chlorides" *J. Org. Chem.* **2006**, *71*, 5117−5125.
74. A. C. Hernandez-Perez, A. Caron, S. K. Collins "Photochemical Synthesis of Complex Carbazoles: Evaluation of Electronic Effects in Both UV- and Visible-Light Methods in Continuous Flow" *Chem. Eur. J.* **2015**, *21*, 16673−16678.
75. L. Cai, T. Moehl, S.-J. Moon, J.-D. Decopet, R. Humphry-Baker, Z. Xue, L. Bin, S. M Zakeeruddin, M. Grätzel "4,9-Dihydro-4,4,9,9-tetrahexyl-*s*-indaceno[1,2-*b*:5,6-*b*′]dithiophene as a π-Spacer of Donor−π–Acceptor Dye and Its Photovoltaic Performance with Liquid and Solid-State Dye-Sensitized Solar Cells" *Org. Lett*. **2014**, *16*, 106−109.
76. K. Rakstys, A. Abate, M. I. Dar, P. Gao, V. Jankauskas ,G. Jacopin , E. Kamarauskas, S. Kazim, S. Ahmad, M. Grätzel, M. K. Nazeeruddin "Triazatruxene-Based Hole Transporting Materials for Highly Efficient Perovskite Solar Cells" *J. Am. Chem. Soc.* **2015**, *137*, 16172−16178.
77. R. Anémian, D.C. Cupertino, P.R. Mackie, S.G. Yeates "Solution phase studies towards the synthesis of triarylamine oligomers using a germanium linker on a solid support" *Tetrahedron Letters* **2005**, *46*, 6717−6721.
78. K. Harada, H. Kubo, J. Abe, M. Haneta, A. Conception, S. Inoue, S. Okada, K. Nishioka "Discovery of potent and orally bioavailable 17β-hydroxysteroid dehydrogenase type 3 inhibitors" *Bioorg. Med. Chem.* **2012**, *20*, 3242–3254.
79. Y. Ma, T. Leng, G. Lai, Z. Li, X. Xu, J. Zou, Y. Shen, C. Wang "A highly selective and sensitive probe based on benzo[1,2-b:4,5-b′]dithiophene: synthesis, detection for Cu(II) and self-assembly" *Tetrahedron* **2016**, *72*, 2219−2225.
80. Q. Zou, H. Tian "Chemodosimeters for mercury(II) and methylmercury(I) based on 2,1,3-benzothiadiazole" *Sensors and Actuators B* **2010**, *149*, 20−27.

81. S. Ohira, I. Rudra, K. Schmidt, S. Barlow, S.-J. Chung, Q. Zhang, J. Matichak, S. R. Marder, J.-L. Brédas "Electronic and Vibronic Contributions to Two-Photon Absorption in Donor–Acceptor–Donor Squaraine Chromophores" *Chem. Eur. J*. **2008**, *14*, 11082−11091.
82. H.-S. Kim, C.-R. Lee, J.-H. Im, K.-B. Lee, T. Moehl, A. Marchioro, S.-J. Moon, R. Humphry-Baker, J.-H. Yum, J. E. Moser, M. Grätzel, N.-G. Park "Lead Iodide Perovskite Sensitized All-Solid-State Submicron Thin Film Mesoscopic Solar Cell with Efficiency Exceeding 9%" *Sci. Rep*. **2012**, *2*, 591.
83. M. M. Lee, J. Teuscher, T. Miyasaka, T. N. Murakami, H. J. Snaith "Efficient Hybrid Solar Cells Based on Meso-Superstructured Organometal Halide Perovskites" *Science* **2012**, *338*, 643.
84. G. E. Eperon, S. D. Stranks, C. Menelaou, M. B. Johnston, L. M. Herz, H. J. Snaith "Formamidinium lead trihalide: a broadly tunable perovskite for efficient planar heterojunction solar cells" *Energy Environ. Sci*. **2014**, *7*, 982−988.
85. J.-W. Lee, D.-J. Seol, A.-N. Cho, N.-G. Park "High-Efficiency Perovskite Solar Cells Based on the Black Polymorph of $HC(NH_2)_2PbI_3$" *Adv. Mater*. **2014**, *26*, 4991−4998.
86. F. Hao, C. C. Stoumpos, D. H. Cao, R. P. H. Chang, M. G. Kanatzidis "Lead-free solid-state organic–inorganic halide perovskite solar cells" *Nat. Photonics*, **2014**, *8*, 489−494.
87. C. R. Kagan, D. B. Mitzi, C. D. Dimitrakopoulos "Organic-inorganic hybrid materials as semiconducting channels in thin-film field-effect transistors" *Science* **1999**, *286*, 945−947.
88. T. Hattori, T. Taira, M. Era, T. Tsuitsui, S. Saito "Highly efficient electroluminescence from a heterostructure device combined with emissive layered-perovskite and an electron-transporting organic compound" *Chem. Phys. Lett*. **1996**, *254*, 103−108.
89. A. Kojima, K. Teshima, Y. Shirai, T. Miyasaka "Organometal halide perovskites as visible-light sensitizers for photovoltaic cells" *J. Am. Chem. Soc*. **2009**, *131*, 6050−6051.
90. J. H. Im, C. R. Lee, J. W. Lee, S. W. Park and N. G. Park "6.5% efficient perovskite quantum-dot-sensitized solar cell" *Nanoscale* **2011**, *3*, 4088−4093.

91. U. Bach, D. Lupo, P. Comte, J. E. Moser, F. Weissortel, J. Salbeck, H. Spreitzer, M. Grätzel "Solid-state dye-sensitized mesoporous TiO_2 solar cells with high photon-to-electron conversion efficiencies" *Nature* **1998**, *395*, 583−585.
92. H. S. Kim, C. R. Lee, J. H. Im, K. B. Lee, T. Moehl, A. Marchioro, S. J. Moon, R. Humphry-Baker, J. H. Yum, J. E. Moser, M. Grätzel, N. G. Park "Lead Iodide Perovskite Sensitized All-Solid-State Submicron Thin Film Mesoscopic Solar Cell with Efficiency Exceeding 9%" *Sci. Rep*. **2012**, *2*, 591.
93. M. M. Lee, J. Teuscher, T. Miyasaka, T. N. Murakami, H. J. Snaith "Efficient hybrid solar cells based on meso-superstructured organometal halide perovskites" *Science* **2012**, *338*, 643−647.
94. G. E. Eperon, S. D. Stranks, C. Menelaou, M. B. Johnston, L. M. Herz, H. J. Snaith "Formamidinium lead trihalide: a broadly tunable perovskite for efficient planar heterojunction solar cells" *Energy Environ. Sci*. **2014**, *7*, 982−988.
95. C. C. Stoumpos, C. D. Malliakas, M. G. Kanatzidis "Semiconducting Tin and Lead Iodide Perovskites with Organic Cations: Phase Transitions, High Mobilities, and Near-Infrared Photoluminescent Properties" *Inorg. Chem*. **2013**, *52*, 9019−9038.
96. a) J. Calabrese, N. L. Jones, R. L. Harlow, N. Herron, D. L. Thorn, Y. Wang "Preparation and characterization of layered lead halide compounds" *J. Am. Chem. Soc.* **1991**, *113*, 2328−2330; b) A. Kojima, K. Teshima, Y. Shirai, T. Miyasaka **"**Organometal halide perovskites as visible-light sensitizers for photovoltaic cells**"** *J. Am. Chem. Soc*. **2009**, *131*, 6050−6051.
97. J. H. Noh, S. H. Im, J. H. Heo, T. N. Mandal, S. I. Seok "Chemical Management for Colorful, Efficient, and Stable Inorganic–Organic Hybrid Nanostructured Solar Cells" *Nano Lett*. **2013**, *13*, 1764−1769.
98. N. J. Jeon, J. H. Noh, W. S. Yang, Y. C. Kim, S. Ryu, J. Seo, S. I. Seok "Compositional engineering of perovskite materials for high-performance solar cells" *Nature* **2015**, *517*, 476−480.
99. L. Etgar, P. Gao, Z. Xue, Q. Peng, A. K. Chandiran, B. Liu, M. K. Nazeeruddin, M. Grätzel "Mesoscopic $CH_3NH_3PbI_3/TiO_2$ heterojunction solar cells" *J. Am. Chem. Soc*. **2012**, *134*, 17396−17399.

100. A. Abrusci, S. D. Stranks, P. Docampo, H.-L. Yip, A. K.-Y. Jen, H. J. Snaith "High-Performance Perovskite-Polymer Hybrid Solar Cells via Electronic Coupling with Fullerene Monolayers" *Nano Lett.* **2013**, *13*, 3124–3128.
101. S. S. Reddy, K. Gunasekar, J. H. Heo, S. H. Im, C. S. Kim, D.-H. Kim, J. H. Moon, J. Y. Lee, M. Song, S.-H. Jin "Highly Efficient Organic Hole Transporting Materials for Perovskite and Organic Solar Cells with Long-Term Stability" *Adv. Energy Mater*. **2016**, *28*, 686−693.
102. J. Wang, K. Liu, L. Ma, X. Zhan "Triarylamine: Versatile Platform for Organic, Dye-Sensitized, and Perovskite Solar Cells" *Chem. Rev.* **2016**, *116*, 14675−14725.
103. H. Zhou, Q. Chen, G. Li, S. Luo, T.-b. Song, H.-S. Duan, Z. Hong, J. You, Y. Liu, Y. Yang "Photovoltaics. Interface engineering of highly efficient perovskite solar cells" *Science* **2014**, *345*, 542−546.
104. C. Huang, W. Fu, C.-Z. Li, Z. Zhang, W. Qiu, M. Shi, P. Heremans, A. K.-Y. Jen, H. Chen "Dopant-Free Hole-Transporting Material with a C_{3h} Symmetrical Truxene Core for Highly Efficient Perovskite Solar Cells" *J. Am. Chem. Soc*. **2016**, *138*, 2528−2531.
105. N. J. Jeon, H. G. Lee, Y. C. Kim, J. Seo, J. H. Noh, J. Lee, S. I. Seok "*o*-Methoxy Substituents in Spiro-OMeTAD for Efficient Inorganic–Organic Hybrid Perovskite Solar Cells" *J. Am. Chem. Soc*. **2014**, *136*, 7837−7840.
106. Z. Hu, W. Fu, L. Yan, J. Miao, H. Yu, Y. He, O. Goto, H. Meng, H. Chen, W. Huang "Effects of heteroatom substitution in spiro-bifluorene hole transport materials" *Chem. Sci*. **2016**, *7*, 5007−5012.
107. P. Ganesan, K. Fu, P. Gao, I. Raabe, K. Schenk, R. Scopelliti, J. Luo, L. H. Wong, M. Grätzel, M. K. Nazeeruddin "A simple spiro-type hole transporting material for efficient perovskite solar cells" *Energy Environ. Sci*. **2015**, *8*, 1986−1991.
108. M. Franckevicius, A. Mishra, F. Kreuzer, J. Luo, S. M. Zakeeruddin, M. Grätzel "A dopant-free spirobi[cyclopenta[2,1-*b*:3,4-*b′*]dithiophene] based hole-transport material for efficient perovskite solar cells" *Mater. Horiz.* **2015**, *2*, 613−618.
109. D. Bi, B. Xu, P. Gao, L. Sun, M. Grätzel, A. Hagfeldt "Facile Synthesized Organic Hole Transporting Material for Perovskite Solar Cell with Efficiency of 19.8%" *Nano Energy* **2016**, *23*, 138−144.

110. Y.-K. Wang, Z.-C. Yuan, G.-Z. Shi, Y.-X. Li, Q. Li, F. Hui, B.-Q. Sun, Z.-Q. Jiang, L.-S. Liao "Dopant-Free Spiro-Triphenylamine/Fluorene as Hole-Transporting Material for Perovskite Solar Cells with Enhanced Efficiency and Stability" *Adv. Funct. Mater*. **2016**, *26*, 1375−1381.
111. M. Saliba, S. Orlandi, T. Matsui, S. Aghazada, M. Cavazzini, J.-P. Correa-Baena, P. Gao, R. Scopelliti, E. Mosconi, K. H. Dahmen, F. De Angelis, A. Abate, A. Hagfeldt, G. Pozzi, M. Grätzel, M. K. Nazeeruddin "A molecularly engineered hole-transporting material for efficient perovskite solar cells" *Nature Energy* **2016**, *1*, 15017.
112. A. Molina-Ontoria, I. Zimmermann, I. Garcia-Benito, P. Gratia, C. Roldan-Carmona, S. Aghazada, M. Grätzel, M. K. Nazeeruddin, N. Martin *"*Benzotrithiophene-Based Hole-Transporting Materials for 18.2 % Perovskite Solar Cells*" Angew. Chem. Int. Ed*. **2016**, *55*, 6270−6274.
113. I. Zimmermann, J. Urieta-Mora, P. Gratia, J. Aragó, G. Grancini, A. Molina-Ontoria, E. Ortí, N. Martín, M. K.Nazeeruddin "High-Efficiency Perovskite Solar Cells Using Molecularly Engineered, Thiophene-Rich, Hole-Transporting Materials:Influence of Alkyl Chain Length on Power Conversion Efficiency" Adv. Energy Mater. **2016**, 1601674.
114. K. Rakstys, M. Saliba, P. Gao, P. Gratia, E. Kamarauskas, S. Paek, V. Jankauskas, M. K. Nazeeruddin "Highly Efficient Perovskite Solar Cells Employing an Easily Attainable Bifluorenylidene-Based Hole-Transporting Material" *Angew. Chem. Int. Ed*. **2016**, *55*, 7464−7468.
115. a) M. C. Alonso García, J. L. Balenzategui "Estimation of photovoltaic module yearly temperature and performance based on Nominal Operation Cell Temperature calculations" *Renewable Energy* **2004**, *29*, 1997−2010; b) H. Zhang, X. Qiao, Y. Shen, M. Wang "Effect of temperature on the efficiency of organometallic perovskite solar cells" J. *Energy Chem*. **2015**, *24*, 729–735.
116. J. Korang, W. R. Grither, R. D. McCulla "Photodeoxygenation of Dibenzothiophene *S*-Oxide Derivatives in Aqueous Media" *J. Am. Chem. Soc.* **2010**, *132*, 4466–4476.

117. S. H. Jeong, J. Y. Lee "Dibenzothiophene derivatives as host materials for high efficiency in deep blue phosphorescent organic light emitting diodes" *J. Mater. Chem.* **2011**, *21*, 14604–14609.
118. M. K. Etherington, F. Franchello, J. Gibson, T. Northey, J. Santos, J. S. Ward, H. F. Higginbotham, P. Data, A. Kurowska, P. Lays Dos Santos, D. R. Graves, A. S. Batsanov, F. B. Dias, M. R. Bryce, T. J. Penfold, A. P. Monkman "Regio- and conformational isomerisation critical to design of efficient thermally-activated delayed fluorescence emitters" *Nat. Commun.* **2017**, *8*, 14987.
119. T.-H. Huang, W.-T. Whang, J. Y. Shen, J. T. Lin, H. Zheng "Organic electroluminescent derivatives containing dibenzothiophene and diarylamine segments" *J. Mater. Chem.* **2005**, *15*, 3233–3240.
120. S. Sundarraj, C. Eickhoff, S. Bahulayan, R. Send, Y. Nishimae, H. Reichelt, J. Tanabe, P. Erk "Compounds with terminal heteroarylcyanovinylene groups and their use in organic solar cells" WO 2015/024848 A l, 26.02.2015.
121. H.-L. Wong, C.-C. Ko, W. H. Lam, N. Zhu, V. W.-W. Yam "Design and Synthesis of a New Class of Photochromic Diarylethene-Containing Dithieno[3,2-b:2′,3′-d]pyrroles and Their Switchable Luminescence Properties" *Chem. Eur. J.* **2009**, *15*, 10005−10009.